FABRICATION OF PRINTABLE FLEXIBLE THERMOELECTRIC MATERIAL AND DEVICES

A Thesis submitted to the

UPES

For the Award of

DOCTOR OF PHILOSOPHY

in
Department of Chemistry

By
VAISHALI RATHI

May 2025

SUPERVISOR (S)

Prof. Ranjeet Brajpuriya

Dr. K. P. S. Parmar

Dr. Ashish Kumar

Department of Chemistry, Applied Science Cluster

School of Advanced Engineering (SOAE)

UPES Dehradun - 248007: Uttarakhand, India

FABRICATION OF PRINTABLE FLEXIBLE THERMOELECTRIC MATERIAL AND DEVICES

A Thesis submitted to the

UPES

For the Award of
Doctor of Philosophy
in
Department of Chemistry

By
VAISHALI RATHI

(SAP ID: 500099685)

May 2025

SUPERVISOR
PROF. RANJEET BRAJPURIYA
Professor, Department of Physics
Applied Science Cluster, SoAE, UPES

CO-SUPERVISOR
DR. K. P. S. PARMAR
Asso. Professor, Department of Physics
Applied Science Cluster, SoAE, UPES

EXTERNAL SUPERVISOR
DR. ASHISH KUMAR
Asso. Professor, Department of Physics & Astronomical Sciences
Central University of Jammu, J & K, India

Department of Chemistry, Applied Science Cluster,
School of Advanced Engineering (SoAE)
UPES Dehradun - 248007: Uttarakhand

DECLARATION

I declare that the thesis entitled "Fabrication of printable flexible thermoelectric material and devices" has been prepared by me under the guidance of Prof. Ranjeet Brajpuriya, Professor (supervisor), Dr. K. P. S. Parmar, Associate Professor (co-supervisor), Applied Science Cluster, School of Advance Engineering (SoAE), UPES, and Dr. Ashish Kumar, Associate Professor, Dept. of Physics & Astronomical Sciences, Central University of Jammu, J & K. No part of this thesis has formed the basis for the award of any degree or Fellowship previously.

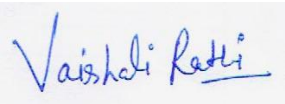

Vaishali Rathi
Department of Chemistry
Applied Science Cluster, SoAE
Upes, Energy Acres, Bidholi Via Prem Nagar
Dehradun-248007, India.

Date: 29/01/2025
Place: Dehradun, Uttarakhand (India)

CERTIFICATE

I certify that Ms. Vaishali Rathi has prepared her thesis entitled "**Fabrication of Printable Flexible Thermoelectric Material and Devices",** for the award of PhD degree of the UPES, under my guidance. She has carried out her research work at the Department of Chemistry, UPES, Dehradun.

Supervisor
Prof. Ranjeet Brajpuriya
Applied Science Cluster, SOAE
UPES, Energy Acres, Bidholi
Dehradun - 248007

Date: 29/01/2025

Co-Supervisor
Dr. K. P. S Parmar
Applied Science Cluster, SOAE
UPES, Energy Acres, Bidholi
Dehradun – 248007

Date: 29/01/2025

जम्मू केंद्रीय विश्वविद्यालय
Central University of Jammu
भौतिकी एवं खगोल विज्ञान विभाग
Department of Physics and Astronomical Sciences
राया-सूचानी (बागला), साम्बा-181143, जम्मू (जम्मू और कश्मीर)
Rahya-Suchani (Bagla), Samba-181143, Jammu (J & K)

29th Jan., 2025

CERTIFICATE

I certify that Ms. Vaishali Rathi has prepared her thesis entitled **"Fabrication of Printable Flexible Thermoelectric Material and Devices"**, for the award of PhD degree of the UPES, under my guidance. She has carried out the work at the Department of Chemistry, UPES, Dehradun.

External Supervisor

Dr. Ashish Kumar

Dept. of Physics & Astronomical Sciences,

Central University of Jammu, (J & K), India

Date: 29th January 2025.

ABSTRACT

Thermoelectric Materials (TE) are significant for sustainable energy harvesting, as they convert waste heat into electricity via the Seebeck effect. This study investigates the fabrication and characterization of flexible, printable organic and organic-inorganic hybrid thermoelectric materials aimed at improving their performance and scalability for energy conversion applications. This study examines p-type and n-type materials, specifically PEDOT: PSS composites and PVDF/Ni nanowires hybrid. This study utilizes advanced doping techniques and nano structuring to enhance electrical conductivity, Seebeck coefficient, and power factor, all while maintaining low thermal conductivity.

Experimental methodologies and materials used throughout the study high purity reagents such as PEDOT: PSS, Bi_2Te_3, rGO, P_3HT, $FeCl_3$, PVDF, and Ni Nanowires were utilized to fabricate both p-type and n-type films. Standard solution processing techniques such as spin-coating and drop casting were employed for film deposition. Structural and morphological characterizations were conducted using XRD, FTIR, Raman spectroscopy, SEM, AFM, XPS. Thermoelectric properties namely electrical conductivity, Seebeck coefficient, and power factor were measured across all compositions to assess performance.

In experimental work significant achievements include the synthesis of PEDOT: PSS/ Bi_2Te_3 binary film and PEDOT: PSS/ Bi_2Te_3/rGO ternary composites through spin coating method, which exhibit marked improvements in TE performance due to optimized morphology and enhanced carrier mobility. Initially, binary poly(3,4-ethylenedioxythiophene): poly (styrene sulfonate) (PEDOT: PSS) and PEDOT: PSS/ Bi_2Te_3 hybrid composite film fabricated by spin coating method. The maximum Seebeck coefficient (22 μVK^{-1}) and power factor (57.18 $\mu Wm^{-1}K^{-2}$ around 300 K) were achieved at 0.4 wt.% Bi_2Te_3. The electrical conductivity (σ) reached a maximum of 1467 Scm^{-1} at 300 K for 0.6 wt.% Bi_2Te_3, which is more than three times higher than that of pure PEDOT: PSS. Building on this, a ternary composite system incorporating rGO into the PEDOT: PSS/ Bi_2Te_3 matrix was developed to further improve TE performance. Five samples with varying rGO content (0-0.3 wt%) were synthesized, and the best performance was observed at 0.1 wt% rGO. This sample was achieved an electrical conductivity of 1522.7 Scm^{-1}, Seebeck coefficient of 24.7 μVK^{-1}, and a PF of 93.16 $\mu Wm^{-1}K^{-1}$, representing a twelve-fold increase over pristine

PEDOT: PSS. In addition, We synthesized $FeCl_3$ doped poly(3-hexylthiophene) (P_3HT) flexible film via drop casting method with varying content of $FeCl_3$ (20 mM, 40 mM and 60 mM) were studied for their structural, morphological, and thermoelectric properties. At 300 K, the P40 sample achieved a notable Seebeck coefficient of 164 μV/K and a maximum power factor of 127.4 $\mu W/Mk^2$. Doping significantly improved electrical conductivity and optimized the Seebeck coefficient, resulting in an enhanced power factor. In addition to these p-type materials, we also addressing one of the most challenging aspects in the field of organic TEs, the development of efficient and stable n-type materials. A novel hybrid composites consisting of PVDF and Ni NWs was synthesized and evaluated for TE performance. The preparation of composite films using different concentrations of Ni NWs, specifically (30-90 wt.%). Electrical measurements indicated that an increase in Ni NWs content resulted in enhanced electrical conductivity (σ), while the Seebeck coefficient (S) exhibited a consistent n-type behaviour. The TE power factor (PF) of the composites attained a optimized value of 242 $\mu Wm^{-1}k^2$ at a temperature of 400 k, exceeding the values documented for similar PVDF based materials in the literature. Furthermore, a flexible TEG was developed utilizing p-type PEDOT and n-type PVDF/Ni nanowires, resulting in a Maximum power output (P_{max}) of 230 nW at ΔT= 25 K. This investigation highlights the capabilities of PVDF/Ni NWs composites in the realm of flexible energy-harvesting devices, suggesting significant possibilities for the improvement of TE performance by strategic material engineering. This research advances the field of organic thermoelectric through the introduction of novel materials designs, scalable fabrication techniques, and thorough evaluations of performance, thereby facilitating the development of next-generation energy harvesting technologies.

ACKNOWLEDGEMENT

First and foremost, I would like to express my heartfelt gratitude to my supervisor, **Prof. Ranjeet Brajpuriya**, my co-supervisor, **Dr. K.P.S. Parmar**, and my external supervisor, **Dr. Ashish Kumar**, for selecting me as a Ph.D. candidate and believing in me throughout this journey. Their unwavering patience allowed me the freedom to explore research aligned with my interests. Under their guidance, I have grown as a scientific researcher and gained a profound understanding of the research process. Their invaluable advice, expertise, patience, and constant belief in my abilities have been priceless. I feel truly fortunate to have had the opportunity to learn from such esteemed mentors.

I would like to sincerely acknowledge our Hon'ble Vice-Chancellor, **Prof. Ram Sharma**, and the Dean of Research & Development at UPES for their support, guidance, and for fostering an environment conducive to research excellence.

I am also deeply grateful to my supervisory team, **Prof. Shalendra Kumar, Dr. Aditya Sharma, and Dr. Tridib Kumar Sinha**, for their valuable suggestions and continuous support throughout my Ph.D. work.

A special thanks to my colleagues and lab mates from the ET & Raman Lab for their support and collaboration. I am especially thankful to **Mrs. Priyanka Bishnoi**, **Mr. Kamal Singh, Mr. Kuldeep Rawat, Mr. Manas Nasit, Mr. Nitin Kumar Gautam, Ms. Gargi Dhiman, and Ms. Ankita Singh** for their help and friendship, which have made this journey smoother and more enjoyable in unexpected and meaningful ways.

I am sincerely thankful to UPES for providing the Ph.D. fellowship and lab facilities, as well as to the CIC, UPES, for their support with essential characterizations and workspace for experiments. My gratitude extends to **Dr. Prakash Bobde** and **Mr. Charu Chandra Pant** for their assistance during my experiments, which played a crucial role in making this research possible.

Lastly, I extend my deepest gratitude to my friends and family, especially my father, **Mr. Bharatveer Rathi**, and my mother, **Mrs. Sunita Rathi**. Thank you for your unconditional love, patience, and unwavering belief in me. You have been my greatest source of strength. I

wholeheartedly dedicate this thesis to my parents, whose constant support and inspiration have guided me throughout my life.

To everyone who has been a part of this incredible journey, my heartfelt thanks.

TABLE OF CONTENTS

LIST OF FIGURES

LIST OF TABLES

ABBREVATION

κ	Thermal Conductivity
S	Seebeck Coefficient
σ	Electrical Conductivity
T	Temperature
AFM	Atomic Force Microscope
BT	Bismuth Telluride
OTE	Organic Thermoelectric
PF	Power Factor
GO	Graphene Oxide
FTIR	Fourier Transmittance Infrared Spectroscopy
PANi	Polyaniline
P3HT	Poly(3-hexylthiophene)
PEDOT: PSS	Poly (3,4-ethylene dioxythiophene) polystyrene sulphonate
rGO	Reduced Graphene Oxide
TE	Thermoelectric
TEM	Thermoelectric material
TEG	Thermoelectric Generator
FESEM	Field Emission Scanning Microscope
TEP	Thermoelectric Power
RT	Room Temperature
XPS	X-ray Photoelectron Spectroscopy
XRD	X-ray diffraction
ZT	Figure of Merit

Chapter 1. **INTRODUCTION**

1.1 THERMOELECTRIC MATERIALS: AN OVERVIEW

Concerns about the depletion of conventional fossil fuels, as well as a growing awareness of the importance of environmentally friendly preservation, have become hot topics in green technology in recent years. With the increasing demand for electricity, global warming, environmental pollution, and the greenhouse effect are the issues we are facing at present, and researchers are focusing on energy harvesting-based power generators to reduce these effects. Thermoelectric (TE) technology is an alternative energy method that uses TE generators to transform waste heat directly into electricity. In recent decades, there has been notable advancement in the field of thermoelectric materials, particularly in improving their performance at high temperature (>650°C). These advancements have made them suitable for applications in waste heat recovery, specifically in high temperature system like automotive exhaust and nuclear energy production systems [1], [2]. Nevertheless, a considerable portion of waste heat generated by industrial and residential activities and processes is currently being emitted into the environment due to the limitations of waste heat recovery (WHR) systems. These systems are either prohibitively expensive or lack the necessary technological capabilities to effectively capture medium or low-temperature waste heat. Ongoing efforts are being made to explore and develop cost-effective, economically viable, and environmentally sustainable waste heat recovery systems utilizing thermoelectric materials (see Fig. 1.1). Additionally, the results concerning the waste heat recovery per industry [3].This environmentally friendly energy-saving technique is regarded as a promising means of easing the strain on energy and the environment. Because of their distinct solid-state architecture, TE generators provide several advantages over traditional power generators in terms of durability and simplicity. By 2024, the TE generator market will have grown significantly and will be worth over $950 million (Zervos).

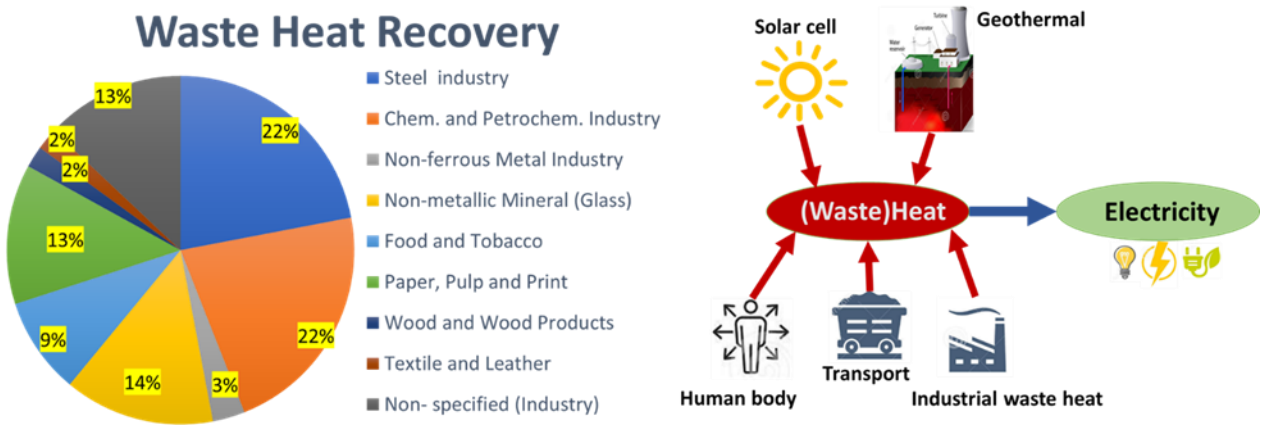

Figure 1.1 Waste Heat Source: Since WHR (Waste Heat Recovery) system are either high cost or technically unable to recover medium as well as low-temperature waste heat, a sizable portion of the waste heat medium and low temperatures from industrial use, automobiles residential activities, and processes is still released into the environment. WHR systems based on thermoelectric materials are more economical, less expensive, and environmentally beneficial and are still being sought.

Particularly, organic TE generators provide the extra advantages of being lightweight, compact size, no mechanical fluids, and low production costs [4]. Because they can directly convert electricity from heat in a steady system whenever there is a temperature difference (T) without depending on either light or mechanical action, TEs attract a sizable share of ongoing research. Additionally, it has a long-life span, requires no maintenance, and may be linked with other energy harvesters. It has been applied to more general purposes as well, such as satellite manufacturing and planet exploration [5], due to the increased heat flux produced by device shrinking, but has also been used more carefully for a larger range of applications like thermal control of micro-nano electronic devices [6]. As the use of milli-microwatts of electricity driven by thermoelectric becomes more common in fields such as micro nanoelectronics [7], nanoscale robotics [8], micro electrochemical systems [9], and wireless telecommunication systems [10], it is possible to generate electricity from a variety of sources, including industrial, human, and automobile sources [7]. Thomas Johann Seebeck reported the first research study on thermoelectric materials in 1822 based on the Seebeck effect [11]. After that, the Peltier and Thomson effect were described by Jean-Charles Peltier [12] and Lord Kelvin [13] in the years 1834 and 1854, respectively. The development of thermoelectric performance materials had slowed in the 20th century and beyond [14]. A lot of high-performance TE materials are made of inorganic materials that are expensive, brittle, rigid, heavyweight, and toxic (for example, Bi, Te, and Pb). This inorganic TE material

exhibits high-temperature performance. Recent research has been focused on creating inexpensive, cheaper, scalable, adaptable, nontoxic, and lightweight TE materials for use in moderate-temperature applications (300 K to 600 K) [15], [16], [17].

Thermoelectricity

TE modules are device that directly converts heat to electricity. When we apply temperature differences across the length of thermoelectric material, carriers spontaneously flow from hot to cold regions. This allows the carriers to produce current, and eventually, the Seebeck effect causes a voltage potential (V) to arise across the material. Which can be described using the equation –

$$S = \frac{\Delta V}{\Delta T}$$

Where S is the Seebeck coefficient. On the other hand, the Peltier effect enables an exothermic and endothermic reaction to take place at semiconductor-metal junctions if the current is applied. Usually, for a complete TE module, we need p-type (electron deficient) and n-type (electron-rich) semiconducting materials which are shown in Fig 1.2 called TE couple. And thermoelectric generation consists of multiple pairs of p-type and n-type legs. The operational voltage of the module increases and current reduces when numerous elements are placed thermally in parallel and electrically in series.

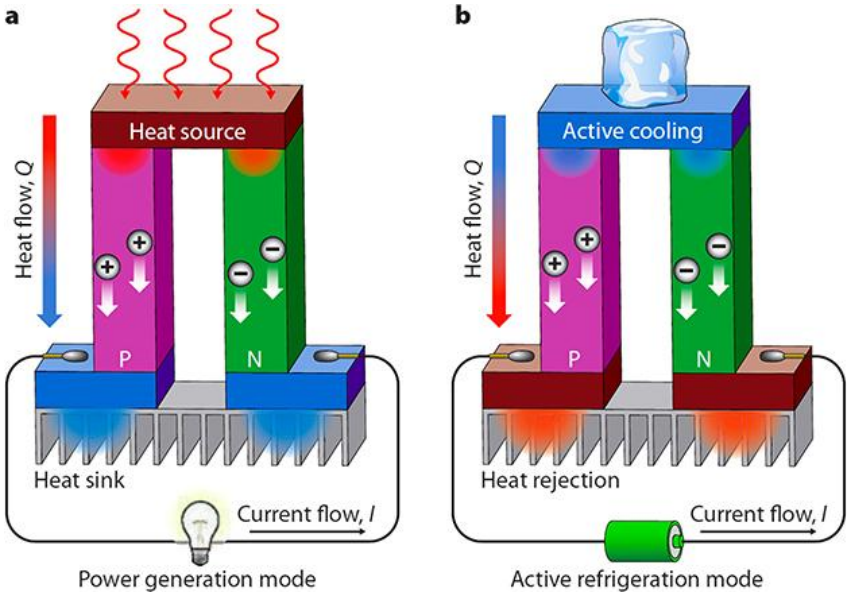

Figure 1.2 Diagram of a thermoelectric generator for (a) voltage production using the Seebeck effect and (b) active cooling using the Pelter effect. (a) current flows across the circuit as a cons consequence when applied temperature differential causes charge carriers (electrons and holes)

to diffuse from the hot end to the cold end. (b) heat is absorbed in the tin top junction and moved to the lower junction and moved to the lower junction when a current is produced to flow through the circuit are taken from [10].

Thermoelectric generators (TEGs) are for generating electricity from thermal energy without the need for any mechanical components. Thermoelectric devices operate on the principle of the thermoelectric effect, whereby temperature differential is directly converted into electricity. TEGs consist of a few thermoelectric elements, typically made of semiconducting materials, which are arranged in a way that creates a temperature difference across them. This temperature difference causes the flow of electrons in the thermoelectric elements, which generates an electrical current. The working principle of TEGs can be explained by considering two legs made of p-type and n-type semiconducting materials. The p-type leg is doped with impurities that create extra holes, while the n-type leg is doped with impurities that create extra electrons. When the TEG is subjected to a temperature difference, the electrons and holes in the two legs are driven to flow in opposite directions, as shown in Fig 1.3. This creates a flow of current that can be used to generate electricity.

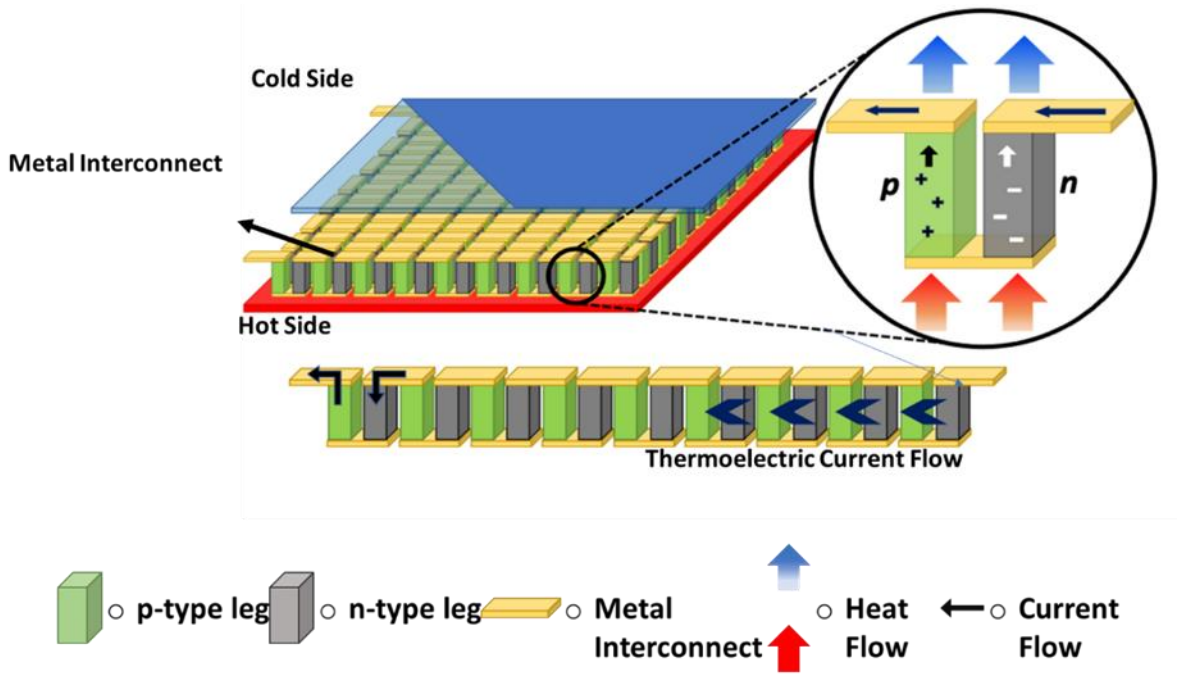

Figure 1.3 The present diagram depicts the internal structure of various p-type and n-type legs in thermoelectric power generators.

The efficiency of TEGs depends on the materials used in the thermoelectric elements as well as the temperature difference across them. Generally, the higher the temperature difference and the better the thermoelectric materials used, higher is the efficiency of the TEG. In a Peltier module, the temperature is lower at the top than at the bottom because heat is being removed from the top. The greater temperature at the top of the Seebeck module generates voltage but the temperature difference has the opposite function in the Peltier module. The materials used in TEGs must also have low thermal conductivity to maintain the temperature difference across the thermoelectric elements. Thermoelectric systems can either convert heat into power directly or turn power into a form of cooling [18].

1.2 APPLICATION OF THERMOELECTRIC MATERIALS

Thermoelectric materials have versatile applications driven by their ability to direct convert heat into electricity and the reverse process. In power generation, these systems facilitate waste heat recovery across industrial processes, automotive applications, and spacecraft, transforming lost heat into usable electric energy to enhance overall efficiency. For TE cooling, these materials offer solid-state solutions for electronics, medical devices, and refrigeration systems, presenting noise-free and environmentally friendly alternatives to conventional compressors. Portable energy devices utilize TE materials for applications in wearable electronics, sensors, and off-grid power systems, facilitating energy harvesting from body heat or ambient thermal gradients to sustainably power small devices.

Over the past decade, significant developments have been made in Organic Thermoelectric (OTE) materials with remarkable thermoelectric performance [19, 20].The OTE materials hold promise for various applications due to their unique properties, like flexibility, cost-effectiveness, environmental friendliness, and tunable characteristics [21, 22]. Because of flexibility and lightweight, OTE materials are often suitable for wearable and flexible electronics and are likely to contribute significantly to developing energy-efficient technologies and sustainable electronic devices [23, 24]. As illustrated in Fig 1.4 (a,b), flexible thermoelectric devices are suitable for portable gadgets and wearables, such as sensors for health monitoring [4].

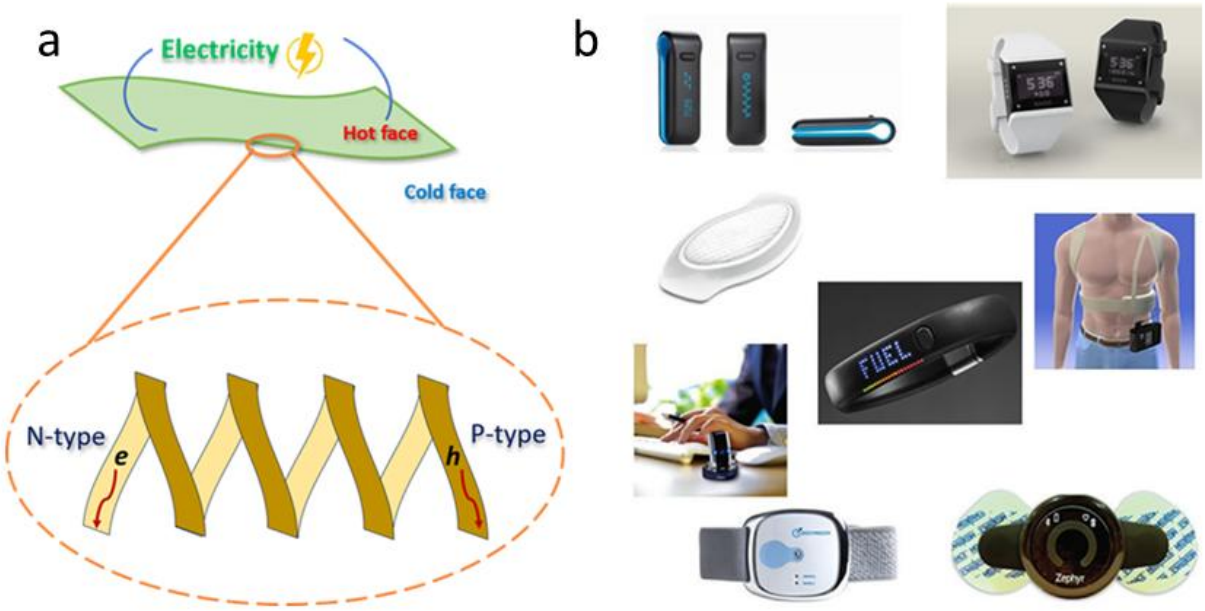

Figure 1.4 (a) A flexible OTE device is depicted, consisting of alternating p-type and n-type. The device can be made using wearable functional fabric that converts body waste heat into electricity through high energy transfer from the hot face to the cold face. (b) The potential use of organic thermoelectric generators (TEGs) is demonstrated, supporting wearable electronics such as watches, fitness trackers, health monitoring and toys.

Materials provide the opportunity to take advantage of established device fabrication and processing methods (such as a roll – to -roll, inkjet, etc.), which would allow the creation of next–generation thermoelectric devices that are lightweight and flexible and are available in a variety of geometries and designs [36]. For instance, some implantable medical devices, like pacemakers, only need 10 MW of electricity to operate semi-permanently without the requirement for a battery replacement procedure [38]. Fig 1.5 shows these technologies are particularly intriguing since thermoelectric energy conversion may easily gather human body heat, one of the most reliable and plentiful sources of wasted energy. Given that the typical individual releases 100-120 W of thermal energy into the atmosphere [39].

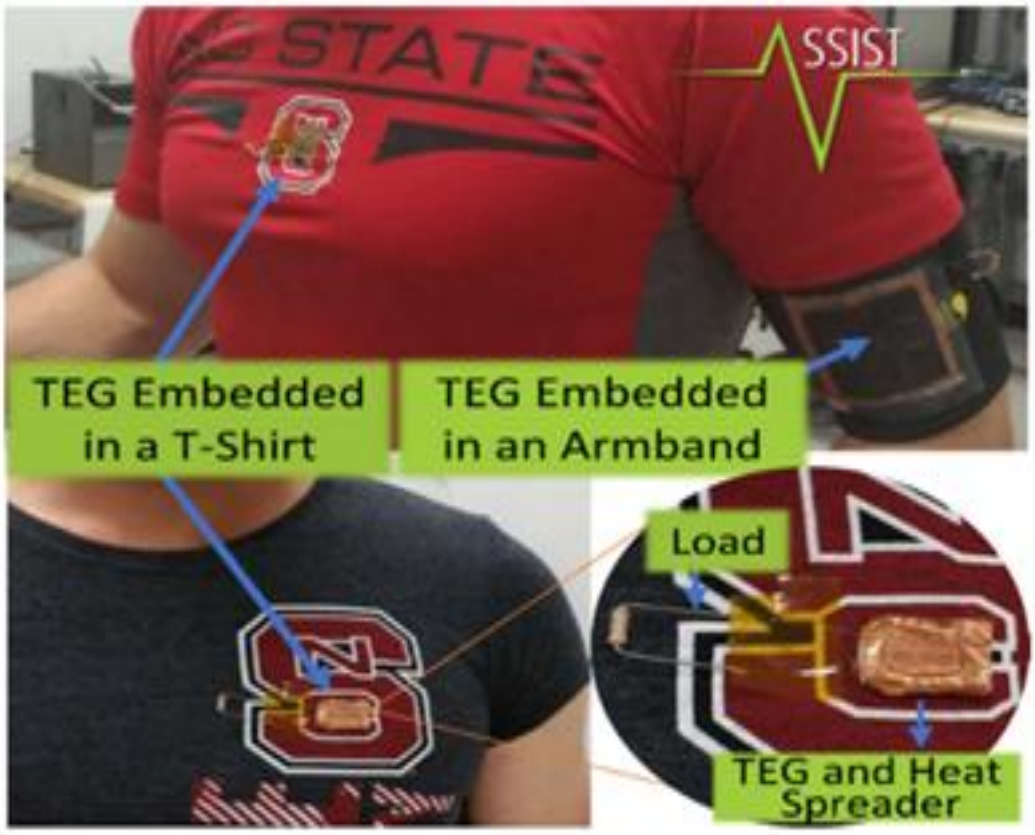

Figure 1.5 Thermal harvesting units embedded in a T-shirt and an armband was developed are taken from [39].

1.3 THERMOELECTRIC PERFORMANCE AND FIGURE OF MERIT (ZT)

The TE efficiency of a TE generator is determined by,

$$\phi_{max} = \frac{P_{out}}{Q_{in}} \quad (1)$$

Where P_{out} is the power produced by the device, including heat losses, and Q_{in} is the quantity of heat that enters the device.

$$\phi_{max} = \phi_c . \frac{\sqrt{1+ZT_{av}}}{\sqrt{1+ZT_{av}}} \frac{-1}{+T_h/T_c} = \phi_c Y \quad (2)$$

Where Th is higher temperature, and T_c is lower temperature, $T_{total} = (\frac{T_h+T_c}{2})$, and the Carnot efficiency is given by $\phi_c = \left(\frac{T_h+T_c}{2}\right), \Big) = T_h$. Y represent the irreversible contribution to efficiency [25].

The dimensionless figure of merit governs the performance of thermoelectric materials. It is denoted by ZT.

$$ZT = \frac{S^2 \sigma}{\kappa} T \quad (3)$$

Where S represents the Seebeck coefficient k represents the thermal conductivity, σ represents the electrical conductivity, and T absolute temperature.

1.3.1 *Seebeck Coefficient*

The correlation between the Seebeck coefficient and Electrical conductivity is typically attributed to the carrier concentration in Equation 4. One common employed method for improving the thermoelectric efficiency of the material is to find the highest PF ($S^2\sigma$) by adjusting the concentration of the charge carrier (n). A concept commonly employed to explain electron transport in metals can be used to explain the relationship between the Seebeck coefficient and carrier concentration of strongly conducting materials [26].

$$S = \frac{8\pi^2 K_b^2}{3eh^2} m^* t \left(\frac{\pi}{3n}\right)^{2/3} \quad (4)$$

Where K_b is the Boltzmann constant and has a value of (1.3806×10^{-23} m^2 kg s^{-2} K^{-1}), h is the Planck's constant and has a value of (6.6260×10^{-34} m^2 kg s^{-1}), e represents the charge of an electron and has a value of (1.602×10^{-19} C) and m* represents effective mass. Traditionally, this concept has been employed to determine how *S* changes as a function of n.

1.3.2 *Electrical Conductivity*

Since Equation 5 indicates that electrical conductivity and charge carrier concentration are proportional to each other, a small charge carrier concentration results in a significant Seebeck coefficient with a lower σ.

$$\sigma = n_e \mu \quad (5)$$

where μ is a symbol of the charge carrier's mobility. The trade-off between S and σ restrict the achievement of maximum PF. When the Seebeck coefficient and electrical conductivity are balanced, a maximum PF is produced and for inorganic TE materials, this usually happens at a

carrier concentrations of between 10^{19} to 10^{21} cm^{-3} [5]. It has not yet been conclusively determined that what carrier concentration are best for organic compounds. OTE materials have a different conduction mechanism than traditional inorganic thermoelectric materials; therefore, the optimal carrier concentration may differ from that of inorganic materials [27]. Conductivity in conducting polymers and organic materials is usually induced by polaron hopping caused by the overlapping of the electron wave function on adjacent sites. When an electron moves down a chain while being trapped by a polarised field, lattice distortion may be created around the intense electron-phonon interactions. In comparison to inorganic materials, which typically have carrier mobility in the range of 1-10^3 $cm^2V^{-1}s^{-1}$, this method of electrical transport produces charge carrier mobility less than 10^{-4}-$10^1$$cm^2$ $V^{-1}s^{-1}$ [28]. The greatest power factor for organic materials will then have a reasonably high carrier concentration.

1.3.3 ***Thermal Conductivity***

One of the three important parameters for TE materials is thermal conductivity (k), which can be explained by equation 6.

$$\kappa = \kappa_e + \kappa_l \tag{6}$$

In this equation, the symbols κ_l and κ_e are employed to denote the lattice thermal conductivity and electronic thermal conductivity, correspondingly. Electrical conductivity and thermal conductivity are proportional to each other according to Wiedemann-Franz's law (WFL) [29, 30]. The Lorenz number (L), which is normally equal to L= 2.4433×10^{-8} WU, is used in this equation. Many organic conductive polymers can be used as TE materials. Liu et. al., reported that the Lorenz number is compatible with its standard Sommerfeld value, and WFL is valid for poly (3,4-ethylene dioxythiophene) polystyrene sulphonate (PEDOT: PSS) [31]. Salamon et. al., discovered that WFL holds for a similar Lorenz number of Tetrathiafulvalene-Tetracyanoquinodimethane (TTF-TCNQ) [32]. However, some researchers have hypothesised that due to different electrical transport driven by polarons, the Lorenz number may not be identified as the traditional Sommerfeld value [27]. The Lorenz number and Sommerfeld value may differ due to the structure and level of doping [27, 33, 34]. The lattice thermal conductivity of materials caused by the transfer of energy by phonons is frequently used in equation 7.

$$K_L = \frac{1}{3} Cvl \tag{7}$$

Where v represents the sound velocity, l represents the phonon mean free path, and C represents the heat capacity. As per observations, the values of C and l for PEDOT: PSS are 1.83×10^{-6} JKm^{-3} and 0.1 nm, respectively [35]. Organic materials frequently have sound velocities between 10^3 and 10^4 ms^{-1}. For example, the sound velocities of poly (3,4-ethylene dioxythiophene) polystyrene sulphonate (PEDOT: PSS) and Poly (3-hexylthiophene) P3HT materials are 1.58 and 2.87 ms^{-1}, respectively [36, 37]. According to literature estimate, the lattice thermal conductivities of PEDOT: PSS, and P3HT are 0.3 Wm^{-1} K^{-1} and 0.5 Wm^{-1} K^{-1}, respectively. Those numbers fall within the established range (0.1- 0.7 $Wm^{-1}K^{-1}$) for thermal conductivities for various polymers [38, 39]. The organic materials are typically having advantages having of a low thermal conductivity, which falls between 0.1 to 0.7 Wm^{-1} K^{-1}, but the electrical conductivity of these materials is frequently low, i.e., 1 Scm^{-1} [37-39]. In comparison, the lattice thermal conductivity and the electrical conductivity of organic materials result in an order of magnitude.

1.3.4 *Factor Affecting Thermoelectric Efficiency*

A perfect TE material must have a higher Seebeck coefficient for enhanced energy conversion [40-42], an increased electrical conductivity σ to decrease the Joule heating effect [43, 44] as well as a poor thermal conductivity (κ) can maintain a temperature difference [45-47] as demonstrated in Fig 1.6. It is exceedingly challenging to reach the perfect values for these characteristics, which are connected to one another [14]. For instance, when σ increases, S typically decreases and κ frequently rises, placing limitations on how much the ZT can be improved. Most of the organic thermoelectric material ZT used in the 1990s ranged from 10^{-3} to 10^{-6} [48, 49].

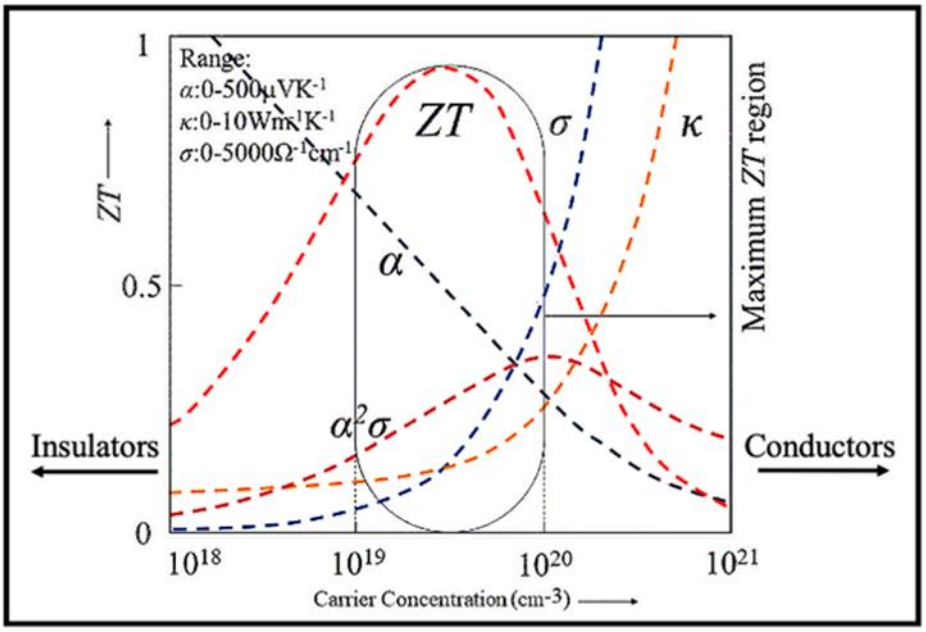

Figure 1.6 Thermoelectric parameters with variation in carrier concentration taken from ref. [50], Where α represents the Seebeck coefficient, σ represents the electrical conductivity, k represents the thermal conductivity, and ZT represents the figure of merit. Image adapted with permission from Rishi Prasad et.al., [50], Springer Nature 2020.

1.4 Organic-Inorganic Hybrid Materials for Thermoelectric Applications

Organic-inorganic hybrid materials improve the performance of TE systems by integrating the flexibility of polymers with the superior electrical conductivity and thermopower of inorganic nanostructures. Nanocomposites including graphene, reduced graphene oxide (rGO), graphene oxide (GO), and bismuth telluride (BT) are essential components in these hybrids. They enhance electrical conductivity, determine nanoscale interfaces for improved phonon scattering, and optimize the PF. These hybrids provide opportunities for the development of high-performance, multifunctional TE materials appropriate for next-generation energy harvesting technologies.

1.5 CHALLENGES IN DEVELOPING HIGH-PERFORMANCE THERMOELECTRIC MATERIALS

Developing high-performance thermoelectric (TE) materials is a complex and multidisciplinary challenge. Achieving a balance between electrical conductivity and thermal conductivity is a primary challenge in the development of high-performance TE materials. High electrical conductivity is a crucial for effective charge transport, whereas low thermal conductivity reduces heat loss, both of which are essential for optimizing the TE figure of merit (ZT). These characteristics are often interdependent; enhancing electrical conductivity generally leads to an increase in thermal conductivity. Strategies including doping, nano structuring, and interface engineering are utilized to decouple these properties. However, attaining optimal results continues to pose a considerable challenge. OTE, including conductive polymers, exhibit susceptibility to degradation when exposed to environmental factors such as humidity, ultraviolet radiation, and thermal cycling. Their low thermal and oxidative stability affects long-term performance and limits applicability in high-temperature. Improving stability via molecular design, crosslinking, or protective coating is a significant research focus; however, achieving durability while maintaining TE properties remains a substantial challenge.

Flexible thermoelectric devices are essential for wearable and portable applications; however, attaining a high ZT in these systems presents significant challenges. Flexible materials frequently compromise performance in favor of mechanical adaptability, as polymers and composites generally exhibit lower electrical conductivity and PF relative to rigid inorganic alternatives. The advancement of flexible materials featuring customized microstructures, enhanced carrier mobility, and effective phonon scattering mobility, and effective phonon scattering mechanisms is crucial for improving the ZT of flexible TE devices. Addressing this challenge necessitates the development of innovative materials designs and processing techniques that combine flexibility with performance.

1.6 MOTIVATION FOR CURRENT RESEARCH

The long-term effects of the world's largest dependency on fossil fuels have increased the demand for alternative energy sources and cutting-edge energy harvesting devices. The future generation of energy technologies among them may include thermoelectric energy conversion as a prominent

actor. Because they can directly convert waste heat energy into electrical energy, via the Seebeck effect or provide both active solid-state cooling and heating from an applied current via the Peltier effect [4].

Organic-inorganic hybrid composite offers significant potential for TE research by integrating the advantageous properties of both material types. Organic components, including conducting polymers, exhibit flexibility, lightweight properties, and low thermal conductivity. In contrast, inorganic components, such as nanostructured semiconductors, deliver high electrical conductivity. These hybrids facilitate synergistic effects that enhance the PF and decrease thermal conductivity, providing them suitable for advanced energy harvesting and wearable technologies.

Efficient TE devices necessitate the integration of p-type and n-type materials to create a functional TE module. Despite notable progress in p-type organic materials such as PEDOT: PSS, the advancement of high-performance n-type organic or hybrid TE materials remains insufficient. Identifying this imbalance is essential for the development of efficient, symmetric devices and for broadening the scope of applications. Investigating doping strategies and hybrid systems is crucial for improving the performance of n-type materials to support their p-type counterparts.

Graphene and rGO composites are significant materials for improving the TE figure of merit (ZT). Their superior electrical conductivity, outstanding mechanical properties, and adjustable electronic structure render them suitable candidates for hybrid systems. Incorporating graphene and rGO into organic matrix enhances charge carrier mobility and electrical conductivity, while also facilitating phonon scattering, which leads to a reduction in thermal conductivity. These composites facilitate the production of high-performance, flexible TE devices are essential for resolving flexibility with efficiency in energy harvesting applications.

Chapter 2. **LITERATURE REVIEW**

2.1 **OVERVIEW OF ORGANIC THERMOELECTRIC MATERIALS**

Thermoelectric generators (TEGs), are fascinating devices that can convert thermal energy into electrical energy. This process of energy conversion is truly remarkable and has significant implications in the field of energy harvesting [51], with the goal of achieving net zero carbon emission by 2050, as outlined in the 26th UN Climate Conference of the Parties (COP26) in 2021, there has been a significant focus on the advancement of renewable energy sources that are free from carbon emission [52]. Thermoelectric generators (TEGs) can efficiently recover waste heat and convert it into electrical energy through the thermoelectric (TE) effect. This process is not only simple to setup, but also requires minimal maintenance. Additionally, TEGs are not limited by the heat source they can utilize, making them a versatile option for energy conversion. Electricity generation can occur when there is a temperature gradient across a junction of two materials, or vice versa. This phenomenon is known as the TE effect and can be further categorized into the Seebeck effect and Peltier effect [53]. Seebeck effect is related with generation of electrical potential from temperature gradient across two ends of a material while Peltier effect represents reverse effect of Seebeck effect.

Over the past few years, OTE materials have garnered considerable interest due to their inherent benefits over traditional inorganic thermoelectric materials. These OTE materials possess various benefits including low cost, ease of fabrication, lightweight, minimal toxicity, and low thermal conductivity (PEDOT: PSS, P3HT) are shows in Fig 2.1. However, the commercialization of OTE generators has been limited by their poor thermoelectric performance. To improve the efficiency of OTE materials, several key parameters must be considered and optimised.

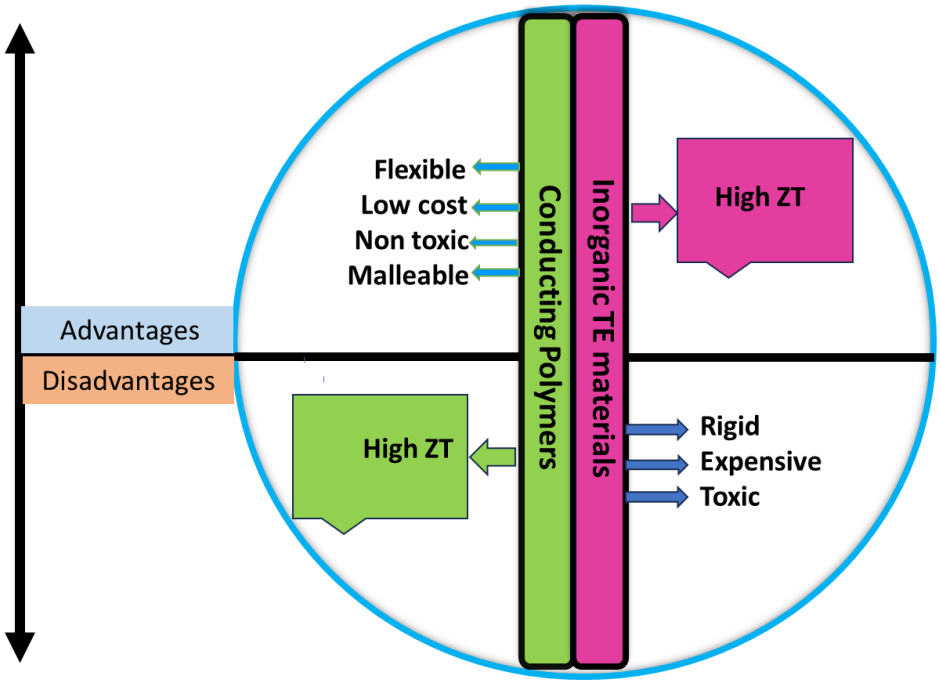

Figure 2.1 Schematic represent the comparison between inorganic TE materials and conductive polymers.

The cost-effectiveness of organic materials is greater than that of their inorganic counterparts [54, 55]. They are advantageous for large-scale applications in industries where cost is a key consideration [56]. It is possible to chemically engineer organic materials in such a way that they will possess specific electronic and thermal properties. A wide range of temperatures and operating conditions can be considered when tailoring the thermoelectric performance of OTE materials [19, 57]. By using organic thermoelectric materials, waste heat can be converted into useful electrical power. This could be a future energy harvesting source, along with industrial processes, automobile exhaust, and even human heat [58, 59]. It is easy to extract and process organic materials, which leave little environmental impact because they are abundant in environmentally friendly elements [60]. Compared to inorganic materials, organic materials are an environmentally friendly alternative. Materials made from organic compounds are flexible and can conform to complex shapes and surfaces [61]. By adjusting the molecular structure, OTE materials can be tuned for their electronic and thermal properties [62]. A fully organic electronic device can be developed by seamlessly integrating OTE materials with other organic electronic components [63].

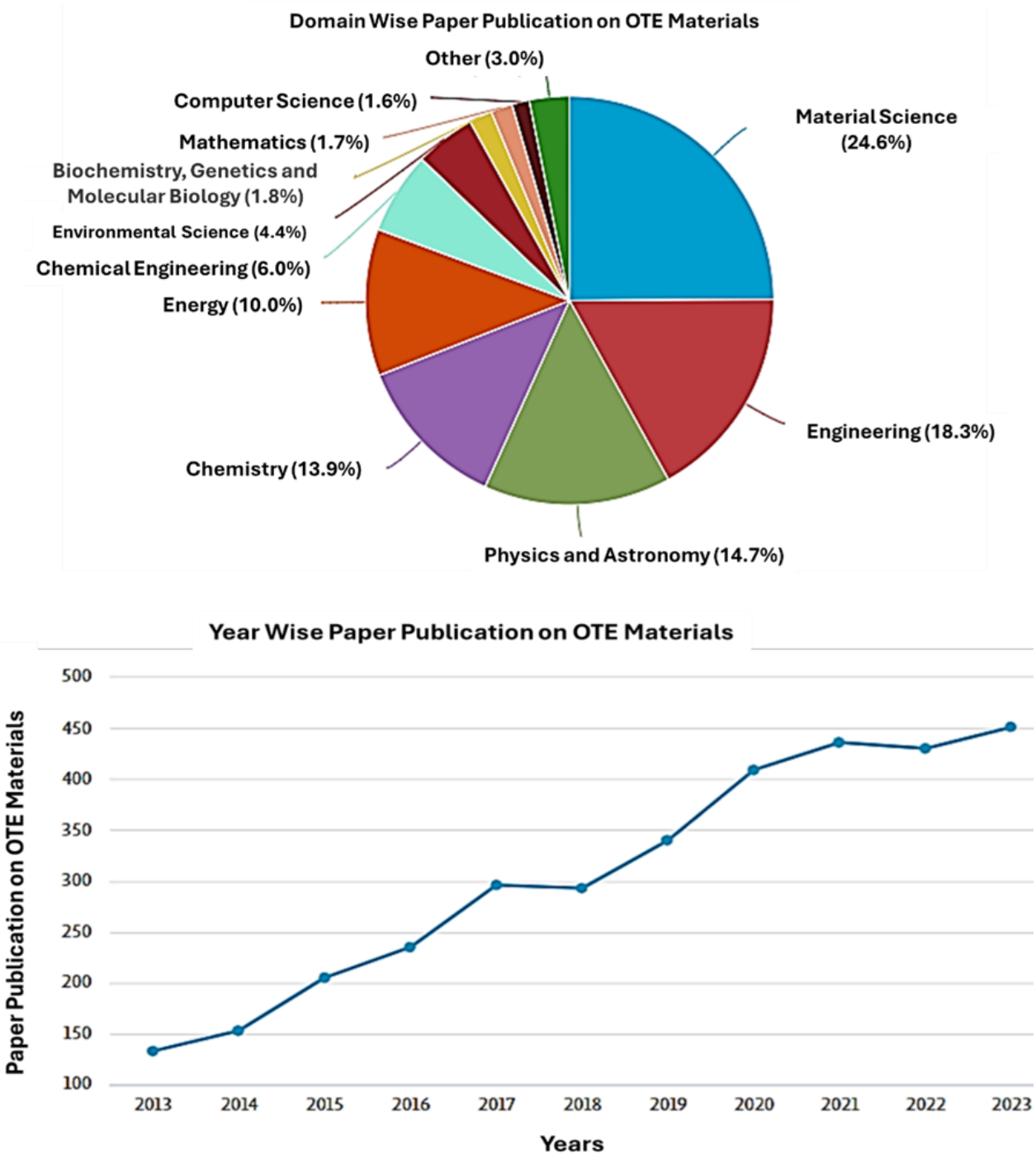

Figure 2.2 The domain wise and year wise publication on OTE materials.

By integrating these systems, electronic systems can become more efficient and sustainable [64, 65]. For instance, Bubnova, Katz, and other authors provided an excellent overview of the solid-state physics of conjugated polymer compounds [65].Wang et al. recently described several

potential OTE materials with maximum power factor (PF) values ranging from 70 $\mu Wm^{-1} K^{-2}$ to 2710 $\mu Wm^{-1} K^{-2}$. In OTE material, the highest ZT value achieved is 0.5, reported in 2015 [66, 67]. The year wise and domain wise publication on OTE shows the importance of the materials [Fig 2.2].

2.2 DISCUSSION ON OTE MATERIALS BASED ON GRAPHITE AND ITS COMPOSITES

Graphene is a newly emerging 2-D crystalline carbon compound with extremely excellent electrical properties and sufficient TE performance. The organic TE materials that have been recently produced, includes GO, rGO, and graphene nanosheets, and their fabrication processes, along with potential applications is discussed here.

2.2.1 *Graphene + organic thermoelectric materials*

Organic materials, especially conductive polymer materials, are inexpensive, lightweight, highly flexible, easy to fabricate, and have very low thermal conductivity, making them particularly promising thermoelectric materials. Conjugated polymers have been identified as the most extensively researched polymer thermoelectric materials. These include PEDOT: PSS poly (3,4-ethylene dioxythiophene) polystyrene sulphonate, Polypyrrole (Py), Polyacetylene (PA), Polyaniline (PANi), and Poly(3-hexylthiophene) (P3HT), and so on. However, these organic conductive materials have some demerits because of their poor electrical transport properties compared to traditional inorganic materials. Graphene is preferred as doping that is hybridised with conductive conjugated polymers to improve electron transport properties due to its good mechanical properties, prosperous electronic state, large surface area, high flexibility, high mobility, and low density. Table 2-1 shows the synthesis method and the properties of graphene and conductive polymers.

Table 2-1 Summary of the synthesis method and thermoelectric performance at room temperature of some common organic materials with graphene

Hybrid	**Synthesis**	**σ (S cm^{-1})**	**S (μV K^{-1})**	**PF (μW $m^{-1}K^{-2}$)**	**K $Wm^{-1}K^{-1}$**	**ZT**	**Ref.**
PANi/Graphene	Solution dispersion	856	15	19	-	-	[68]
PANi/rGO	In situ polymerisation	3677	24	214	-	-	[69]
PANi/Graphene/PANi/DWNT	Layer-by-layer deposition	1080	130	1825	-	-	[70]
PANi/graphene-PEDOT: PSS/PANI/DWNT-PEDOT; PSS	Layer by Layer Deposition	1900	120	2710	-	-	[71]
SWCNT/PEDOT: PSS DMSO, GA	Oxidative chemical polymerisation	400	0.4	25	0.4	0.02	[72]
CNT/PVAc	Solution method	48	45		0.34	0.006	[73]
PANi/graphene nanosheets mechanical blending	Spin coating and mechanical blending	123	34		-	-	[74]
PEDOT: PSS/graphene fullerene	Mixing	700	25		0.4	0.06	[75]
PEDOT: PSS/graphene (100:1)	In situ polymerisation	1469	46.9	3.23	0.19	0.00046	[76]
PEDOT: PSS/graphene (100:2)	In situ polymerisation	3200	59	11.09	0.14	0.021	[76]

The polymers frequently employed in thermoelectric applications encompass poly (3,4- ethylene dioxythiphene) poly (styrene sulfonate) (PEDOT: PSS), polyaniline (PANi), polyvinyl acetate (PVAC), polyacetylene, poly (3-hexyl thiophene) (P3HT), Polypyrole (PPy), and poly (2,7-carbazolyenevinylene). In their study, Zhang et al. [77] incorporated fullerene-decorated reduced graphene oxide (rGO) into PEDOT: PSS. Functionalisation was accomplished through p-p stacking at the liquid-liquid interface. The electrical conductivity of the nanohybrid filler was enhanced by a factor of 7, resulting in a value of 70,000 S m^{-1}. Additionally, the thermopower experienced a 4-fold increase. The thermal conductivity also improved from 0.2 to 2 $Wm^{-1}K^{-1}$.

These enhancements led to the attainment of a ZT value of 0.067 when the nanohybrid was composed of 30 wt.% and had an rGO-fullerene ratio of 7:3. The improvement in TE properties was ascribed to the presence of interfacial phonon scattering and energy filtering. PEDOT: PSS-rGO composite film fabrication has been achieved by utilising the solution spin coating method [78]. the addition of 2 wt. % of reduced graphene oxide enhances the power factor of the composite materials, increasing PF from 2.03 to 11.09 $\mu Wm^{-1}K^{-2}$. Simultaneously, the thermal conductivity of the composite material decreases from 0.24 to 0.14 $Wm^{-1}K^{-1}$. The ZT value is increased by a factor of 10, resulting in a matter of 0.021. The observed increase in PF can be attributed to the robust p-p interactions between rGO and PEDOT: PSS open rings, which facilitate efficient charge transfer within the composite material. The low thermal conductivity of the composite can be attributed to its multilayer porous structure, which serves as a phonon scattering centre. The preparation of highly conductive composites based on PEDOT: PSS-rGO was carried out through in situ polymerisation, as conducted by Yoo's group [79]. The composites exhibited increased electrical conductivity from 453 to 637 S m^{-1} at a concentration of 3 wt.% of rGO. Additionally, the PF showed improvement, rising from 24.17 to 45.68 $\mu Wm^{-1}K^{-2}$. The enhanced electrical conductivity of the composites can be attributed to the existence of well-organised and structured rGO sheets. These sheets facilitate the arrangement of PEDOT: PSS molecules into morphologies that promote efficient charge transport. PANi-graphene nanoplatelets (GNP) nanocomposites were synthesised through the in situ polymerisation of aniline monomer in the presence of GNP [80]. The thermal expansion coefficient (TEP) of the nanocomposites was observed to be influenced by both the concentration of aniline and the protonation of polyaniline (PANi). TEP values reaching up to 33 μVK^{-1} were attained when the weight percentage of PANi was 40%, and the protonation ratio was 0.2. the electrical conductivity has been enhanced to 59 S m^{-1}, leading to a ZT value that surpasses both PANi and GNPs by two orders of magnitude. The incorporation of graphene nanoplatelets (GNP) into the composite material resulted in the elongation of the polymeric chains of polyaniline (PANi). This elongation led to an increase in the mobility of charge carriers, thereby improving the PF. The presence of GNP also contributed to the reduction of thermal conductivity in the composite material. Other authors have also made similar observations regarding the thermal and electrical properties of PANi/graphene composites [81]. PVAc/graphene-iron oxide (GINC) and PVAc-graphene nanocomposites were fabricated through a two-step process involving ultrasonication and subsequent hot compaction. The PVAc-GINC composite demonstrated an

optimal electrical conductivity of 2.18×10^4 S m^{-1} and a thermoelectric power (TEP) value of 38 μVK^{-1} by adjusting the concentrations of GINC and graphene. The PF value of this composite material was measured to be 32.90 $\mu Wm^{-1}K^{-2}$, which is 27 times higher than that of the PVAc-graphene composite. The thermal conductivity value was also determined to be 3.21 $Wm^{-1}K^{-1}$, resulting in a ZT value of 0.0031. The GINC filler enhanced the nanocomposites' electrical conductivity and thermoelectric power (TEP). However, the presence of iron oxide decorated on graphene disrupted the thermally conductive network. As a result, the overall thermoelectric properties of the nanocomposites were improved.

2.2.2 *Synthesis method of Graphene with conductive polymer composites*

Solution Dispersion: They prepared a solution of PANi with graphene via the solution dispersion method, and it exhibits σ is 856 S cm^{-1} and a PF of 19 $\mu W\ m^1\ K^{-2}$ because graphene has outstanding electrical properties and a strong π-π conjugated bond with PANi and graphene [68]. Although graphene agglomeration is not available at high filler content, it still limits the degree of uniformity due to the solution dispersion method. The prevention of graphene aggregation remains an essential issue in the solution dispersion method.

Powder mixing method: ceramic powder mixing process for conductive polymers and graphene. Graphene and organic conductive polymers are mixed mechanically, often by ball milling, to get a uniform dispersion before being heated or cold pressed into a pellet or a foil [74]. Powder mixing can scarcely achieve uniform distribution since the as-prepared graphene or polymer can easily agglomerate.

Layer-by-layer Deposition: By repeatedly exposing a hybrid film to a solution comprising cationic and anionic components, layer-by-layer deposition allows the production of nanoscale films with an arranged layer-by-layer stacking structure [82]. Cho et al. prepared an organised molecular structure of PANi/graphene/PANi/DWNT hybrid with an ordered molecular structure [70]. DWNT and graphene are negatively charged in this case, while PANi is positively charged. A neighbouring layer with a reverse charge can spontaneously produce a structural arrangement. An increase in the number of deposition cycles improves the Seebeck coefficient and electrical conductivity. A PF of 1825 $\mu W\ m^1\ K^{-2}$ was obtained. Update study [71] Graphene and DWNT are stabilised using PEDOT: PSS, producing a thin film of PANi/graphene-PEDOT: PSS/PANi/DWNTs-PEDOT: PSS hybrids, also manufactured by the layer-by-layer (LBL)

process. Fig 2.3 shows that a quad-layer of PANi / graphene-PEDOT: PSS was created through a series of depositions. A quad-layer was produced. You can get the required layer thickness by repeating the sequence. The modified film shows enhanced electrical conductivity of 1900 S cm^{-1} and a record maximum power factor of 2710 μW $m^{1}K^{-2}$. This is comparable to the traditional inorganic thermoelectric material Bi_2Te_3, which has the best RT thermoelectric properties. The LBL method provides an opportunity to prepare various organic materials with graphene rods with increased power factor expectations.

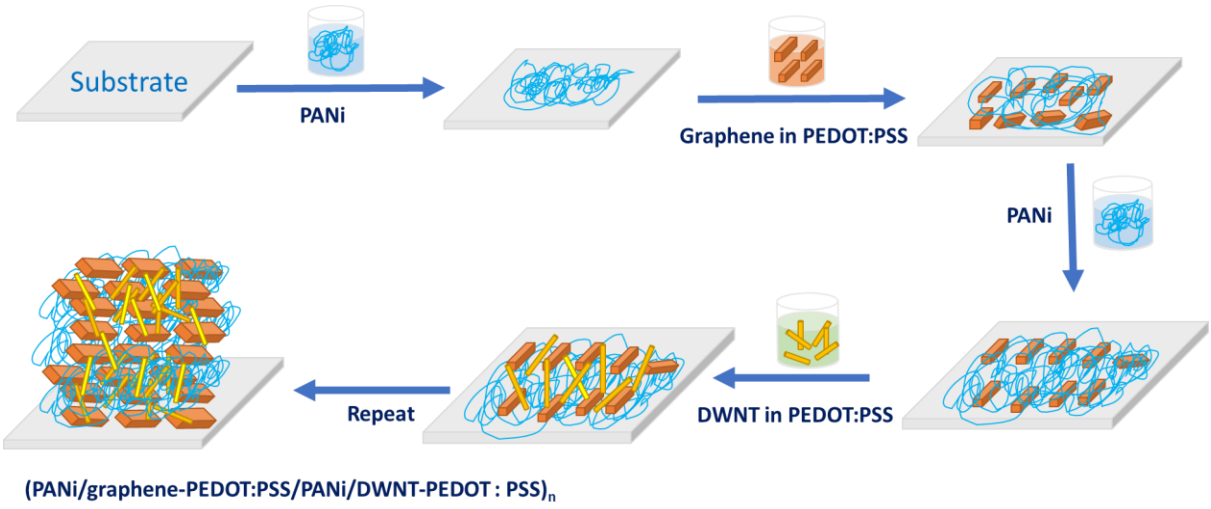

Figure 2.3 Layer-by-layer deposition method of PANi/graphene-PEDOT: PSS/PANi/DWNTs-PEDOT: PSS hybrids.

Ding Zhang et al. [83] developed a multipurpose superelastic thermoelectric sponge based on graphene, which has a high S and a maximum compressive strain of 49.23 μVK^{-1}, or 98%. The sponge maintains good mechanical and thermoelectric stability, and the Seebeck retention coefficient stays at 92.5% after 10,000 compression cycles with 30% elongation. A 4×4 array TE device is placed on top of the working CPU temperature by 8K, offering a workable method for continuously generating power and thermal management. Du et al. [84] fabricated a composite made of graphene nanosheets and PANi, and they reported a high PF of 5.6 μW m^{1} K^{-2} because these composites have a high charge carrier mobility. Using another combination of graphene, fullerene (C_{60}), PEDOT: PSS, Wang et al. [85] obtained a higher PF and figure of merit (32 μW m^{1} K^{-2} and a ZT value of 0.067) at RT. A layer-by-layer synthesis of stabilised CNTs, graphene,

and PANi is a different method that uses graphene. This method displays a power factor of 1825 μW m^1 K^{-2} at 300 K [86]. Gil Ho Kim et al. [87] prepared composite films containing 1,2 and 3 wt% graphene with PEDOT: PSS via the spin coating. Analysis using Raman and X-ray photoelectron microscopy shows the presence of strong interactions that assisted in the dispersed solution of graphene and PEDOT: PSS. Compared with CNT based on identical weight, the interfacial area was raised 2 -10 times by the evenly distributed graphene. A thin film of PEDOT: PSS with a PF of 11.09 μW m^1 K^{-2} and ZT of 0.02 contained two wt% graphene. Du et al. [84] report for the first time a trend of increased Seebeck coefficient and σ with increasing GNs concentration (up to a 1:1 ratio) in the PANi-GNs composites.

The ratios used to create the four different compositions were PANi-GNs 4:1, 3:1, 2:1, and 1:1, respectively. Maximum S and σ noted at a 1:1 PANi-GNs concentration. The observed phenomenon can be attributed to the significant increase in carrier mobility. Adding 50 wt.% of graphene nanosheets (GNs) increased the Pallets and thin film. Specifically, the PF of the pallet risen from 0.64 to 5.6 6 μW m^{-1} K^{-2}, while the PF of the thin film increased from 0.05 to 1.47 μW m^{-1} K^{-2}. Similarly, Xiang et al. [88] manufactured PANi-graphene composites via in-situ aniline monomer polymerisation with graphene nanoplatelets (GNP). The intense interaction between GNP and PANi produces a homogeneous coating of GNs. The authors have created a composite that resembles paper. The S of the synthesised composite varies with the quantities of polyaniline and the initial amount of aniline concentration in the mixture. With a protonation ratio of 0.2 and a composite containing 40 wt.% PANi, its value increases to 33 μVK^{-1}. The addition of GNP boosts the σ of the composite to 559 Scm^{-1}. It was discovered that the ZT value was two orders of magnitude higher than that of PANi or graphene. The TE efficiency of PEDOT: PSS can be improved by carbon nanotubes. It was shown that in literature [87], [88-92] increasing graphene content by 2-3 wt.% caused ZT to rise ten times. Comparing this value to carbon nanotube (CNT) based composites, it is significantly greater. Strong π-π interaction with help from more distribution is the cause. Raman spectroscopy lends support to these connections. Compared to CNT with a similar weight, the contact area is increased by 2-10 times when graphene is dispersed evenly. The higher carrier mobility of graphene increases the electrical conductivity, but the decreased thermal conductivity of graphene/PEDOT: PSS is greater than that of the pure PEDOT: PSS thin film, which contains 35 wt.% of SWCNT [14]. The author provided a comprehensive explanation for this anomaly of the two attributes; first, a clearly explained porous multi-layer

structure serves as a phonon dispersion centre, and second, phonons predominate in the thermal conductivity of such materials. Lattice thermal conductivity (k_l) has a more significant influence than electronic thermal conductivity (k_e) the combination of PEDOT: PSS and two wt.% graphene showed the highest ZT value of 2.1 $\times 10^{-2}$ at 300 K. Compared to pure PEDOT: PSS, this value was ten times greater. A practical and innovative technique for improving TE efficiency is fabricating a composite by adding graphene to PEDOT: PSS. Additionally, Yoo et al. [93] developed a composite made of PEDOT: PSS with graphene and investigated its potential application in waste heat energy recovery. Higher Seebeck and power factors are displayed by the composite that contains three wt.% graphene.

2.2.3 *Graphene+ inorganic thermoelectric materials*

Graphene and CNTs have excellent mechanical stability, high conductivity, and significant charge carrier mobility [94, 95] and are most prominently used in inorganic thermoelectric composites [96-102]. Dong et al. [96] prepared the nanocomposites of PbTe/graphene via a wet chemical method, the powder was prepared via the spark plasma sintering method at 580 K, and the ZT of the obtained product is 0.7 at 670 K has been reported. Composite materials of Graphene: PbTe with a mass ratio of 5%. Ju et al., [97] A Bi_2Te_3 nanowire (NW)/graphene composites film was prepared via the wet chemical method followed by the sintering method at 300 K, the composites film containing 20 wt.% of Bi_2Te_3, ZT value of 0.2 was obtained.

Liang et al., [103] Graphene materials with Bi_2Te_3 were prepared via a hydrothermal process followed by a spark plasma sintering process, and the ZT of the composite material containing 0.2 % graphene at 475 K was 0.21. Yanan Wang et al., [104] In this work, rather than simply aiming for high performance, they attempted to develop flexible thermoelectric composites based on abundant, less expensive, or environmentally friendly inorganic thermoelectric materials. Since n-type flexible thermoelectrical materials are highly desirable, most inorganic materials used in flexible thermoelectric composites so far are made up of rare or hazardous elements, so abundant and inexpensive non-toxic Zn-doped pyrite $Cu_{1-x}Zn_xFeS_2$ (x is 0.01, 0.02, 0.03) flexible PEDOT: PSS with graphene electrical networking is an essential candidate for n-type flexible thermoelectric films. The characterisation of hybrid films, which are designed using a combination of binary and ternary $Cu_{1-x}Zn_xFeS_2$/PEDOT: PSS and $Cu_{0.98}Zn_{0.02}FeS_2$/PEDOT: PSS/graphene), is performed. The σ of the ternary film is four times greater than the binary film, with a maximum

power factor of approximately 23.7 $\mu Wm^{-1}K^{-2}$. The optimal ternary film can retain more than 80% of σ even after 2000 cycles of bending and exhibits extraordinary flexibility due to the network made of PEDOT: PSS and graphene. A prototype thermoelectric device with five legs constructed of optimal foil produced a voltage of 4.8 mV at ΔT at 286 K. Such development of low-cost chalcopyrite-based composite films with high flexibility shows the potential for cost-sensitive flexible thermoelectric (FTE) applications. K.R. Nandana Paris et al., [105] foldable and transparent generators and storage devices (AC < 1 mm thick) with an active layer (AC) thickness of approximately 20 mm are piezoelectric between two graphene monolayers. They were manufactured by sandwiching the material and the solid electrolyte, respectively. The portable photoresistor with a thickness of 30 mm (AC-30) was created by combining a single layer of graphene with a fragile layer of ZnO deposited onto a PET or ITO substrate. Piezoelectric nanogenerators typically showed steady peak voltages of 5.5 V and a power density of 0.2 nA cm^{-2}. Finally, the portable photoresistor prepared in this way exhibited an adequate reaction to visible light, producing a high (in mA, even at low bias potentials) and an on/off current ratio of 1.8. The cold pressing process prepared Agarwal et al., [335] bulk Bi_2Te_3 and graphene materials, and the ZT of the composite material graphene containing 0.05 wt.% at 402 K was 0.92. Beibei Liang et.al. [336] synthesised Bi_2Te_3 and graphene composites via hydrothermal synthesis combined with spark plasma sintering. A Bi_2Te_3 particle was coated with 30-200 nm-sized graphene nanosheets in the precursor nanopowder. At 475K, the maximum value of ZT was 0.21, achieved with a graphene content of 0.2 vol%, which is 31% higher than pure Bi_2Te_3 material. Jakriti Gobpant et al. [106] developed SnTe-based powders using a hybrid microwave solid-state process including SnTe, $Sn_{0.95}Bi_{0.05}Te$, and SnTe with graphene addition. At 325 K, the SnTe with five wt.% graphene demonstrated a reasonable PF, and the thermal conductivity decreased from 10 $\mu W\ m^{-1}\ K^{-2}$ for SnTe to 2 $\mu W\ m^{-1}\ K^{-2}$. The dimensionless parameter ZT of SnTe was raised from 0.07 to 0.35 with five wt.% graphene, a 5-fold increase. Jingdu Dong et al. [96] synthesised PbTe and graphene nanocomposites via an efficient and innovative wet chemical process. PbTe/graphene nanocomposites achieve a ZT value of 0.7 at 670K, a substantially more incredible value. This has a considerably higher ZT than any n-type PbTe synthesised using a conventional methodology, and it is six times greater than the pure PbTe sample.

2.2.4 *rGO + organic composite*

Ube et al. [69] recently created a camphor sulfonic acid (CSA) filled with rGO and PANi film fabricated via an in-situ polymerisation process using an adequately insulated heat rGO. The σ of this composite film is very high at 3677 S $cm^{-1,}$ so the competing PF is 214 μW m^1 K^{-2}. In situ polymerisation may provide a more equal distribution than solution dispersal or powder mixing. Weijie Wang et al. [107] reported that cryogenic milling combined PANi and rGO uniformly, and spark plasma sintering was used to make them more challenging. rGO/PANi hybrid composites have significantly better TE characteristics than pristine bulk PANi. Surprisingly, the maximum S and σ are 15.934 μVK^{-1} and 1858.775 S $m^{-1,}$ respectively, and the highest ZT value of the rGO / PANi hybrid composite was 0.00042.

Shengchang Xina [108] reported that the PF of the film reached up to 7.28 μW $m^{-1}K^{-2}$, significantly greater than pristine polypropylene nanotube. Practical vacuum filtering and HI treatment were used to create the free-standing, foldable polypropylene nanostructure hybrid film successfully. Graphene nanosheet agglomeration was prevented, and conductive channels were produced by the hybrid film's polypropylene nanotube/rGO-linked structure. Mariamu Kassim Ali et al. [109] studied the PANi/doped reduced graphene oxide nanomaterials synthesised using wet chemical polymerisation combined with the hydrothermal method. The nanocomposites with only one wt.% of the SNrGO had a Seebeck coefficient of -1.75 μVK^{-1}, which is n-type thermoelectric materials, with good σ, and intrinsic deficient k reported as 31 S m^{-1} and 0.51 μW m^{-1} K^{-1} respectively, resulting in a 95 μW m^1 K^{-2} PF and have a ZT of 0.05 at RT. Similarly, Kongli, Xu et al. [110] synthesised a nanocomposite made of PEDOT-rGO with significantly improved thermoelectric properties. The thermoelectric performance of a nanocomposite produced by template-directed in situ polymerisation was enhanced considerably at ambient temperature with a PF 13.3 times greater than PEDOT at $5.2\pm 0.9 \times 10^{-6}$ μW m^{-1} K^{-2}.

2.2.5 *rGO + Inorganic composite*

Yong Du et al. [95] prepared a nanocomposite of rGO/Bi_2Te_3 bulk material manufactured via a hot pressing method. The σ of these nanocomposite materials decreased as the measured temperature from 298 K to 573 K. However, the exact value of S increased first and then reduced. Consequently, the PF of the bulk material increased first and then dropped. At 423 K, a nanohybrid

base material containing 0.25 wt% rGO had a PF of 1340 $\mu Wm^1 K^{-2}$. Similarly, Kumar et al. [99] synthesised the nanocomposites of Bi_2Te_3/rGO via refluxing technique and then obtained nanocomposites pressed into pallets. The ZT value of the pallet at ~340 K was ~ 0.35. Table 2 shows graphene's synthesis method and properties with their derivative and inorganic thermoelectric materials.

Ganesh Shridhar Hegde et al. [111] report the TE efficiency of pure $(Bi_{0.98}In_{0.02})_2Te_{2.7}Se_{0.3}$ with rGO composite in the temperature range of 10-325 K. These compounds follow the rhombohedral structure of the space group R_3m. The presence of 0.02 wt.% rGO in the matrix of $(Bi_{0.98}In_{0.02})_2Te_{2.7}Se_{0.3}$ reduced thermal conductivity by 1.6-fold and electrical resistance by 10-fold at 325 K $(Bi_{0.98}In_{0.02})_2Te_{2.7}Se_{0.3}$ / rGO. Because of the interaction between interfacial dispersion and antistites defects. At 325K, the maximum PF of 7 $\mu Wm^1 K^{-2}$ and figure of merit of 0.0026 were obtained with the $(Bi_{0.98}In_{0.02})_2Te_{2.7}Se_{0.3}$ containing 0.01 wt. % rGO. After that, at low temperatures, its TE cooling applications may result from properly optimising the $(Bi_{0.98}In_{0.02})_2Te_{2.7}Se_{0.3}$ containing 0.02 wt. % rGO. Gwansik Kim et al. [112] prepared bulk nanocomposites using $Mg_{1.96}Al_{0.04}Si_{0.97}Bi_{0.03}$ and a few layers of rGO through an ultrasonic-based wet chemical pulverising mixing method to enhance the thermoelectric performance and mechanical stability. Surprisingly high K_{Ic} of 1.88 MPa $m_{1/2}$ was achieved with rGO 3 vol%, and a more excellent ZT value of 0.6 was observed.

Table 2-2 Summarises the synthesis method and thermoelectric performance at room temperature of common inorganic materials with graphene

Material	Synthesis	σ (Scm^{-1})	K ($Wm^{-1}K^{-1}$)	S ($\mu V K^{-1}$)	ZT	Ref.
Bi_2Te_3 / 0.25% rGO	Hot-pressing method	8×10^{-6}	1.3	-80	-	[95]
Bi_2Te_3 / Graphene	Hydrothermal SPS	1.05×10^{-5}	2.5	-113	0.21	[113]
Bi_2Te_3 / Graphene	Wet chemical sintering	3.5×10^{-5}	0.7	-132	0.2	[97]
$(Bi_{0.98}In_{0.02})_2Te_{2.7}Se_{0.}3$/ wt.% rGO composites	Solid-state reaction	3.0×10^{-3}	0.8	-140		[111]
PEDOT: PSS / Bi_2Te_3	Ball milsled	250	0.55	150	0.08	[114]

2.2.6 *C derivatives (CNT, etc.) + organic/inorganic composite*

Because of their exceptional electrical characteristics, carbon nanotubes have been regarded as viable options for various applications, such as touch screens, field emission displays, solar cells, and field effect transistors. The σ of these materials is greater than that of the other polymer composites. They use another dopant since carbon nanotubes are also used as a filler in polymer composites. A study of TE materials has been more interesting with carbon nanotubes. Owing to their dimensional structure, it has been reported that 1- or 2-dimensional thermoelectric materials have lower dimensions than bulk materials and can sometimes perform better. By increasing the density of the state near the fermi energy and reducing the sizes, CNT can increase S [115].

Kim et al. [116] used polyethyleneimine, $NaBH_4$, and diethylenetriamine to treat CNT to create n-type materials with S = 86 μVK^{-1} and σ = 52 S cm^{-1}. A flexible TEG made from 72 CNT foil thermocouples with a 49 K temperature gradient yielded an open circuit voltage of 465 mV. Additionally, multi-walled TE fabrics are manufactured by Hewitt et al. [117] using p-type and n-type CNTs/PVDF composite film, and the sum of the thermoelectric power produced by these textiles is calculated and found to contribute from each p-type and n-type layer. At 50 K, thermoelectric fabric with 72 film layers had a maximum output of 137 mW. This is the fundamental distinction between inorganic TE generators that are commercially available (attached to a π-shaped structure). This is because the π-type inorganic TEG may recycle the surface average temperature difference of the n-type with the maximum output coefficient TEG [118]. A maximum PF of n-type (1500 $\mu W\ m^{-1}K^{-2}$ at room temperature) polyethyleneimine (PEI) doped, reposted layered carbon nanotubes (SWCNT). Both p-type and n-type SWCNTs are flexible TEGs with three pairs of thermocouples and an open circuit voltage of 11.3 mV at a 27.5K temperature gradient. The maximum output power it can generate is 2.51 μW [119]. In addition, the optical switching of the poly (3-hexylthiophene) (P_3HT)/CNT composite materials from p-type to n-type simplifies the production of the TE generator by having only one solution [120]. This is the main difference in the flexible TEG manufacturing method shown in reference [119].

Choongho et al. [99] started with an emerging aqueous CNT/PVAC composite solution. At RT, the σ and k are 48 S cm^{-1} and 0.34 W $m^{-1}\ K^{-1,}$ respectively, and the ZT is more significant than 0.006, containing 20 wt.% CNT. Furthermore, they achieved encouraging ZT values around 0.02,

and PEDOT: PSS doped with DMSO employs a network of the conductive polymer [72]. SWCNT added 35 wt.% into PEDOT: PSS results in the σ reaching 400 S cm^{-1}. Qin Yao et al. [121] found that the SWCNT/PANi nanocomposites exhibit outstanding S compared to the pristine PANi. This can be attributed to the improved carrier mobility in the structured chin of PANi. In contrast to pure polyaniline, composites have a maximum σ of 1.25 $\times 10^4$ S $cm^{-1,}$ a maximum S of 40 μVK^{-1}, and the highest PF of 2 $\times 10^4$ $\mu W\ m^{-1}\ K^{-2}$. In this study, Lei Wang et al. [122] prepared nanocomposites via a mechanical ball mill followed by cold pressing when graphite content is present in materials at a 50 wt.% concentration. The σ and the S rise as the graphite content ensures, yielding a PF of 418 $\mu W\ m^{-1}\ K^{-2}$ and ZT of 1.37×10^3. Yu et al. [123] have described developing a separate CNT network in a composite made of polyvinyl acetate (PVAc). A minimal amount of CNT content is crucial for creating this polymer composite since it will help it develop its distinctive properties. The creation of the CNT network enhances the electrical conductivity, but the k and S parameters are unaffected by the filler concentration. The insulating polyvinyl acetate matrix uses a long drying method at ambient temperature to create a 3-D network. A thermally isolated but electrically connected network assist in improving the figure of merit. PVAc/CNTs exhibit σ and k values 48 S cm^{-1}, and 0.34 $Wm^{-1}\ K^{-1}$ respectively twenty wt.% content of CNT at 300 K. The CNT/polymer composite can maintain conductivity which remains constant when electrical conductivity is greatly improved by the connecting junction between the CNT [124]. Contrary to PVAc/CNT-filled composites, PANI-based carbon nanotube-filled composites have a decoupling effect connected to an enhanced S. SWCNT used the in-situ polymerisation processes to create composites. Compared to polyaniline and pristine CNT the S is 2.74 $\mu VK^{-1}$and 12.2 μVK^{-1} [125], whereas the PANi / CNT composite exhibits improvement performance with the highest value up to 28 μVK^{-1} and behave as a P-type thermoelectric material at 350 K. The primary explanation for this is the energy-altering phenomenon that emerged with CNT and PANi contact. Kinge et. al., [126] have designed a labelled chemical process to create CNT/polyaniline nanocomposites. The straightforward procedure starts with mixing solid ammonium peroxydisulfate with anilinium hydrochloride and CNT. By maintaining a constant CNT concentration and changing the type of CNT, the author of this work highlighted propertiesof polymer nanocomposites, such as their SWCNT, MWCNT, oxidised, or unoxidised states. In comparison to the pure PANi sample, all nanohybrids exhibit superior performance. They showed excellent thermoelectric properties of PANi/unoxidised SWCNT reporting (σ 530 S cm^{-1}, S 33

μVK^{-1}, and PF 0.6 $\mu W\ m^{-1}K^{-2}$) in contrast to another hybrid. This nanohybrid, encompassing oxidised and unoxidised SWCNT or MWCNT, showed the same S with different σ. Similarly, Yu et. al., [123] represents a schematic PEDOT: PSS- coated carbon nanotube junction in Fig 2.4 (a). A graphic depiction of the fluctuation of σ and S with CNT concentration can be found in Fig. 2.4 (b). σ rises with CNT concentration until a point of 60 wt.%. At this point, it starts to fall. With the change in CNT concentration, S exhibits slight changes. With the inclusion of CNT, TE characteristics have been attained. At room temperature, this alteration gives the maximum ZT of 7.2×10^{-5}.

Hewitt et al. [142] have processed TE fabric made of several CNT/polymer composite layers. CNT/polymer composite thin films have a low ZT (0.02). The author created MWCNT-filled polyvinylidene fluoride (PVDF) composite films for this assignment. These films were stacked to produce numerous element modules that resembled felt fabric. Each layer works together to provide a greater thermoelectric voltage, which makes it a desirable alternative to materials based on bismuth telluride for TE applications. Md. Sidul Islam et al., [127] The k, σ, PF of the GO / CNT (1:2 ratio) film improved significantly, obtaining results of 28.6 $Wm^{-1}K^{-1}$, $6.52\times10\ Scm^{-1}$, and $5.33\times10^{-2}\ \mu W\ m^{-1}\ K^{-2}$ respectively. Wang et al., [128] A flexible two-pair TEG was produced using SWCNT/PEDOT: PSS or TiS_2/C_{60} hybrid film as the n-type and p-type respectively, at 20 K with 335 nW of electrical output. Furthermore, screen printing was used to create rolled flexible TE generators employing the p-type and n-type materials PEDOT: PSS and CPE/CNT nanocomposites, respectively [129]. The highest power output and open-circuit voltage of the them 288-leg thermoelectric module is 46 μW and 260 mV at 65 K. Similarly, Y.duet.al. [94] synthesised a MWCNT/P_3HT composite via oxidative polymerisation of 3- hexylthiophene in an MWCNT dispersed chloroform solution. When the temperature increases from 298 to 423 K, the σ drops from 0.13 to 0.11 S $cm^{-1,}$ and the S rises from 9.7 to 11.3 μVK^{-1}. After cold pressing, the MWCNT content was 30 wt.% in composite powder.

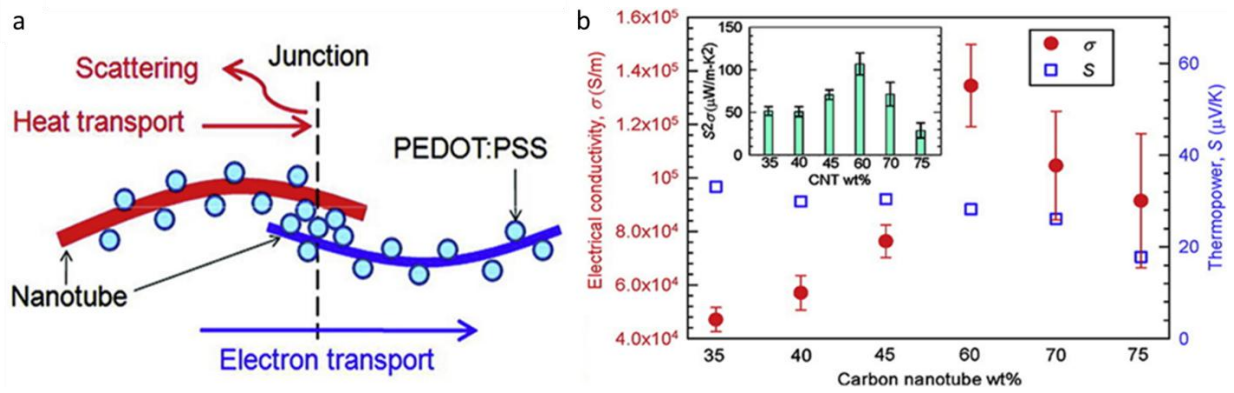

Figure 2.4 (a) Graphical representation of the interconnection of CNTs covered by PEDOT: PSS materials. (b) Electrical conductivities and Seebeck coefficients of the composites at various nanotube concentrations, with an inset illustrative of the TE power factor. Aadapted with permission from Ref. [123] Copyright 2011, American Chemical Society.

The structural characteristics of these composites play a significant role in determining their mechanical, thermal, electrical, and other properties. For the first time, Firuze Soltani [130] reported the effective use of traditional and substrate vibration-assisted ultrasonic spray coating (SVASC) to fabricate highly conductive transparent graphene-doped PEDOT: PSS composite thin films. The graphene dispersion mechanism in PEDOT: PSS and IPA solutions. The -OH groups in IPA can form a connection with the unsaturated carbons at the outermost edges of the broken graphene sheets. These -OH groups combine with sulphur on the hydrophilic sides of PEDOT: PSS or PSS, to generate hydrogen bonds after being mixed with aqueous solution of PEDOT: PSS. These intermolecular interactions help graphene disperse and suspend in the solution, which improves the conductivity of graphene-doped PEDOT: PSS. Fig 2.7 displays the FTIR peaks of the pure PEDOT: PSS, IPA/graphene, IPA/graphene/PEDOT: PSS solutions to support the previously mentioned assertion. The graphene surface interacts with the -OH group in IPA or water to create C-O-H bonds, which are shown by the spikes at 1301, 1164, and 1384 cm^{-1}. In IPA and PEDOT: PSS solution, these interactions oversee the full and stable dispersion of graphene [131]. Fig 2.8 displays the XRD patterns of pure graphene and graphene-doped PEDOT: PSS composite films that have been IPA treated. All the PEDOT: PSS films typically exhibit the low intensity peak of pristine PEDOT: PSS at 23° in their pattern [132, 133]. The peaks of pure PEDOT: PSS and IPA/PEDOT: PSS are nearly overlapped. A prominent peak at 26° overlaid on the PEDOT:

PSS pattern for the graphene-PEDOT: PSS thin film clearly shows the graphene's dispersion throughout the PEDOT: PSS matrix and makes evident the graphene's noteworthy influence on the conductivity of the PEDOT: PSS film. The investigation yielded a maximum electrical conductivity of 298 Scm^{-1} for a thin film composed of graphene-doped PEDOT: PSS. This value represents a ten-fold enhancement when compared to the electrical conductivity of pristine PEDOT: PSS thin films. Similarly, Fei-Peng Du [134] reported PEDOT: PSS/GQDs composites were effectively made using simple casting techniques. PEDOT and PSS chains decoupled and separated into phases because of the strong interactions between GQDs and PEDOT chains via Π-Π bonding. The microstructures (P-GQDs-10 wt%) that were developed improved electrical conductivity and Seebeck coefficient of PEDOT: PSS at the same time. When compared to pristine PEDOT: PSS, the PF of PEDOT: PSS/GQDs was increased by 550%. This work offered a viable path for the application of PEDOT: PSS in highly effective TE conversion. Analysis using Raman spectroscopy and X-ray photoelectron spectroscopy (XPS) revealed the strong Π-Π interaction that promoted the dispersion of graphene and PEDOT: PSS. The ZT value and PF of the composite thin film with 2 wt% graphene was 0.02 and 11.09 $\mu Wm^{-1}K^{-2}$, respectively. This improvement results from both graphene's high electron mobility (200000 $cm^2V^{-1}s^{-1}$) and the easier carrier transfer between PEDOT: PSS and graphene [78].

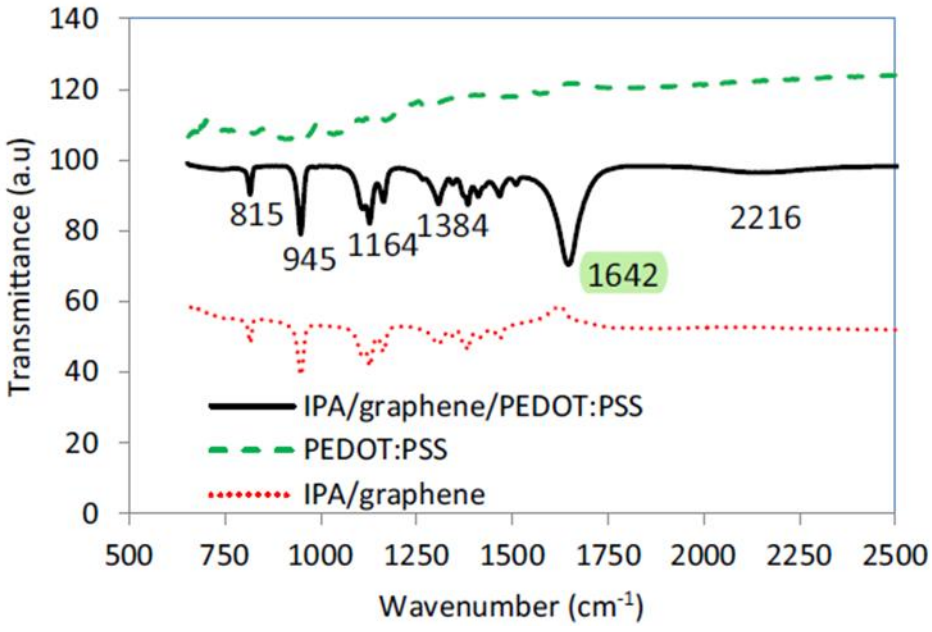

Figure 2.5 FTIR spectra of Pristine PEDOT: PSS, IPA/graphene/PEDOT: PSS and IPA/graphene solution [128].

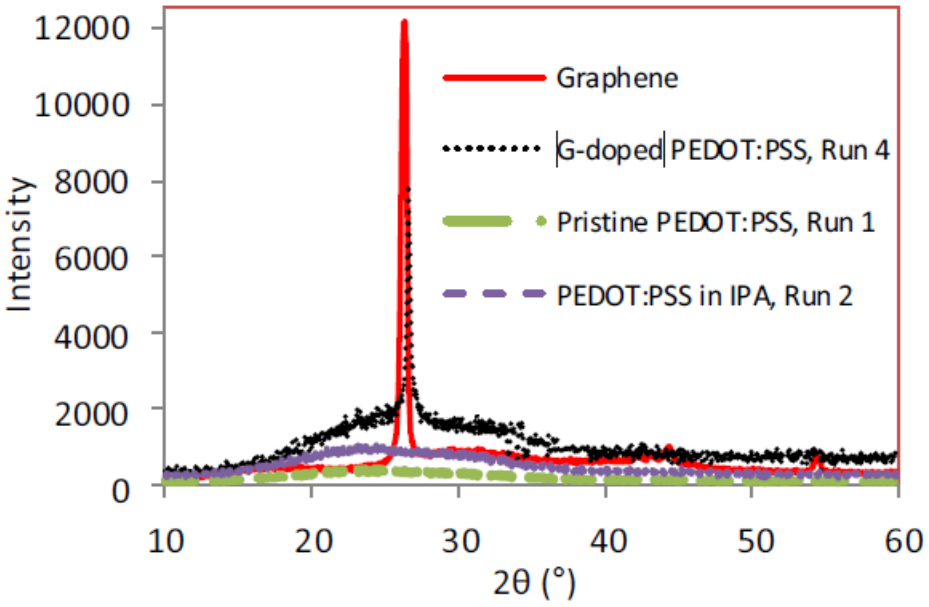

Figure 2.6 XRD patterns of graphene, pristine PEDOT: PSS thin film (Run 1), PEDOT: PSS thin film prepared using IPA as co-solvent (Run 2), and SVAC-fabricated graphene-doped PEDOT: PSS (Run 4) [128].

2.3 N-TYPE DOPING IN ORGANIC THERMOELECTRIC MATERIALS

2.3.1 *Overview of n-type Organic Thermoelectric Materials*

Organic semiconductors are the best substitute for inorganic semiconductors for applications, where a high photoluminescence efficiency, high absorbance, or long spin lifetimes are required. Furthermore, despite the challenge associated with the charge transport in polycrystalline [135]. An organic semiconductor has advantages over inorganic semiconductors. These include their cost-effectiveness, great abundance, and the ability to be processed over large area, but still, they have a disadvantage of working limited at low-temperature purposes only. In addition, the polymer material proved to have a lower thermal conductivity when compared with inorganic materials, making it an optimal choice for thermoelectric applications. Variation of dopant concentration leads to energy bandgap tuning which is useful for thermoelectric applications [136]. A pure organic semiconductor has low electrical conductivity, so doping is necessary for making them

useful for thermoelectric purposes [136],[137]. For example, in trans-polyacetylene, electrical conductivity increases up to 1000 S/cm and carrier mobility up to $1cm^2\ V^{-1}s^{-1}$, when p-doped with AsF_5 (arsenic pentafluoride), or iodine vapors [135].

Electrical conductivity in a semiconductor can arise, when the bandgap between the lowest unoccupied electron (V.B) and highest occupied electron (C.B) becomes small enough through which an electron jump. The introduction of a defect via doping results in a reduction of the bandgap. This process generates an additional energy level located between the valence and conduction bands, referred to as the fermi level, which contributes to the decrease in the bandgap. In the past two decades, there are lots of organic conducting polymers that have been proven, although most of them need a foreign species, dopants increasing their conductivity from low to 10^{-8} Scm^{-1} to its high as 10^{-4} Scm^{-1} in doped semiconductor, so we can tune the conductivity of polymers by carefully manipulating the concentration of dopants [135]. Doping is the process that necessitates the presence of both electron donor and electron acceptor molecular species, along with the induction of a mobile carrier throughout the polymer chain [135],[138],[139]. A positive charge carrier is generated in the conducting polymer chain, if we added a P-type dopant by removing the electron from the HOMO of the organic conducting polymers [140] N-type dopants contribute an electron to the LUMO of the semiconductor. In this process, an integer charge is transferred [135], so this process is known as the integer-charge transfer model shown in Fig 2.9 (a) & (b).

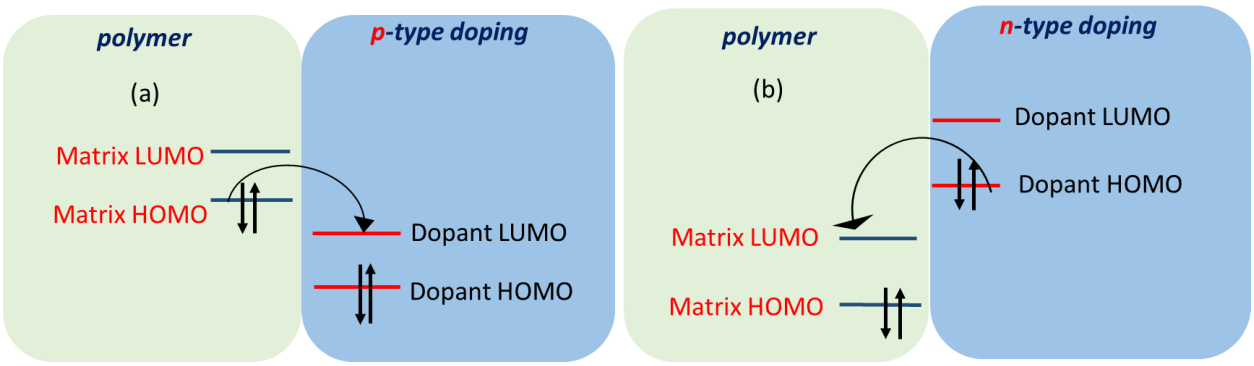

Figure 2.7 Illustrates the process of Organic conducting polymer doping through the integer charge transfer model.

In 2012, Zhu et al. [135] conducted a study on a coordinate polymer, focussing their attention on the recently discovered n-type organic TE materials. Recent advancements have been observed in the case of OTEGs utilising p-type conducting polymers, where an increase in the ZT has been achieved through chemical modulation in the oxidation state of the in the semiconductor and number of charge carriers [137],[141]. whereas in case of n-type conductive polymers and appropriated reduction for controlling the densities of charge carrier was still insufficient. Due to this employing of π-leg module structures was restrained, which enhanced the output voltage via the junction between p- and n-type thermoelectric generators, arranged in series for electrical and in parallel for thermal purpose [137]. Specifically, the lower electrically conductive nature of n-type conductive polymer in contrast to p-type was a basic challenge [137],[142],[139],[143] because of their non-uniform transmitted coefficients (i.e., σ, κ) which leads towards the loss in power in π-leg modules.

2.3.2 *Doping requirements for thermoelectric*

Organic semiconductors are insulators in nature due to their wide bandgap, also they could be tuned by the process of doping. An intramolecular arrangement is formed if there is elimination and introduction of the electrons from the π-system of the organic compound, resulting in the formation of a polaron [135],[144],[145].polarons were generated and their existence was confirmed using various techniques, with optical spectroscopy playing a key role in the investigation. On doping, the optical absorption experienced a notable shifting, considering the formation of polaronic levels; redshifts occurred in optical absorption due to sub gap levels formed on doping which causes geometrical relaxation [144],[145]. In the year of 1970s, conjugated polymers and molecules had their conductivity raised by severalfold by doping them with a combination of alkali metals and halides. Chiang et al. [146] in 1977, was found their electrical conductivity increased by 11 orders of magnitude via doping halogen and AsF5. doping polyacetylene with iodine increased its electrical conductivity by an order of seven, Shirakawa et al. [147] from1977. As early as 1979 Yamamoto et al., [148] examine the thermoelectrical power and the electrical conductivity of the Phthalocyanine with halogen. When they exposed the complexes in the vapor of halogen, its electrical conductivity raised extremely in the order of 10 to 11, and complexes with greater conductivities display lower activation energies as compared to lower conductivities. Similarly, Basescu et al., 1987, was measured the highest values of the

electrical conductivities as 20,000 S/cm by doping iodine. He studied electrical conductivity as a function of temperature at 0.48 K and pressure at 10 Kbar, it showed the highest conductivity at 9000 S/cm [149]. Additionally, the complexes exhibited a favourable thermoelectric power, suggesting that conduction occurred through holes. The mechanism of doping in OSCs could be elucidated by the integer charge transfer model and more precisely explained by hybrid charge transfer it is caused due to the mixing of the orbit of acceptor and orbit of the donor. The electrical conductivity of organic semiconductors can be influenced by the introduction of charge carriers and alterations in structural order, ranging from the molecular level to the macroscale [144],[150]. In the region of crystalline, there is a difference between the electronic coupling within the molecules, resulting in highly anisotropic charge transport. The interaction between the π-electronic levels of the molecules facilitates efficient charge transfer by ensuring that intermolecular contacts are sufficiently closed.

2.3.3 *Current Status and challenges*

Lewis's acid (p-type) and Lewis's base (n-type) are the new techniques for doping, although these are not fully utilized for organic thermoelectric applications. but it could be explored for doping in an organic semiconductor and used for enhancing the performance [136]. Nano-composites of the polymer are proposed as a highly promising approach for achieving both the straightforward synthesis of conducting polymers and the favourable TE properties of inorganic fillers. Therefore, the electric contact resistance was reduced between the inorganic structures by using conducting polymers, while simultaneously maintain the overall thermal conductivity of the composite at a low level. The thermoelectric material with a low degree of dimension had low intrinsic thermal conductivity because of phonon interface scattering, representing an additional methodological approach [151],[152]. Practically, this methodology does not useful at high temperatures to sinter the nanoparticles of organic material. Still, we have not fully understood the capabilities of organic thermoelectric material, such as they appear as a good option for heat recovery for low temperatures. Although we did not completely learn about the thermoelectric characteristics of conducting polymers, they showed strong possibilities for a rise in ZT value coming from the lower value of the power factor. Conjugated polymers with large molecules are very complicated in morphology with polymer chain spiralling, agglomeration in certain regions, and the formation of crystalline region, which are isolated by an amorphous addition. Thus, we get a group of

thermoelectric characteristics is obtained; these properties exhibit significant anisotropy and are particularly influenced by the methods of preparation and processing used. To improve the conductivity of the polymer, it is essential to improve its crystalline nature through the regulation of its structure and surface morphology. The insulating region of the thermoelectric device warrants significant attention within the context of thermoelectric study, metallic conducting polymers are an exceptional case for thermoelectric use because of their low Seebeck coefficient. In the insulating area, transportation is yet a little bit temperature-dependent with localized segments greater than the firmly disarranged system (low ratio of crystalline and doping concentration). In inter-chain transport the coupling among the conjugated polymer chains via the counterion wavefunction is significant and the study of its effect is limited [151],[153]. hence, the electrical conductivity depends on the arrangement of polymer chains, location of the counterions, and the properties of the crystalline phase. The only simple models till now are based on the Seebeck effect, even though its little knowledge. The power factor could be modulated through the change of doping level, it had been shown that to improve the models it is important to classify the entropy-of-mixing offering α^{el}_{mix} (electronic Seebeck coefficient) with an additional practical density of state. A similar accumulation of band is done in semiconductors [151],[153]. The DOS (density of states) developed to improve the electronic Seebeck coefficient. This result is reported from the simple equation of the Seebeck coefficient as alternation in entropy-of-mixing divided with the charge carrier; at the same oxidation level, polarons have two times more electronic Seebeck contribution α^{el}_{mix} in comparison of bipolarons. An investigation is required to examine the solid for the energetic characteristics that govern the ratio of bipolarons to polaron quantities. This analysis is essential for understanding the chemical and morphological attributes that contribute to high electrical conductivity while maintaining polarons as the main charge carrier [151]. Furthermore, it has been notified that polyaniline in the “insulating” domain is a typical example of polaronic arrangement, has a low power factor. At the “insulating-critical” area charge carrier position play a very important role in the case of coupling electron-phonon. So, the vibrational softening endowed $\alpha^{el\text{-}ph}_{vib}$ to segment or pile of segments is vital. Still, this is not yet confirmed or not used for the model. The change of polymer chain structure is more relay on the transportation of bipolarons rather than polarons, so, $\alpha^{el\text{-}ph}_{vib}$ is larger for bipolarons than the polaron. As consequently, to improve the ZT value, the prepared design must concurrently involve the different contributions to the Seebeck coefficient.

2.4 TYPES OF DOPANTS

A Dopant is the collective name for many materials. It is like impurities introduced in the organic semiconductor for modifying the properties of the material. Which improves the performance of OTE material. The thermoelectric efficiency of the material largely affected by doping level. The σ is directly proportional to the doping level and the S is decreases with increase of doping level. Many ionic species and molecular involving acids and bases are also taken as a dopant in organic thermoelectric material, where their molecular structure have control over the diffusion. Such as by managing the dopants shape or size, anchoring the covalently. Bronsted acid, Lewis acid and Lewis bases also counted as molecular dopants [154], Alternation of SOMO level in radical form also needs attention [155].

Fundamentally, chemical polymerization is an oxidative reaction, through this reaction, we get p-type semiconductors, which are electron-deficient on their backbone in this doping method, the organic thermoelectric material soaked into the solution or exposed in the front of a gas containing an oxidizing agent (a molecule with greater electron affinity than the host's ionization potential). The organic semiconductor is oxidized by this dopant. Dopants move into an anionic state which ensures overall charge neutrality of the system. For instance, I_2 converted into I_3^- [151] or a salt solution NO^+PF^- becomes anion PF_6^- while evolution of NO gas takes place. Jin-Chih Chiang et al prepared a base form of polyaniline that is Emeraldine with doping of dilute non-oxidizing aqueous acid like HCl, which makes it metallic conducting, and stable in the air indefinitely. They reported a new type of doping i.e protonic acid doping (In this kind of doping a spontaneous spin unpairing directing to the formation of polaron) in organic thermoelectric material. In this method, a proton is added to the organic thermoelectric material instead of a partial oxidation of its π – conjugated structure like taking place in p-type doping in other organic thermoelectric material. It yields nitrogen base salt in place of carbonium ion a highly reactive form, making it a more chemically stable material in the environment. The large-scale π-conjugation in Emeraldine salt, causes the high conductivity of the material. Its conductivity relied on the two factors first one degree of oxidation of the polyaniline and organic thermoelectric material's degree of protonation [156]. In this type of doping (protonic acid doping), protons covalently bounded with the nitrogen of polyaniline and its positive charge transmitted to the π-conjugated system. So, through chemical polymerization the oxidized form of organic thermoelectric material synthesized directly, for

decreasing the oxidation level of organic thermoelectric material in this type of doping (i.e protonic acid doping) a reducing dopant is used in chemical polymerization [157].

2.4.1 *Molecular dopants*

The basic procedure in chemical doping is the interactivity of the organic thermoelectric material with dopants. Their molecular structure of OTE martials is of utmost importance in its development. A molecular dopant refers to a small, neutral molecule that possesses either a low ionization energy (n-type) or a high electron affinity (p-type), so they donate or accept the electrons from the OTE material. Basic parameter for designing a molecular dopant is charge transfer, like modification of fermi level, replacement of heteroatomic molecule, effect of side-chain etc., molecular packing and interaction within the molecule. Kapov et al. reported the CN6-CP (hexacyano-trimethylene-cyclopropane) as a strong molecular dopant, has -5.87 eV EA. For reducing the diffusion rate, 3D dopant (bulkier structure) showed better results [158] such as $C_{60}F_{36}$ and $C_{60}F_{48}$ here fluorine increases the EA. They both developed by using the vacuum deposition method and has higher EA than F4TCNQ and show stability in the case of thermal diffusion [158] but their size has a side effect on the morphology of OTE material.

Lewis acid as a molecular dopant: - Electronic properties of the organic thermoelectric material can be modified by the process of doping. Doping can be done in two ways -either we add electrons in organic material from the dopant (n-type) or we remove the electron from the organic semiconductor (p-type). Lewis acid and Lewis base is also used as dopants in organic thermoelectric material. Presently, noticed that Lewis acid is an induced p-type charge carrier in the chain of an organic semiconductor, which increases the conductivity remarkably. In 2009, Bazan et al. have reported the effect of Lewis acid on donor-acceptor polymers. Donor-Acceptor is a moiety that has a molecular structure with electron-rich and electron-deficient both connected with a π-conjugated bridge. Here, transfer of charge from electron-rich molecular segment to electron-deficient molecular segment takes with the help of photoexcitation process. The realignment of electron density leads the absorption bands to expand from the UV region to near-infrared regions of the spectrum, relying on the electronic offset between the donor-acceptor segments and over the complete length of the delocalized chain. Final material from this process has applications in organic electronic and optical fields such as non-linear optics, OLEDs (organic light-emitting diodes), etc. Bazan et al. [159] showed that the choice of binding of Lewis acids to

reach the N- atom present at the acceptor unit eliminated the electron density on the π – conjugated system leading to narrowing of the bandgap. Further, a change is observed in the absorption maximum (λmax) from ∼500 to ∼650 nm in the case of 5,50 –bis (benzo thiadiazole)-3,30 -di-n-dodecylsilylene-2,20 - bithiophene (BT/DTS/BT) upon binding of $B(C_6F_5)3$ to the nitrogen atoms in the outer two benzothiadiazole (BT) units. The strength of Lewis acid also tuned the degree of change in the absorption properties. The Strong Lewis acid decreases the bandgap more i.e. most red-shifted absorption spectrum. Bazan et al. studied the effect of $B(C_6F_5)_3$ with D/A (donor-acceptor) conjugated polymers to sort out the participation of steric and electronic to the binding equilibrium and alter the optical properties. They observed that the interaction of $B(C_6F_5)_3$ with the polymers leads to a reduction in both HOMO and LUMO energy levels. Such as Poly{(4,4-bis(2-Ethylhexyl)-cyclopenta-[2,1-b:3,4-b'] dithiophene) – 2,6-diylalt-([1,2,5]-thiadiazole [3,4-c] pyridine) -4,7-diyl} energies of HOMO and LUMO polymer was found out -5.01ev and -3.70 ev respectively. After the addition of $B(C_6F_5)_3$, energies were found to be -5.24ev for HOMO and -4.28ev for LUMO. The difference in energy is 0.35ev which leads to a decrement in the optical bandgap. Here, both level HOMO, as well as LUMO effect by the addition of $B(C_6F_5)_3$ but this effect, is found more noticeable in LUMO level, which mainly occupies near the acceptor segment. This is the reason behind the decrement in the bandgap of energy level and they also noticed an increment in free charge carrier concentration and mobility [160].

In the future for molecular dopants design focus should be on increasing the strength of dopants, solubility/ miscibility, yielding reaction, and processed air/stable dopants. Initially, the doping of conjugated molecules was done with halides and alkali metals but these have the drawback of not producing a covalent bond with the host, and they showed a tendency diffuse within the organic semiconductor matrix. This diffusion can create ohmic contacts or p-n junctions which are unstable under operating conditions [137]. Bulkier molecular dopants have emerged as a possible way to reduce the diffusion rate P_3HT and PEDOT: PSS were the conjugated polymers and conjugate molecules in which p-type molecular doping was introduced. molecular doping is used for decreases the ohmic losses in carrier transmitted layers and to introduced the barriers at the contact of electrodes. hence, the performance of the devices get boost [137]. both effects (reduction in ohmic loss and introduction of barriers) showed successful results in the p-i-n multilayer structure where an n-doped electron and p-doped hole transport layers were used as a sandwich the intrinsic active layers such as photovoltaic layers in organic, emission layers in OLEDs, and

perovskite solar cells. Moreover, molecular doping was used in Zener diodes [161] and organic inversion field-effect transistors [162]. Molecular doping has been a successful doping technique but still, there has been no explanation of their basic process, it's still under debate [137].

2.5 PROCESSING OF DOPED POLYMERS

2.5.1 *post-deposition treatments of PEDOT systems*

Bubnova et al, [163],[157] improved the value of ZT in PEDOT: ToS used TDAE as a de-doping agent, they reported that deficiency of electron on the chain of PEDOT: ToS was balanced when its film was exposed to a high amount of TDEA (high oxidation level) vapor, here de-doping happened and then, electrical resistivity increased hence Seebeck coefficient also increased.
They developed a method through which they fabricated thermoelectric modules with the help of conducting polymers like PEDOT achieved by electrochemical polymerization. This strategy will provide all the thermoelectric elements but only a p-type semiconductor could be used. For increasing the power generation of PEDOT, exposed to the reduction treatment. Through the hydrazine treatment, the doping level in polymeric material was affected, decrement in numbers of charge carrier because electron denoted by reducing agent, neutralized the PEDOT chains (i.e bipolaron and polarons) [164],[165],[166],[167]. In this method, π-bonds increased and the electrical conductivity of the films changed from 350 to 750 Scm^{-1} after 11s. Without reduction treatment, the Seebeck coefficient value of pristine module was at 91μVK^{-1} after reduction with hydrazine vapor method is raised to 413μVK^{-1} during 11s. The Seebeck coefficient value increased because of the decrease of doping levels in PEDOT. The Seebeck coefficient was noticed as constant with temperature since there was a linear relationship between the difference of voltage and the temperature. on the account of the absence of the glass transition temperature T_g in PEDOT [164], T_g at 85°C substrate gave the highest temperature limit application. The power generation was examined as a function of load resistance and the temperature difference was 60°C. here the thickness of PEDOT was in the limit of 2μm to 5μm. From the result, they get information that with the impedance of the generator, the maximum power gets a load resistance of 30 KΩ. The module gives the maximum power without undergoing a chemical reduction of about 2.7 nW whereas after the treatment 5.03 nW was reached. From this research, they suggested power generation increased with changes in doping amount in conducting polymer.

2.6 EMERGING APPROACHES TO DOPING

2.6.1 *N-type doping*

Up until recently, the thermoelectric performance of organic p-type materials has always surpassed the performance of the n-type materials due to difficulties in n-type doping. For electrons to transfer from a dopant to a semiconductor, the HOMO of the dopant must be aligned or higher in energy than the LUMO of the semiconductor. The electron affinity of n-dopants, therefore, tends to be small, making them highly reactive and very sensitive to ambient air and moisture. With other limiting factors such as phase separation, misaligned energy levels, solubility, and an overall lower doping efficiency in n-type materials, finding a stable compatible n-dopant can be challenging. The most common approach is to use highly reductive species which can directly transfer electrons into the organic material. Although this approach encompasses all the difficulties mentioned above, there has been some success. Organic molecule (4-(1,3- dimethyl-2,3-dihydro-1H-benzimidazole-2-yl)phenyl)dimethylamine (N-DMBI) is a widely used n-dopant which has an ionization potential of 4.67eV, making it fairly stable in air [168]. It is proposed that the thermal activation releases hydrogen, and leaves a neutral radical N-DMBI which dopes the acceptor material. When doping has taken place, the N-DMBI is left with a cation that resides beside the localized electron-rich nitrogen atoms and phenyl rings, making the electron transfer irreversible. The N-DMBI neutral radical has been calculated to have a SOMO of 2.36 eV which is small enough to ideally dope most n-type organic semiconductors. Through computational studies, Yan Zeng et al. found that the hydrogen removal process can also be influenced by the semiconductor it's interacting with [169]. Their study shows that interactions between the semiconductor Q-DCV-DPPTT and N-DMBI significantly decrease the energy required for the hydrogen removal resulting in room temperature. There are also other suggestions of a hydride transfer process as a doping mechanism of N-DMBI which is slightly different from a cleaved hydrogen bond [169, 170]. This mechanism is also explored by Yan Zeng's group whom found it could also take place at room temperature in the semiconductor Q-DCV-DPPTT, and by David Keifer's group whom successfully doped the polymer p(gNDI-gT2). Peng Wei et al., also found that n-type molecule PCBM becomes more air-stable upon doping with N-DMBI. The group measured electrical conductivities above 10^{-2} Scm^{-1} after 20 days in the air and attributed this improved air stability to

the dopant-semiconductor packing. However, this N-DMBI is not particularly soluble and aggregates easily at high temperatures and high doping levels [171].

2.6.2 *Self-doping materials*

A much newer approach to doping involves 'self-doping' semiconductors where, without relying on an external dopant, semiconductors can inject free charge into their own electrical pathways. This method solves the problem of phase segregation and miscibility. The main way to achieve a self-doping molecule or polymer is to engineer electron-donating bodies, i.e.: electron-rich amines or an ionic species, which are attached to an electron-deficient backbone or molecule. The experimental study on self-doping polymers first came to light in 1987 by Patil's group [172] and research has since grown significantly, not only for thermoelectric materials but also for OLEDs, OSCs, and the biomedical field. Many successful self-doping n-type polymers have since been reported. One of these polymers is the Phencyclidine (PCP) derived PCP-Na where conductivities in the 10^{-3}Scm^{-1} range were measured. Optical spectroscopy of PCP-Na shows a polaronic species both in film and in solution which is interesting as a close distance between the backbone and electron-donating unit is needed for electron transfer to take place. Having a doped species in solution can be extremely beneficial as the doping will not be hindered too drastically by unideal morphology, assuming it persists in film form. Similarly structured polymers PCF-Na and PFS-Na were also tested but showed no self-doping properties, illustrating how sensitive self-doping is to small structural differences. A similar example is seen where Liu et al. [173] partially fluorinated the polymer poly(9,9′-bis(6″-N,N,N-trimethylammoniumhexyl)fluorene-alt-benzene) (PFB) to induce electron transfer from an electron-rich side group to the fluorinated, electron-withdrawing unit of the polymer backbone. However, electrical conductivities were still low, indicating that even with the most electronegative element, self-doping polymers can still face poor doping efficiencies from structural challenges. To further this point, in a recent study by Tang et al., the strong electron-withdrawing unit benzobisthiadiazo (BBT) [174] is used in the copolymerized polymer PFNBBT. Interestingly, in its quinoidal form, direct electron transfer is observed from an electron-donating fluorene unit to the BBT unit forming a diradical BBT species, however, in aromatic form, no electron transfer takes place. The parameters mentioned so far, i.e.: choice of electron donor group and structural variations, are tunable parameters that can excel research on self-doped polymers.

2.6.3 *Low volatility dopants*

Fullerene-based dopants have advantages they are low volatility and thermally high stability which play a significant role in operating devices below elevated temperature. Due to all these properties of fluoro-fullerene $C_{60}F_{36}$ is in highly use p-dopant in a large spectrum of organic p-i-n devices like memories, solar cells, emitting diodes, and transistors. The fluorination of the C_{60} molecule brings the energy level lower by approximately 1eV [175] so, the effective charge is transmitted from HOMO of the matrix material with an IP near to 5eV, to the LUMO of $C_{60}F_{36.}$ Due to the lower molar ratio of the $C_{60}F_{36}$ dopant, it has higher efficiency, with large charge transfer per molecule with the host i.e N, N'-[(Diphenyl-N, N'-bis) 9,9-dimthyl-fluoren-2-yl]-benzidine. However, $C_{60}F_{36}$ has a drawback which is its higher activation energy deep trap states was formed, whereas it could avoid as its higher charge transfer gives an excellent conductive layer. Its power conversion efficiency is also better than the F_4TCNQ in a solar cell. So, the $C_{60}F_{36}$ could be used as a dopant in place of F_4TCNQ. Successfully, n-type doping in organic material could improve the thermoelectric performance by increasing the charge and charge transferred characters. Because of the n-type semiconductor's low electron affinity, it is hard to dope with a high quantity of charge carrier [176] and bulk doping raised the structural disorder, which decreased the hopping rate [177],[178]. Dazhen Huang et al., showed bismuth, a heavy metal, as a strong candidate for interfacial n-type doping for a thiophene-diketopyrrolopyrrol-based quinoidal molecule. Doping of interfacial Bi in TDPPQ ultra-high thin film gives power factor $113\mu Wm^{-1}K^{-2}$, this was the best PF value obtained for the small molecules of n-type. if metal-doping in organic semiconductors is done in a controlled way then doped thermoelectric materials give high performance. Chemical doping caused a shifting of Fermi level and severely increased in charge carrier concentration at the TDPPQ/Bi interface, as a result, they noticed outstanding electrical conductivity around 3.3 S/cm and 585μV/K was the Seebeck coefficient value, confirming the maximum PF value at $110\mu WmK^{-2}$. so, from the above result, it proved that Bi was an efficient n-dopant. Small shifting of Fermi level indicated that TDPPQ was lightly doped by Bi, this was concluded from UV/Vis measurements [177]. To get know about the mechanism of the chemical doping between Bi and TDPPQ, they carried out the theoretical calculations for TDPPQ/Bi. When an atom of Bi encounters cyano (CN) triple bond of TDPPQ, doublet stat of the TDPPQ/Bi had minimum total energy with weak electron transfer (0.478 ev)

from Bi atom to a molecule of TDPPQ. The report of XPS data displayed that the binding energy of Bi joins with cyano N atom gets closed to N-atom of DPP. Hence, the introduction of Bi in TDPPQ film leads to a reduction in the intensity of the low energy peak and increment in high peak energy of N (1s). They confirmed that the XPS spectra matched with the experimental data, which verified that Bi interacts with the N atom of TDPPQ.

2.6.4 ***Double charge transfer***

Double doping of conjugated polymers with common p-type dopants ionization efficiency could rise to 200%. Double doping appreciably raised the number of charges devoted to being transferred at higher concentrations of dopant. Hence, due to the formation of dianion, the electrical conductivity of the high mobility polymers was enhanced greatly. Development of dianion happened in four different polymers, dopants pairs, which advised that double doping is a universal fundamental applied to an extensive range of organic semiconductors with convenient energy levels. Lately, dimer dopants were to increase the ionization capability of organic semiconductors, in this case, one dopant creates two charges, breaking into two discrete systems which act as a counterion. Such as involvement of dimeric category of n-type dopants subject on 2,3-dihydro-1H-benzimidazole [179],[139] and organometallic sandwich compounds, n-type dopants subject on 2,3-dihydro-1H- benzimidazole [180] formerly this route contain dimerization of two single dopants molecules, volume per dopant molecule which fused into the host organic semiconductor became double. It was needed a dopant that permitted more than one charge per dopant without dimerization. One important requirement is to minimize the volume/weight ratio, so the nanostructure is affected by the transfer of more than one electron per dopant molecule i.e development of diions. This double doping allowed the increment in ionization efficiency, with a maximum if every molecule of dopant give rise to two charges η_{ion}= 200%. Double doping has exceptionally boosted the category of polar conjugated polymers, everyone had an eye on them for the electrode material for batteries, n- and p-type conductors for thermoelectric, as donor or acceptor materials for organic solar cells. [181] an active layer of n- and p-type in electrochemical transistors [182], [183], [184]. FTIR spectroscopy data suggested that double doping was relayed on the length of the side chain and molecular weight. David Kiefer et al. concluded that polymer with high energy level and greater charge carrier mobility useful in bioelectronics and thermoelectric applications and the employment of dopants with the capability to donate two

electrons from the polymers along with high ionization energy will give us a large category of highly conducting materials that exploit double doping.

2.6.5 ***Electrochemical***

Electrochemical polymerization was a suitable strategy to get conductive polymers, like PPy, PANi, and PEDOT, as studied in the literature. Electrochemical cell method used to control the doping amount in a polymer. The electrochemical de-doping/ doping process was done by using electrolyte solution and three-electrode cells. In this method, the working electrode is a conductive polymer where the oxidation/reduction process takes place and for the counter electrode, platinum wire is used and Ag/AgCl is used as a reference electrode [163]. Here conjugated polymers were exposed to the electrolytes and electrodes. Metal electrodes supplied more charge carriers, small charges containing opposite-charge could be entered in conjugated polymer for keeping the electro-neutrality. This all transportation of the charge was happened due to the Weak van der Waals interaction within the polymers chain. Then at particular electrodes oxidation and reduction of conjugated polymer chain takes place, this happened when the electrochemical potential of metal electrons became equal to the electron affinity or ionization potential of the conjugated polymer in the medium of electrolytes [151],[185]. Because of electrochemical doping, optical properties were elaborated in a conjugated polymer that is known as electrochromic. So, a wide bandgap conjugated polymer could become coloured when doping is introduced in it, and a medium bandgap colored state conjugated polymer turns into transparent when oxidized. The most frequently used method is electrochemical because it allowed the dopant anions like ferrocyanide [Fe $(CN)_6^{3-}$] during the formation or else during the synthesis of a thin film. The conductivity of the polymer was highly dependent on the synthesis method because it causes increasing the polymeric structure length, which allows the overlapping of the molecular orbits. In recent times, sirringhaus et al was mainly focused on the estimation of the Seebeck effect in P3HT and pBTTT. Lately. Zhu and Sirringhaus analyzed how the Seebeck coefficient of pBTTTb and P3HT vary in organic field-effect transistors on changing the gate voltage. This work had been done as an alternative for the examined the thermoelectric in doped chemical organic semiconductors by causing changes in its morphology that could be reported in the material.

2.7 **RESEARCH OBJECTIVES**

Based on the literature survey we have finalized some materials which increase the efficiency of organic thermoelectric materials and using these materials will prepare n-type & p-type thermoelectric ink which is applicable for paper and polymer substrates.

- Synthesis of high ZT thermoelectric materials and devices based on organic + inorganic composites.
- **p-type:** PEDOT: PSS, P3HT, Bi_2Te_3, PVDF etc., **n-type:** rGO, Ni NWs, graphene.
- Investigation of *n*-type doping in organic thermoelectric material.
- Preparation of *n*-type & *p*-type ink for paper & polymer substrate printing.
- Demonstration of TEG devices on flexible substrate (paper & polymer).

Chapter 3. SYNTHESIS AND CHARACTERIZATION OF P-TYPE THERMOELECTRIC MATERIALS

3.1 ABSTRACT (PART -A): PEDOT: PSS/BI_2TE_3 (P-TYPE)

The capacity to generate electricity from waste heat or temperature difference has important implications for sustainable energy production and waste heat recovery. Thermoelectricity is the direct conversion of temperature difference (heat) to electric voltage and vice versa. In this work, we synthesized poly(3,4-ethylenedioxythiophene): poly (styrene sulfonate) (PEDOT: PSS) and PEDOT: PSS/ Bi_2Te_3 hybrid composite film using a spin coating method. Poly(3,4-ethylenedioxythiophene): poly (styrene sulfonate) (PEDOT: PSS) is a widely utilized and highly accessible materials. The materials under investigation exhibit notable advantages, such as a significant degree of electric conductivity, excellent stability, favorable solubility, and commendable processing capacity [191-193]. The maximum Seebeck coefficient (22 μVK^{-1}) and power factor (57.18 $\mu Wm^{-1} K^{-2}$ around 300 K) were achieved at 0.4 wt.% Bi_2Te_3. The electrical conductivity (σ) reached a maximum of 1467 Scm^{-1} at 300 K for 0.6 wt.% Bi_2Te_3, which is more than three times higher than that of pure PEDOT: PSS. Two critical components contribute to the improved electrical transport performance, as identified by XRD, Raman spectroscopy, XPS, AFM, and SEM. First, the conductive polymer undergoes a structural transformation from a benzenoid to a quinoid configuration, enhancing conductivity.

3.1.1 *EXPERIMENTAL SECTION*

3.1.1.1 Materials

Bismuth telluride (Bi_2Te_3) and PEDOT: PSS were purchased from Sigma Aldrich, dimethyl sulfoxide (DMSO), isopropyl alcohol (IPA), acetone, ethanol, etc. were procured from Alfa Aesr. All chemical reagents were used as received.

3.1.1.2 Preparation of PEDOT: PSS/Bi_2Te_3 composite films

A 10 wt% PEDOT: PSS/DMSO solution was prepared by mixing an appropriate amount of PEDOT: PSS with DMSO, followed by stirring for 24 hours at room temperature (RT). Subsequently, an adequate quantity of Bi_2Te_3, dispersed in ethanol, was introduced to the mixture and subjected to one hour of ultrasonication to yield homogeneous solutions containing 0.4, 0.6, and 0.85 wt% Bi_2Te_3. Before the film deposition, the glass substrate (1cm×1cm) was ultrasonically cleaned for 15 min in DI water, acetone, and isopropyl alcohol sequentially. They were then dried in a vacuum oven for 24 hours. PEDOT: PSS/Bi_2Te_3 composite films were fabricated using a spin-coating method (1000 rpm for 45 sec followed by 2000 rpm for 45 sec), and the resulting composite film was dried in a vacuum oven at 60°C for one hour. For comparative analysis, a pure PEDOT: PSS film was also prepared using the same procedure. The entire process is illustrated in Fig 3.1.

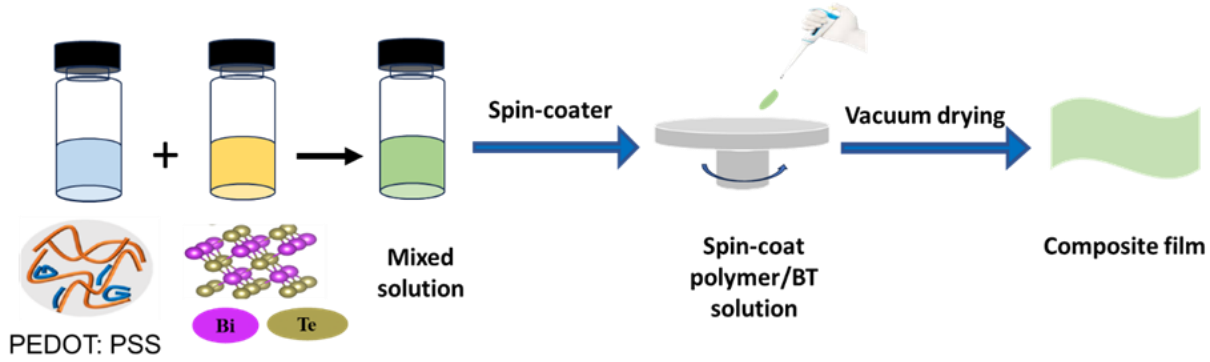

Figure 3.1 Process flow for preparation of PEDOT: PSS/ Bi_2Te_3 composite film by spin coating method.

3.1.2 ***Characterizations***

The surface morphology of the composite films was assessed using a scanning electron microscope (SEM) and atomic force microscope (AFM, Nano Surf Nano). The AFM measurements were performed in the tapping mode with having nm resolution, and the AFM images were analysed using Nano surf Naio. The crystal structure of the synthesized composite film was analyzed by X-ray diffraction (GIXRD, Malvern Panalytical) with Cu Kα radiation (λ = 1.5406 Å) at 40 mA and 45 kV. Conformational changes in PEDOT and PSS within the composite films were investigated using Raman spectra with a 532 nm green laser excitation. X-ray photoelectron spectroscopy (XPS) was employed to characterize the elements and compounds present in the PEDOT: PSS/

Bi_2Te_3 composite films, utilizing a PHI Versa Probe 3 spectrometer. The Al K_α line with an energy of 1486.6 eV was used for analysis, and the binding energy (B.E) values were referenced to the aromatic C 1s peak at 284.6 eV.

3.1.2.1 TE Performance Test:

The Seebeck coefficient was determined by measuring it from the samples using an in-house setup [209] . The Seebeck coefficient was determined by measuring it from the samples using an in-house setup with silver electrodes. K-type thermocouples were used to measure the temperature gradient across the PEDOT: PSS/ Bi_2Te_3 composite film. The Seebeck coefficient, determined as $S = \Delta V/ \Delta T$, is mathematically defined as the ratio of the voltage drop across the length of the material to the temperature gradient along the voltage drop. The electrical conductivity of the sample was determined through the utilization of a current-voltage (I-V) sweeping measurement technique employing four probes.

3.1.3 *RESULT AND DISCUSSION*

3.1.3.1 X-Ray Diffraction (XRD)

The X-ray diffraction (XRD) pattern of the synthesized PEDOT: PSS with varying Bi_2Te_3 content (0.4%, 0.6%, 0.85% wt%) composite films is presented in Fig 3.2(a) The XRD pattern demonstrates that the composite film exhibits a single-phase nature, with no discernible signs of impurity phases within detectable limits. Two distinct peaks at 2θ values of approximately 17.7˚ and 26˚ correspond to lattice spacings of approximately 5.0 and 3.4 Å, respectively. The d-spacing of 3.4 Å calculated from the peak at 26° is identified as the Π-Π stacking distance (d_{010}) of the aromatic rings of PEDOT. whereas the peak at 17.7° is attributed to the Π-Π stacking distance of PSS [210],[211]. In addition of Bi_2Te_3, various other peaks are also observed. The peaks at 2Θ = 17.4, 27.6, 38, 45 correspond to (006), (015), (10 10), and (110) planes, align well with the JCPDS, No. 15-0863 [95]. With a further increase in the concentration of Bi_2Te_3 in the composite film, the diffraction peak corresponding to PEDOT: PSS broadens, while the diffraction peaks associated with Bi_2Te_3 become much sharper. This observation suggests an enhanced crystallinity with the addition of Bi_2Te_3, confirming the presence of Bi_2Te_3 in the composite films.

3.1.3.2 Raman analysis

Raman spectroscopy serves as a valuable tool to investigate the various states of bipolaron, polaron, and neutral films, shedding light on the enhanced thermoelectric (TE) performance of doped PEDOT: PSS film as these states change. Fig 3.2(b) shows the Raman spectra of PEDOT: PSS and PEDOT: PSS/Bi_2Te_3 composites films, which correspond to a C_α-C_β antisymmetric stretching vibration at 1560 cm^{-1}, C=C asymmetric stretching vibration 1510 cm^{-1}, C_α=C_β symmetric stretching vibration band at 1424 cm^{-1}, C-C stretching vibration 1365 cm^{-1} and C-C inter – ring stretching at 1253 cm^{-1} [212]. The vibrational band of PEDOT is placed at 1253, 1365, 1424, and 1510 $cm^{-1,}$ while the vibrational band of PSS is located at 986 and 1560 cm^{-1}, respectively. The band at 986 and 576 cm^{-1} corresponds to the oxyethylene ring deformation – vibrations [213, 214]. The band at 437 cm^{-1} is assigned to the doping of PEDOT by the SO_3^- ion from PSS units [215].The Raman scattering peaks exhibited by the composite films are characterized by a more intense and relatively narrow spectral width [216]. Different conjugated Π – electrons and charge delocalization exist in the two structures. Two resonant structures, the benzoid and the quinoid, have been suggested for the band between 1400 and 1500 cm^{-1}, attributed to the C_α=C_β symmetric stretching of the five-member ring of PEDOT.

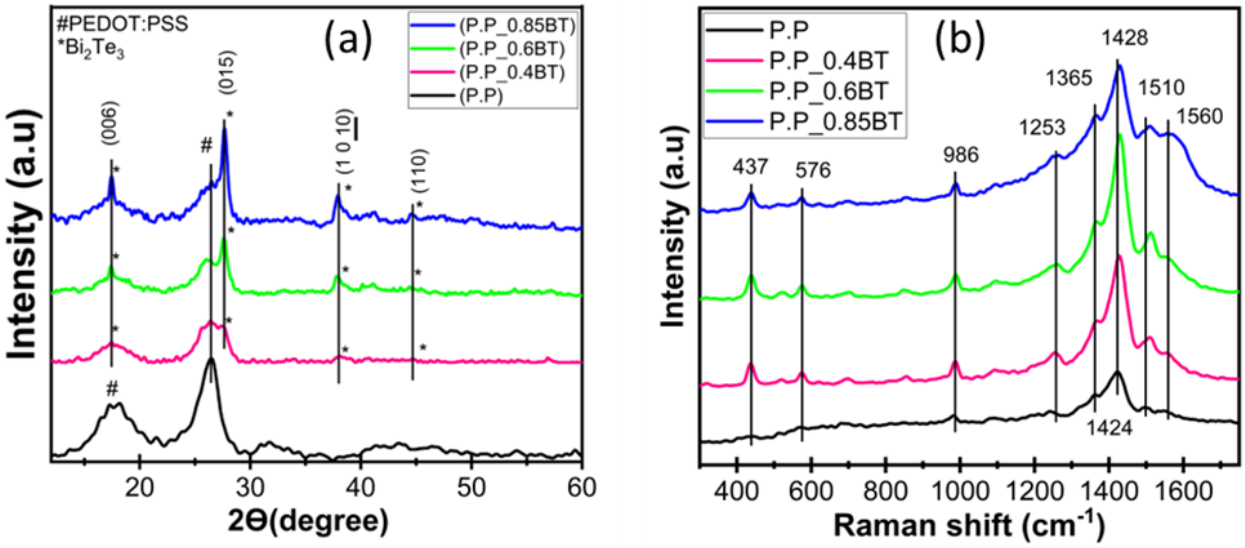

Figure 3.2(a) XRD pattern and (b) Raman spectra of PEDOT: PSS/ Bi_2Te_3 composite film.

Typically, the pristine PEDOT: PSS may contain both benzoid and quinoid structures. But in composite film the band shift from 1424-1428 cm^{-1} suggests a change from a predominant coil formation of the benzoid system to a linear coil conformation of the quinoid structure (Fig 3.3) in the PEDOT chain [217, 218].

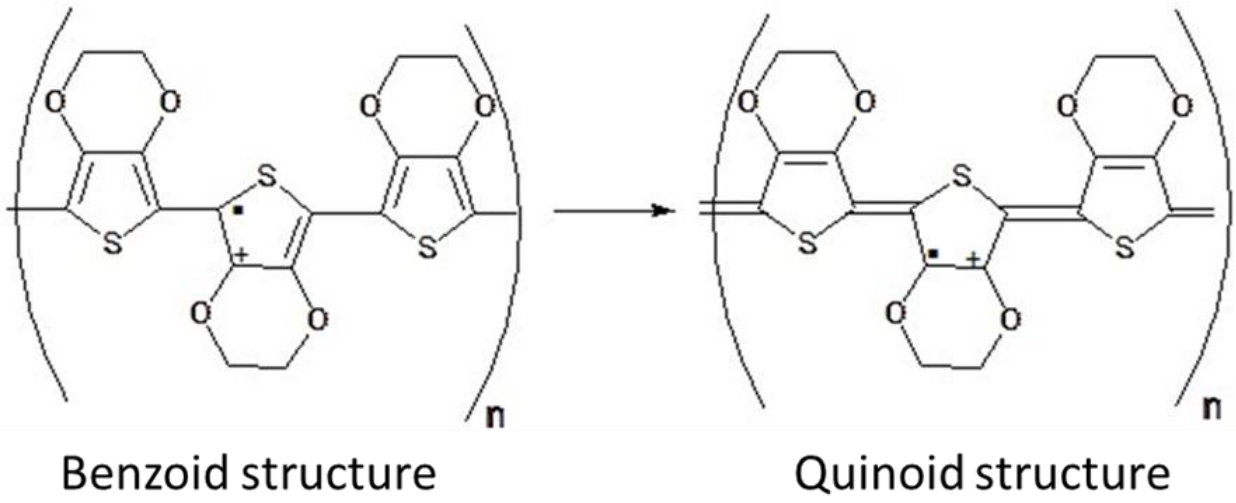

Figure 3.3 Illustrates the transformation process undergone by the PEDOT: PSS chain, changing from its initial benzenoid structure to a quinoid system. The benzenoid structure exhibits a preference for a coiled conformation while quinoid system favors a linear and expended coiled conformation.

3.1.3.3 Atomic Force Microscopic

In Fig 3.4, AFM images depict the surface topography of spin-coated PEDOT: PSS/ Bi_2Te_3 composite films. The height image of the DMSO-doped PEDOT: PSS film exhibited smoothness with a root mean square (Rq) of 8.5 nm within a $2 \times 2\ \mu m^2$ area. As shown in (Fig 3.4a), the surface RMS roughness increased from 8.5 nm to 13.5 nm in PEDOT: PSS with 0.4% Bi_2Te_3 (Fig 3.4b), and further to 14.7 nm and 43 nm for 0.6% and 0.85% Bi_2Te_3, respectively. This escalation is attributed to the structural reconstitution of the PEDOT: PSS film, indicating that Bi_2Te_3 enhances the screening effect between PEDOT and PSS chains. The extended coil-shaped or linear PEDOT aggregates more as a result of the developing Screening effect, and as the quantity of the coil-shaped PEDOT grows, consequently increases the separation of the PSS shells from the PEDOT

core and the conductivity of the PEDOT: PSS film [219]. The bright and dark region are reported to corresponds to PEDOT and PSS, respectively [220, 221].

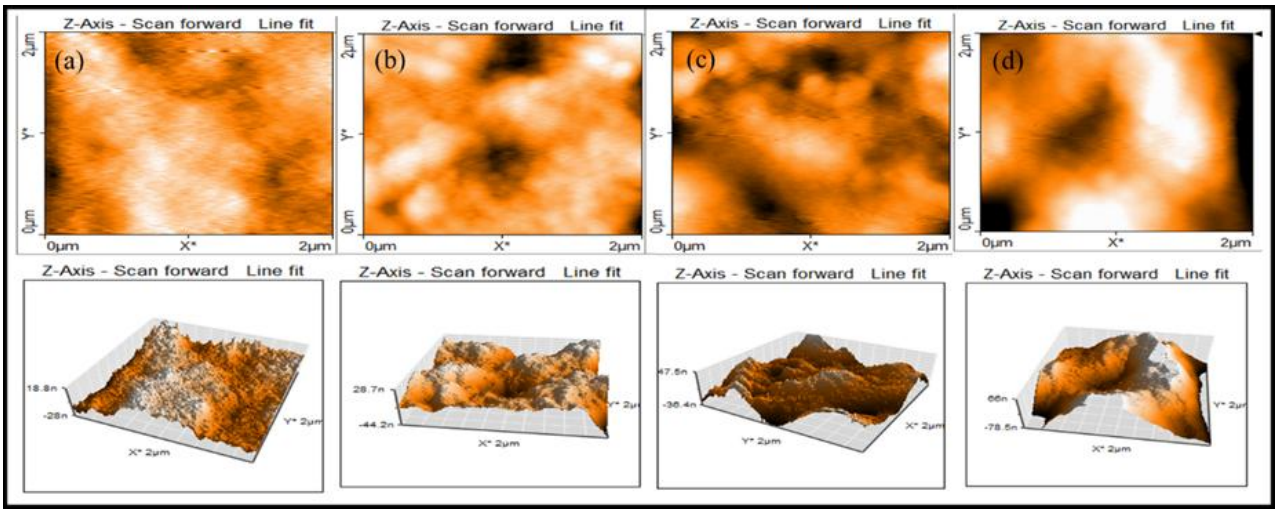

Figure 3.4 AFM image of (a) PEDOT: PSS, (Rrms – 8.5nm) (b) PEDOT: PSS/0.4BT, (Rrms – 13.5nm) (C) PEDOT: PSS/0.6BT, (Rrms – 14.7nm) (d) PEDOT: PSS/0.85BT, (Rrms– 43nm) (Spin coating).

3.1.3.4 Scanning Electron Microscope (SEM)

SEM analyses were conducted to delve deeper into the microstructure and surface morphology of the prepared PEDOT: PSS or PEDOT: PSS/ Bi_2Te_3 composite films, In Fig 3.5 (a) and (b), a uniform surface morphology of the PEDOT: PSS film is exhibited at different scales. In Fig 3.5 (c) and (d), a top view reveals the presence of Bi_2Te_3 particles, indicating their effective integration with PEDOT: PSS. Within the composite film, noticeable bulges on the surface correspond to the presence of Bi_2Te_3 within the film. The PEDOT: PSS encapsulates the Bi_2Te_3, which effectively binds them together.

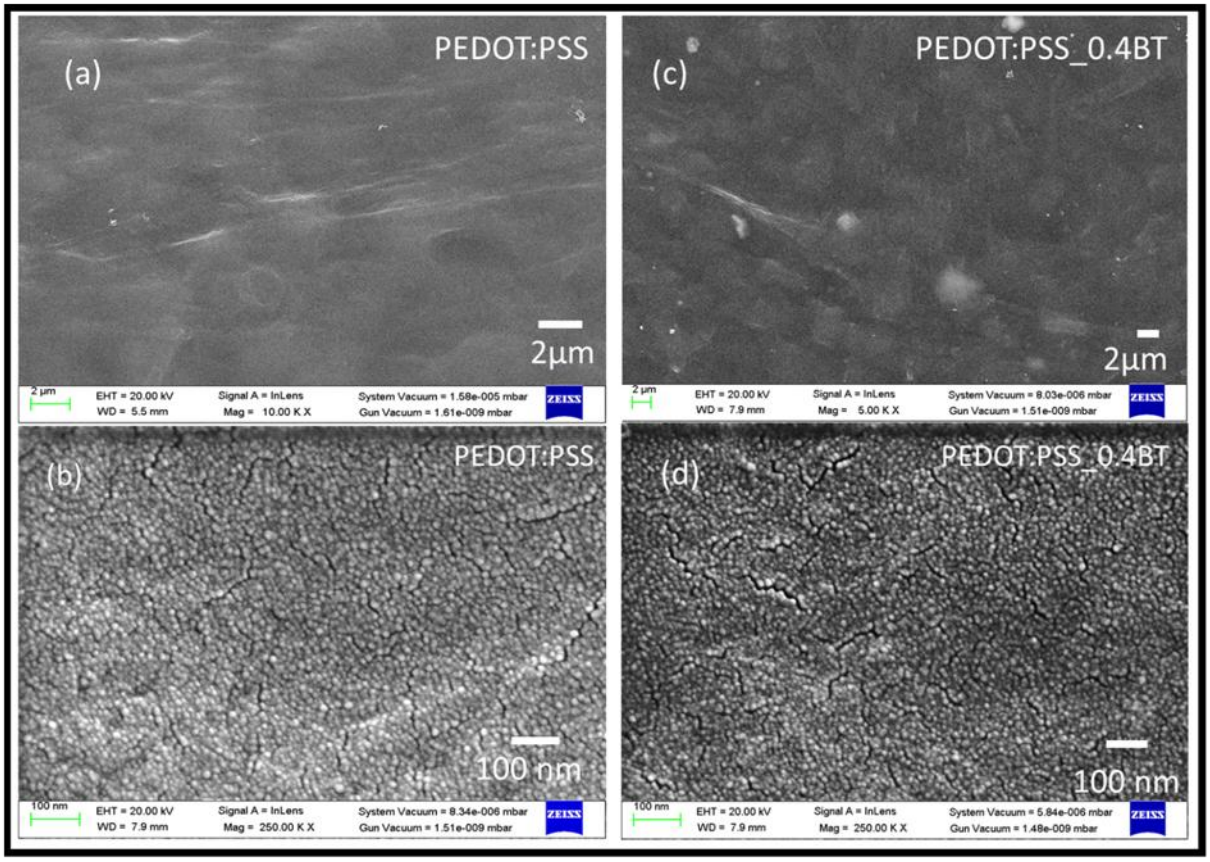

Figure 3.5 SEM images of (a), (b) PEDOT: PSS and (c),(d) PEDOT: PSS/0.4% Bi_2Te_3 composites films in scale 2µm, 100nm respectively.

This binding phenomenon occurs precisely when the Bi_2Te_3 content falls within the range of 0.4 wt.%. The energy filtering effect of the composites can be enhanced by encapsulating inorganic thermoelectric (TE) nanostructures with a polymeric material. This enhancement leads to an increase in the Seebeck coefficient (S) without compromising the electrical conductivity (σ) of the composites [222], as discussed later. With the gradual enhancement of the content, certain Bi_2Te_3 have gathered into clusters and extended from the films. This phenomenon impedes the transportation of carriers, consequently leading to a degradation in the electrical transport properties [223].

3.1.3.5 X-ray Photoelectron Spectroscopy (XPS)

X-ray photoelectron spectroscopy (XPS) offers valuable insights into the interaction between PEDOT: PSS and Bi_2Te_3 by analyzing the binding energy. Fig 3.6 displays the XPS spectra of

both PEDOT: PSS and PEDOT: PSS/ Bi_2Te_3 composite films. The carbon (C) 1s peak centered at 284.6 eV is broad and asymmetric in nature and therefore it is fitted with four different peaks as shown in Fig 3.6 (a_1). These peaks correspond to specific chemical bonds, namely C-C/C-H, C-S, C=C-O, and C-O-C/C-O, respectively. The obtained results exhibit a high level of accordance with the findings presented in the earlier study [224, 225]. Upon the addition of 0.4 wt.% Bi_2Te_3, a slight shift towards lower binding energy levels is observed for two peaks (C-S at 285.2 and C=C-O at 286.3 eV), as shown in Fig 3.6 (b_1). This shift is attributed to the interaction between PEDOT: PSS and the van der Waals force acting upon the Te atom layer of Bi_2Te_3, transforming the PEDOT: PSS structure from a benzene-type to a quinone-type design and enhancing its conductivity. The oxygen (O) 1s spectra, depicted in Fig 3.6 (a_2, b_2), exhibit a bimodal peak in two distinct regions with energy ranging from 530 to 535 eV. These peaks correspond to the oxygen atoms present in the PEDOT units, which occur in a higher binding energy region (533 eV). On the other hand, the oxygen atoms within the PSS units exhibit their characteristic peaks in relatively lower critical energy regions (531 eV), as shown in Fig 3.6 (a_2). At the same time, no noticeable shift of high energy peaks was detected in the PEDOT. However, a slight change was observed within the PSS region in the composite film shown in Fig 3.6 (b_2). The observed shifts in the peaks within the O 1s spectra of the PSS units confirm that Bi_2Te_3 interacts with the sulfonic acid groups of the PSS chain. In the PEDOT: PSS sample, two distinct peaks corresponding to the sulfur (S) 2p orbitals were observed, indicating the presence of sulfur atoms within the film. Because of the different binding energy of the S atom of thiophene in PEDOT and sulfonate in PSS [214]. Specifically, the lower energy peaks at 164.9 and 163.6 eV can be attributed to the S atoms in PEDOT, while the higher energy peaks at 168.8 and 167.6 eV correspond to the S atom in PSS (Fig 3.6 (a_3)). But in composite film (Fig 3.6 (b_3)), two more peaks were observed at 159.9, and 165.5, corresponding to the Bi_2O_3 and Bi_2Te_3. This indicate that Bi 4f is present in the PEDOT: PSS/ Bi_2Te_3 composite film. However, the shift of the S (2p) peaks was less noticeable between the PEDOT: PSS and PEDOT: PSS/Bi_2Te_3 composite films. XPS spectra of Te $3d_{5/2}$ exhibit two distinct sub-peaks at 573.1 and 576.6 eV, respectively. Similarly, the Te $3d_{3/2}$ shows two sub-peaks at 583.7 and 586.9 eV. The observed spectral peaks at 576.6 and 586.9 eV can be attributed to tellurium oxide species on the surface. During the process of fitting the 3d spectra, it was noted that peaks corresponding to secondary oxide were also observed [226] shown in Fig 3.6 (b_4).

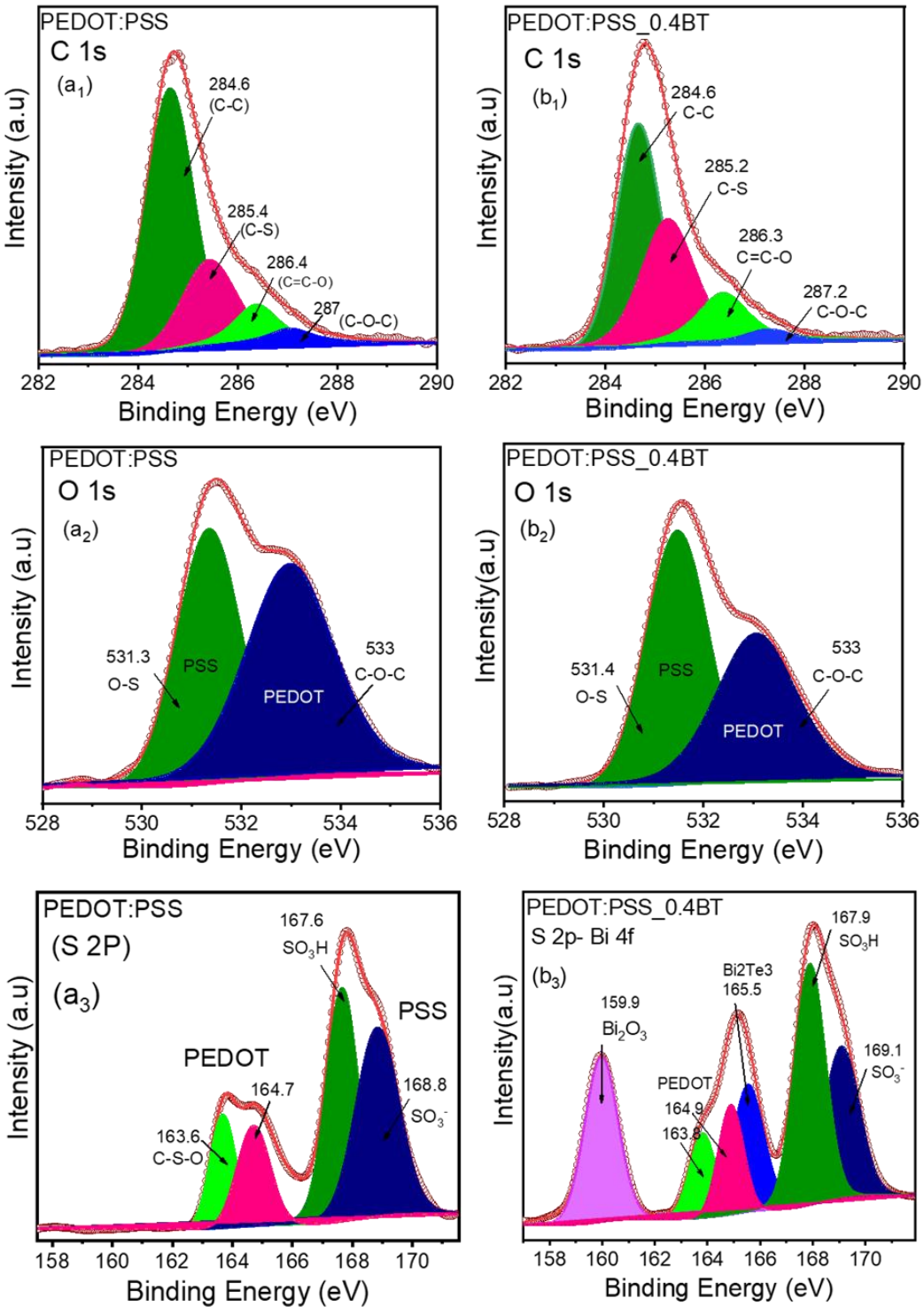
PEDOT:PSS
C 1s
(a1)
284.6
(C-C)
285.4
(C-S)
286.4
(C=C-O)
287
(C-O-C)
Intensity (a.u)
Binding Energy (eV)
PEDOT:PSS_0.4BT
C 1s
(b1)
284.6
C-C
285.2
C-S
286.3
C=C-O
287.2
C-O-C
PEDOT:PSS
O 1s
(a2)
531.3
O-S
PSS
PEDOT
533
C-O-C
PEDOT:PSS_0.4BT
O 1s
(b2)
531.4
O-S
PSS
PEDOT
533
C-O-C
Intensity(a.u)
PEDOT:PSS
(S 2P)
(a3)
167.6
SO3H
PSS
PEDOT
164.7
168.8
SO3-
163.6
C-S-O
PEDOT:PSS_0.4BT
S 2p- Bi 4f
(b3)
167.9
SO3H
Bi2Te3
165.5
159.9
Bi2O3
169.1
SO3-
PEDOT
164.9
163.8

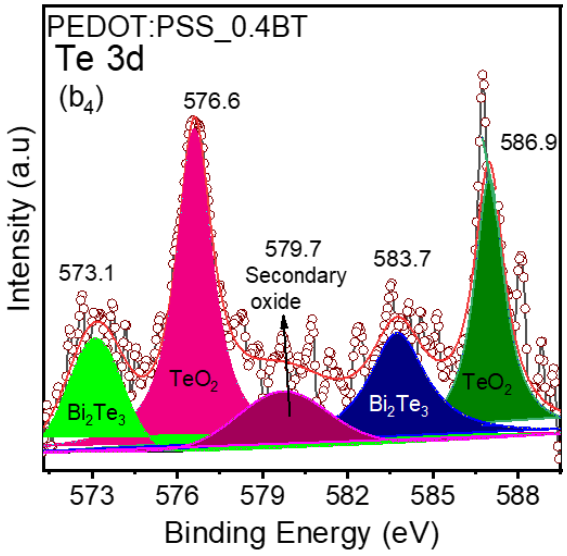

Figure 3.6 XPS spectra of PEDOT: PSS and PEDOT: PSS/ 0.4% Bi_2Te_3 composite. Fig a_1,b_1-C1s, a_2,b_2-O1s, a_3,b_3- S2p, S2p-Bi3d, b_4-Te3d, respectively.

3.1.3.6 Thermoelectric performance of PEDOT: PSS/Bi_2Te_3 composite film

The electrical conductivity of all the samples was measured using the four-probe technique. Fig 3.7 (a) exhibits the graphical representation of the relationship between temperature and electrical conductivity observed in the flexible PEDOT: PSS film and the composite films as a variation of Bi_2Te_3 content. At 300 K, pure PEDOT: PSS film exhibited an electrical conductivity of 574 Scm^{-1}. After the addition of Bi_2Te_3, the electrical conductivity of the composite film increases when the content of Bi_2Te_3 increases. The electrical conductivity 1181 Scm^{-1}, 1467 Scm^{-1}, and 878 Scm^{-1}, after blending with 0.4 wt.%, 0.6 wt.%, 0.85 wt.% Bi_2Te_3 respectively. It was seen that the electrical conductivity σ is maximum, 1467 Scm^{-1} for 0.6 wt.% Bi_2Te_3 at 300 K. The observed maximum electrical conductivity exhibits a magnitude exceeding that of pure PEDOT: PSS by a factor exceeding three times. This conductivity value is also higher than that of the reported PEDOT: PSS/Te composite film (19.3 Scm^{-1}) [196], PEDOT: PSS (Clevios PH1000)/Bi_2Te_3 composite (55-250 Scm^{-1}) [227], and PEDOT: PSS/single-walled CNT composite (280-400 Scm^{-1}) [228]. The observed phenomenon can be ascribed to incorporating Bi_2Te_3 particles, which serve as a carrier for the PEDOT: PSS material. This interaction induces a conformational change in the PEDOT chains, transitioning them from a coiled to a linear structure. Therefore, the facilitated movement of charge carriers within the polymer chains is greatly enhanced [229, 230]. The

observed phenomenon reveals a slight increase in the electrical conductivity across all the samples as temperature increases, thus suggesting characteristics of semiconducting behavior. The significant enhancement in σ can be elucidated by considering two factors: 1) Bi_2Te_3 serves as conduits for carrier transport. 2) the structural transition of PSS from the curled benzenoid configuration to the extended quinone configuration results in a notable enhancement in carrier concentration and mobility. The observed reduction in σ within the composite films can be primarily attributed to excessive Bi_2Te_3 agglomeration. This agglomeration weakens the interaction and disrupts the carrier transport between the Bi_2Te_3 and PEDOT: PSS matrix [222, 223].

The Seebeck coefficient, also known as the 'thermoelectric power', is a fundamental and inherent characteristic of materials. In a broad sense, an ideal thermoelectric (TE) material should exhibit a high Seebeck coefficient and significant carrier mobility. Fig 3.7 (b) depicts the Seebeck coefficient values of the samples under investigation, which incorporate varying weight percentages of Bi_2Te_3, namely, 0 wt.%, 0.4 wt.%, 0.6 wt%, and 0.85 wt.%. the Seebeck coefficient of all the composite films were positive and increased with increasing temperature, similar to the behavior observed in the electrical conductivity. This trend suggests that the primary Seebeck effect is of p-type. The Seebeck coefficient, of the pure PEDOT: PSS film demonstrated a value of 12.02 μVK^{-1} at a temperature 300 K. The sample consisting of 0.4 wt.% Bi_2Te_3 exhibited the high Seebeck value of 22 μVK^{-1} at the same temperature. For the same sample (0.4 wt% Bi_2Te_3), the maximum Seebeck coefficient is observed at 42.26 μVK^{-1} at 400 K. The Seebeck coefficient of the composite films in their as-prepared state exhibited a lower value than that of the reported bulk Bi_2Te_3 material [231]. There is no discernable improvement in the Seebeck coefficient for the PEDOT: PSS/ Bi_2Te_3 composite films for higher concentration of Bi_2Te_3, which is thought to be caused by the Bi_2Te_3 particle's strong composite formation with the PEDOT: PSS chains and destruction of electrically connecting junctions between the Bi_2Te_3 particles. To provide a comprehensive understanding, it is imperative to elucidate that the Seebeck coefficient is ascertained through the process of charge diffusion, which is mainly driven by the disparity in entropy between the surfaces of high and low temperatures within the internal energy of charge carriers present in a thermoelectric material [202]. The Seebeck effect exhibits a consistent variation trend that aligns with the electrical conductivity behavior. Specifically, the Seebeck coefficient increases from 22 μVk^{-1} to 42.26 μVk^{-1} at 400 K, suggesting an energy filtration effect

from combining organic and inorganic materials. As the concentration of Bi_2Te_3 increases, there is a simultaneous decrease observed in both the electrical conductivity and the Seebeck coefficient. The decrease in the Seebeck coefficient can primarily be ascribed to the elimination of energy barriers existing between PEDOT: PSS and Bi_2Te_3 [222].

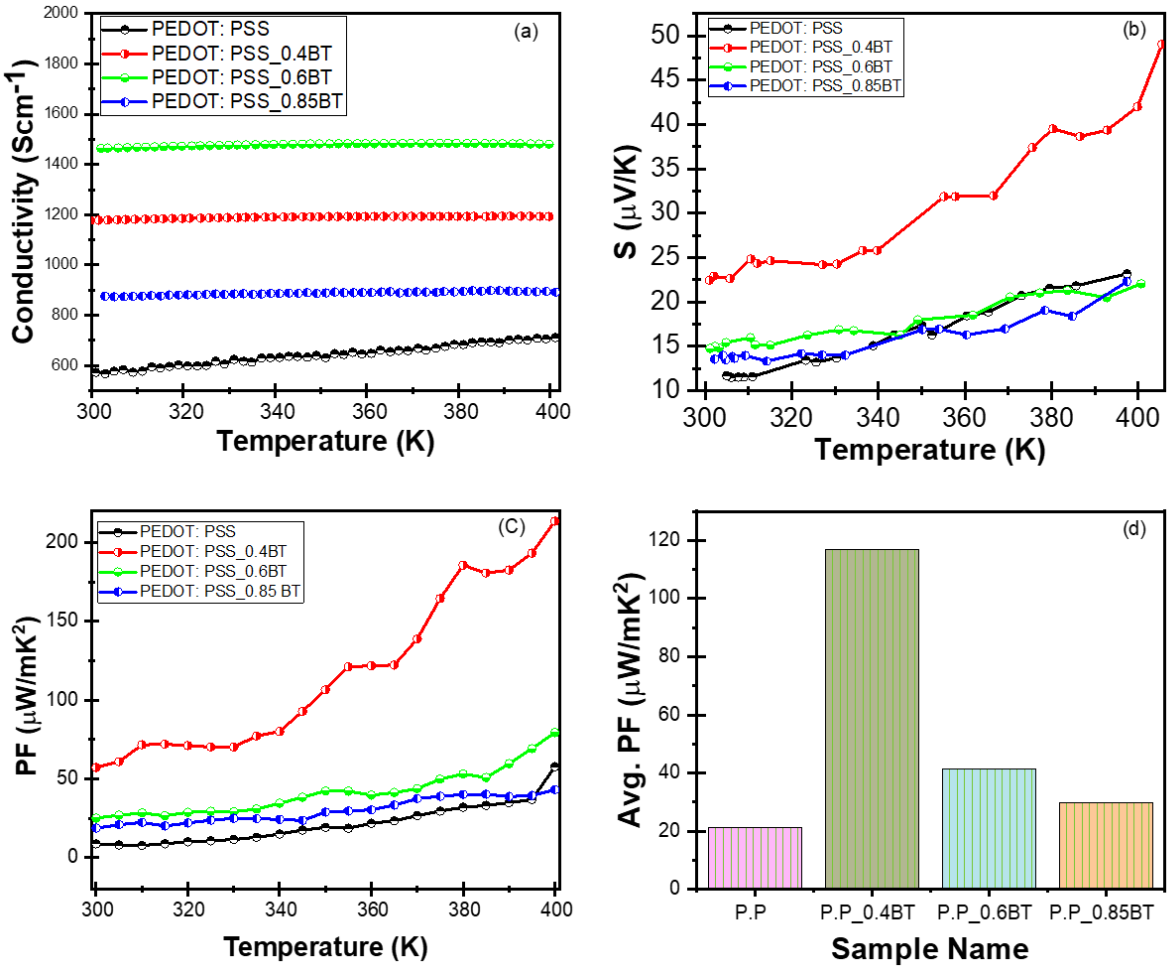

Figure 3.7 Thermoelectric measurements of PEDOT: PSS/ Bi_2Te_3 composite films. (a) Electrical conductivity, (b) Seebeck coefficient, (c) Power factor, and (d) averaged power factor.

The PF values for as prepared PEDOT: PSS and varying weight percentages of Bi_2Te_3, namely, 0.4 wt.%, 0.6 wt%, and 0.85 wt.%. were found to be 8.7, 57.1, 25.1, and 18.6 and $\mu Wm^{-1} K^{-2}$, respectively shown in Fig 3.7 (c, d). The Seebeck coefficient, Electrical conductivity and PF values further increased at higher temperatures as given in below table 3-1.

Table 3-1 Measured Seebeck coefficient, Electrical conductivity and power factor (PF) values for as prepared PEDOT: PSS with varying weight percentages of Bi_2Te_3, at 300 K.

Materials	S (μVK^{-1})	σ (S cm^{-1})	PF ($\mu Wm^{-1} K^{-2}$)
PEDOT: PSS	12.02	576.9	8.7
PEDOT: PSS_0.4Bi_2Te_3	22	1180.5	57.18
PEDOT: PSS_0.6Bi_2Te_3	14.5	1466.6	25.10
PEDOT: PSS_0.85Bi_2Te_3	13	881.6	18.6

It can be noted that compared to PEDOT: PSS, the composite film comprising 0.4 wt.% Bi_2Te_3 showed higher PF values of 42.26 $\mu Wm^{-1} K^{-2}$ around 300 K, resembling well with trends observed in other properties. The thermal conductivity κ could not be measured since the composite film is deposited on the glass substrates and has a layer thickness of just a few microns. Here, we estimate the ZT value using the PEDOT: PSS κ values ($\kappa = 0.29 \pm 0.05$ $Wm^{-1} K^{-1}$) published by Liu et al. [33]. This suggests that the ideal ZT value is around 0.2 of PEDOT: PSS and Bi_2Te_3 [223].

3.1.4 ***Conclusion:***

The preparation of PEDOT: PSS and Bi_2Te_3 composite films was successfully achieved using the a low-cost Spin coating method. Raman spectroscopy revealed that the interaction between the PEDOT: PSS and Bi_2Te_3 results in a transformation of the structure from a benzenoid form to a quinoid structure, leading to enhanced conductivity, which is a favorite for linear structure. Moreover, forming an interfacial barrier between PEDOT: PSS and Bi_2Te_3 results in an energy filtering effect, enhancing the Seebeck coefficient (S). These factors contribute positively to the electrical transport properties of the composite films. The optimal electrical conductivity (σ) of PEDOT: PSS and Bi_2Te_3 composite film is achieved when the Bi_2Te_3 content is 0.6 wt.%. However, the maximum Seebeck coefficient (22 μVK^{-1}) and power factor (57.18 $\mu Wm^{-1} K^{-2}$ around 300 K) is reached at 0.4 wt.% Bi_2Te_3.

3.2

3.2 ABSTRACT (PART B): PEDOT: PSS/0.4%Bi_2Te_3/rGO (P-TYPE)

We report a significant enhancement in the thermoelectric power of PEDOT by fabricating a novel ternary composite film by incorporating Bi_2Te_3 and rGO. A series of five samples of PEDOT: PSS/Bi_2Te_3/rGO ternary composite films were synthesized by spin coating method having different weight % (0.0, 0.1, 0.2, 0.3wt. %) of rGO in PEDOT: PSS/0.4 wt% Bi_2Te_3 mixture along with pure PEDOT: PSS sample. The Seebeck coefficient, electrical conductivity, and power factor increased in composite films compared to pure PEDOT: PSS films. In this work, we adopt a promising approach to enhance the electrical conductivity and Seebeck coefficient by incorporating both rGO and Bi_2Te_3 in the PEDOT: PSS films. These PEDOT: PSS/ Bi_2Te_3/rGO ternary composite films fabricated by the spin coating method are aimed to bring superior electrical and thermoelectric properties of rGO and Bi_2Te_3 to PEDOT: PSS polymer host. Based on the literature, the ternary composite films mentioned above have not yet been studied. In addition, a thermoelectric generator (TEG) device consisting of p-leg PEDOT: PSS/Bi_2Te_3/rGO and n-leg PVDF/Ni NWs is also demonstrated on flexible polyimide substrates. This novel PEDOT: PSS/Bi_2Te_3/rGO ternary composite film significantly outperforms previously reported organic thermoelectric materials. The results indicate that the combined effect of PEDOT: PSS, Bi_2Te_3, and rGO greatly enhances thermoelectric performance, offering a promising and efficient route for the application of PEDOT in advanced thermoelectric conversion processes.

3.2.1 *Materials and Method*

PEDOT: PSS, Graphite flakes, and Bi2Te3 were procured from Sigma Aldrich, USA Sulphuric acid, Hydrochloric acid, H_3PO_4, H_2O_2, $KMnO_4$, Dimethyl sulfoxide (DMSO), Ethylene glycol (EG), Hydrazine hydrate, Acetone, Ethyl alcohol, and Isopropyl alcohol (IPA), DI water were purchased from Alfa Aeser, UK and Moly Chem, India. The chemicals utilized in the experiment were of analytical grade and were employed without any subsequent purification process.

3.2.1.1 Synthesis of reduced graphene oxide (rGO)

Graphene oxide (GO) was synthesized using the modified Hummers method through oxidation and exfoliation of graphite sheets by the thermal treatment of the solution. The stepwise synthesis method used is elaboreted as follows. Firstly, a mixture of 180 ml H_2SO_4 and 10 ml H_3PO_4 was stirred for 15-20 min at 40-45° C. After that, 1.5 gm graphite flakes were added to the mixture

with continuous stirring and $KMnO_4$ (7.5 gm) was added to the suspension very slowly at 50 °C which gave the greenish coloured solution. The solution was kept overnight in a stirrer, where the colour changed to reddish brown. After that, 100 ml DI water and 10 ml H_2O_2 were added slowly and sequencely. The mixture was left undisturbed for a period of 3-4 hours, allowing the particles to segregate at the bottom. The excess water is then carefully filtered. The resulting mixture undergoes multiple washes through centrifugation, with 1M solution of HCl in DI water. This process is repeated several times until a gel-like substance is formed with a neutral pH, which undergoes vacuum drying at a temperature of 60 °C for 12 hours, resulting in the formation of GO powder. Again, hydrazine hydrate was used as a reducing agent for the GO suspension. The mixture undergoes sonication for 6 hours in order to transition from GO to rGO. The rGO suspension underwent filtration, followed by multiple washes with ethanol and DI water, before being collected for future use.

3.2.1.2 Preparationn of PEDOT: PSS/Bi_2Te_3 /rGO ternary composite film

PEDOT: PSS film was fabricated utilizing the drop-casting technique. A dispersed solution of PEDOT: PSS and Bi_2Te_3 were prepared by separately dissolving the components in DMSO and ethanol, respectively. The amount of DMSO and ethanol are the same throughout the manuscript. The solution was treated with ultrasonication for a duration of 1h. The experimental procedure involved the combination of an optimal quantity of PEDOT: PSS solution with a 0.4 wt% Bi_2Te_3 solution, which was subsequently subjected to stirring for 2 hours at room temperature (RT). The 0.4 wt% Bi_2Te_3 ratio was selected based on our earlier investigations [257]. Separately, a solution of rGO in ethanol was ultrasonicated to get a homogenously dispersed solution. Appropriate amounts of this rGO solution were added to PEDOT: PSS/ 0.4 wt% Bi_2Te_3 solution to get homogenous solutions containing different weight % (0.1, 0.2, 0.3wt. %) of rGO. Glass substrates (1×1 cm^2) underwent a thorough cleaning process involving sequential ultrasonic treatment in deionized (DI) water, IPA, and acetone for a duration of 15 each. Ternary composite films of PEDOT: PSS/Bi_2Te_3/rGO were synthesized employing a spin coating method (1000 rpm followed by 2000 rpm) and subsequent drying of the resultant composite films in a vacuum oven at 70°C for five hours. The thickness of the films was measured and found to be approximately 8-10 μm). The schematic diagram for the synthesis procedure is depicted in Fig 3.8. Pure PEDOT: PSS and PEDOT: PSS/ 0.4 wt% Bi_2Te_3 films were also synthesized using the identical procedure for

comparative analysis. A total of five film samples were used for various characterisations. The sample notations (S0, S1, S2, S3, and S4) and compositions are listed in Table 3-2. For n-type thermoelectric material, Polyvinylidene Fluoride and Nickel nanowire (PVDF/ Ni NW) solution was prepared and will be discussed separately.

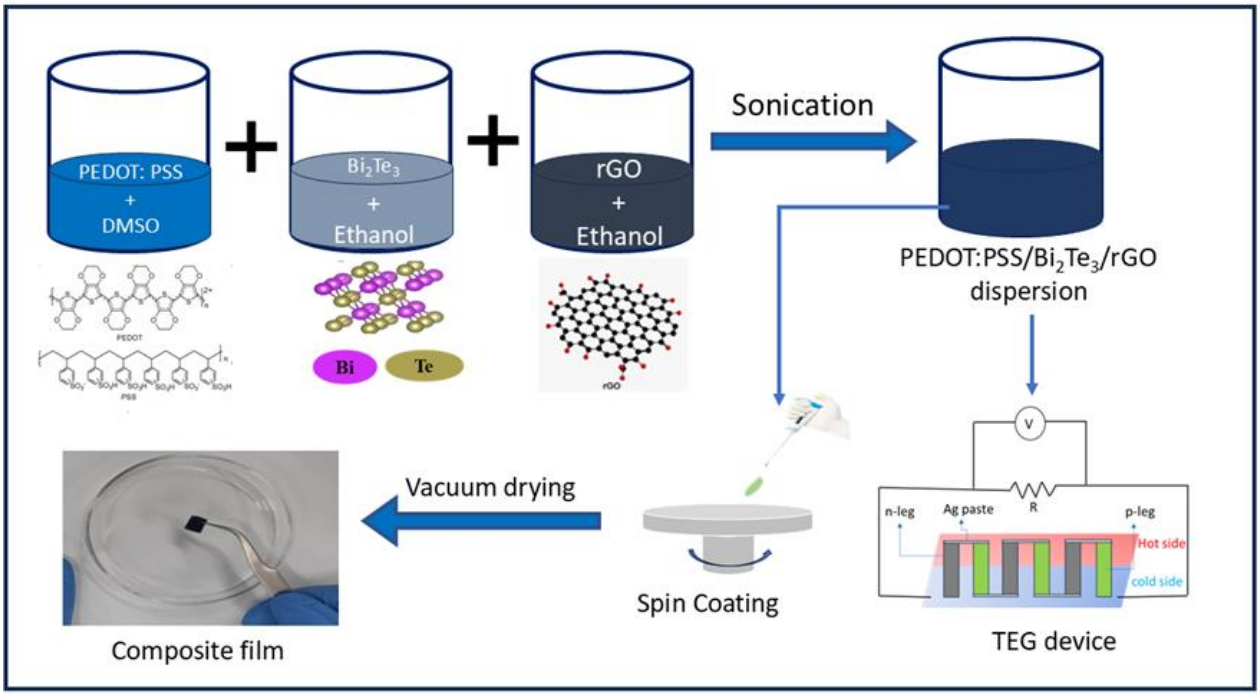

Figure 3.8 The Schematic illustrates the process flow for preparing the PEDOT: PSS/Bi_2Te_3/rGO ternary composite film using the spin coating method.

Table 3-2 The sample name and compositions used in the present investigation.

Sample Name	**Notation**
PEDOT: PSS (Pristine)	S0
PEDOT: PSS/0.4 wt% Bi_2Te_3	S1
PEDOT: PSS/0.4 wt% Bi_2Te_3 /0.1wt%rGO	S2
PEDOT: PSS/0.4 wt% Bi_2Te_3 /0.2wt%rGO	S3
PEDOT: PSS/0.4 wt% Bi_2Te_3/0.3wt%rGO	S4

3.2.2 *Characterizations*

The crystal structure of the ternary composite film was analyzed using the grazing incidence X-ray diffraction (GIXRD, Malvern Panalytical, USA) technique. The measurements were performed with a Cu Kα radiation source (λ=1.5406 Å) at an applied current of 40 mA and voltage of 45 kV. The investigation examined the conformational changes occurring in PEDOT and PSS composite films. A Raman spectrum was obtained using a green laser emitting light at 532 nm to produce excitation (RI, India). The X-ray Photoelectron Spectroscopy (XPS), analysis was conducted utilizing a (PHI 5000 Versa probe Scanning Microscope, ULVAC-PHI Inc., USA). The high-resolution spherical capacitor energy analyzer thoroughly examines various energy levels, allowing for a detailed evaluation of specific elements through XPS full spectrum analysis. The spectra were acquired through the exposure of the samples to incident radiation emitted by a monochromatic Al-Kα X-ray source operating at an energy level of 1486.6 eV. The XPS data was analysed, and peak deconvolution was carried out to inform the chemical and electronic states of the constituent elements and bonds in the prepared composite films. The composite films were analysed using a scanning electron microscope (SEM) to examine their morphology and microstructure. The Seebeck coefficient was determined using a custom experimental setup developed in-house [258]. A four-probe current-voltage (I-V) measurement technique was employed to determine the electrical conductivity of the sample.

3.2.3 *Result and Discussion:*

3.2.3.1 XRD

The X-ray diffraction patterns of PEDOT: PSS, PEDOT: PSS/Bi_2Te_3, and PEDOT: PSS/ Bi_2Te_3/rGO composite films are displayed in Fig 3.9. S0 sample shows two distinct broad diffraction peaks at 17° and 26°, corresponding to lattice spacing of around 5.0 and 3.4 Å., indicating the mostly amorphous nature of PEDOT: PSS film. The diffraction peak at 26° is attributed to the interplanar distance (d_{010}) associated with the π-π stacking arrangement of the aromatic rings in PEDOT. In comparison, peaks at 17° are reported to be caused by the Π-Π stacking distance of PSS [210, 211]. The addition of Bi_2Te_3 in the PEDOT: PSS matrix results in several other peaks in the experimental data in sample S1. The observed additional characteristic peaks at 2θ values of 17.7°, 27°, 38°, and 44° are attributed to the crystallographic (006), (015),

(10 10), and (110) planes of Bi_2Te_3, respectively. These observed peaks agree with the reference data (JCPDS No. 15-0863) [95]. For samples S2, S3, and S4, another peak is observed at 25°, which is reported to the (002) plane of rGO [259]. Also, with the increase in wt% of rGO (samples S2, S3, and S4), the intensity of two distinctive peaks at 26°and 27° weaken. This suggests that the aggregation of rGO plays a role in this phenomenon. The interaction between aggregated rGO and PEDOT chains leads to the destruction of PSS [260]. This behavior is also observed in the SEM images.

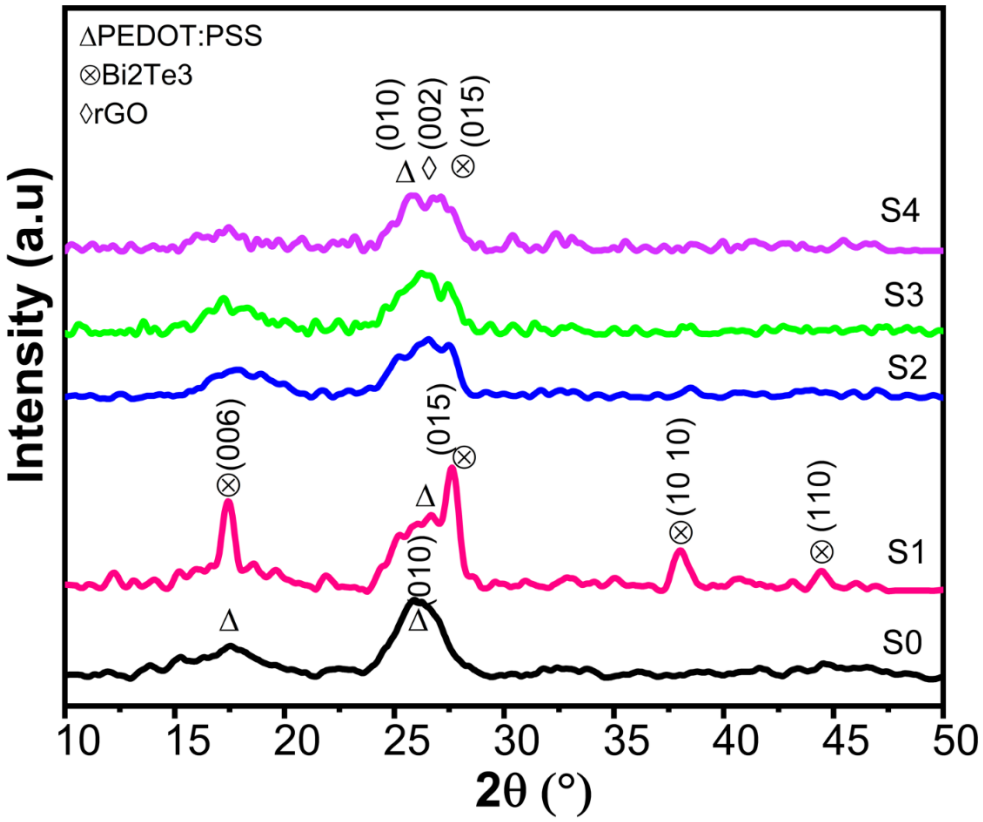

Figure 3.9 GIXRD of Raman spectra of S0 (PEDOT: PSS), S1 (PEDOT: PSS/Bi_2Te_3), and S2, S3, and S4 (PEDOT: PSS/ Bi_2Te_3/rGO) composite films.

3.2.3.2 SEM

Fig 3.10 (a to e) shows the scanning electron microscopy (SEM) images of composite films. SEM micrographs of the S0 film (Fig 3.10 a) show a consistent and homogenous surface morphology. After adding Bi_2Te_3 in S1 (Fig 3.10 b) and rGO in S2, some bulge-type structures appear on the film surface, as shown in Fig 3.10 (c & d). The presence of several Π bonds within the structure of PEDOT: PSS is a well-established fact. Also, it is widely reported that rGO possesses a

significant number of π bonds, enabling their efficient incorporation into a PEDOT: PSS matrix through strong π-π interactions with PEDOT chains [261]. With the further addition of rGO in PEDOT: PSS agglomeration occurs in films, as is evident in Fig 3.10 (e), which corresponds to sample S4. The rGO material exhibits exclusive π-π interactions with PEDOT chains while displaying relatively weaker interactions with PSS chains [261]. The rGO strong multiphase interactions may cause the PEDOT and PSS chains phase to separate, forming the grains on the surfaces of ternary composite PEDOT: PSS/ Bi_2Te_3/rGO/ [262, 263].

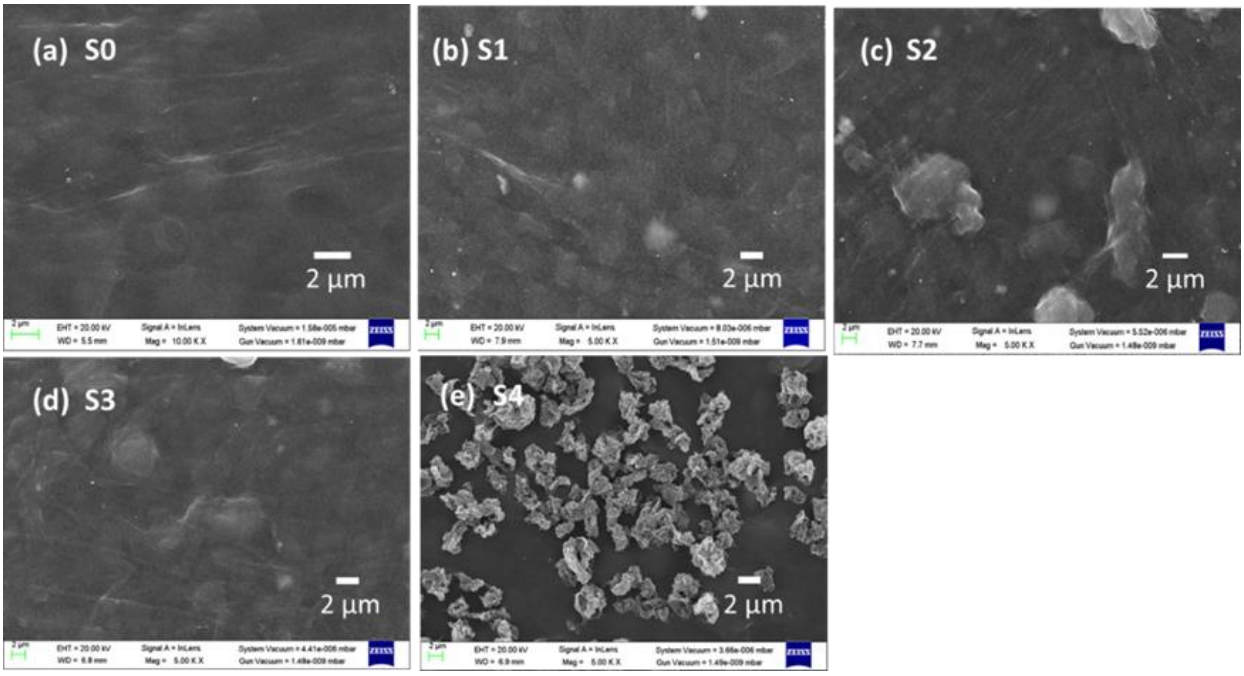

Figure 3.10 SEM images of S0 (PEDOT: PSS), S1 (PEDOT: PSS/0.4% Bi_2Te_3), and S2 (PEDOT: PSS/ 0.4%Bi_2Te_3/0.1%rGO, S3, (PEDOT: PSS/ 0.4%Bi_2Te_3/0.2% rGO and S4 (PEDOT: PSS/ 0.4% Bi_2Te_3/0.3% rGO) composite films.

3.2.3.3 Raman Spectroscopy

The Raman spectra provide insights into carbon-based materials' defects and disordered structures. Fig 3.11 displays the measured Raman spectra of all films. The G band in carbon materials can be ascribed to the vibrational modes of sp^2-bonded carbon atoms. In contrast, the D band signifies the vibrational modes of carbon atoms that possess dangling bonds. The presence of the D peak also means the existence of defects and disordered structures within carbon-based materials [264].

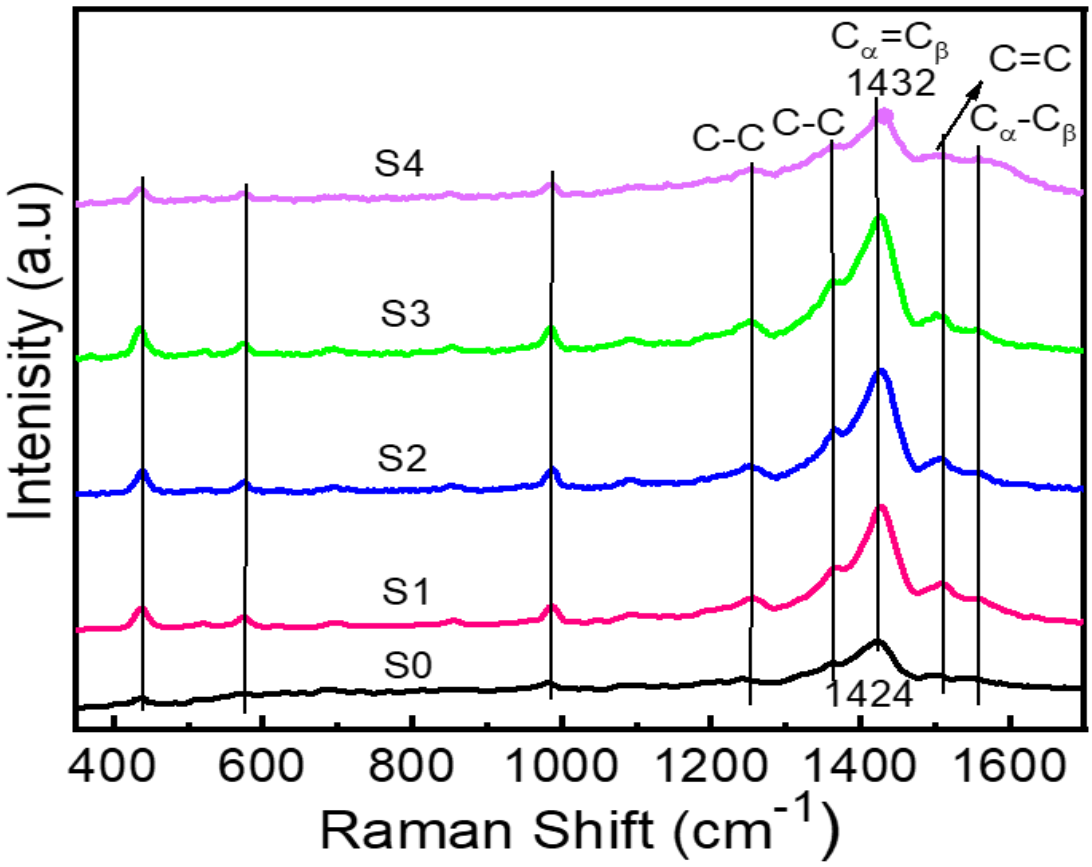

Figure 3.11 Raman spectra of S0 (PEDOT: PSS), S1 (PEDOT: PSS/Bi_2Te_3), and S2, S3, and S4 (PEDOT: PSS/Bi_2Te_3/rGO) composite films. The shifting of the C=C symmetric stretching vibrational mode peak at 1424 cm^{-1} to higher wavenumber is attributed to the π-π interaction between the electron-rich rGO and the aromatic structures of PEDOT.

The Raman spectra of all samples exhibit noticeable characteristic peaks, including the presence of weak peaks associated with C–C bond stretching at 1251 cm^{-1}, C–C stretching vibrational band at 1363 cm^{-1}, and the dominant band at 1424 cm^{-1} associated with C=C symmetric stretching, C=C asymmetric stretching at 1507 cm^{-1} and antisymmetric stretching at 1557 cm^{-1}. The band at 986 cm^{-1} and 574 cm^{-1} corresponds to the oxyethylene ring deformation vibrations [213, 214]. The observed band at 436 cm^{-1}) can be attributed to incorporating the SO_3^- ion from PSS units, which acts as a dopant in the PEDOT material [215]. It can be noticed that the C=C symmetric stretching vibrational mode peak at 1424 cm^{-1} of sample S0 is shifting to a higher wavenumber of approximately 1432 cm^{-1}, with the addition of rGO. The shift is also reported in the literature

and is attributed to the π-π interaction between the electron-rich rGO and the aromatic structures of PEDOT [254]. From analysis of the Raman spectra, it is evident that there is a significant interaction between rGO and PSS and PEDOT chains. This interaction leads to the separation of the PEDOT: PSS phase and promotes the alignment of PEDOT in a structured manner, as also reported elsewhere [265].

3.2.3.4 XPS

XPS is a highly effective measurement technique for identifying the elements present and their chemical bonding with other elements. For XPS, only selected samples were used for comparison. Fig 3.12 exhibits the XPS spectra of pristine PEDOT: PSS (S0), binary composite PEDOT: PSS/Bi_2Te_3 (S1) and ternary composite PEDOT: PSS/Bi_2Te_3/0.1rGO (S2) samples. Analysis of C (1s), O (1s), S (2p), Bi (4f), and Te (3d) peaks have been carried out. The C (1s) peak, with a central position at 284.6, exhibits a broad and asymmetric shape. A deconvolution fitting procedure involving the utilization of distinct peaks is shown in Fig 3.12 (A to C). The observed peaks in the C (1s) spectrum of S2 can be attributed to distinct chemical bonds, namely, the C–C and C–H bonds at 284.6 eV, C–S at 285.1 eV bond, C=C–O bond at 286.1 eV, and C–O–C bond at 287.1 eV, respectively [224, 225]. The result obtained in this study demonstrates a significant degree of accordance with the findings reported in the previous research [134, 224, 225]. The incorporation of rGO in the structure shows an apparent π-π interaction between PEDOT chains and rGO, emphasizing favourable compatibility between the rGO and PSS chains [134]. The O (1s) spectra in Fig 3.12 (D to F) demonstrate two peaks with different binding energy. The observed peaks indicate the presence of an O atom within the PEDOT chain, localized within a higher B.E range at approximately 533 eV. In contrast, the O-atoms within the PSS chain demonstrate distinct peaks in a lower B.E range at 531.3 eV, as shown in Fig 3.12. The S0 film shows two discernible peaks (Fig 3.12 G), which can be attributed to the 2p orbitals of sulfur. This observation provides evidence for the existence of sulfur atoms within the film. The observed lower energy peaks at 164.9 and 163.7 eV can be ascribed to the presence of S atoms within the PEDOT chain. Conversely, the higher B.E peaks at 168.9 and 167.7 eV indicate the sulfur atom within the PSS chain [214, 266, 267]. In Fig 3.12 (H and I) for samples binary (S1) and ternary (S2) composite film, additional peaks were observed at 159.8 eV and 165.5 eV in the binary ternary composite film, indicating the presence of Bi_2O_3 and Bi_2Te_3, respectively. The presence of Bi(4f)

has been observed in the binary (S1) and ternary composite film (S2), suggesting its incorporation within the film. Fig 3.12 (J & K) shows the XPS spectra of the $Te_{5/2}$ electron orbital, which reveal the presence of two distinct sub-peaks at energy levels of 573.2 and 576.7 eV, respectively. Similarly, the $Te_{3/2}$ orbital shows two distinct peaks located at 583.5 and 586.9 eV. The observed spectral peaks at 576.7 and 586.9 eV suggest the existence of tellurium oxide (TeO_2) on the surface being examined in the ternary composite films. Extra peaks were identified in the context of carrying out the 3d spectral analysis. These peaks can be assigned to the existence of secondary oxide [226].

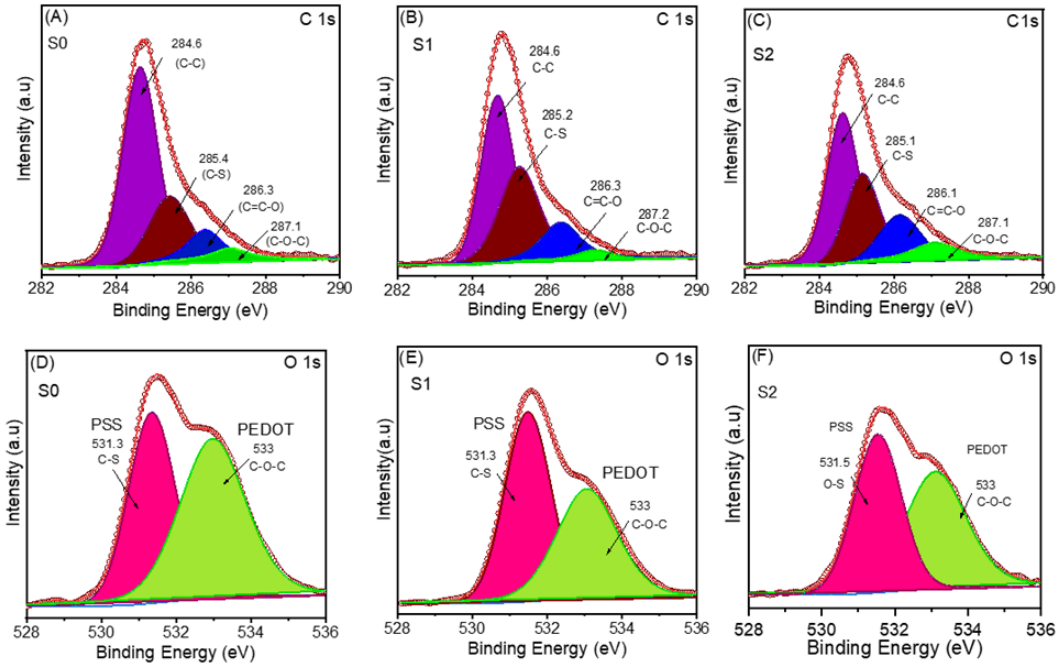

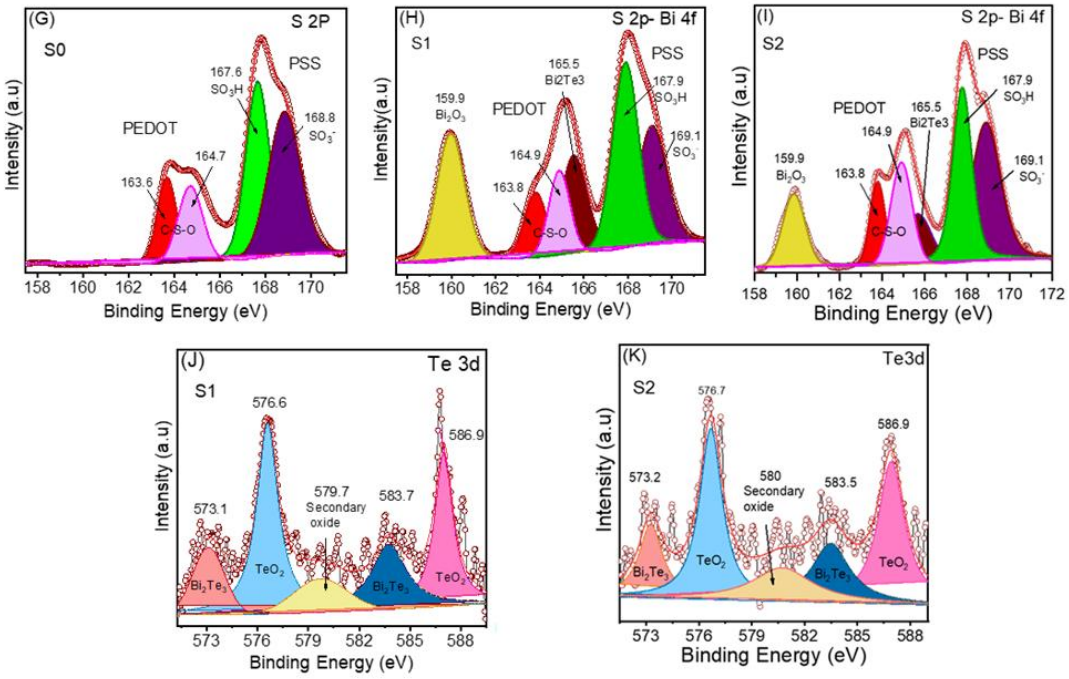

Figure 3.12 XPS spectra of PEDOT: PSS (S0), PEDOT: PSS/0.4% Bi_2Te_3 (S1) and PEDOT: P.S.S/0.4% Bi_2Te_3/0.1% rGO (S2) composite films.

Figures (A), (B) and (C) show XPS deconvolution for C(1s) peak in S0, S1, and S2 samples, respectively. Figures (D), (E) and (F) compare the binding energies of the O (1s) peak for S0, S1, and S2 samples. Figures (G), (H) and (I) show the Sulphur(2p) peak in S0, Sulphur (2p) and Bi (4f) peaks in S1 and S2 samples, respectively. Lastly, figures (J) and (K) compare XPS binding energies deconvolution of Te (3d) peak in S1 and S2 samples, respectively.

3.2.3.5 Electrical properties

The four-probe method examined the temperature-dependent sheet resistance (R_S) and electrical conductivity (σ) for all samples. Studies have shown that the conductivity of PEDOT: PSS can be enhanced by adding Bi_2Te_3 in PEDOT: PSS composite film [202, 268]. This enhancement in conductivity has been observed to be 2-3 orders of magnitude. Fig 3.13 (a) depicts the change in conductivity of S0, S1, S2, S3, and S4 composite films as a function of temperature. The electrical conductivity in all the samples increases with increasing temperature, indicating the semiconductor nature of the composites formed. The electrical conductivity of the pure PEDOT: PSS film (S0) was 573.12 Scm^{-1} at room temperature. The addition of Bi_2Te_3 in PEDOT: PSS film (S1) increased

the electrical conductivity value of 1177.5 Scm^{-1}. A previous study also reported the electrical conductivity and Seebeck coefficient of PEDOT: PSS/Bi_2Te_3 samples with varying concentrations of Bi_2Te_3 [257]. When rGO was added to the composite, the room temperature conductivity was observed at 1522.4 Scm^{-1}, 1741.1 Scm^{-1} and 1076.6 Scm^{-1} for S2 (0.1wt.% rGO), S3 (0.2 wt.% rGO), and S4 (0.3wt.% rGO) films, respectively. The highest electrical conductivity was observed for S3 and was more than 3.5 times of S0 at 300 K. The electrical conductivity of the nanocomposites exhibits a significant correlation of rGO within the PEDOT: PSS matrix. The incorporation of rGO at a concentration up to 0.3wt.% within the PEDOT: PSS matrix leads to an enhancement of π-π conjugation along the polymer chain. This phenomenon generates a significant population of charge carriers that exhibit delocalized behavior, enabling their facile movement between energetically favorable sites [268].

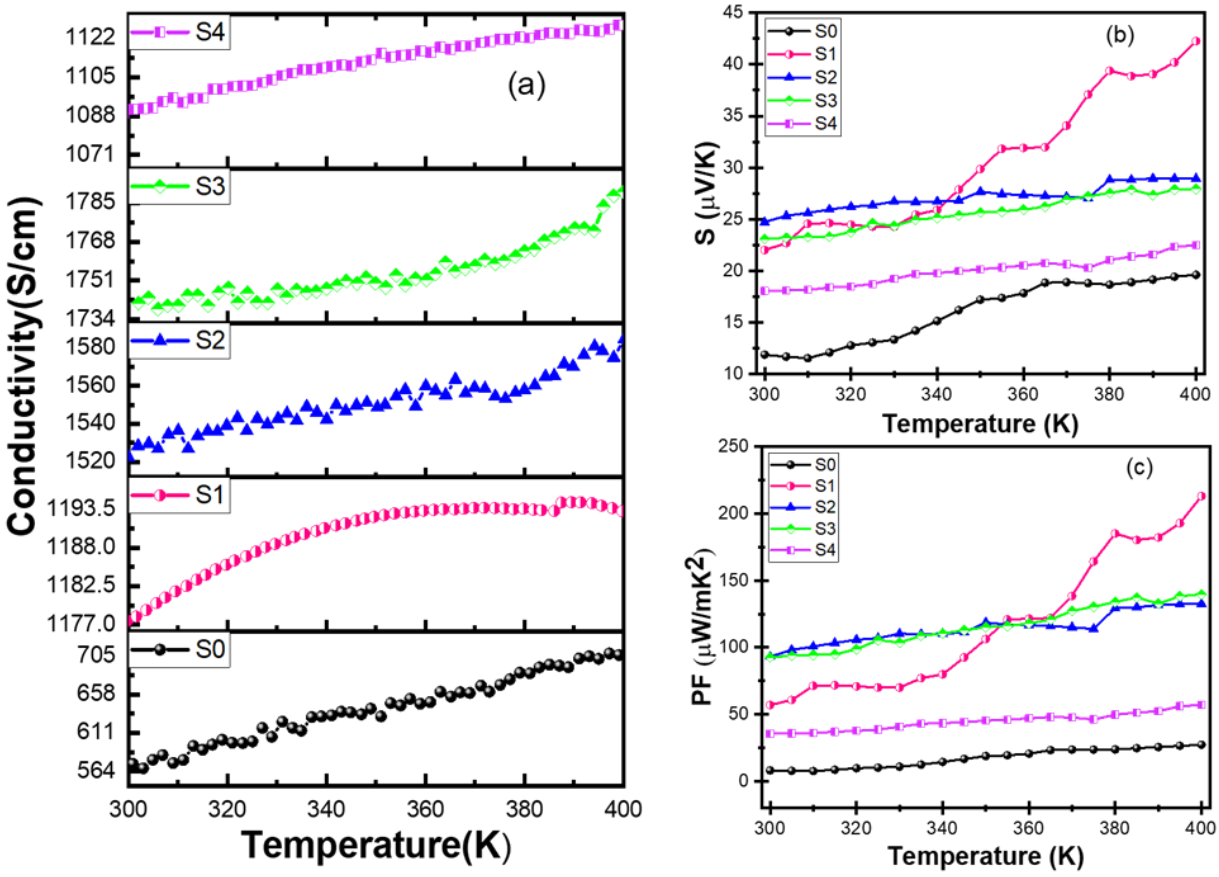

Figure 3.13(a) Measured Electrical conductivity, (b) Seebeck coefficient, and (c) power factor of PEDOT: PSS (S0), PEDOT: SS/0.4% Bi_2Te_3 (S1) and PEDOT: SS/0.4% Bi_2Te_3/0.1% rGO (S2) composite films.

3.2.3.6 Seebeck Coefficient measurement.

Fig 3.13 (b) shows the measured Seebeck coefficient values of all samples. All samples exhibited a positive Seebeck coefficient, which displayed an upward trend with rising temperature, resembling the observed behaviour in literature [253, 269]. All the rGO composite films exhibit higher Seebeck coefficients at 300 K temperature than the value of 11.8 μVK^{-1} observed in pure PEDOT: PSS (S0), and 22 μVK^{-1} in PEDOT: PSS/0.4% Bi_2Te_3 (S1) samples. The S2 sample showed the highest value of the Seebeck coefficient, measuring 24.7 μVK^{-1} at 300 K. The Seebeck coefficient S3 sample showed a similar magnitude (23.07 μVK^{-1}) and trend as that of S2. In comparison, S4 samples exhibit a moderate Seebeck coefficient value of 18.05 μVK^{-1} at the same temperature (300 K). The observation indicates that less carriers are transported in the interface when higher filler contents are present. This occurrence can be attributed to the inefficiency of the relation between the PEDOT chain and fillers, as previously reported in the literature [254]. The Seebeck coefficients of the composite film exhibit a positive correlation with temperature, indicating an increase as temperature rises. This observation implies an energy filtration effect from combining organic and inorganic materials. The observed phenomenon involves an accompanying reduction in the electrical conductivity and Seebeck coefficient as the concentration of rGO is enhanced. The observed decrease in the Seebeck coefficient values for further higher concentrations of rGO can be predominantly attributed to eliminating energy barriers between the polymer and inorganic materials [222].

Furthermore, power factor (PF) values were determined for as prepared PEDOT: PSS (pure) and different weight percentages of rGO added in PEDOT: SS/0.4% Bi_2Te_3, namely, S0, S1, S2, S3, and S4 respectively resulting in PF values of 8.12 $\mu Wm^{-1} K^{-2}$, 57.04 $\mu Wm^{-1} K^{-2}$, 93.16 $\mu Wm^{-1} K^{-2}$, 92.6 $\mu Wm^{-1} K^{-2}$, 35.5 $\mu Wm^{-1} K^{-2}$, respectively at 310 K as shown in Fig 3.12 (c). The calculated values of PF exhibit similarities to the σ and S patterns for different compositions, as shown in Table 3-3. It can be seen clearly that the ternary composite film S2 exhibits the highest PF value, 93.16 $\mu Wm^{-1}K^{-2}$ at 300 K, making it a highly appropriate composition for TE applications. A comparison of results from the present investigation with the literature clearly indicates better performance of our ternary composite films for thermoelectric applications.

Thermoelectric generator (TEG) device performance

We prepared inks of p-type PEDOT: PSS/0.4wt%Bi_2Te_3/0.1wt%rGO and n-type PVDF/Ni NWs solutions. The synthesis and characterisation of n-type PVDF/Ni N.W.s solutions for thermoelectric application will be part of a separate study. A thermoelectric generator (TEG) demonstration device was fabricated using two inks on the flexible polyimide substrate. Figure 1 shows the schematic of TEG devices. The output voltage as a function of the temperature difference ΔT varies from 10 to 35 K, and the open circuit voltage due to the Seebeck effect increases linearly with increasing the temperature difference of ΔT between the hot and cold ends of the TE module. An output voltage of 9.84 mV at ΔT= 35 K and the maximum power output of 242.16 nW is attained with the load resistance of 100 Ω at ΔT= 35 K.

Table 3-3 Comparison of Thermoelectric parameters of PEDOT: PSS/Bi_2Te_3 /rGO composite films at room temperature with other's work.

Samples	**Composite Method**	**Electrical Conductivity (Scm^{-1})**	**Seebeck Coefficient (μVK^{-1})**	**Power Factor ($\mu Wm^{-1}K^{-2}$)**	**References**
Bi_2Te_3/rGO	Hydrothermal	42	**–**187	1.46	[270]
Bi_2Te_3 alloy NS/ PEDOT: PSS	Drop casting/ solution casting	1295 .21	47.5	32.26	[240]
PEDOT: PSS/rGO	In-situ polymerization	637	24.375	45.7	[271]
PEDOT NW/ Bi_2Te_3	Hydrothermal	249.5	13.3	9.06	[203]
PEDOT: PSS/ rGO	Wet chemical method	1160	12.5	32.6	[253]
PEDOT: PSS/graphene	Spin coating method	32.13	58.7	11.09	[78]
PEDOT: PSS/ Bi_2Te_3	Physical Mixing method	421	18.6	9.9	[202]
Chalcopyrite/PEDOT: PSS/graphene	Drop casting	77.4	**–**61.7	23.4	[272]
PEDOT: PSS/0.4 wt% Bi_2Te_3	Spin coating	1177.57	22	57.04	Present study
PEDOT: PSS/0.4 wt% Bi_2Te_3/ 0.1wt% rGO	Spin coating	1522.4	24.7	93.16	Present study

PEDOT: PSS/0.4 wt% Bi_2Te_3/ 0.2wt% rGO	Spin coating	1738.8	23.07	92.6	Present study
PEDOT: PSS/0.4 wt% Bi_2Te_3/ 0.3wt% rGO	Spin coating	1089	18.05	35.53	Present study

3.2.4 ***Conclusions***

In summary, PEDOT: PSS/Bi_2Te_3/rGO ternary composite films with varying concentrations of rGO were fabricated using the spin coating method. This study reports significantly enhanced thermoelectric (TE) properties of PEDOT: PSS by incorporating Bi_2Te_3 and rGO, providing a promising pathway for high-efficiency TE conversion. The structural and morphological characteristics of the composites were thoroughly evaluated using various analytical techniques. Raman spectroscopy revealed a notable interaction between PEDOT: PSS and rGO, where this interaction induces a structural transformation. This transformation is advantageous for linear structures as it increases conductivity. Strong intermolecular interactions between organic and inorganic chains through π-π bonding and between rGO and PSS chains via hydrophilic groups result in PEDOT and PSS chains' decoupling and phase separation. The thermoelectrical analysis of PEDOT: PSS/Bi_2Te_3/rGO composites showed remarkable improvements in electrical conductivity and the Seebeck coefficient. At room temperature, the PEDOT: PSS/0.4% Bi_2Te_3/0.1% rGO (S2) ternary composite films exhibited the highest electrical conductivity (1522.4 Scm^{-1}), Seebeck coefficient (24.7 μVK^{-1}), and power factor (P.F.) (93.16 $\mu Wm^{-1}K^{-2}$). The PF of the optimized ternary composite concentration showed a significant increase of 5-6 folds compared to pure PEDOT: PSS (S0) samples. A thermoelectric generator (TEG) consisting of three pairs of p-leg PSS/0.4% Bi_2Te_3/0.1% rGO and n-leg PVDF/Ni NWs was also fabricated. The maximum power output of 242.1 nW was achieved with an output voltage of 9.84 mV at $\Delta T = 35$ K. These findings highlight the notable improvement in electrical conductivity and Seebeck coefficient, underscoring the potential of PEDOT: PSS in advanced applications such as energy harvesting and waste heat recovery. Considering the demand for cost-effective, flexible, lightweight, and environmentally friendly materials with outstanding TE performance, the composite films examined in this study exhibit significant potential as viable candidates for high T.E. performance and solid-state devices. The TEG constructed with this material demonstrated

commendable performance, indicating its potential applicability in practical scenarios such as wearable electronics, energy harvesting from waste heat, and portable power sources for compact electronics devices.

Chapter 4. **$FECL_3$ -DOPED P3HT FILMS: A ROUTE TO HIGH-PERFORMANCE FLEXIBLE TE MATERIALS**

4.1 **ABSTRACT: P3HT/$FECL_3$ (P-TYPE)**

Conductive polymers exhibit several desirable properties such as cost-effectiveness, non-toxicity, and low thermal conductivity, making them highly suitable for thermoelectric (TE) applications. In this study, $FeCl_3$-doped poly (3-hexylthiophene) (P3HT) flexible films were synthesized via the drop-casting method, with $FeCl_3$ concentrations of 20, 40, and 60 mM. This study aimed to investigate the structural, morphological, and TE properties of doped P3HT films. Characterization techniques, including XRD, FTIR, and Raman spectroscopy, revealed that the doping process significantly altered the P3HT microstructure. XRD analysis indicated a transition from a crystalline to a more amorphous structure, whereas FTIR and Raman spectroscopy confirmed the formation of localized states, as evidenced by shifts in vibrational modes. Surface morphology analysis using SEM and AFM further demonstrated pronounced changes due to $FeCl_3$ doping, and XPS verified the successful integration of $FeCl_3$ into the P3HT matrix. The TE performance of the P3HT films was examined thoroughly. $FeCl_3$ doping notably enhanced the electrical conductivities of the films. At 300 K, the P40 sample exhibited a notable Seebeck coefficient of 164 µV/K and a maximum power factor of 127.4 $\mu W/Mk^2$. These findings suggest that this doping approach can significantly improve the thermoelectric efficiency. The freestanding flexible P3HT films demonstrated an exceptionally high p-type Seebeck coefficient, underscoring their potential for thermoelectric applications. Future research should focus on optimizing the doping conditions and exploring the practical integration of these materials into real-world thermoelectric devices.

4.1.1 *Experimental Procedure*

4.1.1.1 Materials

P3HT (Mol. weight 37,685 g mol^{-1}, regio regularity 98.5%) and $FeCl_3$ were procured from Sigma-Aldrich (USA). Solvents nitrobenzene and chloroform were obtained from Alfa Aesar (USA). The chemicals utilized in this investigation were employed in their received form without any further processing.

4.1.1.2 Fabrication of P_3HT film

The P3HT powder was dissolved in chloroform in a magnetic stirrer for two hours to form a homogenous 20 mg/ml solution. The P3HT films were drop casted onto polyimide substrate and allowed to air dry before being baked for thirty minutes at 70 °C in oven. The produced films adhered to the substrate effectively and exhibited a golden hue. The $FeCl_3$ in nitrobenzene solution was prepared at three different concentrations of 20, 40, and 60 mM. The dried P_3HT films were then doped with $FeCl_3$ by submerging in nitrobenzene $FeCl_3$ solution for two minutes. The prepared film samples are labelled as P0 (undoped film), P20 (20 mM $FeCl_3$), P40 (40 mM $FeCl_3$), and P60 (60 mM $FeCl_3$). After immersion in $FeCl_3$, the original golden color of the pristine films underwent an immediate transformation into a shiny black shade, providing clear evidence of successful doping. Additionally, interestingly all doped films detached from the substrates and formed freestanding flexible films. The measured thickness was around ~12 μm for doped films and ~8 μm for undoped film P0. This increase in thickness after doping can be ascribed to the fluffy texture caused by the intercalation of dopants. This method of sample preparation is scalable to large area deposition on hard (glass) as well as flexible (Kapton Tape) substrates with desired specifications. Fig 4.1 illustrates the steps involved in preparing the films, and photographs of the actual films.

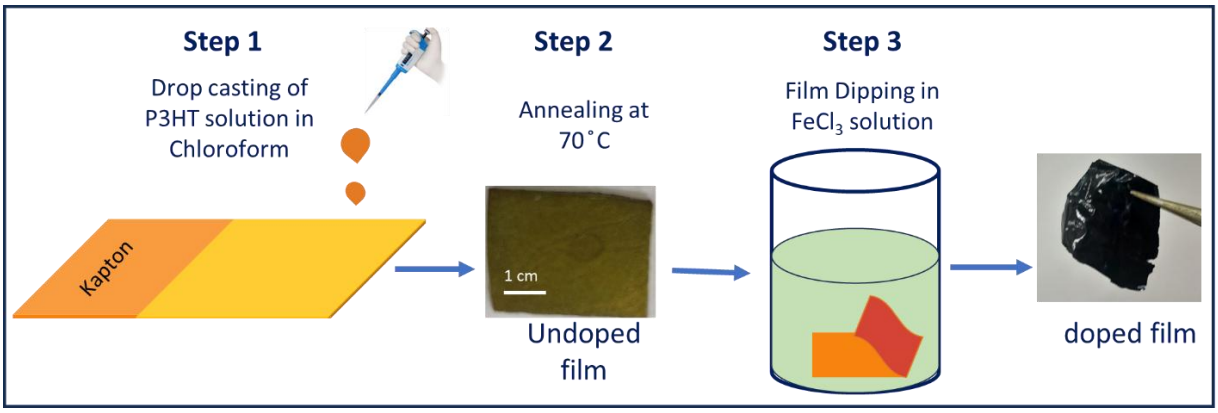

Figure 4.1 An illustration of the P3HT film synthesis process for undoped and doped (freestanding) films.

4.1.1.3 Films characterization

The prepared films were characterized for structural, electronic and thermoelectric properties. The crystal structure of the composite films was examined through grazing incidence X-ray diffraction (GIXRD, Malvern Panalytical, USA) with Cu Kα radiation (λ = 1.54 Å). Raman spectroscopy with 532 nm green laser excitation was employed to investigate conformational changes in the film structure. High-resolution morphological data were obtained using FESEM (Field-Emission Scanning Electron Microscope, Zeiss Gemini), and AFM (NT-MDT-INTEGRA microscope), for the morphology variation studies. All measurements were conducted at RT to ensure consistency throughout the imaging process. FTIR (Perkin Elmer) studies were conducted to verify the changes in the chemical configuration after doping. For temperature-dependent thermoelectric measurements (Seebeck coefficient and resistivity), our in house developed setup was used [22].

4.1.2 *Result & Discussion*

4.1.2.1 Microstructural analysis (XRD, RAMAN)

For all characterizations carried out, a uniform labelling of samples was followed as:

Sample	Label
Undoped P_3HT film (0% $FeCl_3$)	P0
20 mM $FeCl_3$ in P3HT	P20
40 mM $FeCl_3$ in P3HT	P40
60 mM $FeCl_3$ in P3HT	P60

X-ray diffraction spectrum was measured for low angles (0° to 30°) for all freshly prepared thin free standing film samples as shown in Fig 4.2. Peaks were identified with JCPDS catalogue (nae h polymers ka). XRD spectra of the undoped film exhibited three distinct diffraction peaks at 2θ values of 5.3°, 10.7°, and 16.15°. These peaks are associated with the crystallographic planes (200), (300), and (100), respectively. Intense peaks are indicative of a predominantly crystalline structure characterized by edge-on stacking of P3HT planes, as also reported in previous studies [23, 24]. Additionally, the minor peaks (humps) observed at 27° suggested the presence of amorphous regions in the undoped film. The polymer chains in the undoped film demonstrate a highly organized arrangement driven by π–π interactions between the aromatic rings. This organization results in a stacked structure with an interchain spacing of 0.167 nm, resembling a zipper-like arrangement of lateral alkyl chains [20, 24]. In contrast, the XRD analysis of the doped films revealed a wider and low-intensity (100) peak at a reduced 2θ value of 4.59°, with a full width at half maximum (FWHM) of approximately 0.97°. The reduced 2θ value for the (100) peak suggests an increased out-of-plane stacking distance of 0.193 nm, which is attributed to the intercalation of ions, leading to an expansion in interplanar separation [13, 16, 23-25].

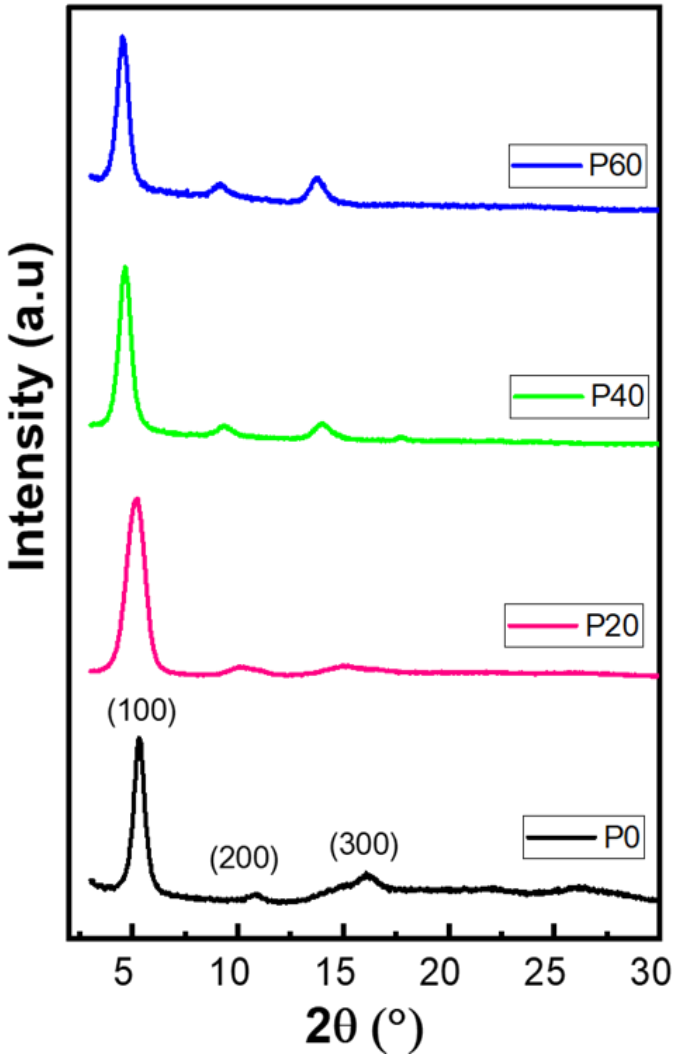

Figure 4.2 X-Ray diffraction pattern of undoped (P0) and $FeCl_3$ doped P3HT (P20, P40, and P60) films.

The Raman spectra of the undoped sample (P0) and the doped samples (P20, P40, and P60) were recorded and analyzed in the 600 –1600 cm^{-1} range (Fig 4.3). In the undoped samples, the most intense peak band is at 1440 cm^{-1} which is associated with the stretching vibration band corresponding to the C_α=C_β bond. Upon doping, this mode experienced a blue shift, appearing at 1444 cm^{-1} [26]. This blue shift is corelated to an increase in the frequency within the bipolarons band. The transition of this lower-energy mode to higher energies suggests a reduction in molecular planarity due to ion interactions during the doping process [26]. Additionally, the band at 1374 cm^{-1}, linked to the C_β-C_β intra-ring stretching vibrations, exhibits broadening and a slight

red shift to 1368 cm^{-1} upon doping. This shift indicates a higher prevalence of amorphous structures in the doped samples, as also corroborated by XRD analysis. Furthermore, the doped samples display inter-ring C-C stretching at 1203 cm^{-1} and C-S-C deformation bands within the range of 719–721 cm^{-1}. The observed red shift and broadening of the C-S-C modes suggest deformation of the thiophene rings in P3HT, likely due to the tensile strain introduced by the dopants. This strain induces a more linear conformation, specifically the quinoid configuration [24] [26].

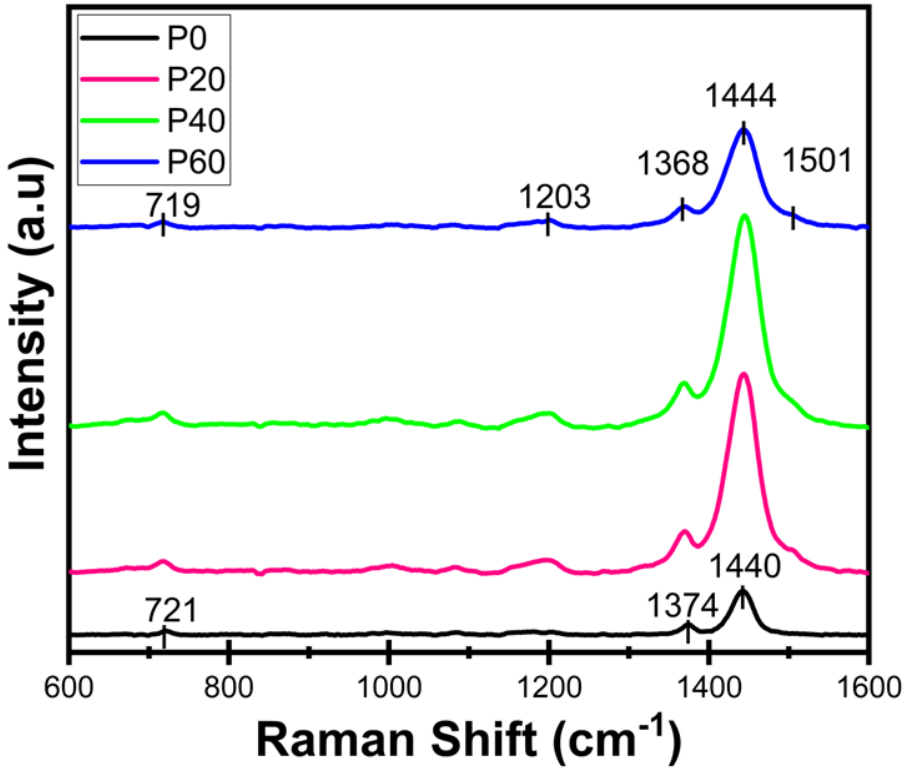

Figure 4.3 Raman spectra of undoped (P0) and $FeCl_3$ doped P3HT *(P20, P40, and P60) films.*

4.1.2.2 Surface Morphology (FESEM and AFM)

The surface morphology of undoped and $FeCl_3$-doped P3HT films were characterized by the FE-SEM and AFM techniques, as shown in Fig 4.4 and 5.5, respectively. The SEM images (Fig 4.4, a-d) reveal that the undoped films exhibit a smoother surface than their doped counterparts. The SEM analysis also showed a granular morphology, with an average particle size of esteemed to be approximately 68 nm for doped samples, as determined using ImageJ software. Additionally, energy-dispersive X-ray spectroscopy (EDX) was performed (Fig 4.4 (e)) to analyse the chemical

composition of the P3HT-$FeCl_3$ polymer composite, confirming the presence of carbon (C), oxygen (O), sulphur (S), iron (Fe), and chlorine (Cl). A detailed table summarizing these elements is provided as an inset of Fig 4.4 (e).

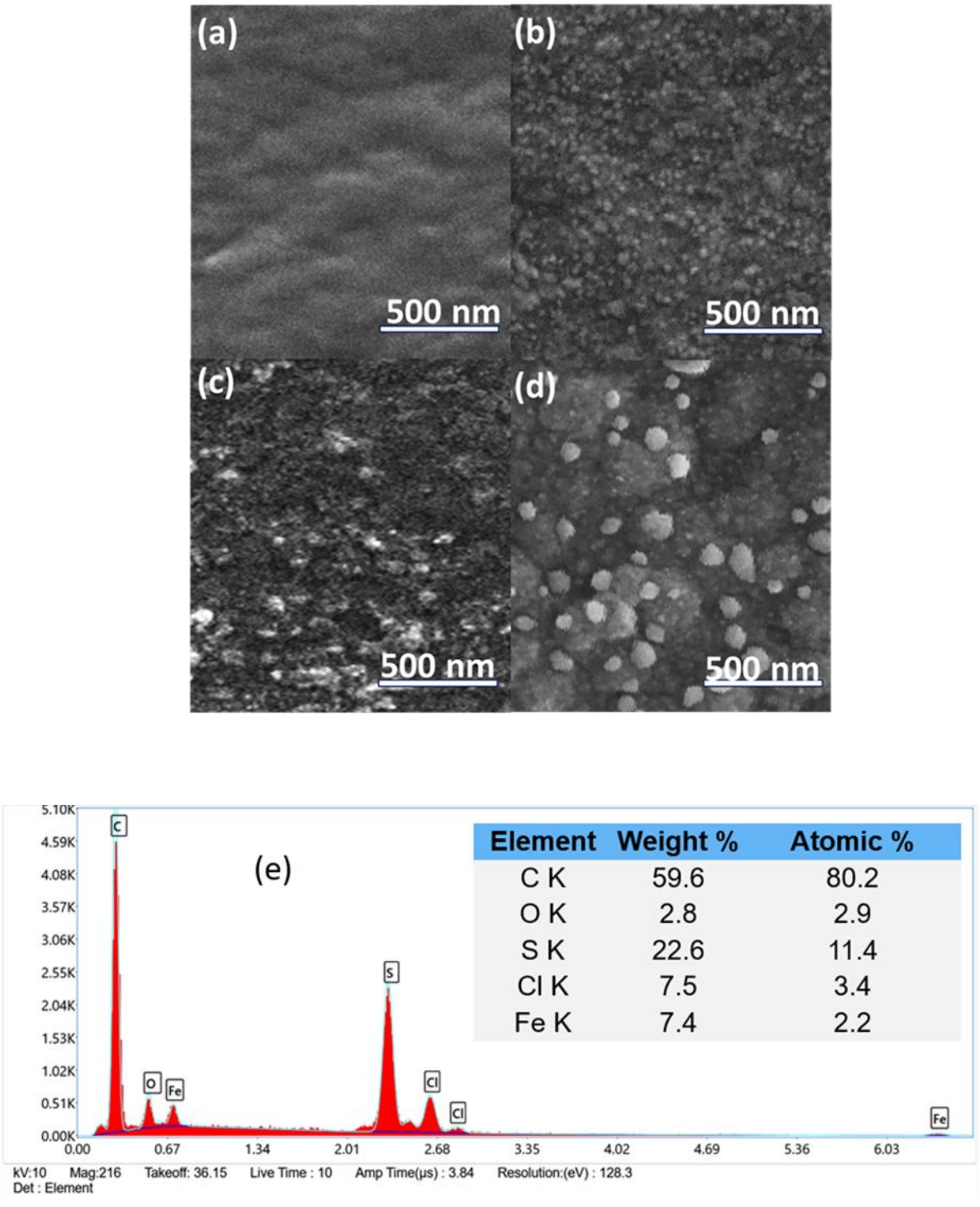

Element	Weight %	Atomic %
C K	59.6	80.2
O K	2.8	2.9
S K	22.6	11.4
Cl K	7.5	3.4
Fe K	7.4	2.2

Figure 4.4 FESEM images of doped and undoped film (a) undoped (pristine) P0, (b) P20 doped, (c) P40 doped, and (d) P60, (e) EDX spectra.

The AFM images (Fig 4.5) further corroborate the granular morphology of the undoped films, indicating a root mean square (RMS) surface roughness of approximately 14.5 nm within a 5×5 μm^2 area. Notably, the introduction of $FeCl_3$ as a dopant leads to an increase in surface roughness, as evidenced by the AFM images of the doped samples (P20, P40, and P60). Both FESEM and AFM technique suggest increase in surface granular structure formation after addition of $FeCl_3$ in P_3HT.

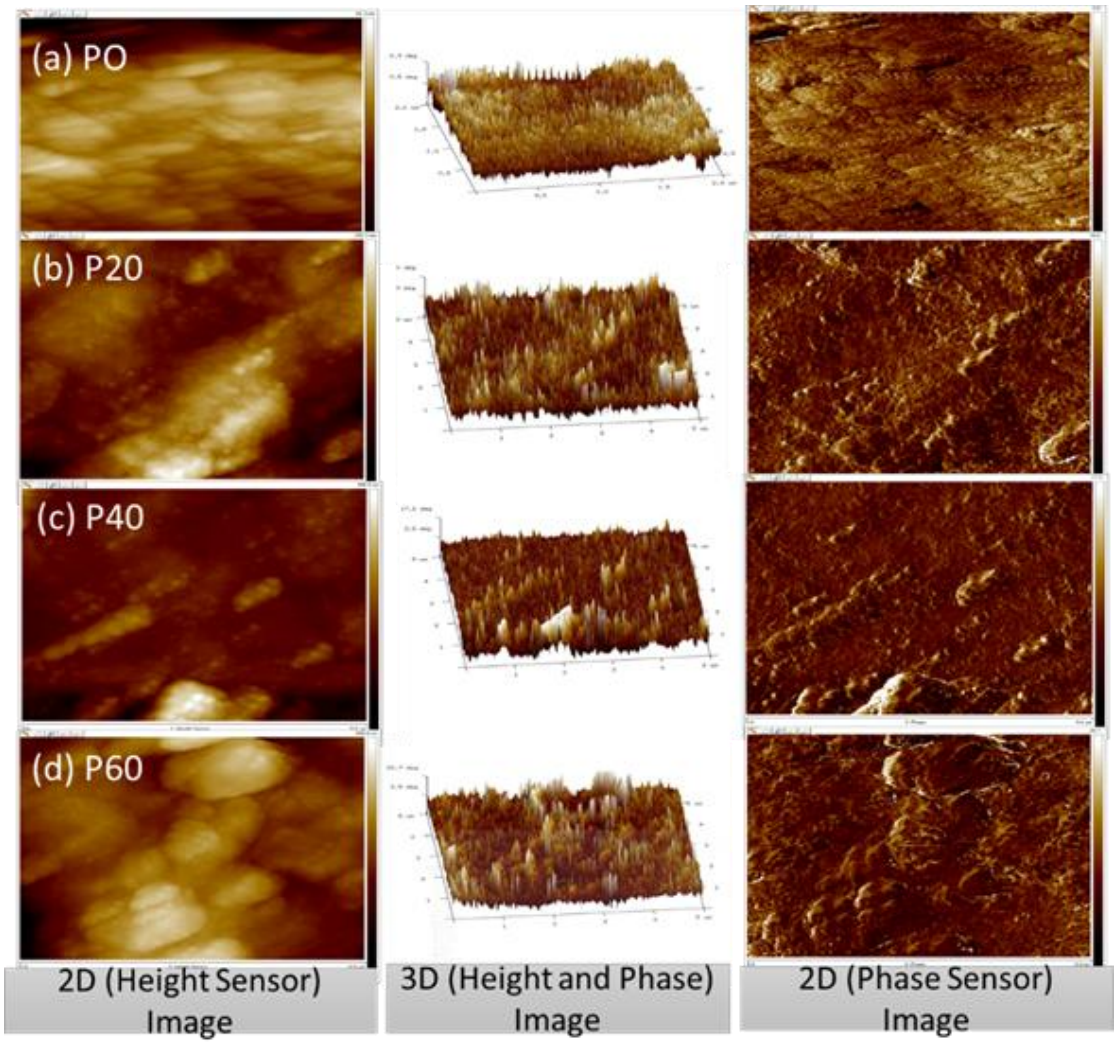

Figure 4.5AFM images of doped and undoped film (a) undoped (pristine) P0, (b) P20 doped, (c) P40 doped, and (d) P60 doped.

4.1.2.3 Electronic Structure (FTIR and XPS)

FTIR spectra of the doped (P0) and undoped (P20, P40, and P60) samples are shown in Fig 4.6. In the undoped P3HT samples, the C-H in-plane vibrations are represented by the band at 1021 cm^{-1}, while the C-H out-of-plane vibrations are commonly connected with absorption bands at 713 and 820 cm^{-1}. The peak at 1346 cm^{-1} is assigned to deformational vibration of the $–CH_3$ group in P_3HT. For the doped samples, FTIR spectra show various peak bands at wavenumbers 1384, 1282, 1142, 1089, 977 854, and 820 cm^{-1}, which are generally associated with polaronic states [26, 27]. The band at 1142 cm^{-1} in the doped films is significantly more intense than at 1384 cm^{-1} and 1282 cm^{-1}. This suggests that the primary charge carriers in the doped samples are bipolarons. The result is supplemented by X-ray photoelectron spectroscopy (XPS).

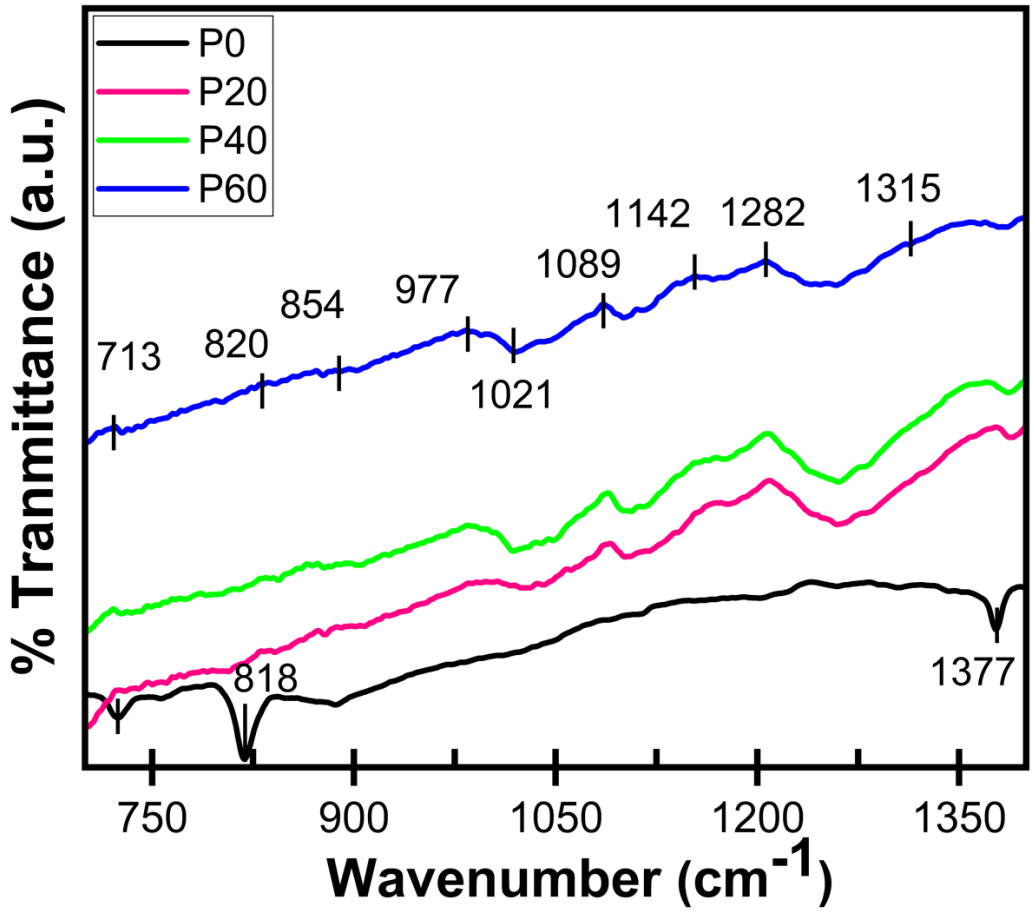

Figure 4.6 FTIR spectra of undoped (P0) and $FeCl_3$ doped P3HT (P20, P40, and P60) films.

X-ray photo electron spectroscopy (XPS) measurement was carried out on selected samples only, i.e. for undoped P3HT sample and P3HT doped P3HT (P40) sample. The binding energy spectra reveals that the undoped films exhibit characteristic peaks corresponding to C1s, O1s, S2p, and Cl2p (from solvent $CHCl_3$) see in Fig 4.7(a). The doped samples showed additional peak for Fe2p, indicating the presence of iron from the dopant $FeCl_3$. Deconvolution of the broad and asymmetric C1s peak (284.6 eV), presence of two peaks (Fig 4.7 (b)) attributed to the C-C/C-H and C-S bonds, respectively [28]. The carbon atoms bonded to sulfur exhibit a higher binding energy (B.E.) of 285.1 eV, attributed to the greater electronegativity of the sulfur atom in P3HT, which causes electron density withdrawal from the neighboring carbon atoms. In the C1s spectrum of the doped P40 films (Fig 4.7c), a distinct binding energy peak at 285.3 eV is observed, indicative of a higher concentration of carbon in specific chemical environments. This observation is consistent with the findings for samples with higher doping levels [29]. The S2p spectra of the undoped sample (P0) in Fig 4.7(d) shows the splitting between $S2p_{3/2}$ and $S2p_{1/2}$ peaks with a separation Δ_{BE} = 1.6 eV. These values are characteristic of S-C bonding within the thiophene ring [30]. In the doped samples (P40), illustrated in Fig 4.7(e), the S2p spectra display components with higher B.E ($S2p_{3/2}$ at 167 eV), which are likely associated with the oxidation of the thiophene ring caused by the dopant [28, 31]. The Fe2p spectra of the P40 films, shown in Fig 4.7(g), indicate that the $Fe2p_{3/2}$ peak can be deconvoluted into two distinct components exhibit B.E. of 708.9 and 712.7 eV. These are linked to the different oxidation states of Fe [32]. According to Tosi et al., $FeCl_3$ dopant may form Fe_2Cl_6 dimers, which undergo partial decomposition into $Fe_2Cl_5^+$ and $Fe_2Cl_7^-$ species [33]. The decomposition products correspond to the peaks at 708.9 and 712.7 eV, respectively [34]. Additionally, the XPS spectra in Fig 4.7(f) reveal a distinct peak between the B.E. of 196 eV and 204 eV, indicating the presence of chlorine in P3HT. The binding energies of chlorine 2p in $FeCl_3$ are observed at 196.9 and 200 eV. The presence of peaks corresponding to the $2p_{3/2}$ and $2p_{1/2}$ electrons of ionic chlorine (Cl^-) suggests that the compound intercalated into P3HT contains Cl^- ions [35].

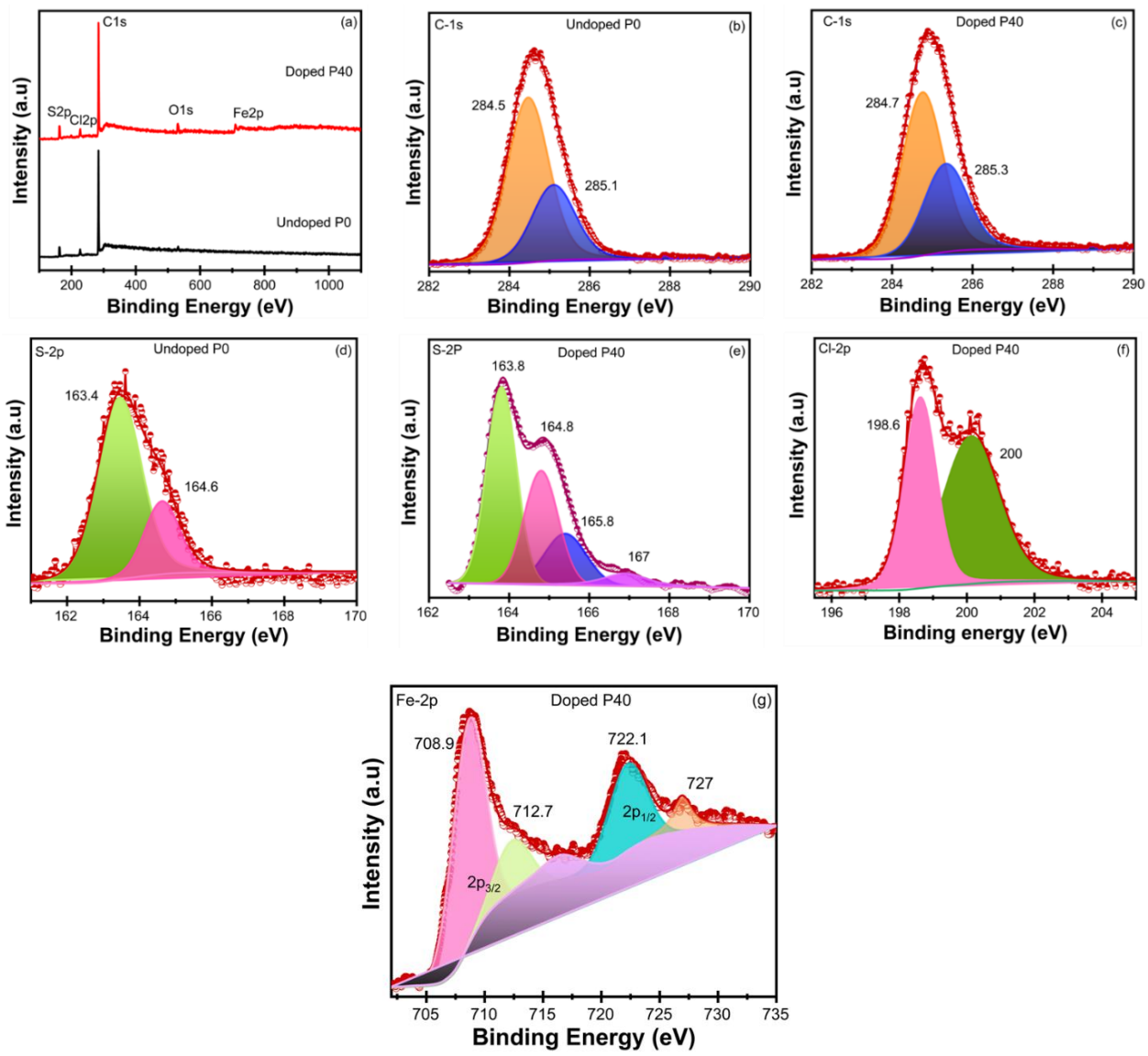

Figure 4.7 XPS binding energy spectra of undoped (P0) film and $FeCl_3$ doped film (P40) film.

4.1.2.4 Thermoelectric measurements (Seebeck Coefficient and Resistivity)

The performance indicators of thermoelectric materials are primarily Seebeck coefficient, and electrical conductivity. Higher electrical conductivity of thermoelectric material is essential for high figure of merit (zT) of material. It also indicates low internal resistance of emf/voltage source. The Seebeck coefficient serve as a measure of voltage created in accordance to a temperature differential across the material. A higher value denotes a larger voltage corresponding to a given temperature gradient. The performance of the material in converting thermal energy into electrical power is quantified by the power factor (PF), which is product of the σ and S squared.

The electrical conductivity measurements of the undoped and $FeCl_3$-doped P3HT samples are shown in Fig 4.8(a). The samples, labelled P0, P20, P40, and P60, correspond to different doping concentrations, specifically 20, 40, and 60 mM of $FeCl_3$ solution. The electrical conductivity of the undoped films was found to be 4.37×10^{-4} Scm^{-1} at room temperature (RT). It showed a gradual increase as the temperature increased. Upon doping with $FeCl_3$, the electrical conductivity at RT significantly increased, reaching 2.2 Scm^{-1}, 46.67 Scm^{-1}, and 13.7 Scm^{-1} at RT for the P20, P40, and P60 samples, respectively. This represents an increase in the electrical conductivity by 30–40 times compared to the pristine films. However, for the P60 films, the electrical conductivity did not increase higher with further doping and remained comparable or lesser to P40 at RT, as illustrated in Fig 4.8(a). The P60 films, which are highly doped, exhibited the strongest temperature dependence, with σ improved from 13.7 Scm^{-1} to 69.8 Scm^{-1} as the temperature was elevated from increased from 300 K to 400 K. This behaviour is intriguing and warrants further investigation in future studies. In contrast, the P20 and P40 samples showed minimal temperature dependence.

The Seebeck coefficient for the undoped sample (P0) was found to be approximately 25 μVK^{-1} the p-type character at RT, as shown in Fig 4.8(b). The $FeCl_3$-doped films exhibited significantly higher positive Seebeck coefficients, characteristic of dominant positive ion conduction, a behavior often observed in ionic polymer conductors. Specifically, the Seebeck coefficients for the P20, P40, and P60 films were recorded at 112.7 μVK^{-1}, 164.9 μVK^{-1}, and 128.9 μVK^{-1}, respectively, near room temperature. Notably, the S for doped P3HT films also surpasses that of traditional inorganic thermoelectric materials. A significant rise in σ (from 0.7 to 2980 S/cm) and a marginal improvement in the S (from 17.6 to 21.9 μVK^{-1}) are seen when PEDOT films are treated with a superacid in methanol [36]. The results indicate one of the highest values that have also been reported for conductive polymers. Careful observation reveals that the P40 sample achieved a maximum S of 164.9 μVK^{-1} at RT, which increased to 181.1 μVK^{-1} at 400 K. This pronounced positive Seebeck coefficient suggests that conduction in these films is previously ascribed primarily to the movement of positive ions. Studies have attributed ionic conduction in $FeCl_3$ to the formation of ionized species, specifically $(Fe_2Cl_5)^+$ and $(Fe_2Cl_7)^-$, which are in equilibrium with bitetrahedral Fe_2Cl_6 molecules [33]. The hopping mechanism of Cl^- ions from $(Fe_2Cl_7)^-$ leads to conduction observed in $FeCl_3$-doped P3HT films. It is anticipated that the primary charge carriers in the doped films are positive ions, though there remains a possibility of electronic conduction,

either p-type or n-type, as well [33]. The high-power factor observed in these doped P3HT films, as illustrated in Fig 4.8(c), can be attributed to the combined impact of their elevated electrical conductivity and Seebeck coefficient. Notably, the P40 has shown the maximum PF of 127.4 $\mu Wm^{-1}K^{-2}$ at RT, which increased to 178.5 $\mu Wm^{-1}K^{-2}$ at 400 K.

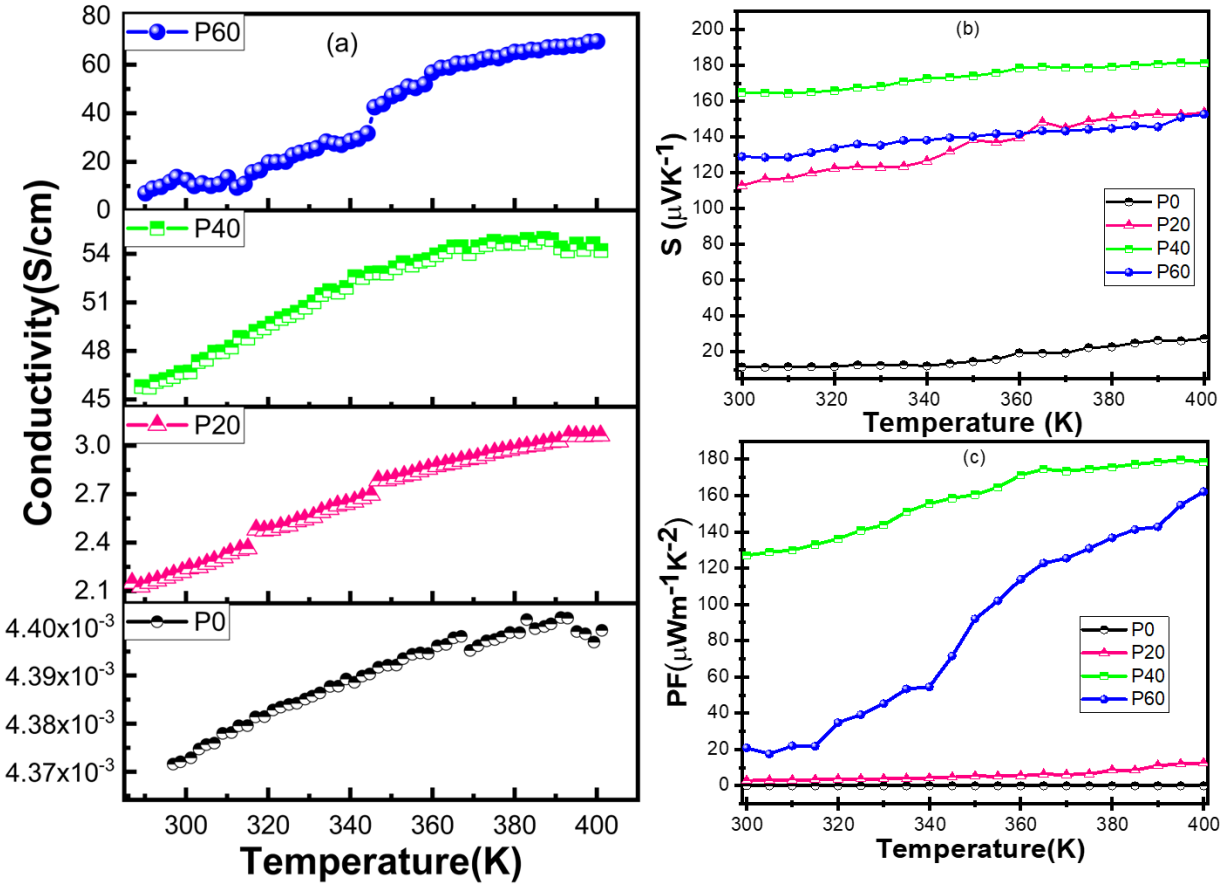

Figure 4.8 (a) Electrical conductivity, (b) Seebeck Coefficient and (c) Power factor of undoped and doped film P0 (undoped), and P20, P40, P60 (doped).

4.1.3 ***Discussion***

The study of undoped (P0) and $FeCl_3$-doped P3HT (P20, P40, and P60) films provides a complete study of how doping affects the structural, morphological, and thermoelectric properties of P3HT, thereby enhancing our understanding of their suitability for thermoelectric applications. The XRD patterns of undoped P3HT (P0) display sharp peaks, which signify a highly crystalline structure.

The observed peaks indicate specific planes of the polymer and indicate edge-on-stacking with organized Π- Π interactions among the aromatic rings. But doping with $FeCl_3$ decreases the intensity and moves these peaks to lower angles, which indicates the interplanar space has expanded by the addition of $FeCl_3$ ions. This results in disorder and disrupts the crystalline structure of the polymer, as indicate by the broad and less intense peaks observed in the doped films. Raman spectroscopy further supports for these findings. The shift of the $C_\alpha = C_\beta$ stretching mode from 1440 cm^{-1} in the doped samples suggests a structure transformation of polymer, leading to enhance electrical conductivity. The surface morphology, observed by FESEM and AFM, supports the structural findings. Undoped P3HT films show smooth surfaces characterized by small, uniform granules. The RMS roughness of the undoped film measured approximately 14.5 nm, with a notable increased roughness and granular structure indicate that the disruption of the polymer matrix by $FeCl_3$ resulted in localized agglomeration and ion clustering. The EDX spectra confirmed the incorporation of Fe and Cl elements in the doped films, validating the presence of $FeCl_3$ and its interaction with the P3HT chain. The structural and morphological changes are essential for understanding the electronic and thermoelectric properties of the films. FTIR spectra exhibit distinct peaks in both undoped and doped films, indicating the vibrational modes of the polymers structure. Doped samples show new peaks linked to polaronic states, suggesting that the dopant generates charge carriers, especially bipolarons. The carriers improve the electrical conductivity of the material. Additional information on the chemical changes caused by doping is provided by XPS analysis. The C1s and S2p spectra peaks in undoped films correspond to the characteristics bond present in P3HT. After doping new peaks for Fe2p and shifts in the S2p peaks, suggesting oxidation of the thiophene ring. The observe changes indicate that $FeCl_3$ interacts with P3HT, modifying its electronic structure and introducing ionic species such as $Fe_2Cl_7^-$ and Cl^-, which facilitate conduction. The doping of the films results in a significant increase in the electrical conductivity. The undoped film exhibits low conductivity (4.37×10^{-4} Scm^{-1}) and a Seebeck coefficient of 25 μVK^{-1} at room temperature. The electrical conductivity significantly increased after doping, reaching a maximum of 46.67 Scm^{-1} for P40. The enhancement in charge carrier density is due to the intercalation of $FeCl_3$ ions. The Seebeck coefficient increased with doping, achieving a maximum of 164.9 μVK^{-1} for P40. The simultaneous enhancement of conductivity and Seebeck coefficient is rare and highlights the significance of ionic conduction in the doped films. The PF, a critical parameter for TE performance, attained a value of 127.7 $\mu Wm^{-1}K^{-2}$ at

400K. The anomalous behaviour observed in the P60 film, with reduced σ and S compared to P40 film, suggests that excessive doping leads to over-disruption of the polymer matrix, reducing the effective charge carrier mobility. The observed power factor of 1.25 $\mu Wm^{-1}K^{-2}$ for 60 mM $FeCl_3$-doped P3HT films at RT shows a 4 times enhancement over pristine P3HT. this is superior to previously reported PF values for $FeCl_3$ -doped P3HT films. Such as Kim et.al. 2013, where PF~ 0.9 $\mu Wm^{-1}K^{-2}$ was achieved at similar doping concentration. Similarly, Bubnova et al. 2012, who demonstrated PF~ 1.2 $\mu Wm^{-1}K^{-2}$ using vapor-phase doping methods. Our drop-casting method offers a simpler, scalable alternative while maintaining competitive TE performance. The enhanced TE performance of $FeCl_3$ -doped P3HT films can be attributed to the synergistic effects of structural, electronic, and morphological changes induced by doping. P40 emerges as the optimal doping level, balancing structural integrity with charge carrier density, leading to superior TE performance. This study highlights the potential of $FeCl_3$-doped P3HT films as promising candidates for flexible TE applications.

4.1.4 ***Conclusion***

The current study aimed to elucidate the role of polaronic contributions in the conduction mechanism of conducting polymers. Our results demonstrate an effective strategy for enhancing the S and PF of P3HT by doping with varying concentrations of $FeCl_3$. This research underscores the potential for optimizing the TE performance of P3HT polymers. The P40-doped films exhibited a notable improved in the S (164.9 μVK^{-1}), while maintaining high σ (46.67 Scm^{-1}), resulting in an impressive PF of 127.4 $\mu Wm^{-1}K^{-2}$ at RT. This marks a substantial improvement over the undoped P0 sample, which exhibited a power factor of just 5.89×10^{-5} $\mu Wm^{-1}K^{-2}$. The approach of enhancing the power factor through the strategic manipulation of interactions between organic and inorganic polymer nanocomposites shows significant promise for the development of high-performance, large-area, and flexible polymer TE materials. These findings suggest that $FeCl_3$ is an efficient dopant for boost the efficiency of p-type polymers, leading to improved efficiency and stability. Moreover, the use of $FeCl_3$ could pave the way for more extensive studies of the TE properties of organic semiconductors. This study aims to inspire further research on the application of solution-processable polymer semiconductors for TE applications, with a focus on both neutral molecules and doping methodologies.

Chapter 5. **SYNTHESIS AND CHARACTERIZATION OF N-TYPE THERMOELECTRIC MATERIALS**

5.1 **ABSTRACT: PVDF/NI NWS (N-TYPE)**

This study presents the fabrication and analysis of PVDF/Ni NWs composite films for TE applications. The preparation of composite films using different concentrations of Ni NWs, specifically (30-90 wt.%). In our discussion, The Ni nanowires were incorporated into PVDF to create composite TE materials with n-type Seebeck coefficient. An investigation was conducted to examine the impact of varying weight ratios of Ni nanowires on the TE properties of the composites. This was accomplished by dispersing PVDF with Ni NWs in DMF solvent, followed by a drying process to a yield a uniform film structure. Structural analysis uses such as XRD, and FTIR confirmed the existence of α and β crystalline phases within the PVDF matrix, with Ni NWs creating a conductive path throughout the materials. SEM confirm the uniform dispersion of Ni NWs within the PVDF matrix, which plays a significant role in improving TE performance. The chemical states and interactions inside the composite were thoroughly revealed by XPS characterization. Electrical measurements indicated that an increase in Ni NWs content resulted in enhanced electrical conductivity (σ), while the Seebeck coefficient (S) exhibited a consistent n-type behaviour. Experimental observations indicate that the conductivity of the composite exhibits a notable enhancement when the Nickel nanowire content attains 75 wt.%. The conductivity could be enhanced by 4000 times. The TE power factor (PF) of the composites attained a optimized value of 242 $\mu Wm^{-1}K^{-2}$ at a temperature of 400 k, exceeding the values documented for similar PVDF based materials in the literature. Furthermore, a thermoelectric generator (TEG) device has been developed, comprising a p-leg configuration of PEDOT: PSS and an n-leg configuration of PVDF/Ni NWs, all incorporated onto flexible polyimide substrates. A flexible TEG was developed utilizing p-type PEDOT and n-type PVDF/Ni nanowires, resulting in a Maximum power output (P_{max}) of 230 nW at ΔT= 25 K. This investigation highlights the capabilities of PVDF/Ni NWs

composites in the realm of flexible energy-harvesting devices, suggesting significant possibilities for the improvement of TE performance by strategic material engineering.

5.2 EXPERIMENTAL DETAILS

5.2.1 *Materials and chemicals*

The PVDF was procured from sigma Aldrich, dimethylformamide (DMF), Hydrazine hydrate solution ($N_2H_4.H_2O$) was obtained from Molychem. Nickel chloride hexahydrate (Ni_2Cl_2.6H2O) was acquired from SRL. Sodium hydroxide (NaOH) was procured from Molychem. All reagents used in the experiment were of high purity.

5.2.2 *Synthesis of Nickel Nanowire:*

The material $Ni_2Cl_2.6H_2O$ was dissolved in a solution containing of 30 ml of deionized (DI) water and 37.5 ml of ethanol. The resulting mixture was subsequently agitated for a period of 30 minutes, leading to the emergence of a light green solution. Subsequently, a NaOH pallet with a concentration of 5 mol/L was carefully administrated in a dropwise manner until the pH of the resultant solution attained a value of 14. The solution was carefully placed in a magnetic field with a minimal strength and a temperature 60 °C. To aid in the reduction process, 40 ml of a hydrazine hydrate solution with a weight percentage of 85% was added. A black-grey solid formed after a 20 min reaction time and stayed a float on the solution's surface. To get rid of any leftover byproducts, the product was collected using an external magnetic and repeatedly carefully cleaned with ethanol and DI water. After completion of the process, the product was dried for two hours at 60 °C under vacuum condition. After that, the material is crushed finely till it turns into a black solid that may be used. The following is the chemical equation that describe the process.
The reaction is represented by the following chemical equation [325].

$$N_2H_4 + 4NaOH + 2NiCl_2 \longrightarrow 2Ni + N_2 + 4NaCl + 4H_2O \quad (1)$$

5.2.3 *Fabrication of PVDF/Ni NWs composite Films:*

As depicted in Fig 5.1, a mixture of 200 mg PVDF powder and 10 ml DMF was prepared in a beaker. The mixture underwent subjected to magnetic stirring at a room temperature for a duration 2 hours until complete dissolution was achieved. In addition, varying compositions of Ni NWs

powder were introduced and subjected to ultrasonication bath at a temperature 60 °C for a 1 h. This process aimed to achieve a homogenous dispersion of Ni NWs within the combined solution. The solution blend was then transferred to a vacuum drying oven at of 40 °C for 12 h. This meticulous procedure resulted in the formation of PVDF/Ni NWs composite films. We conducted an experiment to investigate the impact of Ni varying content on the σ and S. For this purpose, we developed a variety of PVDF/Ni chain composite films with different Ni concentrations (30 wt%, 50 wt%, 70 wt%, and 90 wt%).

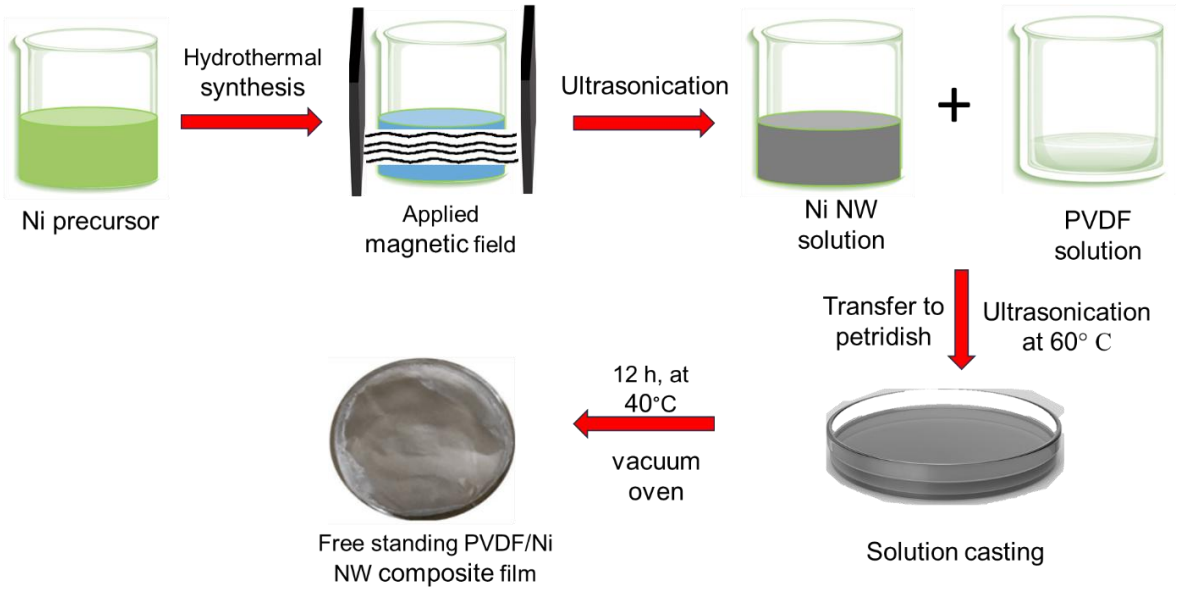

Figure 5.1Illustrates the visual representation detailing the preparation process for PVDF/Ni NWs composite films.

Table 5-1 describe the composition and sample notation for each sample.

Sr No	Composition	Name Notation
1.	Pure Nickel Nanowires	Ni NW
2.	Pure PVDF	PVDF
3.	30 wt.% Ni NWs in PVDF	30% Ni/PVDF
4.	50 wt.% Ni NWs in PVDF	50% Ni/PVDF
5.	70 wt.% Ni NWs in PVDF	70% Ni/PVDF
6.	90 wt.% Ni NWs in PVDF	90% Ni/PVDF

5.3 CHARACTERIZATION AND MEASUREMENTS:

The crystal structure and composition of Ni NWs and PVDF/Ni NWs composite films were analyzed using grazing incident X-ray diffraction (GIXRD) with Cu Kα radiation (ƛ = 1.54 Å) on a Malvern Panalytical at 40 mA and 45 kV. An investigation was carried out using Fourier-transform infrared spectroscopy (FTIR) attenuated total reflectance (ATR) to examine the changes in chemical structure following the introduction of dopants. The sample were carefully dried before being analyzed using the FTIR spectrum analyser from Perkin Elmer. This instrument allowed us to determine the various crystalline forms of PVDF. Utilizing field emission scanning electron microscopy (FESEM Zeiss Gemini), we aim to obtain precise and detailed morphological data. This will enable us to analyse and investigate any potential changes in morphology through the applications of advanced technology. X-ray Photoelectron Spectroscopy (XPS), analysis was performed using a PHI 5000 Versa Probe Scanning Microscope from ULVAC-PHI Inc., USA. Our in-house developed setup was utilised for temperature-dependent thermoelectric measurements, for the Seebeck coefficient and resistivity.

5.4 RESULTS AND DISCUSSION

5.4.1 *Characterization of Ni NWs*

The crystal structure of the Ni NWs that were prepared was analyzed using XRD. The corresponding result can be seen in Fig 5.2a. Three distinct peaks observed at 2Θ = 44.4°, 51.8°, and 76.4°, corresponding to the miller indices (111), (200), and (220). The peaks are accurately attributed to the face-centred cubic structure of Ni (JCPDS file card No. 04-0850) [325]. It is evident that the phase of the Ni sample was pure as no diffraction peaks were observed. Fig 5.2 b provides an analysis of the purity of Ni using EDS. Based on the EDS pattern, it can be observed that the samples consist primarily of Ni, indicating a high level of purity. The morphologies of the Ni NWs samples were examined utilising SEM. As observed in Fig 5.2c, the Ni NWs that were created exhibited a distinctive chain-like structure, with lengths varying between 3 µm to 30 µm. The magnified image of the Ni NWs sample (Fig 5.2d) reveals the composition of Ni chains, which are comprised of cylindrical particles with an average diameter ranging 0.29 µm to 0.55 µm.

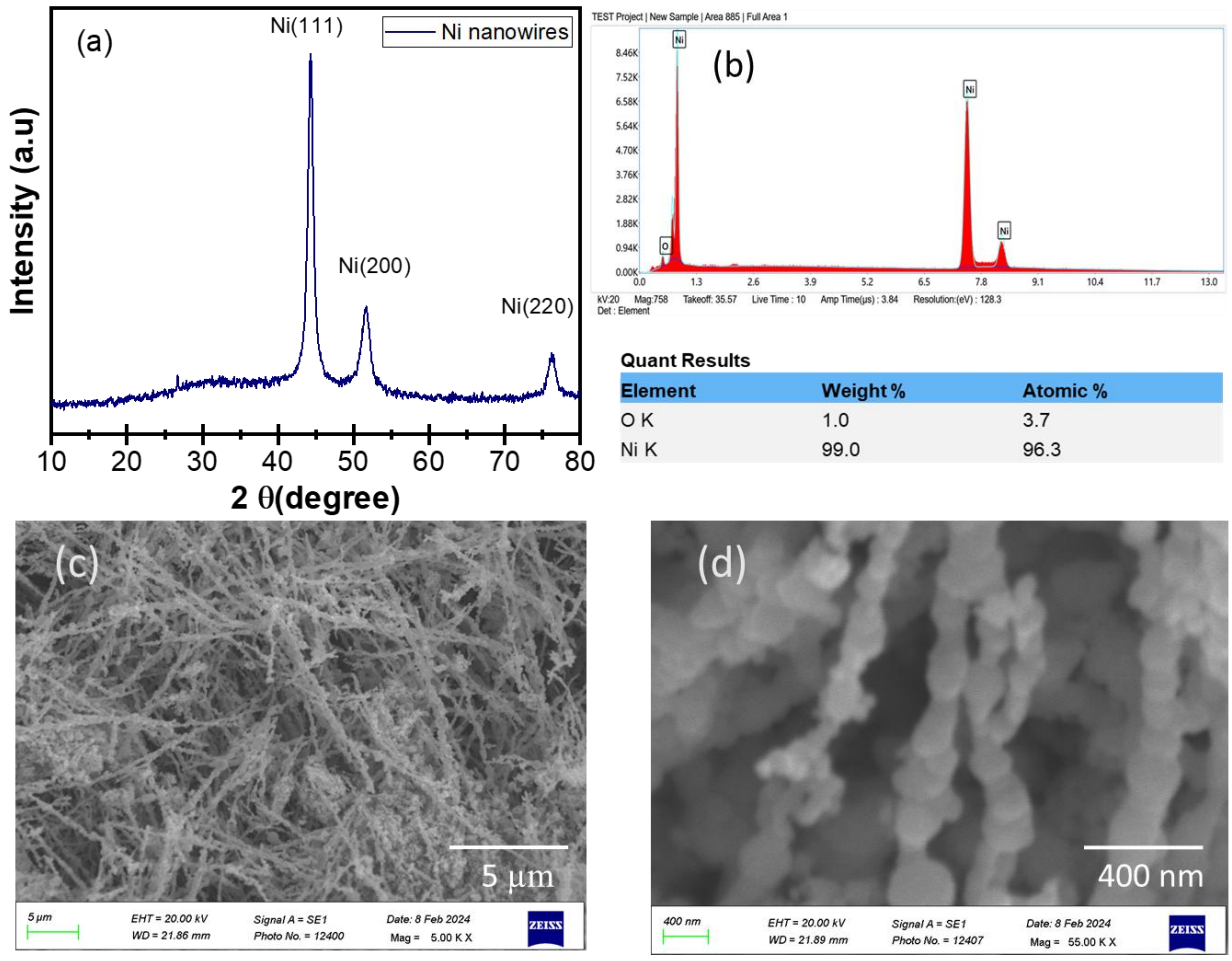

Figure 5.2 displays the characterization of Nickel nanowires: (a) XRD pattern showing peaks corresponding to Ni (111), Ni (200), and Ni (220) planes, confirming the crystalline nature; (b) EDS spectrum with quantitative results indicating a high purity of Ni (99 wt%); (c) SEM image at lower magnification showing the morphology of interconnected nanowires; (d) SEM image at higher magnification revealing the surface structure of the nanowires.

5.4.2 ***Crystal structure and characteristics of PVDF/Ni NWs nanocomposite films***

The XRD patterns of the prepared PVDF/Ni NWs composites are presented in Fig 5.3 (a), where the two characteristic peaks of PVDF (2Θ = 18.4°, 19.9°) are clearly observed. Observations indicate that the PVDF matrix is predominantly filled with a significant quantity of Ni NWs. The intense diffraction peaks of the Ni NWs dominate the relatively weaker diffraction peaks of PVDF. Furthermore, the four composites exhibit diffraction peaks at 44.4°, 51.8°, and 76.4°, which can

be attributed to the crystal Faces of Nickel, specifically (111), (200), (220) [325]. In addition, as the concentration of Ni NWs rises from 30 to 90 wt%, the intensity of the associated characteristics peaks also increases correspondingly. Furthermore, no other peaks are observed, suggested the absence of NiO in PVDF/Ni NW composites. The composite consisted purely of PVDF and Ni chains. The observation is crucial for maintain the conductivity of the nanocomposite films.

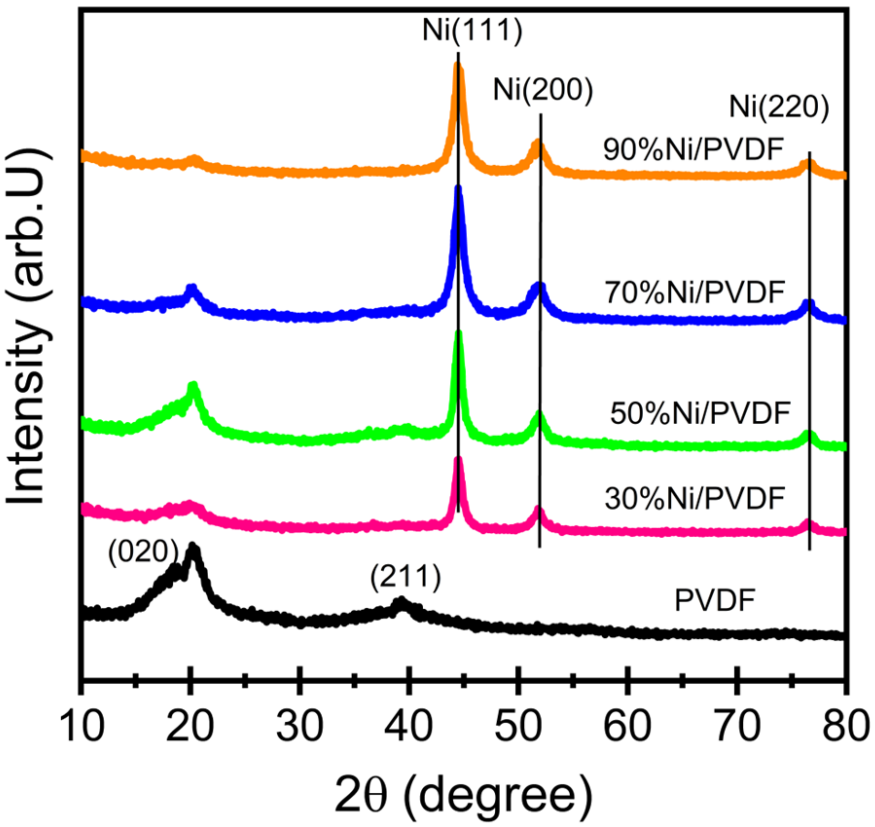

Figure 5.3 XRD pattern of PVDF and PVDF/Ni NWs composite films with varying content of Nickel nanowires (30wt%, 50 wt%, 70wt%, and 90 wt%), the diffraction peaks at 44.5°, 51.8°, and 76.4° correspond to the Ni (111), Ni (200), and Ni (220) planes, respectively. PVDF peaks are observed at 20.2°, and 36.2° corresponding to (020) and (211) planes, with the intensity of Ni peaks increasing as the Ni content in the composites increases.

FTIR

The FTIR spectrum of a PVDF/Ni NWs composite is presented in Fig 5.4. The analysis of absorption peaks in the PVDF/Ni NWs composite indicate the presence of both α and β phases.

The absorption peaks observed at 770, 809, and 942 cm^{-1} correspond to the α phase, while the peaks at 871 cm^{-1} and 1166 cm^{-1} indicate the presence of the β phase. The absorption peaks at 871 cm^{-1} are attributed to the rocking vibration of CH_2 and the stretching vibrations of CF_2 [326, 327]. Additionally, the absorption peaks at 1070, 1166, and 1402 cm^{-1} are associated with the stretching vibration of CF_2, the skeleton vibrations of C-C, and the deformation of CH_2 due to rocking vibrations respectively. In addition, the intensity of every absorption peak diminishes as the amount of Ni NWs increases. This suggests that the Ni NWs take up a significant portion of PVDF matrix, resulting in a weak interaction between the atom.

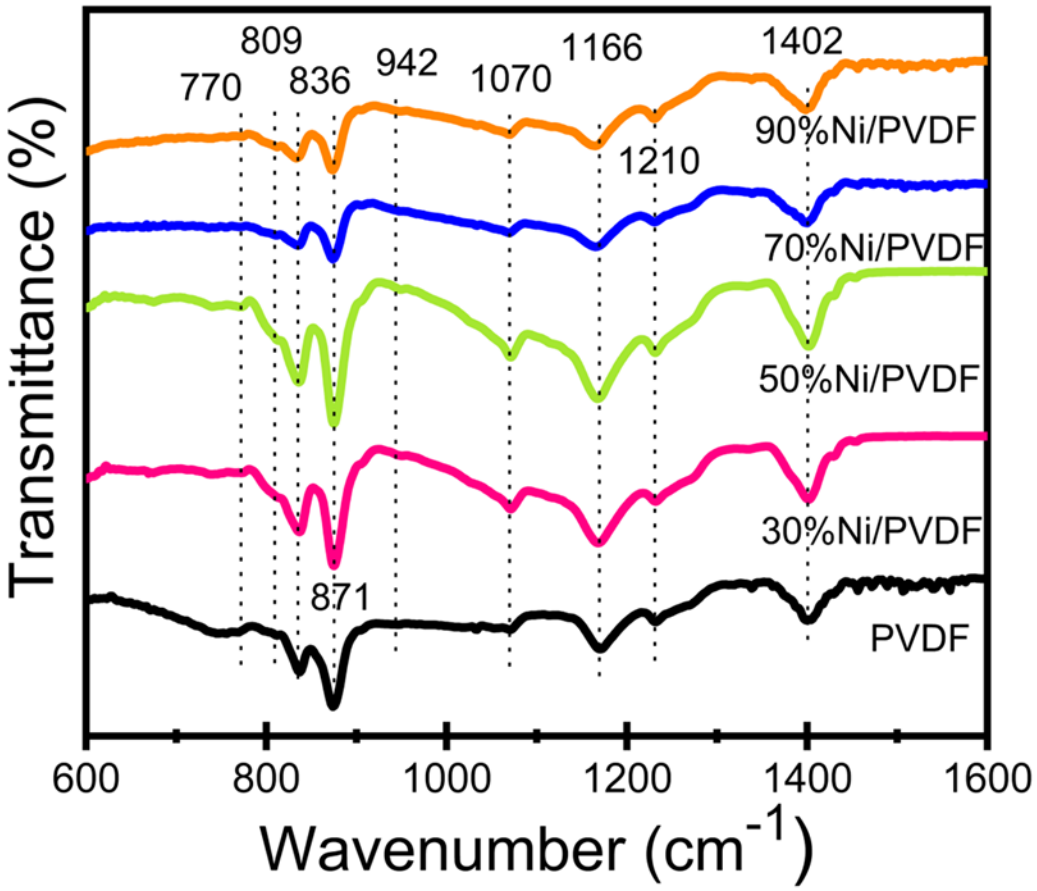

Figure 5.4 displays the FTIR spectrum of PVDF and PVDF/Ni NWs composite films with varying content of Nickel nanowires (30 wt%, 50 wt%, 70wt%, and 90 wt%), PVDF/Ni NWs composites with varying content of Nickel nanowires.

5.4.3 *Surface morphologies of PVDF/Ni NWS Composite films*

Fig 5.5 (a) presents the FESEM micrographs of Ni NWs that were synthesized using liquid phase chemical reduction. The Ni NWs appear to be arranged in a stacked formation, with each nanowire maintain its individual structure and showing excellent dispersibility. The length of the Ni NWs ranges from 10-100 µm. based on the illustration, it is evident that the diameter of Ni NWs exhibits a high level of uniformity, measuring approximately 250 nm. The synthesised Ni NWs demonstrate a significant aspect ratio, achieving an optimal value of 400. The SEM images in Fig. 5.5 (b) to (e) depict of PVDF/Ni NWs composites containing varying weight percentages of Ni NWs 30-90wt %. With an increase in Ni NWs content from 30 to 90 wt%, the size of Ni NWs increases, while the PVDF matrix become less separated. In addition, the PVDF matrix contains Ni NWs that are evenly distributed, with no significant agglomeration. This observation suggests a significant interaction between the Ni NWs and PVDF, leading to an improvement in electrical conductivity.

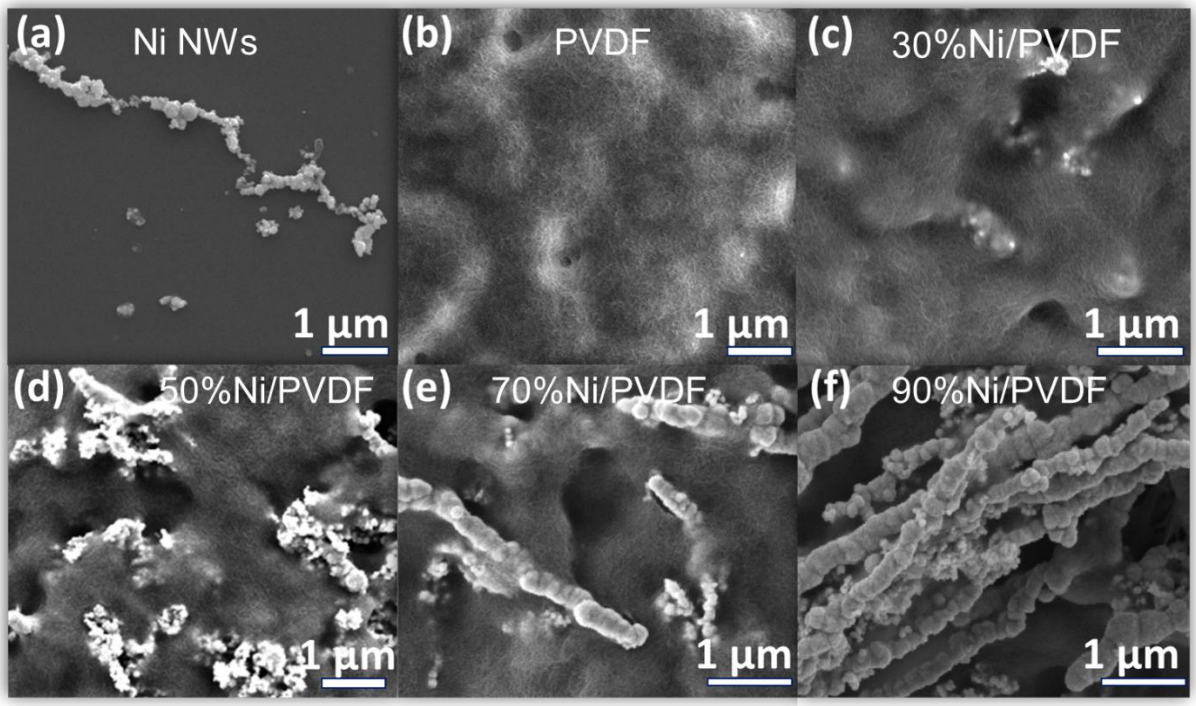

Figure 5.5 FESEM micrographs of (a) pure Ni Nanowires, (b) pure PVDF (c) 30% Ni/PVDF (d) 50% Ni/PVDF (e) 70% Ni/PVDF and (f) 90% Ni/PVDF. The images illustrate the morphological

evolution as the Ni NW concentration increases, showing improved nanowire connectivity and network density at higher Ni content. (Scale bar: 1μm).

5.4.3.1 XPS

The chemical binding state and elemental composition of the PVDF and PVDF/Ni NWs nanocomposite were analysed by XPS. The full spectrum of PVDF indicates the existence of C, O, and F. In contrast, the PVDF/Ni NWs predominantly consist of C, O, F and Ni. Fig 5.6 presents XPS spectra for both pristine PVDF and PVDF/Ni NWs. Fig 5.6 (a, b) presents the C1s spectra derived from C atoms in both PVDF and PVDF/Ni NWs. The deconvoluted spectra for the C1s indicate the contributions of various carbon species to the C1s spectra. In the C1s spectra of pristine PVDF and the PVDF/Ni nanowires composite, two prominent peaks corresponding to the -CH_2, and CF_2 group are observed [328]. In PVDF four distinct peaks are observed, each varying with binding energy CH_2 at 284.7, CF_2 at 289.5, F-C-OH at 289, and C-C/C-H at 283.3 eV. In the analysis of PVDF/Ni NWs reveals the existence of CH_2 and CF_2 at B.E of 284.7, and 289.4 eV, respectively. No changes are observed in CH_2; however, slight changes are noted in CF_2 (0.1 eV), indicating a shift towards lower binding energy compared to the values recorded for pure PVDF. A further peak is also observed in the composite film, corresponding to the C-O bond at 287.1 eV [329]. In the O 1s spectra shows in Fig 5.6 (c, d), the main peak for pure PVDF and PVDF/Ni NWs are observed at 530.6 eV and 532.2 eV, confirm the existence of C=O and C-O bonds, respectively. In Fig 5.6 (e), spectra of F 1s for pure PVDF displays a peak at 686.3 eV, which corresponds to F-atoms in the -CF_2- species. In the composite film shown in Fig 5.6 (f), this peak shifts slightly to a higher binding energy of 686.4 eV. This shift is attributed to the chemical interactions between the hydrogen atoms in the -$H\delta^+$-$C\delta^+$-$F\delta^+$- dipoles PVDF and the Π orbitals of PVDF/Ni NWs [330].

The Ni 2p spectrum in Fig 5.6 (g) is split into two spin-orbit doublets of two peaks that are typical of Ni metals and Ni $^{2+}$(NiF_2) corresponding to 876, 859.1, 853.4 eV, and 872.8 respectively. The doublet structure in the Ni 2p spectra seen in Fig 5.6 (h) has binding energies of approximately 859.1 and 876 eV, respectively, and may be attributed to the Ni $2p_{3/2}$ and Ni $2p_{1/2}$ lines. The B.E separation for metallic Nickel is 17.4 eV, while for NiO, it is 18.4 eV, according to the reference spectrum.

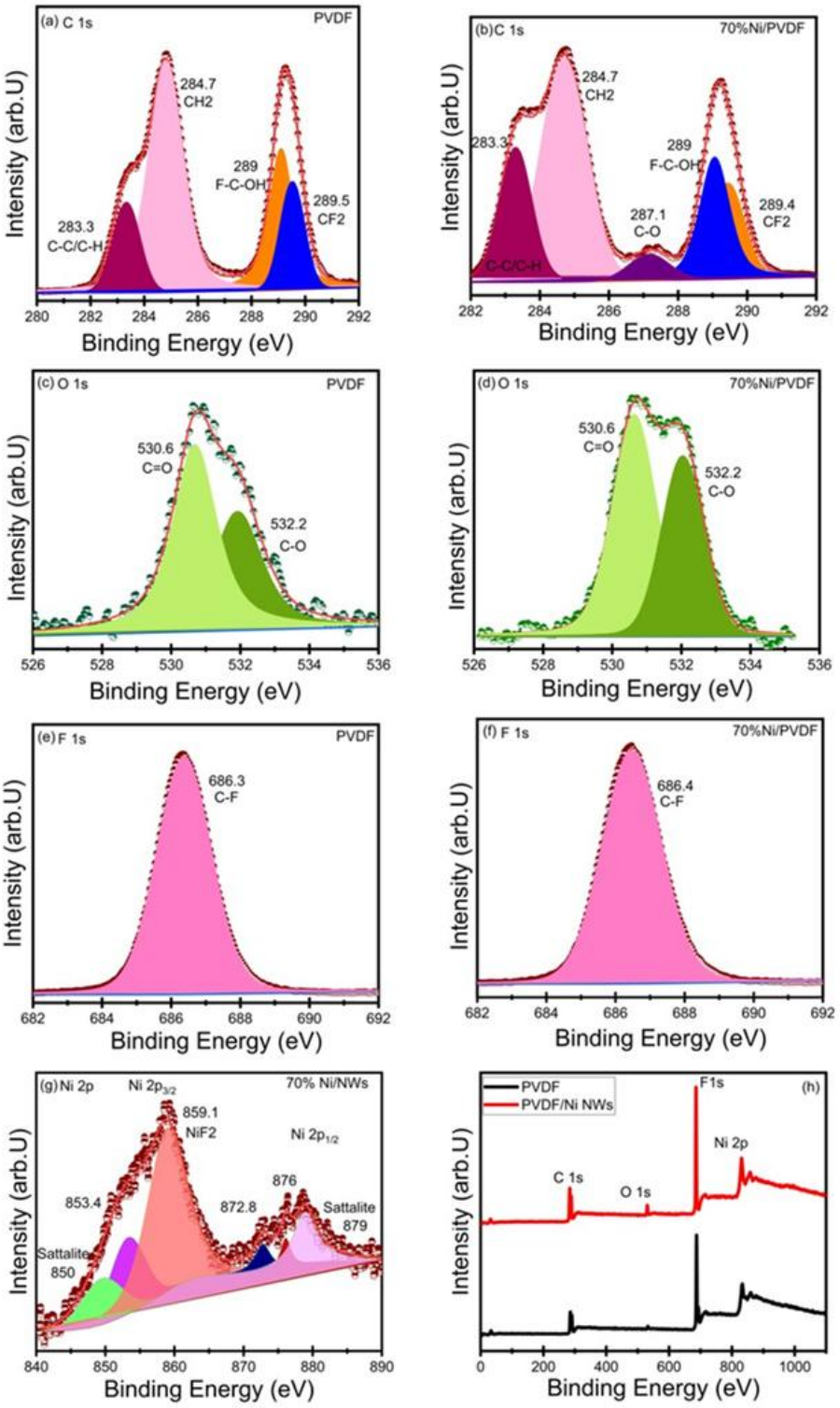

Figure 5.6 X-ray photoelectron spectroscopy (XPS) analysis of pristine PVDF and 70 % Ni NWs/PVDF composite films. (a, b) High-resolution C 1s spectra showing deconvoluted peaks corresponding to CH_2, C-C/C-H, C-O, CF_2 and F-C=O-H functional groups in PVDF and

70%Ni/PVDF, respectively. Indicating the chemical interaction between Ni NWs and PVDF. (c, d) O 1s spectra demonstrating the presence of C=O and C-O bonding in PVDF and 70 %Ni/PVDF. (e, f) F 1s spectra revealing the C-F bonding environment in PVDF and 70%Ni/PVDF. (g) High-resolution Ni 2p spectra of 70%Ni/PVDF showing peaks associated with NiF_2, Ni $2p_{3/2}$, and Ni $2p_{1/2}$, along with satellite peaks, confirming the presence of Ni. (h) Survey spectra of PVDF (black line), identifying the elemental composition (C, O and F) and 70%Ni/PVDF (red line) confirming the presence of Ni in the composite films.

The Ni in the matrix is therefore likely metallic Ni rather than NiO, according to this binding energy difference [331]. The above observation suggests that Ni NWs have successfully substituted in the PVDF matrix. There are two shakeup-type satellite peaks located at around 850 and 879 eV [332]. The results of the XRD also clearly support the presence of Ni NWs. Fig 5.6 (h) show the complete survey spectrum of the PVDF, PVDF/NWs composite film.

5.4.4 ***Thermoelectric properties of PVDF/Ni NWs nanocomposite films***

In comparison to organic conductive polymers, PVDF resin exhibit excellent dielectric properties, restricting the movement of carriers solely to the 3D conductive network formed by conductive fillers. The movement path of carrier under constraints leads to a substantial increase in the sample's volume resistance while successfully achieving a substantial reduction in the Seebeck coefficient. Fig. 5.7 illustrates the relationship between temperature dependence of electronic transport in the PVDF/Ni NWs composites. The measurements were taken 300-400 K, and the composite were prepared with different weight ratios of Ni NWs 30%, 50%, 70%, and 90%. Fig 5.7 (a) when the Ni NWs content in the PVDF/Ni NWs nanocomposite is between 30 wt% to 90 wt%, the Seebeck coefficients are consistently negative. This suggests that the PVDF/Ni NWs nanocomposite exhibit n-type TE behaviour.

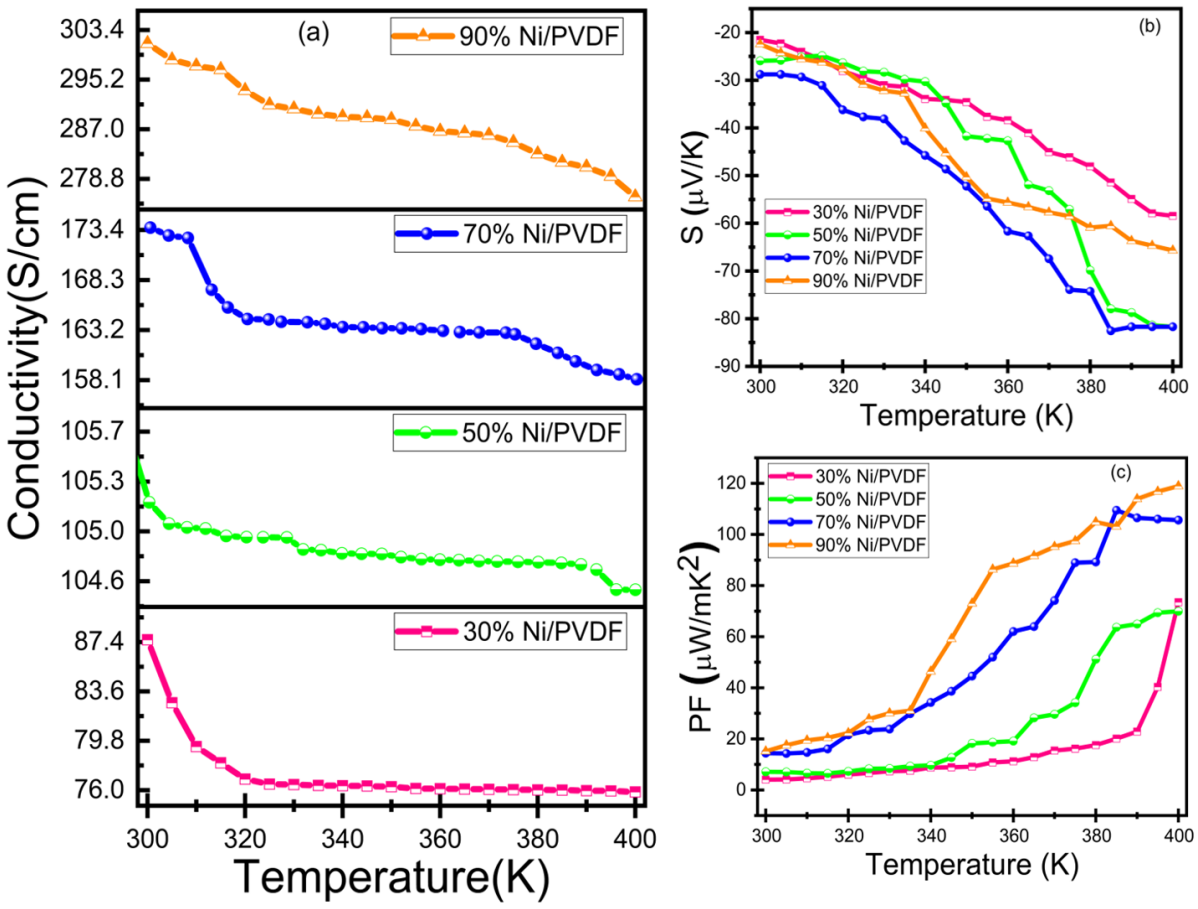

Figure 5.7 Display thermoelectric properties of Ni/PVDF composite films with varying Ni content (30-90 wt.%) as a function of temperature (300-400 K). (a) Electrical conductivity (σ) (b) Seebeck coefficient (S) (c) Power factor

This resembles the S observed in pure nickel. The results indicate that the TE properties of a conductive composite, composed of non-conductive polymer materials and conductive particles, are influenced by the TE properties of the incorporated conductive particles. In addition, the Seebeck coefficient firstly increases than decreases gradually as the amount of Ni NWs increases, which can be attributed to the increasing presence of Nickel nanowires. The S of at (300, 400) K is (-22, -59) μVK^{-1}, (-26, -88)) μVK^{-1}, (-29, -88.1)) μVK^{-1} and (-23, -66) for the β-PVDF/Ni NWs composites with the weight ratio of 30%, 50%, 70%, and 90% respectively. Fig 5.7 (b) illustrates that β-PVDF has a poor σ of 10^{-2} Scm^{-1}. The σ value measured at 300 K for PVDF/Ni NWs composites are 88, 105.2, 173.7, and 301.1 Scm^{-1}, corresponding to weight ratios of 30%,50%,70%, and 90%, respectively. The results demonstrate a clear correlation between

electrical conductivity and the increasing weight ratio of β-PVDF/Ni NWs, indicating an increase in conductivity as the weight ratio increases. The electrical conductivity shows a minor change in relation to temperature range. The observed reduction in σ with increasing temperature is indicative of metallic behavior. The increased electron-phonon scattering within the Ni NWs contributes to this phenomenon, as shown in Fig 5.7b and 5.7c demonstrates the temperature dependence of the power factor ($PF=S^2\sigma$) for the β-PVDF/Ni NWs composites within the temperature range of 300 to 400 K. The PF exhibits an increase correlation of with the increasing concentration of Ni NWs within the β-PVDF/Ni NWs composites. The PF values obtained for the PVDF/Ni NWs composite, with weight % of 30, 50,70, and 90% are (4.4, 73.5), (7.1, 70), (14.3,105.6) and (15.1, 118.9) at temperature of (300, 400k), respectively. The data obtained from multiple research studies are presented in the subsequent sections to compare our findings with those documented in the existing literature. Dun et al. synthesized PVDF/Te nanorod composites exhibiting a thermal conductivity factor of 45.8 $\mu Wm^{-1}K^{-2}$ at ambient temperature. Pammi et al. synthesized composite films of PVDF/Cu_2Se nanowires, achieving a PF of 111 $\mu Wm^{-1}K^{-2}$ at room temperature. Dun et al. synthesized Bi_2Se_3 nanoplate films exhibiting a PF of 103 $\mu Wm^{-1}K^{-2}$. Ju et al. synthesized polyaniline-coated SnSe nanosheet in combination with PVDF, resulting in a PF of 134 $\mu Wm^{-1}K^{-2}$ at a temperature of 400 K. Zhou et al. synthesized PVDF/Ag_2Se NWs film composites exhibiting a PF of 189 $\mu Wm^{-1}K^{-2}$ at ambient temperature. The current investigation reveals that the β-PVDF/Ni NWs composites exhibit a PF of 242 $\mu Wm^{-1}K^{-2}$ at a temperature of 400 K. the observed improvement in the performance factor for PVDF/Ni NWs composites in the present work can be ascribed to the notable increment in the σ of Ni NWs within the composites.

5.4.5 *Thermoelectric Generator (TEG) performance using p-leg PEDOT: PSS and n-leg PVDF/Ni NWs*

The fabrication of a TEG involves the assembly of six pairs of p-type PEDOT: PSS and n-type PVDF/Ni NWs. A TEG demonstration device was constructed utilizing two distinct inks applied to a flexible polyimide substrate showing in Fig 5.8. The output voltage in a relation to the temperature gradient ΔT range from 10 to 35 K. The open circuit voltage resulting from the Seebeck effect demonstrates a linear increase in correlation with the rising temperature gradient ΔT between the hot and cold ends of the thermoelectric module. When the external load resistance

is aligned with the internal resistance, the system achieves its maximum power output (P_{max}) [333]. P_{max} is defined by equation (1).

$$P_{max} = \frac{E^2 R_{ex}}{(R_{ex}+R_{in})^2} \quad (1)$$

The output voltage (mV), denoted as E, is influenced by the external resistance (Ω), represented as $R_{ex,}$ and the internal resistance (Ω) of the fabricated TEG [334].The observed output voltage measures 9.5 mV at a ΔT of 35 K, while the P_{max} recorded is 230 nW, achieved with a load resistance of 100 Ω at ΔT=35 K.

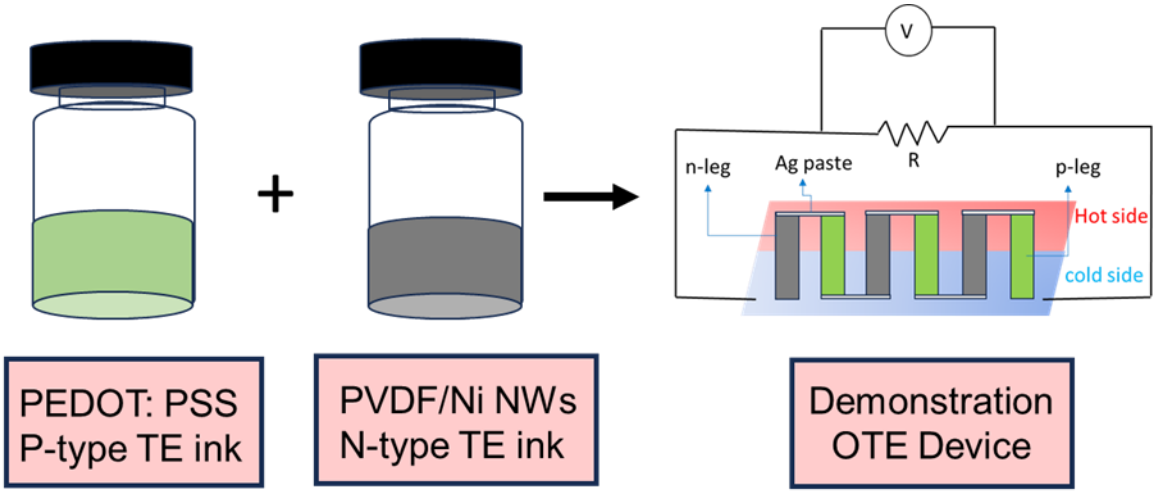

Figure 5.8 Schematic illustration of the material device setup for an organic thermoelectric (OTE) Generator. PEDOT: PSS (p-type TE ink) and PVDF/Ni NWs (n-type TE ink) are used as the active materials, which are integrated into an OTE device with alternating p-typee and n-type legs to generate electricity from a temperature gradient.

5.5 CONCLUSION

In this investigation, we achieved the fabrication of PVDF/Ni NWs composite films incorporating different concentration of Ni NWs at 30 to 90 wt.%. Subsequently, we characterized their thermoelectric properties. Nanosized range Ni NWs was fabricated by hydrothermally method. The films were synthesized through the dispersion of PVDF and Ni NWs in a suitable solvent, subsequently undergoing a drying process to yield uniform composite films. The characterization indicated that the Ni NWs exhibited a uniform dispersion within the PVDF matrix, thereby establishing a conductive network essential for the improvement of TE performance. The XRD

and FTIR analysis validate the existence of both α and β phases within the PVDF matrix, with Ni NWs predominating in the composite. Details on the chemical states and interactions in the composite were revealed by XPS characterisation. The increase of Ni NWs content led to an improvement in σ and a subsequent improvement in the PF, attributed to the inherent conductive properties of Ni NWs. The Seebeck coefficient consistently exhibited negative values, signifying n- type behavior throughout all composite materials analyzed. The measurements of σ and S indicated that a rise in Ni NWs content resulted in enhanced σ. Conversely, a slight decrement in the S was observed at increased Ni concentrations. The observed PF values exhibited notable enhancements, particularly at elevated concentrations of Ni NWs, achieving 242 $\mu Wm^{-1}K^{2}$ at 400 K. this value exceeds that of numerous previously documented PVDF-based composites. In conclusion, we successfully demonstrated a TEG device that incorporates p-leg PEDOT: PSS and n-leg PVDF/Ni NWs composites. The apparatus demonstrated a P_{max} of 230 nW at temperature 35 K. The findings of this investigations indicate that PVDF/Ni NWs composites exhibit significant promise as materials for TE applications, suggesting their potential utility in the development of flexible energy harvesting devices.

Chapter 6. **CONCLUSION AND FUTURE SCOPE**

6.1 **CONCLUSION**

This comprehensive investigation highlights the notable progress made in improving Thermoelectric (TE) performance by the fabrication of novel organic-inorganic composite materials. The investigations examined a variety of systems, such as PEDOT: PSS/Bi_2Te_3, PEDOT: PSS/ Bi_2Te_3/rGO ternary composites, $FeCl_3$-doped P_3HT films, and Ni NWs incorporated PVDF films. Each composite exhibited significant enhancements in crucial thermoelectric parameters, electrical conductivity, Seebeck coefficient, and power factor, while preserving flexibility and scalability for practical applications. The incorporation of Bi_2Te_3 in the PEDOT: PSS composites significantly improved the Seebeck coefficient and electrical conductivity, attributed to structural reorganization and energy filtering effects. The incorporation of rGO into PEDOT: PSS/ Bi_2Te_3 matrix enhanced charge transport, resulting in an impressive power factor of 93.16 $\mu Wm^{-1}K^{-2}$. In a similar manner, the incorporation of $FeCl_3$ into P_3HT films showcased the ability of targeted doping to markedly enhance TE performance. The P40 samples demonstrated an ideal combination of elevated electrical conductivity (46.67 Scm^{-1}) and a Seebeck coefficient of 164.9 μVK^{-1}. Conversely, excessive doping led to diminished performance, highlighting the critical need for meticulous control of dopant levels.

The incorporation of Ni NWs within PVDF matrix presents a promising direction for n-type thermoelectric materials. Ni NWs functioned as efficient conductive networks, improving electrical conductivity while preserving mechanical flexibility. The composite with the highest performance, containing 70 wt.% Ni NWs, demonstrated a Seebeck coefficient of -88 μVK^{-1} and achieved a power factor of 242 $\mu Wm^{-1}K^{-2}$ at a temperature of 400 K. the integration of these materials into a flexible thermoelectric generators demonstrates their potential for energy harvesting from waste heat in wearable and adaptable electronic systems.

These studies collectively show the potential of hybrid organic-inorganic materials to overcome the limitations of traditional TE materials, including brittleness and elevated thermal conductivity. Optimising material composition and utilizing nanoscale interactions resulted in enhanced TE

properties while maintaining advantageous attributes such as low weight, flexibility, and environmental sustainability.

6.2 FUTURE SCOPE

Composite materials for TE applications demonstrate considerable potential for enhancing energy efficiency. Advanced doping strategies and molecular engineering have the potential to further improve efficiency. Multilayered or gradient architectures provide precise control over thermal and electrical properties, facilitating the development of customized devices for applications including wearable electronics and self-powered sensors. Studies on long-term stability, mechanical durability, and environmental performance are essential for practical applications.
Enhancing synthesis methods for economical industrial production will expedite their shifts from experimental works to practical applications. These lightweight, flexible materials hold great potential for advancing energy harvesting, waste heat recovery, and sustainable technologies, developing the stage for effective and scalable thermoelectric solutions.

BIBLIOGRAPHY

[1] Y, Lee, D.-Y. Jo, T. Kim, J.-H. Jo, J. Park, H. Yang, D.J. Kim, 'Interfaces, Effectual interface and defect engineering for auger recombination suppression in bright InP/ZnSeS/ZnS' *quantum dots*, vol. 14, pp. 12479-12487, 2022, doi: https://doi.org/10.1021/acsami.1c20088.

[2] L. Zhang, B. Xia, X.-L. Shi, W.-D. Liu, Y. Yang, 'Achieving high thermoelectric properties in PEDOT: PSS/SWCNTs composite films by a combination of dimethyl sulfoxide doping and NaBH4 dedoping', *Carbon*, vol. 196, pp. 718-726, 2022, doi: https://doi.org/10.1016/j.carbon.2022.05.043.

[3] E.J. Motoasca, 'Environments, Energy sustainability through the use of thermoelectric materials in waste heat recovery systems recent developments and challenges', (2019) 237-254, https://doi.org/10.1007/978-981-13-3284-5_11.

[4] H. Wang, C. Yu, 'Organic Thermoelectrics: Materials Preparation, Performance Optimization, and Device Integration', *Joule 3*, (2019) pp. 53-80, DOI: 10.1016/j.joule.2018.10.012.

[5] G.J. Snyder, E.S. Toberer, 'Complex thermoelectric materials, *Nature Materials'*, vol. 7 (2008), pp. 105-114, https://doi.org/10.1038/nmat2090.

[6] S. Lal, D. Gautam, K.M. Razeeb, 'Fabrication of micro-thermoelectric devices for power generation and the thermal management of photonic devices', *Journal of Micromechanics and Microengineering*, vol 29 (2019), pp. 065015, DOI 10.1088/1361-6439/ab18f1.

[7] R.D. Dharmasena, K.D. Jayawardena, Z. Saadi, X. Yao, R.M.I. Bandara, 'Energy Scavenging and Powering E-Skin Functional Devices', *Proceedings of the IEEE.*, vol. 107 (2019), pp. 2118-2136, DOI: 10.1109/JPROC.2019.2929286.

[8] M.H. Malakooti, N. Kazem, J. Yan, C. Pan, E.J. Markvicka, K. Matyjaszewski, C. Majidi, 'Liquid Metal Supercooling for Low-Temperature Thermoelectric Wearables', *Advanced Functional Materials*, vol. 29, pp. 1906098, 2019, doi: https://doi.org/10.1038/s41467-022-29773-9.

[9] S.J. Chen, Y.C. Wu, 'Active Thermoelectric Vacuum Sensor Based on Frequency Modulation', *Micromachines*,vol. 11, pp. 15, 2020, doi: https://doi.org/10.3390/mi11010015.

[10] D. Newell, M. Duffy, 'Review of Power Conversion and Energy Management for Low-Power, Low-Voltage Energy Harvesting Powered Wireless Sensors', *IEEE Transactions on Power Electronics.*, vol. 34 (2019), pp. 9794-9805, DOI: 10.1109/TPEL.2019.2894465.

[11] T.J. Seebeck, 'Ueber den Magnetismus der galvanischen Kette', 1822.

[12] J.C.A. Peltier, 'Nouvelles expériences sur la caloricité des courans électriques', *Ann Chem Phys,* 1834.

[13] W. Thomson, ‘On a Mechanical Theory of Thermo-Electric Currents’, *Proceedings of the Royal Society of Edinburgh 3.*, vol. (1857), pp. 91-98, https://doi.org/10.1017/S0370164600027310.

[14] M.S. Dresselhaus, G. Chen, M.Y. Tang, R.G. Yang, H. Lee, D.Z. Wang, Z.F. Ren, J.P. Fleurial, P. Gogna, ‘New Directions for Low-Dimensional Thermoelectric Materials’, *Advanced Materials*, vol. 19, pp. 1043-1053, 2007, doi: https://doi.org/10.1002/adma.200600527.

[15] L, Pan, X.L. Shi, C. Song, W.D. Liu, Q. Sun, C. Lu, Q. Liu, Y. Wang, Z.G.J.A.F.M. Chen, ‘Graphite Nanosheets as Multifunctional Nanoinclusions to Boost the Thermoelectric Performance of the Shear-Exfoliated Bi2O2Se’, *Advanced Functional materials*, vol. 32, pp. 2202927, 2022, doi: https://doi.org/10.1002/adfm.202202927.

[16] Q, X. Hu, W.-D. Liu, L. Zhang, W. Sun, H. Gao, X.L. Shi, Y.-L. Yang, Q. Liu, Z.G. Chen, ‘SWCNTs/Ag2Se film with superior bending resistance and enhanced thermoelectric performance via in situ compositing’, C*hemical Engineering Journal*, vol. 457, pp. 141024, 2023, doi: https://doi.org/10.1016/j.cej.2022.141024.

[17] X, Y. Mao, X.L. Shi, L.C. Zhai, W. D. Liu, Y.X. Chen, H. Gao, M. Li, D. Z. Wang, H. Wu, Z.H. Zheng, ‘Technology, High thermoelectric and mechanical performance in the n-type polycrystalline SnSe incorporated with multi-walled carbon nanotubes’, *Journal of Materials Science & technology*, vol. 114, pp. 55-61, 2022, doi: https://doi.org/10.1016/j.jmst.2021.12.002.

[18] M. Vedernikov, E. Iordanishvili, ‘AF Ioffe and origin of modern semiconductor thermoelectric energy conversion’, *Seventeenth International Conference on Thermoelectrics Proceedings ICT98 (Cat. No. 98TH8365), IEEE.*, 1998, pp. 37-42, DOI: 10.1109/ICT.1998.740313.

[19] L, Deng, Y. Liu, Y. Zhang, S. Wang, P.J. Gao, ‘Organic Thermoelectric Materials: Niche Harvester of Thermal Energy’, *Advanced Functional Materials*, vol. 33, pp. 2210770, 2023, doi: https://doi.org/10.1002/adfm.202210770.

[20] Y. Liu, J. Zhi, W. Li, Q. Yang, L. Zhang, Y.J.M. Zhang, Oxide materials for thermoelectric conversion, *Molecules*, 28 (2023) 5894. https://doi.org/10.3390/molecules28155894

[21] F, Ali, M.J.P. Koc, ‘3D Printed Polymer Piezoelectric Materials: Transforming Healthcare through Biomedical Applications’, *Polymers*, vol. 15, pp. 4470, 2023, doi: https://doi.org/10.3390/polym15234470.

[22] X. Li, C. Wan, T. Tao, H. Chai, Q. Huang, Y. Chai, Y.J. Wu, ‘An overview of the development status and applications of cellulose-based functional materials’, *Cellulose*, (2023) 1-39, https://doi.org/10.1007/s10570-023-05616-8.

[23] A.K. Katiyar, A.T. Hoang, D. Xu, J. Hong, B.J. Kim, ‘2D Materials in Flexible Electronics: Recent Advances and Future Prospectives’, /Chemical Reviews (2023), https://doi.org/10.1021/acs.chemrev.3c00302.

[24] A, M.J.P. Al-Amri, 'Recent Progress in Printed Photonic Devices: A Brief Review of Materials, Devices, and Applications', *Polymers*,vol. 15, pp. 3234, 2023, doi: https://doi.org/10.3390/polym15153234.

[25] C. Goupil, W. Seifert, K. Zabrocki, E. Müller, G. Snyder, 'Thermodynamics of Thermoelectric Phenomena and Applications', *Entropy.*, vol. 13, pp. 1481-1517, 2011 https://doi.org/10.3390/e13081481.

[26] M. Cutler, J.F. Leavy, R.L. Fitzpatrick, Electronic Transport in Semimetallic Cerium Sulfide, *Physical Review*., vol. 133, pp. A1143-A1152, 1964, https://doi.org/10.1103/PhysRev.133.A1143.

[27] Y. Wang, J. Zhou, R. Yang, 'Thermoelectric Properties of Molecular Nanowires', *The Journal of Physical Chemistry C*., vol. 115, pp. 24418-24428, 2011, https://doi.org/10.1021/jp208490q.

[28] V. Coropceanu, J. Cornil, D.A. da Silva Filho, Y. Olivier, R. Silbey, J.L. Brédas, 'Charge Transport in Organic Semiconductors', *Chemical Reviews., vol.* 107, pp. 926-952, 2007, https://doi.org/10.1021/cr050140x.

[29] R. Franz, G. Wiedemann, 'Ueber die Wärme-Leitungs fähigkeit der Metalle', vol. 165, pp. 497-531, 1853. https://doi.org/10.1002/andp.18531650802

[30] C. Kittel, P. McEuen, 'Introduction to solid state physics', *John Wiley & Sons*, 2018.

[31] T. Park, C. Park, B. Kim, H. Shin, E. Kim, 'Flexible PEDOT electrodes with large thermoelectric power factors to generate electricity by the touch of fingertips, *Energy & Environmental Science',* vol. 6, pp. 788-792, 2016, https://doi.org/10.1039/C3EE23729J.

[32] M.B. Salamon, J.W. Bray, G. DePasquali, R.A. Craven, G. Stucky, A. Schultz, 'Thermal conductivity of tetrathiafulvalene-tetracyanoquinodimethane (TTF-TCNQ) near the metal-insulator transition', *Physical Review B,* vol. 11, pp. 619-622, 1975, https://doi.org/10.1103/PhysRevB.11.619.

[33] J. Liu, X. Wang, D. Li, N.E. Coates, R.A. Segalman, D.G. Cahill, 'Thermal Conductivity and Elastic Constants of PEDOT: PSS with High Electrical Conductivity', *Macromolecules., vol.* 48, pp. 585-591, 2015, https://doi.org/10.1021/ma502099t.

[34] A. Weathers, Z.U. Khan, R. Brooke, D. Evans, M.T. Pettes, J.W. Andreasen, X. Crispin, L. Shi, 'Significant Electronic Thermal Transport in the Conducting Polymer Poly(3,4-ethylenedioxythiophene)', *Advanced Materials*, vol. 27, pp. 2101-2106, 2015.

[35] M. Pietralla, 'High thermal conductivity of polymers: Possibility or dream', *Journal of Computer-Aided Materials Design*., vol. 3, pp. 273-280, 1996, https://doi.org/10.1007/BF01185664.

[36] N.G. Semaltianos, C. Koidis, C. Pitsalidis, P. Karagiannidis, S. Logothetidis, W. Perrie, D. Liu, S.P. Edwardson, E. Fearon, R.J. Potter, G. Dearden, K.G. Watkins, 'Picosecond laser

patterning of PEDOT: PSS thin films', *Synthetic Metals.*, vol. 161, pp. 431-439, 2011, https://doi.org/10.1016/j.synthmet.2010.12.022.

[37] R. Cagnolati, D. Fioretto, G. Ruggeri, G. Socino, 'Elastic characterization of poly (3-n. decylpyrrole) thin films by Brillouin light scattering', *Synthetic Metals.*, vol. 60, pp. 255-258, 1993, https://doi.org/10.1038/s41467-022-29773-9.

[38] D. Moses, A. Denenstein, 'Experimental determination of the thermal conductivity of a conducting polymer: Pure and heavily doped polyacetylene', *Physical Review B*, vol. 30, pp. 2090-2097, 1994, https://doi.org/10.1103/PhysRevB.30.2090.

[39] J, Jin, M.P. Manoharan, Q. Wang, M.A. Haque, 'In-plane thermal conductivity of nanoscale polyaniline thin films', *Applied Physics Letters*, vol. 95, pp. 033113, 2009, doi: https://doi.org/10.1103/PhysRevB.30.2090.

[40] J.P. Heremans, V. Jovovic, E.S. Toberer, A. Saramat, K. Kurosaki, A. Charoenphakdee, S. Yamanaka, G.J. Snyder, 'Enhancement of thermoelectric efficiency in PbTe by distortion of the electronic density of states, *Science (New York, N.Y.)*., vol. 321. pp. 554-557, 2008, DOI: 10.1126/science.1159725.

[41] H. Ohta, S. Kim, Y. Mune, T. Mizoguchi, K. Nomura, S. Ohta, T. Nomura, Y. Nakanishi, Y. Ikuhara, M. Hirano, H. Hosono, K. Koumoto, 'Giant thermoelectric Seebeck coefficient of a two-dimensional electron gas in SrTiO3', *Nature Materials*, vol. 6, pp. 129-134, 2007, https://doi.org/10.1038/nmat1821.

[42] P, Reddy, S.-Y. Jang, R.A. Segalman, A. Majumdar, 'Thermoelectricity in Molecular Junctions', *Science*, vol. 315, pp. 1568-1571, 2007, doi: 10.1126/science.1137149.

[43] J, N. Coleman, M. Lotya, A. O'Neill, S.D. Bergin, P.J. King, U. Khan, K. Young, A. Gaucher, S. De, R.J. Smith, I.V. Shvets, S.K. Arora, G. Stanton, H.-Y. Kim, K. Lee, G.T. Kim, 'Two-Dimensional Nanosheets Produced by Liquid Exfoliation of Layered Materials', *Science*, vol. 331, pp. 568-571, 2011, doi: 10.1126/science.1194975.

[44] L. Shi, D. Li, C. Yu, W. Jang, D. Kim, Z. Yao, P. Kim, A. Majumdar, 'Measuring Thermal and Thermoelectric Properties of One-Dimensional Nanostructures Using a Microfabricated Device', *Journal of Heat Transfer.*, vol. 125, pp. 881-888, 2003, https://doi.org/10.1115/1.1597619.

[45] D. Vashaee, A. Shakouri, Improved Thermoelectric Power Factor in Metal-Based Superlattices, *Physical Review Letters.*, vol. 92, pp. 106103, 2004, https://doi.org/10.1103/PhysRevLett.92.106103.

[46] A.I. Boukai, Y. Bunimovich, J. Tahir-Kheli, J.-K. Yu, W.A. Goddard Iii, J.R. Heath, 'Silicon nanowires as efficient thermoelectric materials', *Nature*, vol. 451, pp. 168-171, 2008, https://doi.org/10.1038/nature06458.

[47] J. Tang, H.-T. Wang, D.H. Lee, M. Fardy, Z. Huo, T.P. Russell, P. Yang, 'Holey Silicon as an Efficient Thermoelectric Material', *Nano Letters.*, vol.10, pp. 4279-4283, 2010, https://doi.org/10.1021/nl102931z.

[48] Q. Zhang, Y. Sun, W. Xu, D. Zhu, 'Conducting Polymers on the Playground of Thermoelectricity: Lessons Learned from Four High-Mobility Polymeric Semiconductors', *Macromolecules.*, vol.47. pp. 609-615, 2014, https://doi.org/10.1021/ma4020406.

[49] Y. Chen, Y. Zhao, Z. Liang, 'Solution processed organic thermoelectrics: towards flexible thermoelectric modules, *Energy & Environmental Science'* vol. 8, pp. 401-422, 2008, DOI https://doi.org/10.1039/C4EE03297G.

[50] R. Prasad, S. Bhame, 'Review on texturization effects in thermoelectric oxides, *Materials for Renewable and Sustainable Energy'* vol. 9 (2020), https://doi.org/10.1007/s40243-019-0163-y.

[51] Q, Yan, M.G. Kanatzidis, 'High-performance thermoelectrics and challenges for practical devices',*Nature Materials*, vol. 21, pp. 503-513, 2022, doi: https://doi.org/10.1038/s41563-021-01109-w.

[52] A, P. Kythreotis, C. Howarth, T.G. Mercer, H. Awcock, A.E.B.A. Jonas, 'Re-evaluating the changing geographies of climate activism and the state in the post-climate emergency era in the build-up to COP26', *Journal of British Academy*, vol. 9, pp. 69-93, 2021, doi: https://doi.org/10.5871/jba/009s5.069.

[53] V. Rathi, R. Brajpuriya, R. Gupta, K. Parmar, A. Kumar, 'Graphene-derived composites: a new Frontier in thermoelectric energy conversion', Energy Advances, vol. 3, pp. 389-4124, DOI: 10.1039/D3YA00526G.

[54] K. Jaroszewska, B. Szczęśniak, B. Szyja, J. Choma, M.J.M.T. Jaroniec, 'Inorganic mesoporous oxides: From research to industrial applications', *Materials Today* (2023), https://doi.org/10.1016/j.mattod.2023.11.017.

[55] B.G. Krishna, D.S. Ghosh, S.J. Tiwari, 'Hole and electron transport materials: A review on recent progress in organic charge transport materials for efficient, stable, and scalable perovskite solar cells' *Chemistry of Inorganic Materials*, (2023) 100026, https://doi.org/10.1016/j.cinorg.2023.100026.

[56] T, Tracy, L. Wu, X. Liu, S. Cheng, X.J. Li, 3D 'printing: Innovative solutions for patients and pharmaceutical industry', *International Journal of Pharmaceutics* vol. 631, pp. 122480, 2023, https://doi.org/10.1016/j.ijpharm.2022.122480.

[57] K, Balasubramanian, A.K. Pandey, R. Abolhassani, H.-G. Rubahn, S. Rahman, Y.K. Mishra, 'Tetrapods based engineering of organic phase change material for thermal energy storage', *Chemical Engineering Journal*, vol. 462, pp. 141984, 2023, doi: https://doi.org/10.1016/j.cej.2023.141984.

[58] Z, H. Zheng, X.L. Shi, D.W. Ao, W.D. Liu, M. Li, L.Z. Kou, Y.X. Chen, F. Li, M. Wei, 'Harvesting waste heat with flexible Bi2Te3 thermoelectric thin film', *Nature Sustainability*, vol. 6, pp. 180-191, 2023, doi: https://doi.org/10.1038/s41893-022-01003-6.

[59] S, Lan, Q. Li, X. Guo, S. Wang, R.J.E. Chen, Fuel saving potential analysis of bifunctional vehicular waste heat recovery system using thermoelectric generator and organic Rankine cycle, *Energy*, vol. 263, pp. 125717, 2023, https://doi.org/10.1016/j.energy.2022.125717.

[60] M. Asaduzzaman, M.H. Ali, N.A. Pratik, N.J. Lubaba, M. X, 'Exhaust Heat Harvesting of Automotive Engine Using Thermoelectric Generation Technology' *Energy Conversion and Management: X*, pp. 100398, 2023, https://doi.org/10.1016/j.ecmx.2023.100398.

[61] J, Caban, J. Vrabel, D. Górnicka, R. Nowak, M. Jankiewicz, J. Matijošius, M.J.E. Palka, 'Overview of Energy Harvesting Technologies Used in Road Vehicles', *Energies* vol. 16, pp. 3787, 2023, https://doi.org/10.3390/en16093787.

[62] P. Judeinstein, C.J. Sanchez, 'Hybrid organic–inorganic materials: a land of multidisciplinarity', *Journal of Materials Chemistry*, vol. 6, pp. 511-525, 1996, DOI https://doi.org/10.1039/JM9960600511.

[63] X, L. Shi, J. Zou, Z. Chen, 'Advanced thermoelectric design: from materials and structures to devices', Chemical Reviews, vol. 120, pp. 7399-7515, 2020, doi: https://doi.org/10.1021/acs.chemrev.0c00026.

[64] Y, Sun, C.A. Di, W. Xu, D.J. Zhu, 'Advances in n-type organic thermoelectric materials and devices', *Advanced Electronic Materials* vol. 5, pp. 1800825, 2019, doi: https://doi.org/10.1002/aelm.201800825.

[65] Y.H. Pai, J. Tang, Y. Zhao, Z.J.A.E.M. Liang, Ionic Organic Thermoelectrics with Impressively High Thermopower for Sensitive Heat Harvesting Scenarios', *Advanced Energy Materials* 'vol.13, pp. 2202507, 2023, https://doi.org/10.1002/aenm.202202507.

[66] B, N.J. Stram, 'Key challenges to expanding renewable energy', *Energy Policy* ,vol. 96, pp. 728-734, 2016, https://doi.org/10.1016/j.enpol.2016.05.034.

[67] Q, Zhang, Y. Sun, W. Xu, D.J. Zhu, 'Organic thermoelectric materials: emerging green energy materials converting heat to electricity directly and efficiently', *Advanced Materials*, vol. 26, pp. 6829-6851, 2014, https://doi.org/10.1002/adma.201305371.

[68] L. Wang, Q. Yao, H. Bi, F. Huang, Q. Wang, L. Chen, 'Large thermoelectric power factor in polyaniline/graphene nanocomposite films prepared by solution-assistant dispersing method', *Journal of Materials Chemistry A.*, vol. 2, pp. 11107-11113, 2014 DOI: https://doi.org/10.1039/C4TA01541J.

[69] T. Ube, J. Koyanagi, T. Kosaki, K. Fujimoto, T. Yokozeki, T. Ishiguro, K. Nishio, 'Fabrication of well-isolated graphene and evaluation of thermoelectric performance of polyaniline–graphene composite film', *Journal of Materials Science.*, vol. 54, pp. 3904-3913, 2019, https://doi.org/10.1007/s10853-018-3129-z

[70] H, Wang, J.H. Hsu, S.I. Yi, S.L. Kim, K. Choi, G. Yang, C. Yu, 'Thermally Driven Large N-Type Voltage Responses from Hybrids of Carbon Nanotubes and Poly(3,4-ethylenedioxythiophene) with Tetrakis(dimethylamino)ethylene', *Advanced Materials* vol. 27, pp. 6855-6861, 2015, doi: https://doi.org/10.1002/adma.201502950.

[71] C, Cho, K.L. Wallace, P. Tzeng, J.H. Hsu, C. Yu, J.C. Grunlan, 'Outstanding Low Temperature Thermoelectric Power Factor from Completely Organic Thin Films Enabled by Multidimensional Conjugated Nanomaterials', *Advanced Energy Materials* vol. 6, pp. 1502168, 2016, doi: https://doi.org/10.1002/aenm.201502168.

[72] D. Kim, Y. Kim, K. Choi, J.C. Grunlan, C. Yu, 'Improved Thermoelectric Behavior of Nanotube-Filled Polymer Composites with Poly(3,4-ethylenedioxythiophene) Poly(styrenesulfonate)', *ACS Nano.*, vol. 4, pp. 513-523, 2010, https://doi.org/10.1021/nn9013577.

[73] C. Yu, Y.S. Kim, D. Kim, J.C. Grunlan, 'Thermoelectric behavior of segregated-network polymer nanocomposites', *Nano letters.*, vol. 8, pp. 4428-4432, 2008, https://doi.org/10.1021/nl802345s.

[74] B. Abad, I. Alda, P. Díaz-Chao, H. Kawakami, A. Almarza, D. Amantia, D. Gutierrez, L. Aubouy, M. Martín-González, 'Improved power factor of polyaniline nanocomposites with exfoliated graphene nanoplatelets (GNPs)', *Journal of Materials Chemistry A.*, vol.1, pp. 10450-10457, 2013, https://doi.org/10.1038/s41467-022-29773-9.

[75] K. Zhang, Y. Zhang, S. Wang, 'Enhancing thermoelectric properties of organic composites through hierarchical nanostructures', *Scientific Reports.*, vol. 3, pp. 3448, 2013, https://doi.org/10.1038/srep03448.

[76] Y. Lu, Y. Song, F. Wang, 'Thermoelectric properties of graphene nanosheets-modified polyaniline hybrid nanocomposites by an in situ chemical polymerization', *Materials Chemistry and Physics.*, vol.138, pp. 238-244, 2013, https://doi.org/10.1016/j.matchemphys.2012.11.052.

[77] K, Zhang, Y. Zhang, S.J. Wang, 'Enhancing thermoelectric properties of organic composites through hierarchical nanostructures', *Scientific Reports*, vol. 3, pp. 3448, 2013, doi: https://doi.org/10.1038/srep03448.

[78] G.H. Kim, D.H. Hwang, S.I. Woo, 'Thermoelectric properties of nanocomposite thin films prepared with poly (3, 4-ethylenedioxythiophene) poly (styrenesulfonate) and graphene', *Physical Chemistry Chemical Physics* vol.14, pp. 3530-3536, DOI https://doi.org/10.1039/C2CP23517J.

[79] D, Yoo, J. Kim, J.H. Kim, 'Direct synthesis of highly conductive poly (3, 4-ethylenedioxythiophene): poly (4-styrenesulfonate)(PEDOT: PSS)/graphene composites and their applications in energy harvesting systems, *Nano Research* vol. 7, pp. 717-730, 2014, doi: https://doi.org/10.1007/s12274-014-0433-z.

[80] J, Xiang, L.T.J.P. Drzal, 'Templated growth of polyaniline on exfoliated graphene nanoplatelets (GNP) and its thermoelectric properties', *Journal of Polymer Research*, vol. 53, pp. 4202-4210, 2012, doi: https://doi.org/10.1016/j.polymer.2012.07.029.

[81] Y, Du, S.Z. Shen, W. Yang, R. Donelson, K. Cai, P.S. Casey, 'Simultaneous increase in conductivity and Seebeck coefficient in a polyaniline/graphene nanosheets thermoelectric nanocomposite', *Synthetic Metals* vol. 161, pp. 2688-2692, 2012, doi: https://doi.org/10.1016/j.synthmet.2011.09.044.

[82] G. Decher, ''Multilayer Thin Films: Sequential Assembly of Nanocomposite Materials, 2003, pp. 1-46.

[83] D. Zhang, Y. Mao, P. Bai, Q. Li, W. He, H. Cui, F. Ye, C. Li, R. Ma, Y. Chen, 'Multifunctional Superelastic Graphene-Based Thermoelectric Sponges for Wearable and Thermal Management Devices', *Nano Letters*., vol. 22, pp. 3417-3424, 2022, https://doi.org/10.1021/acs.nanolett.2c00696.

[84] Y. Du, S.Z. Shen, W. Yang, R. Donelson, K. Cai, P.S. Casey, 'Simultaneous increase in conductivity and Seebeck coefficient in a polyaniline/graphene nanosheets thermoelectric nanocomposite, *Synthetic Metals* vol. 161, pp. 2688-2692, 2012, https://doi.org/10.1016/j.synthmet.2011.09.044.

[85] K. Zhang, Y. Zhang, S. Wang, 'Enhancing thermoelectric properties of organic composites through hierarchical nanostructures', *Scientific Reports*., vol. 3, 2013, https://doi.org/10.1038/srep03448.

[86] C, Cho, B. Stevens, J.-H. Hsu, R. Bureau, D.A. Hagen, O. Regev, C. Yu, J.C. Grunlan, 'Completely Organic Multilayer Thin Film with Thermoelectric Power Factor Rivaling Inorganic Tellurides', *Advanced Materials,* vol. 27, pp. 2996-3001, 2015, doi: https://doi.org/10.1002/adma.201405738.

[87] G.H. Kim, D.H. Hwang, S.I. Woo, 'Thermoelectric properties of nanocomposite thin films prepared with poly(3,4-ethylenedioxythiophene) poly(styrenesulfonate) and graphene', *Physical Chemistry Chemical Physics*, vol. 14, pp. 3530-3536, 2012, DOI https://doi.org/10.1039/C2CP23517J.

[88] J. Xiang, L.T. Drzal, 'Templated growth of polyaniline on exfoliated graphene nanoplatelets (GNP) and its thermoelectric properties', *Polymer*., vol. 53 pp. 4202-4210, 2012, https://doi.org/10.1016/j.polymer.2012.07.029.

[89] S.H. H. wang, H.W. Park, Y.B. Park, 'Piezoresistive behavior and multi-directional strain sensing ability of carbon nanotube–graphene nanoplatelet hybrid sheets', *Smart Materials and Structures.*, vol. 22, pp. 015013, 2012, DOI 10.1088/0964-1726/22/1/015013.

[90] H.X. Kong, 'Hybrids of carbon nanotubes and graphene/graphene oxide', *Current Opinion in Solid State and Materials Science*., vol. 17, pp. 31-37, 2013, https://doi.org/10.1016/j.cossms.2012.12.002.

[91] W, Li, D. He, J. Bai, 'The influence of nano/micro hybrid structure on the mechanical and self-sensing properties of the carbon nanotube-microparticle reinforced epoxy composites', *Composites Part A: Applied Science and Manufacturing*, vol. 54, pp. 28-36, 2013, doi: https://doi.org/10.1016/j.compositesa.2013.07.002.

[92] Q. Wang, Q. Yao, J. Chang, L. Chen, 'Enhanced thermoelectric properties of CNT/PANI composite nanofibers by highly orienting the arrangement of polymer chains', *Journal of Materials Chemistry.*, vol. 22, pp. 17612-17618, 2012, https://doi.org/10.1039/C2JM32750C.

[93] D. Yoo, J. Kim, J.H. Kim, 'Direct synthesis of highly conductive poly(3,4-ethylenedioxythiophene): poly(4-styrenesulfonate) (PEDOT: PSS)/graphene composites and their applications in energy harvesting systems', *Nano Research.*, vol.7, pp. 717-730, 2014, https://doi.org/10.1007/s12274-014-0433-z.

[94] Y. Du, S.Z. Shen, W.D. Yang, K.F. Cai, P.S. Casey, 'Preparation and characterization of multiwalled carbon nanotube/poly(3-hexylthiophene) thermoelectric composite materials', *Synthetic Metals.*, vol. 162, pp. 375-380, 2012, https://doi.org/10.1016/j.synthmet.2011.12.023.

[95] Y, Du, J. Li, J. Xu, P. Eklund, 'Thermoelectric Properties of Reduced Graphene Oxide/Bi2Te3 Nanocomposites', *Energies*, vol. 12, pp. 2430, 2019, doi: https://doi.org/10.3390/en12122430.

[96] J. Dong, W. Liu, H. Li, X. Su, X. Tang, C. Uher, 'In situ synthesis and thermoelectric properties of PbTe–graphene nanocomposites by utilizing a facile and novel wet chemical method', *Journal of Materials Chemistry A.*, vol.1, pp. 12503-12511, 2013, https://doi.org/10.1039/C3TA12494K.

[97] H. Ju, M. Kim, J. Kim, 'A facile fabrication of n-type Bi2Te3 nanowire/graphene layer-by-layer hybrid structures and their improved thermoelectric performance', *Chemical Engineering Journal*., vol. 275, pp.102-112, 2012, https://doi.org/10.1016/j.cej.2015.04.042.

[98] K. Agarwal, V. Kaushik, D. Varandani, A. Dhar, B.R. Mehta, 'Nanoscale thermoelectric properties of Bi2Te3 – Graphene nanocomposites: Conducting atomic force, scanning thermal and kelvin probe microscopy studies', *Journal of Alloys and Compounds*., vol. 681, pp.394-401, 2016.

[99] S. Kumar, S. Singh, P.K. Dhawan, R.R. Yadav, N. Khare, 'Effect of graphene nanofillers on the enhanced thermoelectric properties of Bi₂Te₃ nanosheets: elucidating the role of interface in de-coupling the electrical and thermal characteristics', *Nanotechnology*., vol. 29, pp. 135703, 2018, https://doi.org/10.1016/j.jallcom.2016.04.161.

[100] Y. Zhang, H. Ma, B. Sun, B. Liu, H. Liu, L. Kong, B. Liu, X. Jia, X. Chen, 'Thermoelectric performance of graphene composited BiSbTe bulks by high pressure synthesis', *Journal of Alloys and Compounds*., vol.715, pp. 344-348, 2017, https://doi.org/10.1016/j.jallcom.2017.05.004.

[101] H. Ju, J. Kim, 'Preparation and structure dependent thermoelectric properties of nanostructured bulk bismuth telluride with graphene', *Journal of Alloys and Compounds.*, vol. 664, pp. 639-647, 2016, https://doi.org/10.1016/j.jallcom.2016.01.002.

[102] W.H. Shin, K. Ahn, M. Jeong, J.S. Yoon, J.M. Song, S. Lee, W.S. Seo, Y.S. Lim, 'Enhanced thermoelectric performance of reduced graphene oxide incorporated bismuth-antimony-telluride by lattice thermal conductivity reduction', *Journal of Alloys and Compounds*., vol. 718, pp. 342-348, 2017, https://doi.org/10.1016/j.jallcom.2017.05.204.

[104] Y. Wang, H. Pang, Q. Guo, N. Tsujii, T. Baba, T. Baba, T. Mori, 'Flexible n-Type Abundant Chalcopyrite/PEDOT: PSS/Graphene Hybrid Film for Thermoelectric Device Utilizing Low-Grade Heat', *ACS Applied Materials & Interfaces.*, vol.13, pp. 51245-51254, 2021, https://doi.org/10.1021/acsami.1c15232.

[105] K.R. Nandanapalli, D. Mudusu, J. Bae, W. Jeong, G.D. Moon, S. Lee, 'Larger, flexible, and skin-mountable energy devices with graphene single layers for integratable, wearable, and health monitoring systems', *Materials Today Chemistry.*, vol. 23, pp. 100764, 2022, https://doi.org/10.1016/j.mtchem.2021.100764.

[106] J. Gobpant, N. Somdock, P. Limsuwan, A. Sakulkalavek, R. Sakdanuphab, 'Graphene addition improved figure of merit in SnTe prepared by the rapid hybrid microwave solid-state method', *Journal of Physics and Chemistry of Solids.*, vol. 161, pp. 110490, 2022, https://doi.org/10.1016/j.jpcs.2021.110490.

[107] W. Wang, Q. Zhang, J. Li, X. Liu, L. Wang, J. Zhu, W. Luo, W. Jiang, 'An efficient thermoelectric material: preparation of reduced graphene oxide/polyaniline hybrid composites by cryogenic grinding'., *RSC Advances*, vol. 5, 8988-8995, 2015, DOI: 10.1039/C4RA12051E.

[108] S. Xin, N. Yang, F. Gao, J. Zhao, L. Li, C. Teng, 'Free-standing and flexible polypyrrole nanotube/reduced graphene oxide hybrid film with promising thermoelectric performance', *Materials Chemistry and Physics.*, vol. 212, pp. 440-445, 2018, https://doi.org/10.1016/j.matchemphys.2018.03.025.

[109] M, K. Ali, A. Hessein, M.A. Hassan, M. Ghali, N. M. Shaalan, K. Nakamura, A.A. El-Moneim, 'Heteroatom-doped reduced graphene oxide/polyaniline nanocomposites with improved n-type thermoelectric performance', *Journal of Applied Polymer Science*, vol. 138, pp. 50852, 2021, doi: https://doi.org/10.1002/app.50852.

[110] H. Song, C. Liu, H. Zhu, F. Kong, B. Lu, J. Xu, J. Wang, F. Zhao, 'Improved Thermoelectric Performance of Free-Standing PEDOT: PSS/Bi2Te3 Films with Low Thermal Conductivity', *Journal of Electronic Materials*, vol. 42, pp.1268-1274, 2013, https://doi.org/10.1007/s11664-013-2587-y.

[111] G.S. Hegde, V. Parol, A. Rao, A.N. Prabhu, J.J.B. Levinsky, G.R. Blake, 'Thermoelectric properties of co-doped (Bi0.98In0.02)2Te2.7Se0.3 /reduced graphene oxide composites prepared by solid-state reaction', *Materials Research Bulletin*., vol. 145, pp. 111517, 2022, https://doi.org/10.1016/j.materresbull.2021.111517.

[112] G. Kim, S.W. Kim, H.J. Rim, H. Lee, J. Kim, J.W. Roh, B.-W. Kim, K.H. Lee, W. Lee, 'Improved trade-off between thermoelectric performance and mechanical reliability of Mg2Si by hybridization of few-layered reduced graphene oxides', *Scripta Materialia*., vol. 162, pp. 402-407, 2019, https://doi.org/10.1016/j.scriptamat.2018.11.052.

[113] K. Ahmad, C.J.N. Wan, 'Enhanced thermoelectric performance of Bi2Te3 through uniform dispersion of single wall carbon nanotubes', *Nanotechnology*, vol. 28, pp. 415402, 2017, DOI 10.1088/1361-6528/aa810b.

[114] B. Zhang, J. Sun, H.E. Katz, F. Fang, R.L. Opila, 'Promising thermoelectric properties of commercial PEDOT:PSS materials and their bi2Te3 powder composites', *ACS Appl Mater Interfaces.*, vol. 2, pp. 3170-3178, 2010, https://doi.org/10.1021/am100654p.

[115] A, Dey, O.P. Bajpai, A.K. Sikder, S. Chattopadhyay, M.A.S.J.R. Khan, S.E. Reviews, 'Recent advances in CNT/graphene based thermoelectric polymer nanocomposite: A proficient move towards waste energy harvesting', *Renewable and Sustainable Energy Reviews* vol. 53, pp. 653-671, 2016, doi: https://doi.org/10.1016/j.rser.2015.09.004.

[116] N. Kim, S. Kee, S.H. Lee, B.H. Lee, Y.H. Kahng, Y.R. Jo, B.J. Kim, K.J.A.m. Lee, *Advanced Materials*, vol. 26 (2014) pp. 2268, 2014, https://doi.org/10.1002/adma.201304611.

[117] C.A. Hewitt, A.B. Kaiser, S. Roth, M. Craps, R. Czerw, D.L. Carroll, 'Multilayered Carbon Nanotube/Polymer Composite Based Thermoelectric Fabrics', *Nano Letters.*, vol. 12, pp. 1307-1310, 2012, https://doi.org/10.1021/nl203806q.

[118] Y. Du, K.F. Cai, S.Z. Shen, R. Donelsonand, J.Y. Xu, H.X. Wang, T. Lin, 'Multifold enhancement of the output power of flexible thermoelectric generators made from cotton fabrics coated with conducting polymer', *RSC Advances*, vol. 7, pp. 43737-43742, 2017, DOI: 10.1039/C7RA08663F.

[119] W. Zhou, Q. Fan, Q. Zhang, L. Cai, K. Li, X. Gu, F. Yang, N. Zhang, Y. Wang, H. Liu, W. Zhou, S. Xie, 'High-performance and compact-designed flexible thermoelectric modules enabled by a reticulate carbon nanotube architecture', *Nature Communications*., vol. 8, 2017, https://doi.org/10.1038/ncomms14886.

[120] B, Dörling, J.D. Ryan, J.D. Craddock, A. Sorrentino, A.E. Basaty, A. Gomez, M. Garriga, E. Pereiro, J.E. Anthony, M.C. Weisenberger, A.R. Goñi, C. Müller, M. Campoy-Quiles, 'Photoinduced p- to n-type Switching in Thermoelectric Polymer-Carbon Nanotube Composites', *Advanced Materials* vol. 28, pp. 2782-2789, 2016, doi: 10.1002/adma.201505521.

[121] Q. Yao, L. Chen, W. Zhang, S. Liufu, X. Chen, 'Enhanced thermoelectric performance of single-walled carbon nanotubes/polyaniline hybrid nanocomposites, *ACS Nano*., vol. 4, 2445-2451, 2010, https://doi.org/10.1021/nn1002562.

[122] L. Wang, D. Wang, G. Zhu, J. Li, F. Pan, Thermoelectric properties of conducting polyaniline/graphite composites, *Materials Letters*, 65 (2011) 1086-1088, https://doi.org/10.1016/j.matlet.2011.01.014.

[123] C. Yu, K. Choi, L. Yin, J.C. Grunlan, Light-Weight Flexible Carbon Nanotube Based Organic Composites with Large Thermoelectric Power Factors, *ACS Nano.,* vol. 5, pp. 7885-7892, 2011, https://doi.org/10.1021/nn202868a.

[124] S. Kirkpatrick, 'Percolation and Conduction', *Reviews of Modern Physics*, vol. 45, pp. 574-588, 1973, DOI: https://doi.org/10.1103/RevModPhys.45.574.

[125] C. Meng, C. Liu, S. Fan, 'A Promising Approach to Enhanced Thermoelectric Properties Using Carbon Nanotube Networks', *Advanced Materials* 22, (2010), pp. 535-539, 2010, DOI:10.1002/adma.200902221.

[126] R, C.Y. King, F. Roussel, J.-F. Brun, C.J.S.m. Gors, 'Carbon nanotube-polyaniline nanohybrids: influence of the carbon nanotube characteristics on the morphological, spectroscopic, electrical and thermoelectric properties', *Synthetic Metals*, vol. 162, pp. 1348-1356, 2012, doi: https://doi.org/10.1016/j.synthmet.2012.05.029.

[127] M.S. Islam, H. Ohmagari, M.A. Rahman, Y. Shudo, M. Fukuda, J. Yagyu, Y. Sekine, L.F. Lindoy, S. Hayami, 'Enhanced thermoelectric properties exhibited by unreduced freestanding graphene oxide/carbon nanotube membranes', *Materials Advances*., vol. 2, pp. 5645-5649, DOI: 10.1039/D1MA00299F.

[128] L. Wang, Z. Zhang, L. Geng, T. Yuan, Y. Liu, J. Guo, L. Fang, J. Qiu, S. Wang, 'Solution-printable fullerene/TiS2 organic/inorganic hybrids for high-performance flexible n-type thermoelectrics', *Energy and Environmental Science.,* vol. 11, pp. 1307-1317, 2018, DOI https://doi.org/10.1039/C7EE03617E.

[129] H. Fang, B.C. Popere, E.M. Thomas, C.K. Mai, W.B. Chang, G.C. Bazan, M.L. Chabinyc, R.A. Segalman, 'Large-scale integration of flexible materials into rolled and corrugated thermoelectric modules', *Journal of Applied Polymer Science.,* vol. 134, 2017, https://doi.org/10.1002/app.44208.

[130] F, Soltani-kordshuli, F. Zabihi, M.J. Eslamian, a.I. Technology, 'Graphene-doped PEDOT: PSS nanocomposite thin films fabricated by conventional and substrate vibration-assisted spray coating (SVASC)', *Engineering Science and Technology, an International Journal*, vol. 19, pp. 1216-1223, 2016, doi: https://doi.org/10.1016/j.jestch.2016.02.003.

[131] M. Acik, G. Lee, C. Mattevi, A. Pirkle, R.M. Wallace, M. Chhowalla, K. Cho, Y. Chabal, 'The Role of Oxygen during Thermal Reduction of Graphene Oxide Studied by Infrared Absorption Spectroscopy', *The Journal of Physical Chemistry C.*, vol. 115, pp. 19761-19781, 2015, https://doi.org/10.1021/jp2052618.

[132] J.-S. Yeo, J.-M. Yun, D.-Y. Kim, S. Park, S.-S. Kim, M.-H. Yoon, T.-W. Kim, S.-I. Na, 'Significant Vertical Phase Separation in Solvent-Vapor-Annealed Poly(3,4-ethylenedioxythiophene):Poly(styrene sulfonate) Composite Films Leading to Better Conductivity and Work Function for High-Performance Indium Tin Oxide-Free Optoelectronics', *ACS Applied Materials & Interfaces.*, vol. 4, pp. 2551-2560, 2012, https://doi.org/10.1038/s41467-022-29773-9.

[133] W. Hong, Y. Xu, G. Lu, C. Li, G. Shi, 'Transparent graphene/PEDOT–PSS composite films as counter electrodes of dye-sensitized solar cells', *Electrochemistry Communications*., vol. 10, pp. 1555-1558, 2008, https://doi.org/10.1016/j.elecom.2008.08.007.

[134] F, P. Du, N.-N. Cao, Y.-F. Zhang, P. Fu, Y.-G. Wu, Z.-D. Lin, R. Shi, A. Amini, C.J Cheng, 'PEDOT: PSS/graphene quantum dots films with enhanced thermoelectric properties via strong interfacial interaction and phase separation', *Scientific Reports*, vol. 8, pp. 6441, 2018, doi: https://doi.org/10.1038/s41598-018-24632-4.

[135] L.M. Cowen, J. Atoyo, M.J. Carnie, D. Baran, B.C. Schroeder, 'Review Organic Materials for Thermoelectric Energy Generation', *ECS Journal of Solid State Science and Technology*., vol. 6, pp. N3080, 2016, DOI 10.1149/2.0121703jss.

[136] J. Guo, G. Li, H. Reith, L. Jiang, M. Wang, Y. Li, X. Wang, Z. Zeng, H. Zhao, X. Lu, G. Schierning, K. Nielsch, L. Liao, Y. Hu, 'Doping High-Mobility Donor–Acceptor Copolymer Semiconductors with an Organic Salt for High-Performance Thermoelectric Materials', *Advanced Electronic Materials*., vol. 6, 1900945, 2020, https://doi.org/10.1002/aelm.201900945.

[137] I. Salzmann, G. Heimel, M. Oehzelt, S. Winkler, N. Koch, Molecular Electrical Doping of Organic Semiconductors: Fundamental Mechanisms and Emerging Dopant Design Rules, *Accounts of Chemical Research* 49 (2016) 370-378, https://doi.org/10.1021/acs.accounts.5b00438.

[138] M.S. Freund, B.A. Deore, 'Self-Doped Conducting Polymers', Wiley, 2007.

[139] B. Lüssem, M. Riede, K. Leo, 'Doping of organic semiconductors', *physica status solidi* (a)., vol. 210, pp. 9-43, 2013, https://doi.org/10.1002/pssa.201228310.

[140] C.S. A. Assadi, M. Willander, O. Inganas, *Appl. Phys. Lett*., vol. 53 (1988), https://doi.org/10.1007/BF02705409.

[141] A. Assadi, C. Svensson, M. Willander, O. Inganas, 'Field-Effect Mobility of Poly(3-Hexylthiophene)', *Appl. Phys. Lett*., vol. 53, pp. 195, 1988, DOI:10.1063/1.100171.

[142] D.T. Duong, C. Wang, E. Antono, M.F. Toney, A. Salleo, 'The chemical and structural origin of efficient p-type doping in P3HT', *Organic Electronics*., vol.14, pp.1330-13362013, https://doi.org/10.1016/j.orgel.2013.02.028.

[143] K.-H. Yim, G.L. Whiting, C.E. Murphy, J.J.M. Halls, J.H. Burroughes, R.H. Friend, J.-S. Kim, 'Controlling Electrical Properties of Conjugated Polymers via a Solution-Based p-Type Doping', *Advanced Materials*., vol. 20, pp. 3319-3324, 2008, DOI: 10.1002/adma.200800735.

[144] B. Russ, A. Glaudell, J.J. Urban, M.L. Chabinyc, R.A. Segalman, 'Organic thermoelectric materials for energy harvesting and temperature control', *Nature Reviews Materials*., vol.1, pp. 16050, 2016, https://doi.org/10.1038/natrevmats.2016.50.

[145] J.L. Bredas, G.B. Street, 'Polarons, bipolarons, and solitons in conducting polymers', *Accounts of Chemical Research.*, vol. 18, pp. 309-315, 1985, https://doi.org/10.1021/ar00118a005.

[146] T. Suzuki, H. Yamochi, G. Srdanov, K. Hinkelmann, F. Wudl, 'Bis(ethylenedioxy)tetrathiafulvalene: the first oxygen substituted tetrathiafulvalene', *Journal of the American Chemical Society.*, vol. 111, pp. 3108-3109, 1989, https://doi.org/10.1021/ja00190a079.

[147] A. Casian, V. Dusciac, I. Coropceanu,' 'Huge carrier mobilities expected in quasi-one-dimensional organic crystals', *Physical Review B.*, vol. 66, pp.165404, 2002, DOI: https://doi.org/10.1103/PhysRevB.66.165404.

[148] Y. Yamamoto, K. Yoshino, Y. Inuishi, 'Electrical Properties of Phthalocyanine-Halogen Complexes', *Journal of the Physical Society of Japan*., vol. 47, pp. 1887-1891,1979, https://doi.org/10.1143/JPSJ.47.1887.

[149] N. Basescu, Z.X. Liu, D. Moses, A.J. Heeger, H. Naarmann, N. Theophilou, 'High electrical conductivity in doped polyacetylene', *Nature.*, vol. 327, pp. 403-405, 1987, https://doi.org/10.1038/327403a0.

[150] M. Chabinyc, 'Thermoelectric polymers: Behind organics' thermopower', *Nat Mater.*, vol. 13, pp. 119-121, 2014, https://doi.org/10.1038/nmat3859.

[151] O. Bubnova, X. Crispin, 'Towards polymer-based organic thermoelectric generators', *Energy & Environmental Science*., vol. 5, pp. 9345-9362, 2014, DOI https://doi.org/10.1039/C2EE22777K.

[152] M. Dresselhaus, G. Chen, M. Tang, R. Yang, H. Lee, D. Wang, Z.F. Ren, J.-P. Fleurial, P. Gogna, 'New Directions for Low-Dimensional Thermoelectric Materials', *Advanced Materials.*, vol. 19, pp. 1043-1053, 2007 https://doi.org/10.1002/adma.200600527.

[153] J.O. Sofo, G.D. Mahan, 'Optimum band gap of a thermoelectric material', *Physical Review B.*, vol. 49, pp. 4565-4570, 1994, DOI: https://doi.org/10.1103/PhysRevB.49.4565.

[154] I.E. Jacobs, A.J. Moulé, 'Controlling Molecular Doping in Organic Semiconductors', *Advanced Materials.*, vol. 29, pp. 1703063, 2017, https://doi.org/10.1002/adma.201703063.

[155] W. Zhao, J. Ding, Y. Zou, C.-a. Di, D. Zhu, 'Chemical doping of organic semiconductors for thermoelectric applications', *Chemical Society Reviews.*, vol. 49, pp. 7210-7228, 2020, DOI https://doi.org/10.1039/D0CS00204F.

[156] J.-C. Chiang, A.G. MacDiarmid, 'Polyaniline': 'Protonic acid doping of the emeraldine form to the metallic regime', *Synthetic Metals.*, vol.13, pp. 193-205, 1986, https://doi.org/10.1016/0379-6779(86)90070-6.

[157] O. Bubnova, Z.U. Khan, A. Malti, S. Braun, M. Fahlman, M. Berggren, X. 'Crispin, Optimization of the thermoelectric figure of merit in the conducting polymer poly(3,4-

ethylenedioxythiophene)', *Nature Materials*., vol. 10, pp. 429-433, 2011, https://doi.org/10.1038/nmat3012.

[158] S. Wang, G. Zuo, J. Kim, H. Sirringhaus, 'Progress of Conjugated Polymers as Emerging Thermoelectric Materials', *Progress in Polymer Science.,* vol.129, pp. 101548, 2022, https://doi.org/10.1016/j.progpolymsci.2022.101548.

[159] M. Winokur, Y.B. Moon, A.J. Heeger, J. Barker, D.C. Bott, H. Shirakawa, 'X-Ray Scattering from Sodium-Doped Polyacetylene: Incommensurate-Commensurate and Order-Disorder Transformations', *Physical Review Letters.,* vol. 58, pp. 2329-2332, 1987, DOI: https://doi.org/10.1103/PhysRevLett.58.2329.

[160] G.C. Welch, G.C. Bazan, 'Lewis Acid Adducts of Narrow Band Gap Conjugated Polymers', *Journal of the American Chemical Society*, vol. 133, pp. 4632-4644, 2011, https://doi.org/10.1021/ja110968m.

[161] H. Kleemann, R. Gutierrez, F. Lindner, S. Avdoshenko, P.D. Manrique, B. Lüssem, G. Cuniberti, K. Leo, 'Organic Zener Diodes: Tunneling across the Gap in Organic Semiconductor Materials', *Nano Letters.,* vol.10, pp. 4929-4934,2010, https://doi.org/10.1021/nl102916n.

[162] B. Lüssem, M.L. Tietze, H. Kleemann, C. Hoßbach, J.W. Bartha, A. Zakhidov, K. Leo, 'Doped organic transistors operating in the inversion and depletion regime', *Nature Communications.,* vol.4, pp. 2775, 2013, https://doi.org/10.1038/ncomms3775.

[163] S. Peng, D. Wang, J. Lu, M. He, C. Xu, Y. Li, S. Zhu, 'A Review on Organic Polymer-Based Thermoelectric Materials', *Journal of Polymers and the Environment*., vol. 25, pp. 1208-1218, 2017, https://doi.org/10.1007/s10924-016-0895-z.

[164] M. Culebras, M.M. de Lima Jr, C. Gómez, A. Cantarero, 'Organic thermoelectric modules produced by electrochemical polymerization', *Journal of Applied Polymer Science.,* vol.134 2017, https://doi.org/10.1002/app.43927.

[165] M. Culebras, C.M. Gómez, A. Cantarero, 'Enhanced thermoelectric performance of PEDOT with different counter-ions optimized by chemical reduction', *Journal of Materials Chemistry A.,* vol. 2, pp. 10109-10115, 2014, https://doi.org/10.1039/C4TA01012D.

[166] M. Culebras, C.M. Gómez, A. Cantarero, 'Review on Polymers for Thermoelectric Applications', *Materials (Basel*)., vol. 7, pp. 6701-6732, 2014, https://doi.org/10.3390/ma7096701.

[167] M. Culebras, B. Uriol, C.M. Gómez, A. Cantarero, 'Controlling the thermoelectric properties of polymers: application to PEDOT and polypyrrole', *Physical Chemistry Chemical Physics.,* 17 (2015) 15140-15145, DOI: 10.1039/C5CP01940K.

[168] H. Yoshino, G.C. Papavassiliou, K. Murata, 'Low-Dimensional organic conductors as thermoelectric materials', *Journal of Thermal Analysis and Calorimetry*., vol. 92, 457-460,2008, https://doi.org/10.1007/s10973-007-8970-2.

[169] Y. Zeng, W. Zheng, Y. Guo, G. Han, Y. Yi, 'Doping mechanisms of N-DMBI-H for organic thermoelectrics: hydrogen removal vs. hydride transfer', *Journal of Materials Chemistry A.*, vol. 8, pp. 8323-8328, 2020, DOI https://doi.org/10.1039/D0TA01087A.

[170] D. Kiefer, A. Giovannitti, H. Sun, T. Biskup, A. Hofmann, M. Koopmans, C. Cendra, S. Weber, L.J. Anton Koster, E. Olsson, J. Rivnay, S. Fabiano, I. McCulloch, C. Müller, 'Enhanced n-Doping Efficiency of a Naphthalenediimide-Based Copolymer through Polar Side Chains for Organic Thermoelectrics', *ACS Energy Letters*., vol. 3, pp. 278-285, 2018, https://doi.org/10.1021/acsenergylett.7b01146.

[171] T, Menke, P. Wei, D. Ray, H. Kleemann, B.D. Naab, Z. Bao, K. Leo, M.J.O.E. Riede, 'A comparison of two air-stable molecular n-dopants for C60', *Organic Electronics*, vol. 13, pp. 3319-3325, 2012, doi: https://doi.org/10.1016/j.orgel.2012.09.024.

[172] A.O. Patil, Y. Ikenoue, N. Basescu, N. Colaneri, J. Chen, F. Wudl, A.J. Heeger, 'Self-doped conducting polymers', *Synthetic Metals.*, vol. 20, pp. 151-159, 1987, https://doi.org/10.1016/0379-6779(87)90554-6.

[173] W. Zhou, Q. Fan, Q. Zhang, L. Cai, K. Li, X. Gu, F. Yang, N. Zhang, Y. Wang, H. Liu, W. Zhou, S. Xie, 'High-performance and compact-designed flexible thermoelectric modules enabled by a reticulate carbonnanotube architecture', *Nature Communications.*, vol. 8, pp. 14886, 2017, https://doi.org/10.1038/ncomms14886.

[174] Z. Zhang, Q. Tao, H. Bai, H. Tang, Y. Cao, Y. Shi, J. Wu, X. Su, X. Tang, 'Regulation of exciton for high thermoelectric performance in (Bi, Sb)2Te3 alloys via doping with Pb and multi-scale microstructure', *Journal of the European Ceramic Society.*, vol. 41, pp. 7703-7710, 2021, https://doi.org/10.1016/j.jeurceramsoc.2021.08.041.

[175] C.W. Tang, 'Two-layer organic photovoltaic cell', *Applied Physics Letters*., vol. 48, pp. 183-185, 1986, https://doi.org/10.1063/1.96937.

[176] C. Wan, X. Gu, F. Dang, T. Itoh, Y. Wang, H. Sasaki, M. Kondo, K. Koga, K. Yabuki, G.J. Snyder, R. Yang, K. Koumoto, 'Flexible n-type thermoelectric materials by organic intercalation of layered transition metal dichalcogenide TiS2' *Nat Mater*., vol. 14, pp. 622-627, 2015, https://doi.org/10.1038/nmat4251.

[177] Y.H. Sun, L. Qiu, L.P. Tang, H. Geng, H.F. Wang, F.J. Zhang, D.Z. Huang, W. Xu, P. Yue, Y.S. Guan, F. Jiao, Y.M. Sun, D.W. Tang, C.A. Di, Y.P. Yi, D.B. Zhu, *Adv. Mater*., vol. 28, pp. 3351, 2016, DOI: 10.1002/adma.201505922.

[178] F. Zhang, Y. Zang, D. Huang, C.-a. Di, X. Gao, H. Sirringhaus, D. Zhu, 'Modulated Thermoelectric Properties of Organic Semiconductors Using Field-Effect Transistors', *Advanced Functional Materials*., vol. 25, pp. 3004-3012, 2015, https://doi.org/10.1002/adfm.201404397.

[179] D.T. Duong, C. Wang, E. Antono, M.F. Toney, A. Salleo, 'The chemical and structural origin of efficient p-type doping in P3HT', *Org. Electron.*, vol. 14, pp. 1330, 2013, https://doi.org/10.1016/j.orgel.2013.02.028.

[180] G. Horowitz, D. Fichou, X. Peng, Z. Xu, F. Garnier, 'A field-effect transistor based on conjugated alpha-sexithienyl', *Solid State Communications*., vol. 72, pp. 381-384, 1989, https://doi.org/10.1016/0038-1098(89)90121-X.

[181] T.D. Anthopoulos, G.C. Anyfantis, G.C. Papavassiliou, D.M. de Leeuw, 'Air-stable ambipolar organic transistors', *Applied Physics Letters.*, vol. 90, pp. 122105, 2007, https://doi.org/10.1002/ange.201302396.

[182] H.T. Nicolai, M. Kuik, G.A. Wetzelaer, B. de Boer, C. Campbell, C. Risko, J.L. Brédas, P.W. Blom, 'Unification of trap-limited electron transport in semiconducting polymers', *Nat Mater*., vol. 11, pp. 882-887, 2012, https://doi.org/10.1038/nmat3384.

[183] H. Méndez, G. Heimel, A. Opitz, K. Sauer, P. Barkowski, M. Oehzelt, J. Soeda, T. Okamoto, J. Takeya, J.B. Arlin, J.Y. Balandier, Y. Geerts, N. Koch, I. Salzmann, 'Doping of Organic Semiconductors: Impact of Dopant Strength and Electronic Coupling', *Angew Chem Int. Ed.*, vol. 52, pp. 7751, 2013, https://doi.org/10.1038/nmat3384.

[184] J.E. Anthony, A. Facchetti, M. Heeney, S.R. Marder, X. Zhan, 'n-Type organic semiconductors in organic electronics', *Adv Mater*., vol. 22, pp. 3876-3892, 2010, https://doi.org/10.1002/adma.200903628.

[185] E.S. Chen, E.C.M. Chen, N. Sane, L. Talley, N. Kozanecki, S. Shulze, 'Classification of organic molecules to obtain electron affinities from half wave reduction potentials: The aromatic hydrocarbons', *The Journal of Chemical Physics*., vol. 110, pp. 9319-9329, 1999, https://doi.org/10.1063/1.478854.

[186] M. Hong, T.C. Chasapis, Z.G. Chen, L. Yang, M.G. Kanatzidis, G.J. Snyder, J. Zou, 'n-Type Bi2Te3-xSex 'Nanoplates with Enhanced Thermoelectric Efficiency Driven by Wide-Frequency Phonon Scatterings and Synergistic Carrier Scatterings', *ACS nano.*, vol. 10, pp. 4719-4727, 2016, https://doi.org/10.1021/acsnano.6b01156.

[187] L. Yang, Z.-G. Chen, M. Hong, G. Han, J. Zou, 'Enhanced Thermoelectric Performance of Nanostructured Bi2Te3 through Significant Phonon Scattering', *ACS applied materials & interfaces.*, vol. 7, pp. 23694-23699, 2015, https://doi.org/10.1021/acsami.5b07596.

[188] Q, Yao, L. Chen, W. Zhang, S. Liufu, X.J.A.n. Chen, 'Enhanced thermoelectric performance of single-walled carbon nanotubes/polyaniline hybrid nanocomposites', *ACS Nano*, vol. 4, pp. 2445-2451, 2010, doi: https://doi.org/10.1021/nn1002562.

[189] N. Toshima, 'Conductive polymers as a new type of thermoelectric material', *Macromolecular Symposia Wiley Online Library*., pp. 81-86, 2002, https://doi.org/10.1002/1521-3900(200208)186.

[190] J, Li, X. Tang, H. Li, Y. Yan, Q.J. Zhang, 'Synthesis and thermoelectric properties of hydrochloric acid-doped polyaniline', *Synthetic Metals*, vol. 160, pp. 1153-1158, 2010, doi: https://doi.org/10.1016/j.synthmet.2010.03.001.

[191] N, Kim, S. Kee, S.H. Lee, B.H. Lee, Y.H. Kahng, Y.R. Jo, B.J. Kim, K.J.A.m. Lee, 'Highly conductive PEDOT: PSS nanofibrils induced by solution-processed crystallization', *Advanced Materials*, vol. 26, pp. 2268-2272, 2014, doi: https://doi.org/10.1002/adma.201304611.

[192] A, Cho, S. Kim, S. Kim, W. Cho, C. Park, F.S. Kim, J.H. Kim, 'Influence of imidazole-based acidity control of PEDOT: PSS on its electrical properties and environmental stability', *Journal of Polymer Science Part B: Polymer Physics*, vol. 54, pp. 1530-1536, 2016, doi: https://doi.org/10.1002/polb.24048.

[193] Y, Wen, J. Xu, 'Scientific importance of water-processable PEDOT–PSS and preparation, challenge and new application in sensors of its film electrode: a review', *Journal of Polymer Science Part A: Polymer Chemistry*, vol. 55, pp. 1121-1150, 2017, doi: https://doi.org/10.1002/pola.28482.

[194] Z, U. Khan, O. Bubnova, M.J. Jafari, R. Brooke, X. Liu, R. Gabrielsson, T. Ederth, D.R. Evans, J.W. Andreasen, M.J. Fahlman, 'Acido-basic control of the thermoelectric properties of poly (3, 4-ethylenedioxythiophene) tosylate (PEDOT-Tos) thin films', *Journal of Materials Chemistry C*, vol. 3, pp. 10616-10623, 2015, doi: 10.1039/C5TC01952D.

[195] G, H. Kim, L. Shao, K. Zhang, K.P.J.N.m. Pipe, 'Engineered doping of organic semiconductors for enhanced thermoelectric efficiency', *Nature Materials*, vol. 12, pp. 719-723, 2013, doi: https://doi.org/10.1038/nmat3635.

[196] K, C. See, J.P. Feser, C.E. Chen, A. Majumdar, J.J. Urban, R.A Segalman, 'Water-processable polymer− nanocrystal hybrids for thermoelectrics', *Nano Letters*, vol. 10, pp. 4664-4667, 2010, doi: https://doi.org/10.1021/nl102880k.

[197] X, Zhao, S. Hu, M. Zhao, T.J. Zhu, 'Thermoelectric properties of Bi0.5Sb1. 5Te3/polyaniline hybrids prepared by mechanical blending', *Materials Letters*, vol. 52, pp. 147-149, 2002, doi: https://doi.org/10.1016/S0167-577X(01)00381-0.

[198] Y, Li, Q. Zhao, Y.-g. Wang, K.J. Bi, 'Synthesis and characterization of Bi2Te3/polyaniline composites, *Materials Science in Semiconductor Processing*, vol. 14, pp. 219-222, 2011, doi: https://doi.org/10.1016/j.mssp.2011.02.019.

[199] N, Toshima, M. Imai, S.J. Ichikawa, 'Organic–inorganic nanohybrids as novel thermoelectric materials: hybrids of polyaniline and bismuth (III) telluride nanoparticles', *Journal of Electronic Materials*, vol. 40, pp. 898-902, 2011, doi: https://doi.org/10.1007/s11664-010-1403-1.

[200] H, Liu, J. Wang, X. Hu, R.I. Boughton, S. Zhao, Q. Li, M.j Jiang, 'Structure and electronic transport properties of polyaniline/NaFe4P12 composite', *Chemical Physics Letters*, vol. 352, pp. 185-190, 2002, doi: https://doi.org/10.1016/S0009-2614(01)01389-6.

[201] C, G. Wu, D. DeGroot, H. Marcy, J. Schindler, C. Kannewurf, Y.-J. Liu, W. Hirpo, M.J. 'The postintercalative intralamellar polymer growth in polyaniline/metal oxide nanocomposites is

facilitated by molecular oxygen', *Chemistry of Materials*, vol. 8, pp. 1992-2004, 1996, doi: https://doi.org/10.1021/cm9600236.

[202] H, Song, C. Liu, H. Zhu, F. Kong, B. Lu, J. Xu, J. Wang, F. Zhao, 'Improved thermoelectric performance of free-standing PEDOT: PSS/Bi2Te3 films with low thermal conductivity', *Journal of Electronic Materials*, vol. 42, pp. 1268-1274, 2013, doi: https://doi.org/10.1007/s11664-013-2587-y.

[203] Z, H. Tian, H.-H. Liu, N. Wang, Y.X. Liu, X. Zhang, 'Facile preparation and thermoelectric properties of PEDOT nanowires/Bi 2 Te 3 nanocomposites', *Journal of Material Science: Materials in Electronics*,vol. 29, pp. 17367-17373, 2018, doi: https://doi.org/10.1007/s10854-018-9834-1.

[204] Y. Du, K.F. Cai, S. Chen, P. Cizek, T. Lin, 'Facile Preparation and Thermoelectric Properties of Bi2Te3 Based Alloy Nanosheet/PEDOT: PSS Composite Films', *ACS Applied Materials & Interfaces*., vol.6, pp. 5735-5743, 2014, https://doi.org/10.1021/am5002772.

[205] K. Chatterjee, M. Mitra, K. Kargupta, S. Ganguly, D. Banerjee, 'Synthesis, characterization and enhanced thermoelectric performance of structurally ordered cable-like novel polyaniline–bismuth telluride nanocomposite, *Nanotechnology* vol. 24, pp. 215703, 2014, DOI: 10.1088/0957-4484/24/21/215703.

[206] Y. Li, J. Dong, X. Wu, B. Huo, P. Liu, B. Li, C.-Y. Guo, 'Elevating Thermoelectric Performance by Compositing Dibromo-Substituted Thienoacene with SWCNTs', *ACS Applied Materials & Interfaces*., 2024, https://doi.org/10.1021/acsami.4c07042.

[207] C, Du, M. Cao, G. Li, Y. Hu, Y. Zhang, L. Liang, Z. Liu, G. Chen, 'Toward Precision Recognition of Complex Hand Motions: Wearable Thermoelectrics by Synergistic 2D Nanostructure Confinement and Controlled Reduction, *Advanced Functional Materials,* vol. 32, pp. 2206083, 2022, doi: https://doi.org/10.1002/adfm.202206083.

[208] C. Kim, K.-e. Kim, J. Cho, D.H. Lopez, 'Investigation of simultaneous carrier/phonon scattering and bipolar conduction effects in inorganic/organic composites: Implications for thermoelectric performance', *APL Materials*., vol. 11, 2023, https://doi.org/10.1063/5.0160384.

[209] A. Kumar, A. Patel, S. Singh, A. Kandasami, D. Kanjilal, 'Apparatus for Seebeck coefficient measurement of wire, thin film, and bulk materials in the wide temperature range (80–650 K)', *Review of Scientific Instruments.*, vol. 90, 2019, https://doi.org/10.1063/1.5116186.

[210] K, Aasmundtveit, E. Samuelsen, L. Pettersson, O. Inganäs, T. Johansson, R.J. Feidenhans, 'Structure of thin films of poly (3, 4-ethylenedioxythiophene)', *Synthetic Metals*, vol. 101, pp. 561-564, 1999, doi: https://doi.org/10.1016/S0379-6779(98)00315-4.

[211] N. Kim, B.H. Lee, D. Choi, G. Kim, H. Kim, J.-R. Kim, J. Lee, Y.H. Kahng, K. Lee, 'Role of Interchain Coupling in the Metallic State of Conducting Polymers', *Physical Review Letters.*, vol. 109, pp, 106405, 2012, https://doi.org/10.1103/PhysRevLett.109.106405.

[212] X.J. Wang, K.Y. Wong, 'Effects of a base coating used for electropolymerization of poly(3,4-ethylenedioxythiophene) on indium tin oxide electrode', *Thin Solid Films*., vol. 515 pp. 1573-1578, 2016, https://doi.org/10.1016/j.tsf.2006.05.015.

[213] S, Garreau, G. Louarn, J.P. Buisson, G. Froyer, S.J.M. Lefrant, 'In situ spectroelectrochemical Raman studies of poly(3,4-ethylenedioxythiophene) (PEDT)', *Macromolecules* vol. 32, pp. 6807-6812, 1999, doi: https://doi.org/10.1021/ma9905674.

[214] H. Park, S.H. Lee, F.S. Kim, H.H. Choi, I.W. Cheong, J.H. Kim, 'Enhanced thermoelectric properties of PEDOT: PSS nanofilms by a chemical dedoping process', *Journal of Materials Chemistry A*, vol. 2, pp. 6532-6539, 2014, https://doi.org/10.1039/C3TA14960A.

[215] S.R.S. Kumar, N. Kurra, H.N. Alshareef, 'Enhanced high temperature thermoelectric response of sulphuric acid treated conducting polymer thin films', *Journal of Materials Chemistry C.*, vol.4, pp. 215-221, 2016, DOI: 10.1039/C5TC03145A.

[216] R, Anitha, S.S. Menon, G. Bhalerao, P. Siddham, K. Baskar, S.J. Singh, 'Electrical properties of nitric acid and DMSO treated PEDOT: PSS/n-Si hybrid heterostructures for optoelectronic applications', *Journal of Applied Polymer Science*, vol. 137, pp. 48952, 2020, doi: https://doi.org/10.1002/app.48952.

[217] S. Garreau, G. Louarn, J.P. Buisson, G. Froyer, S. Lefrant, 'In Situ Spectroelectrochemical Raman Studies of Poly(3,4-ethylenedioxythiophene) (PEDT)', *Macromolecules.,* vol. 32, pp. 6807-6812, 1999, https://doi.org/10.1021/ma9905674.

[218] M. Łapkowski, A. Proń, 'Electrochemical oxidation of poly(3,4-ethylenedioxythiophene) in situ conductivity and spectroscopic investigations', *Synthetic Metals*, vol. 110, pp. 79-83, 2000, https://doi.org/10.1016/S0379-6779(99)00271-4.

[219] D.H. Kim, N.H. Park, T.W. Kim, 'Highly efficient flexible organic light-emitting devices based on PEDOT: PSS electrodes doped with highly conductive Pyronin B', *Nano Energy.*, vol. 65, pp. 104027, 2019, https://doi.org/10.1016/j.nanoen.2019.104027.

[220] F. Soltani-Kordshuli, F. Zabihi, Y. Xie, M. 'Eslamian, Conductive CNT-and Graphene-Doped PEDOT:PSS Thin Films Fabricated by Ultrasonic Spray Coating', *Engineering Science and Technology, an International Journal* 2015, https://doi.org/10.1016/j.jestch.2016.02.003.

[221] M. Wang, M. Zhou, L. Zhu, Q. Li, C. Jiang, 'Enhanced polymer solar cells efficiency by surface coating of the PEDOT: PSS with polar solvent', *Solar Energy.*, vol. 129, pp. 175-183, 2016, https://doi.org/10.1016/j.solener.2016.02.003.

[222] W.S. Kim, G. Anoop, I.-S. Jeong, H.J. Lee, H.B. Kim, S.H. Kim, G.W. Goo, H. Lee, H.J. Lee, C. Kim, J.-H. Lee, B.S. Mun, J.-W. Park, E. Lee, J.Y. Jo, 'Feasible tuning of barrier energy in PEDOT: PSS/Bi2Te3 nanowires-based thermoelectric nanocomposite thin films through polar solvent vapor annealing', *Nano Energy.,* vol. 67, pp. 104207, 2020, https://doi.org/10.1016/j.nanoen.2019.104207.

[223] D. Zheng, H. Jin, Y. Liao, P. Ji, 'Bi2Te3 nanowires tuning PEDOT: PSS structure for significant enhancing electrical transport property', *Materials Letters.*, vol. 338, pp. 134019, 2023, https://doi.org/10.1016/j.matlet.2023.134019.

[224] D.B. Cairns, S.P. Armes, M.M. Chehimi, C. Perruchot, M. Delamar, 'X-ray Photoelectron Spectroscopy Characterization of Submicrometer-Sized Polypyrrole−Polystyrene Composites', *Langmuir.*, vol.15, pp. 8059-8066, 1999, https://doi.org/10.1021/la990443k.

[225] X. Zhao, M. Dong, J. Zhang, Y. Li, Q. Zhang, 'Vapor-phase polymerization of poly (3, 4-ethylenedioxythiophene) nanofibers on carbon cloth as electrodes for flexible supercapacitors', *Nanotechnology*, vol. 27, pp. 385705, 2016, 10.1088/0957-4484/27/38/385705.

[226] J. Yadav, M.D. Anoop, N. Yadav, N.S. Rao, F. Singh, T. Ichikawa, A. Jain, K. Awasthi, R. Singh, M. Kumar, 'Tuning of charge carriers in Bi2Te3 thin films via swift heavy ion irradiation', *Journal of Materials Science: Materials in Electronics.*, vol. 34, pp. 175, 2023, https://doi.org/10.1007/s10854-022-09478-x.

[227] B. Zhang, J. Sun, H.E. Katz, F. Fang, R.L. Opila, 'Promising Thermoelectric Properties of Commercial PEDOT: PSS Materials and Their Bi2Te3 Powder Composites', *ACS Applied Materials & Interfaces*, vol. 2, pp. 3170-3178, 2010, https://doi.org/10.1021/am100654p.

[228] D, Kim, Y. Kim, K. Choi, J.C. Grunlan, C.J. Yu, 'Improved thermoelectric behavior of nanotube-filled polymer composites with poly (3, 4-ethylenedioxythiophene) poly (styrenesulfonate)', *ACS Nano*, vol. 4, pp. 513-523, 2010, doi: https://doi.org/10.1021/nn9013577.

[229] K. Biswas, J. He, I.D. Blum, C.I. Wu, T.P. Hogan, D.N. Seidman, V.P. Dravid, M.G. Kanatzidis, 'High-Performance Bulk Thermoelectrics with All-Scale Hierarchical Architectures', *Nature*, vol. 489, pp. 414, 2012, https://doi.org/10.1038/nature11439.

[230] H. Song, C. Liu, H. Zhu, K. Fangfang, B. Lu, J. Xu, J. Wang, F. Zhao, 'Improved Thermoelectric Performance of Free-Standing PEDOT: PSS/Bi2Te3 Films with Low Thermal Conductivity', *Journal of Electronic Materials.*, vol. 42, 2013, https://doi.org/10.1007/s11664-013-2587-y.

[231] H. Scherrer, D. Rowe, T. Kajikawa, K. Matsubara, J.-P. Issi, H.J. Goldsmid, C.M. Bhandari, A.T. Burkov, V.K. Zaitsev, M.I. Fedorov, 'Thermoelectrics Handbook: Macro to Nano, 2018.

[232] S, Twaha, J. Zhu, Y. Yan, B.J.R. Li, s.e. reviews, 'A comprehensive review of thermoelectric technology: Materials, applications, modelling and performance improvement, *Renewable and Sustainable Energy Reviews*, vol. 65, pp. 698-726, 2016, doi: https://doi.org/10.1016/j.rser.2016.07.034.

[233] G, Tan, L.-D. Zhao, M.G. Kanatzidis, 'Rationally designing high-performance bulk thermoelectric materials', *Chemical Reviews* vol. 116, pp. 12123-12149, 2016, doi: https://doi.org/10.1021/acs.chemrev.6b00255.

[234] L, D. Zhao, S.-H. Lo, Y. Zhang, H. Sun, G. Tan, C. Uher, C. Wolverton, V.P. Dravid, M.G.J.n. Kanatzidis, 'Ultralow thermal conductivity and high thermoelectric figure of merit in SnSe crystals', *Nature*, vol. 508, pp. 373-377, 2014, doi: https://doi.org/10.1038/nature13184.

[235] X, Hu, G. Chen, X.J.C.S. Wang, 'Technology, An unusual coral-like morphology for composites of poly (3, 4-ethylenedioxythiophene)/carbon nanotube and the enhanced thermoelectric performance', *Composites Science and Technology* vol. 144, pp. 43-50, 2017, doi: https://doi.org/10.1016/j.compscitech.2017.03.018.

[236] K, Xu, G. Chen, D.J. Qiu, 'Convenient construction of poly (3, 4-ethylenedioxythiophene)–graphene pie-like structure with enhanced thermoelectric performance', *Journal of Materials Chemistry A* vol. 1, pp. 12395-12399, 2013, doi: https://doi.org/10.1039/C3TA12691A.

[237] M, He, F. Qiu, Z.J.E. Lin, E. Science, 'Towards high-performance polymer-based thermoelectric materials', *Energy & Environmental Science*, vol. 6, pp. 1352-1361, 2013, doi: https://doi.org/10.1039/C3EE24193A.

[238] J, Luo, D. Billep, T. Waechtler, T. Otto, M. Toader, O. Gordan, E. Sheremet, J. Martin, M. Hietschold, D.R. Zahn, 'Enhancement of the thermoelectric properties of PEDOT: PSS thin films by post-treatment', *Journal of Materials Chemistry A*, vol. 1, pp. 7576-7583, 2013, doi: https://doi.org/10.1039/C3TA11209H.

[239] S, K. Yee, N.E. Coates, A. Majumdar, J.J. Urban, R. Segalman, 'Thermoelectric power factor optimization in PEDOT: PSS tellurium nanowire hybrid composites', *Physical Chemistry Chemical Physics*, vol. 15, pp. 4024-4032, 2013, doi: https://doi.org/10.1039/C3CP44558E.

[240] Y, Du, K. Cai, S. Chen, P. Cizek, T.J.A.a.m. Lin, interfaces, 'Facile preparation and thermoelectric properties of Bi2Te3 based alloy nanosheet/PEDOT: PSS composite films', *ACS Applied Maerials & Interfaces*, vol. 6, pp. 5735-5743, 2014, doi: https://doi.org/10.1021/am5002772.

[241] B, Zhang, J. Sun, H. Katz, F. Fang, R.J.A.a.m. Opila, interfaces, 'Promising thermoelectric properties of commercial PEDOT: PSS materials and their Bi2Te3 powder composites', *ACS Applied Maerials & Interfaces* vol. 2, pp. 3170-3178, 2010, doi: https://doi.org/10.1021/am100654p.

[242] Y, Xia, J. Ouyang, 'PEDOT: PSS films with significantly enhanced conductivities induced by preferential solvation with cosolvents and their application in polymer photovoltaic cells', *Journal of Materials Chemistry*, vol. 21, pp. 4927-4936, 2011, doi: https://doi.org/10.1039/C0JM04177G.

[243] C, Liu, F. Jiang, M. Huang, B. Lu, R. Yue, J.J. Xu, 'Free-standing PEDOT-PSS/Ca3Co4 composite films as novel thermoelectric materials', *Journal of Electronic Materials*, vol. 40, pp. 948-952, 2011, doi: https://doi.org/10.1007/s11664-010-1465-0.

[244] E, J. Bae, Y.H. Kang, K.-S. Jang, C. Lee, S.Y.J.N. Cho, 'Solution synthesis of telluride-based nano-barbell structures coated with PEDOT: PSS for spray-printed thermoelectric

generators', *NanoScale*, vol. 8, pp. 10885-10890, 2016, doi: https://doi.org/10.1039/C5NR07032E.

[245] A, Sahu, B. Russ, N.C. Su, J.D. Forster, P. Zhou, E.S. Cho, P. Ercius, N.E. Coates, R.A. Segalman, 'Bottom-up design of de novo thermoelectric hybrid materials using chalcogenide resurfacing', *Journal of Materials Chemistry A.*, vol. 5, pp. 3346-3357, 2017, doi: https://doi.org/10.1039/C6TA09781B.

[246] Y, Chen, J. Xu, Y. Yang, S. Li, W. Yang, T. Peng, X. Mao, Y. Zhao, 'PEDOT: PSS/graphene/PEDOT ternary film for high performance electrochemical electrode', *Journal of Material Science: Materials in Electronics*, vol. 26, pp. 8292-8300, 2015, doi: https://doi.org/10.1007/s10854-015-3494-1.

[247] J, C. Yu,J.I. Jang, B.R. Lee, G.-W. Lee, J.T. Han, M.H. Song, 'Highly efficient polymer-based optoelectronic devices using PEDOT: PSS and a GO composite layer as a hole transport layer', *ACS Applied Maerials & Interfaces*, vol. 6, pp. 2067-2073, 2014, doi: https://doi.org/10.1021/am4051487.

[248] W, Wang, M.A. Ruderer, E. Metwalli, S. Guo, E.M. Herzig, J. Perlich, P.J. 'Effect of methanol addition on the resistivity and morphology of PEDOT: PSS layers on top of carbon nanotubes for use as flexible electrodes', *Müller-Buschbaum, interfaces.*, vol. 7, pp. 8789-8797, 2015, doi: https://doi.org/10.1021/acsami.5b01327.

[249] K, Jo,T. Lee, H.J. Choi, J.H. Park, D.J. Lee, D.W. Lee, B.-S.J.L. Kim, 'Stable aqueous dispersion of reduced graphene nanosheets via non-covalent functionalization with conducting polymers and application in transparent electrodes', *Langmuir* vol. 27, pp. 2014-2018, 2011, doi: https://doi.org/10.1021/la104420p.

[250] K.S. Novoselov, A.K. Geim, S.V. Morozov, D.-e. Jiang, Y. Zhang, S.V. Dubonos, I.V. Grigorieva, A. Firsov, 'Electric field effect in atomically thin carbon films', *Science*, vol. 306, 2004, 666-669, 10.1126/science.1102896.

[251] A.K.J. Geim, 'Graphene: status and prospects', *Science* vol. 324, 2009, 1530-1534, 10.1126/science.1158877.

[252] L.L. Zhang, R. Zhou, X.J. Zhao, 'Graphene-based materials as supercapacitor electrodes', 20 (2010) 5983-5992.

[253] F, Li, K. Cai, S. Shen, S.J. Chen, 'Preparation and thermoelectric properties of reduced graphene oxide/PEDOT: PSS composite films', *Synthetic Metals*, vol. 197, pp. 58-61, 2014, doi: https://doi.org/10.1016/j.synthmet.2014.08.014.

[254] J, Xiong, F. Jiang, H. Shi, J. Xu, C. Liu, W. Zhou, Q. Jiang, Z. Zhu, Y.J.A.a.m. Hu, 'Liquid exfoliated graphene as dopant for improving the thermoelectric power factor of conductive PEDOT: PSS nanofilm with hydrazine treatment', *Interfaces.*, vol. 7, pp. 14917-14925, 2015, doi: https://doi.org/10.1021/acsami.5b03692.

[255] S, Zhou, Y. Guo, J.J.P.C.C.P. Zhao, ‘Enhanced thermoelectric properties of graphene oxide patterned by nanoroads’, *Physical Chemistry Chemical Physics*, vol. 18, pp. 10607-10615, 2016, doi: https://doi.org/10.1039/C6CP01012A.

[256] Y, Yan, Q.-F. Liang, H. Zhao, C.-Q. Wu, B.J. Li, ‘Thermoelectric properties of one-dimensional graphene antidot arrays’, *Physics Letters A*, vol. 376, pp. 2425-2429, 2012, doi: https://doi.org/10.1016/j.physleta.2012.06.010.

[257] V. Rathi, K. Singh, K.P.S. Parmar, R.K. Brajpuriya, A. Kumar, ‘Boosting Thermoelectric Performance of PEDOT: PSS/Bi2Te3 Hybrid Films via Structural and Interfacial Engineering’, *Organic Electronics.*, pp. 107103, 2024, https://doi.org/10.1016/j.orgel.2024.107103.

[258] A, Kumar, A. Patel, S. Singh, A. Kandasami, D.J.R.o.S.I. Kanjilal, ‘Apparatus for Seebeck coefficient measurement of wire, thin film, and bulk materials in the wide temperature range (80–650 K)’, *Review of Scientific Instruments*, vol. 90, pp, 2019, doi: https://doi.org/10.1063/1.5116186.

[259] H. Maharana, P. Kumar Rai, A. Basu, ‘Surface-mechanical and electrical properties of pulse electrodeposited Cu–graphene oxide composite coating for electrical contacts’, *Journal of Materials Science.*, vol. 52, 2017, https://doi.org/10.1007/s10853-016-0405-7.

[260] A, Giuri, S. Masi, S. Colella, A. Listorti, A. Rizzo, A. Kovtun, S. Dell'Elce, A. Liscio, C.J. ‘Rheological and physical characterization of PEDOT: PSS/graphene oxide nanocomposites for perovskite solar cells’, *Science.*, vol. 57, pp. 546-552, 2017, doi: https://doi.org/10.1002/pen.24554.

[261] Y, Li, X. Liu, J. Wang, H. Liu, S. Li, Y. Hou, W. Wan, W. Xue, N. Ma, J. Zhang, ‘Chemical nature of redox-controlled photoluminescence of graphene quantum dots by post-synthesis treatment’, *The Journal of Physical Chemistry*, vol. 120, pp. 26004-26011, 2016, doi: https://doi.org/10.1021/acs.jpcc.6b07935.

[262] X, Wu, J. Liu, D. Wu, Y. Zhao, X. Shi, J. Wang, S. Huang, G.J. He, ‘Highly conductive and uniform graphene oxide modified PEDOT: PSS electrodes for ITO-Free organic light emitting diodes’, *Journal of Materials Chemistry*: C, vol. 2, pp. 4044-4050, 2014, doi: https://doi.org/10.1039/C4TC00305E.

[263] P, “Goutham Raj,” A. Kanwat, J. Jang, ‘Enhanced organic photovoltaic properties via structural modifications in PEDOT: PSS due to graphene oxide doping’, *Material Bulletin*, vol. 74, pp. 346-352, 2016, doi: https://doi.org/10.1016/j.materresbull.2015.10.044.

[264] D, P. Kepić, Z.M. Marković, S.P. Jovanović, D.B. Peruško, M.D. Budimir, I.D, ‘Preparation of PEDOT: PSS thin films doped with graphene and graphene quantum dots’, *Synthetic Metals*, vol. 198, pp. 150-154, 2014, doi: https://doi.org/10.1016/j.synthmet.2014.10.017.

[265] Y, G. Seol, T.Q. Trung, O.-J. Yoon, I.-Y. Sohn, N.Lee, ‘Nanocomposites of reduced graphene oxide nanosheets and conducting polymer for stretchable transparent conducting

electrodes', *Journal of Materials Chemistry* vol. 22, pp. 23759-23766, 2012, doi: https://doi.org/10.1039/C2JM33949H.

[266] Z. Guo, J. Tang, J. Yao, Y. Li, 'Kinetic control in the synthesis of highly conductive solution-processable PEDOTs', '*Polymer Chemistry*., vol. 15, pp. 2191-2198, https://doi.org/10.1039/D4PY00220B.

[267] Y. Li, H. Xiang, J. Wang, B. Gao, J. Tang, C. Xiao, X. Wang, F. Wang, 'Template molecular weight-dependent PEDOT surface energy: impact on the photovoltaic performance of bulk-heterojunctions, *Journal of Materials Chemistry A*., vol. 10, pp. 23165-23174, 2022 https://doi.org/10.1039/D2TA06861C.

[268] S, Khasim, A. Pasha, N. Badi, M. Lakshmi, Y.K. Mishra, 'High performance flexible supercapacitors based on secondary doped PEDOT–PSS–graphene nanocomposite films for large area solid state devices', *RSC Advances*, vol. 10, pp. 10526-10539, 2020, doi: 10.1039/D0RA01116A.

[269] D. Ding, F. Sun, f. xia, Z. Tang, 'High-performance and flexible thermoelectric generator based on solution-processed composites of reduced graphene oxide nanosheets and bismuth telluride nanoplates', *Nanoscale Advances*, vol. 2, 2020, DOI: 10.1039/D0NA00118J.

[270] C, Kulsi, M. Mitra, K. Kargupta, D.J. Banerjee, 'Thermoelectric properties of nanostructured bismuth telluride (Bi2Te3) with annealing time and its composite with reduced graphene oxide (RGO)', *Journal of Material Science: Materials in Electronics*, vol. 30, pp. 1850-1860, 2019, doi: https://doi.org/10.1007/s10854-018-0457-3.

[271] D. Yoo, J. Kim, J.H. Kim, 'Direct synthesis of highly conductive PEDOT: PSS/graphene composites and their applications in energy harvesting systems', *Nano Research*, vol. 7, pp. 717-730, 2014 10.1007/s12274-014-0433-z.

[272] Y, Wang, H. Pang, Q. Guo, N. Tsujii, T. Baba, T. Baba, T.J. Mori, 'Flexible n-Type abundant chalcopyrite/PEDOT: PSS/graphene hybrid film for thermoelectric device utilizing low-grade heat', *Interfaces*., vol. 13, pp. 51245-51254, 2021, doi: https://doi.org/10.1021/acsami.1c15232.

[273] T. Mori, S. Priya, 'Materials for energy harvesting: At the forefront of a new wave', *MRS Bulletin*., vol. 43, pp. 176-180, 2018, https://doi.org/10.1557/mrs.2018.32.

[274] Z. Soleimani, S. Zoras, B. Ceranic, S. Shahzad, Y. Cui, 'A review on recent developments of thermoelectric materials for room-temperature applications', *Sustainable Energy Technologies and Assessments*, vol. 37, 100604, 2020, https://doi.org/10.1016/j.seta.2019.100604.

[275] I. Petsagkourakis, K. Tybrandt, X. Crispin, I. Ohkubo, N. Satoh, T. Mori, 'Thermoelectric materials and applications for energy harvesting power generation', *Science and Technology of Advanced Materials*., vol. 19, pp. 836-862, 2018, https://doi.org/10.1080/14686996.2018.1530938.

[276] N. Nandihalli, C.-J. Liu, T. Mori, 'Polymer based thermoelectric nanocomposite materials and devices: Fabrication and characteristics', *Nano Energy*., vol. 78, pp. 105186, 2020 https://doi.org/10.1016/j.nanoen.2020.105186.

[277] D, Vashaee, A.J. Shakouri, 'Improved thermoelectric power factor in metal-based superlattices', *Physics Review Letters*, vol. 92, pp. 106103, 2004, doi: https://doi.org/10.1103/PhysRevLett.92.106103.

[278] D. Zhao, S. Fabiano, M. Berggren, X. Crispin, 'Ionic thermoelectric gating organic transistors', *Nature Communications.*, vol. 8, 2017, https://doi.org/10.1103/PhysRevLett.92.106103

[279] F. Jiao, A. Naderi, D. Zhao, J. Schlueter, M. Shahi, J. Sundström, H. Granberg, J. Edberg, U. Ail, J. Brill, T. Lindström, M. Berggren, X. Crispin, 'Ionic thermoelectric paper', *Journal of Materials Chemistry A.*, vol. 5, pp. 16883-16888, 2017, *Journal of Materials Chemistry A*, vol. 5 pp. 16883-16888, 2017.

[280] K. Choi, S.L. Kim, S.i. Yi, J.H. Hsu, C. Yu, 'Promoting Dual Electronic and Ionic Transport in PEDOT by Embedding Carbon Nanotubes for Large Thermoelectric Responses', *ACS Applied Materials & Interfaces*., vol. 10 pp. 23891-23899, 2018 https://doi.org/10.1021/acsami.8b06850.

[281] H. Wang, U. Ail, R. Gabrielsson, M. Berggren, X. Crispin, 'Ionic Seebeck effect in conducting polymers', *Advanced Energy Materials.*, vol. 5, pp. 2015, 10.1002/aenm.201500044.

[282] X. Guan, H. Cheng, J. Ouyang, 'Significant enhancement in the Seebeck coefficient and power factor of thermoelectric polymers by the Soret effect of polyelectrolytes', *Journal of Materials Chemistry A.*, vol. 6, pp. 19347-19352, 2018, https://doi.org/10.1039/C8TA08387H

[283] D. Zhao, A. Martinelli, A. Willfahrt, T. Fischer, D. Bernin, Z.U. Khan, M. Shahi, J. Brill, M.P. Jonsson, S. Fabiano, X. Crispin, 'Polymer gels with tunable ionic Seebeck coefficient for ultra-sensitive printed thermopiles', *Nature Communications*., vol. 10, 2019, https://doi.org/10.1038/s41467-019-08930-7.

[284] H, Wang, D. Zhao, Z.U. Khan, S. Puzinas, M.P. Jonsson, M. Berggren, X.J. Crispin, 'Ionic thermoelectric figure of merit for charging of supercapacitors', *Advanced Electronic Materials*, vol. 3, pp. 1700013, 2017, doi: https://doi.org/10.1002/aelm.201700013.

[285] M, He, J. Ge, Z. Lin, X. Feng, X. Wang, H. Lu, Y. Yang, F.J.E. Qiu, E. Science, 'Thermopower enhancement in conducting polymer nanocomposites via carrier energy scattering at the organic–inorganic semiconductor interface', *Energy & Environmental Science*, vol. 5, pp. 8351-8358, 2012, doi: https://doi.org/10.1039/C2EE21803H.

[286] B, z. Endrődi, J.n. Mellár, Z.n. Gingl, C. Visy, C.J. Janáky, 'Molecular and supramolecular parameters dictating the thermoelectric performance of conducting polymers: a case study using poly (3-alkylthiophene)',*The Journal of Physical Chemistry* vol. 119, pp. 8472-8479, 2015, doi: https://doi.org/10.1021/acs.jpcc.5b00135.

[287] Y. Xuan, X. Liu, S. Desbief, P. Leclère, M. Fahlman, R. Lazzaroni, M. Berggren, J. Cornil, D. Emin, X. Crispin, 'Thermoelectric properties of conducting polymers: The case of poly(3-hexylthiophene)', *Physical Review B.*, vol. 82, pp. 115454, 2010, https://doi.org/10.1103/PhysRevB.82.115454.

[288] C. Bounioux, P. Díaz-Chao, M. Campoy-Quiles, M.S. Martín-González, A.R. Goñi, R. Yerushalmi-Rozen, C. Müller, 'Thermoelectric composites of poly(3-hexylthiophene) and carbon nanotubes with a large power factor', *Energy & Environmental Science.* Vol. 6, pp. 918-925, 2013, https://doi.org/10.1039/C2EE23406H.

[289] J. Rivnay, S. Inal, B.A. Collins, M. Sessolo, E. Stavrinidou, X. Strakosas, C. Tassone, D.M. Delongchamp, G.G. Malliaras, 'Structural control of mixed ionic and electronic transport in conducting polymers', *Nature Communications.,* vol. 7, pp. 11287, 2016, https://doi.org/10.1038/ncomms11287.

[290] B. Endrődi, J. Mellár, Z. Gingl, C. Visy, C. Janáky, 'Reasons behind the improved thermoelectric properties of poly(3-hexylthiophene) nanofiber networks', *RSC Advances.,* vol. 4 pp. 55328-55333, 2014, https://doi.org/10.1039/C4RA09037C

[291] S. Tokito, P. Smith, A.J. Heeger, 'Highly Conductive and Stiff Fibres of Poly(2,5-dimethoxy-p-phenylenevinylene) Prepared from Soluble Precursor Polymer', *Polymer*., vol. 32 pp. 464, 1991, https://doi.org/10.1016/0032-3861(91)90450-W.

[292] Q. Zhang, Y. Sun, W. Xu, D. Zhu, 'Thermoelectric energy from flexible P3HT films doped with a ferric salt of triflimide anions', *Energy & Environmental Science.,* vol. 5, pp. 9639-9644, 2012, https://doi.org/10.1039/C2EE23006B.

[293] C, Bounioux, P. Díaz-Chao, M. Campoy-Quiles, M.S. Martín-González, A.R. Goni, R. Yerushalmi-Rozen, C.J.E. Müller, E. Science, 'Thermoelectric composites of poly (3-hexylthiophene) and carbon nanotubes with a large power factor, *Energy & Environmental Science*, vol. 6, pp. 918-925, 2013, doi: https://doi.org/10.1039/C2EE23406H.

[294] R.K. Singh, J. Kumar, R. Singh, R. Kant, R.C. Rastogi, S. Chand, V. Kumar, 'Structure–conductivity correlation in ferric chloride-doped poly(3-hexylthiophene)', *New Journal of Physics*, vol.8, pp. 112, 2006, 10.1088/1367-2630/8/7/112.

[295] M, Brinkmann, 'Structure and morphology control in thin films of regioregular poly(3-hexylthiophene)', *Journal of Polymer Science Part B: Polymer Physics.,* vol. 49, pp. 1218-1233, 2011, doi: https://doi.org/10.1002/polb.22310.

[296] C.Y. Yang, C. Soci, D. Moses, A.J. Heeger, 'Aligned P3HT film: Structural order and transport properties', *Synthetic Metals*, vol. 155, pp. 639-642, 2005, https://doi.org/10.1016/j.synthmet.2005.08.019.

[297] J. Yamamoto, Y. Furukawa, 'Electronic and Vibrational Spectra of Positive Polarons and Bipolarons in Regioregular Poly(3-hexylthiophene) Doped with Ferric Chloride', *The Journal of Physical Chemistry B.*, vol. 119, pp.4788-4794, 2015, https://doi.org/10.1021/jp512654b.

[298] R.K. Singh, J. Kumar, R. Singh, R. Kant, S. Chand, V. Kumar, Micromorphology, photophysical and electrical properties of pristine and ferric chloride doped poly(3-hexylthiophene) films, *Materials Chemistry and Physics*., vol. 104, pp. 390-396, 2007 https://doi.org/10.1016/j.matchemphys.2007.01.024.

[299] S. Gregory, R. Hanus, A. Atassi, J. Rinehart, J. Wooding, A. Menon, M. Losego, G. Snyder, S. Yee, 'Quantifying charge carrier localization in chemically doped semiconducting polymers', *Nature Materials*., vol. 20, pp.1-8, 2007, https://doi.org/10.1038/s41563-021-01008-0.

[300] A. Singh, Z. Salmi, N. Joshi, P. Jha, P. Decorse, H. Lecoq, S. Lau-Truong, M. Jouini, D.K. Aswal, M.M. Chehimi, 'Electrochemical investigation of free-standing polypyrrole–silver nanocomposite films: a substrate free electrode material for supercapacitors', *RSC Advances.,* vol. 3, pp. 24567-24575, 2013, https://doi.org/10.1039/C3RA42786B.

[301] C.D. Wagner, 'Handbook of x-ray photoelectron spectroscopy: a reference book of standard data for use in x-ray photoelectron spectroscopy', 1979.

[302] G.J. Beamson, 'High Relution XPS of Organic Polymers', *The Scienta ESCA 300 Database,* (1992).

[303] A.P. Grosvenor, B.A. Kobe, M.C. Biesinger, N.S. McIntyre, 'Investigation of multiplet splitting of Fe 2p XPS spectra and bonding in iron compounds', S*urface and Interface Analysis., vol.* 36, pp.1564-1574, 2004.

[304] Z, Akdeniz, M.P. Tosia, 'Ionic Conduction and Molecular Structure of Molten FeCl3', *Surface And Interface Analysis* vol. 53, pp. 960-962, 1998, doi: https://doi.org/10.1002/sia.1984.

[305] M. Russo, G. Polzonetti, A. Furlani, A. Bearzotti, I. Fratoddi, P. Altamura, 'X-ray Photoelectron Spectroscopy and Scanning Electron-microscopy Characterization of Novel Poly(monosubstituted)acetylenes Containing Doping Species', *Journal Of Vacuum Science & Technology A-Vacuum Surfaces and Films.,* vol. 16 pp. 35-44, 1998, https://doi.org/10.1116/1.581006.

[306] Z, Yan, Z. Zhuxia, L. Tianbao, L. Xuguang, X. Bingshe, 'XPS and XRD study of FeCl3–graphite intercalation compounds prepared by arc discharge in aqueous solution', *Spectrochimica Acta Part A: Molecular and Biomolecular Spectroscopy*, vol. 70, pp. 1060-1064, 2008, doi: https://doi.org/10.1016/j.saa.2007.10.031.

[307] X. Wang, A.K. Kyaw, C. Yin, F. Wang, Q. Zhu, T. Tang, P.I. Yee, J.J. Xu, 'Enhancement of thermoelectric performance of PEDOT: PSS films by post-treatment with a superacid', *RSC Advances* vol. 8, pp. 18334-18340, 2018, DOI 10.1039/C8RA02058B.

[308] M, S. Dresselhaus, G. Chen, M.Y. Tang, R. Yang, H. Lee, D. Wang, Z. Ren, J.P. 'Fleurial, P.J. Gogna, 'New directions for low-dimensional thermoelectric materials', vol. 19, pp. 1043-1053, 2007, doi: https://doi.org/10.1002/adma.200600527.

[309] G, J. Snyder, E.S. Toberer, 'Complex thermoelectric materials', *Advanced Materials*, vol. 7, pp. 105-114, 2008, doi: https://doi.org/10.1038/nmat2090.

[310] L, “E.J.S. Bell,” Cooling, heating, generating power, and recovering waste heat with thermoelectric systems, *Science*, vol. 321, pp. 1457-1461, 2008, doi: 10.1126/science.115889.

[311] D.M. Rowe, Thermoelectrics handbook: macro to nano, CRC press2018.

[312] W, Liu, K.C. Lukas, K. McEnaney, S. Lee, Q. Zhang, C.P. Opeil, G. Chen, Z.J Ren, E. ‘Science, Studies on the Bi2Te3–Bi2Se3–Bi2Se3 system for mid-temperature thermoelectric energy conversion, *Energy & Environmental Science*, vol. 6, pp. 552-560, 2013, doi: https://doi.org/10.1039/C2EE23549H.

[313] Y, Pei, A.D. LaLonde, N.A. Heinz, G.J. Snyder, High thermoelectric figure of merit in PbTe alloys demonstrated in PbTe–CdTe, *Advanced Energy Materials*, vol. 2, pp. 670-675, 2012, doi: https://doi.org/10.1002/aenm.201100770.

[314] E, K. Lee, L. Yin, Y. Lee, J.W. Lee, S.N. Cha, D. Whang, G.S. Hwang, K.J. Hippalgaonkar, ‘Large thermoelectric figure-of-merits from SiGe nanowires by simultaneously measuring electrical and thermal transport properties’, *Nano Letters* vol. 12, pp. 2918-2923, 2012, doi: https://doi.org/10.1021/nl300587u.

[315] B.T. McGrail, A. Sehirlioglu, E.J Pentzer, ‘Polymer composites for thermoelectric applications’, 54 (2015) 1710-1723.

[316] L, D. Zhao, J. He, C.-I. Wu, T.P. Hogan, X. Zhou, C. Uher, V.P. Dravid, M.G. Kanatzidis, ‘Thermoelectrics with earth abundant elements: high performance p-type PbS nanostructured with SrS and CaS’, *Journal of the American Chemical Society*, vol. 134, pp. 7902-7912, 2012, doi: https://doi.org/10.1021/ja301772w.

[317] H, Yang, L.A. Jauregui, G. Zhang, Y.P. Chen, Y.J. Wu, ‘Nontoxic and abundant copper zinc tin sulfide nanocrystals for potential high-temperature thermoelectric energy harvesting’, *Nano Letters*, vol. 12, pp. 540-545, 2012, doi: https://doi.org/10.1021/nl201718z.

[318] D.X. Crispin, E. Science, Polymer-based organic thermoelectric generators, *Energy & Environmental Science* (2012), https://doi.org/10.1039/C2EE22777K.

[319] C. Gao, G. Chen, ‘Conducting polymer/carbon particle thermoelectric composites: Emerging green energy materials’, *Composites Science and Technology.*, vol. 124, pp. 52-70, 2016, https://doi.org/10.1016/j.compscitech.2016.01.014.

[320] C. Dun, C.A. Hewitt, H. Huang, J. Xu, D.S. Montgomery, W. Nie, Q. Jiang, D.L. Carroll, ‘Layered Bi2Se3 Nanoplate/Polyvinylidene Fluoride Composite Based n-type Thermoelectric Fabrics’, *ACS Applied Materials & Interfaces.*, vol. 7, pp. 7054-7059, 2015, https://doi.org/10.1021/acsami.5b00514.

[321] D. Fa, B. Yu, Y. Miao, ‘Synthesis of ultra-long nanowires of nickel phosphate by a template-free hydrothermal method for electrocatalytic oxidation of glucose’, *Colloids and Surfaces A: Physicochemical and Engineering Aspects’* vol. 564, pp. 31-38, 2019, https://doi.org/10.1016/j.colsurfa.2018.12.035.

[322] C. Yu, X. Liang, T. Zhao, P. Zhu, G. Li, R. Cao, R. Sun, C.P. Wong, 'Synthesis and electromagnetic shielding performance of nickel nanowires with controllable morphology', *Materials Letters*., vol. 236, pp. 112-115, 2019, https://doi.org/10.1016/j.matlet.2018.10.074.

[323] L. Jin, S. Ma, W. Deng, C. Yan, T. Yang, X. Chu, G. Tian, D. Xiong, J. Lu, W. Yang, 'Polarization-free high-crystallization β-PVDF piezoelectric nanogenerator toward self-powered 3D acceleration sensor', *Nano Energy.,* vol. 50, pp. 632-638, 2018, https://doi.org/10.1016/j.nanoen.2018.05.068.

[324] L.L. Sun, B. Li, Z.G. Zhang, W.H. Zhong, 'Achieving very high fraction of β-crystal PVDF and PVDF/CNF composites and their effect on AC conductivity and microstructure through a stretching process', *European Polymer Journal.*, vol. 46, pp. 2112-2119, 2010, https://doi.org/10.1016/j.eurpolymj.2010.09.003.

[325] B, Zhao, C.B. Park, 'Tunable electromagnetic shielding properties of conductive poly (vinylidene fluoride)/Ni chain composite films with negative permittivity', *Journal of Materials Chemistry:C*, vol. 5, pp. 6954-6961, 2017, doi: https://doi.org/10.1039/C7TC01865G.

[326] B. Zhao, C. Zhao, M. Hamidinejad, C. Wang, R. Li, S. Wang, K. Yasamin, C.B. Park, 'Incorporating a microcellular structure into PVDF/graphene–nanoplatelet composites to tune their electrical conductivity and electromagnetic interference shielding properties', *Journal of Materials Chemistry C.*, vol. 6, pp. 10292-10300, 2018, https://doi.org/10.1039/C8TC03714K.

[327] Y, Feng, W. Li, Y. Hou, Y. Yu, W. Cao, T. Zhang, W.J. Fei, 'Enhanced dielectric properties of PVDF-HFP/BaTiO 3-nanowire composites induced by interfacial polarization and wire-shape', *Journal of Materials Chemistry:C*, vol. 3, pp. 1250-1260, 2015, doi: https://doi.org/10.1039/C4TC02183.

[328] W. Zhang, Z. Shi, F. Zhang, X. Liu, J. Jin, L. Jiang, 'Superhydrophobic and superoleophilic PVDF membranes for effective separation of water-in-oil emulsions with high flux', *Advanced materials (Deerfield Beach, Fla.).,* vol.25, pp. 2071-2076, 2013, https://doi.org/10.1002/adma.201204520.

[329] P. Kaspar, D. Sobola, K. Castkova, R. Dallaev, E. Šťastná, P. Sedlak, A. Knápek, T. Trčka, V. Holcman, 'Case Study of Polyvinylidene Fluoride Doping by Carbon Nanotubes', *Materials 14*, pp. 1428,2021, https://doi.org/10.3390/ma14061428.

[330] R.P.S. Chakradhar, G. Prasad, P. Bera, C. Anandan, 'Stable superhydrophobic coatings using PVDF–MWCNT nanocomposite, *Applied Surface Science,* vol. 301, pp. 208-215, 2014, https://doi.org/10.3390/ma14061428.

[331] D. Briggs, C. D. Wanger, W. M. Riggs, L. E. Davis, J. F. Moulder 'Handbook of X-ray Photoelectron Spectroscopy, *Physical Electronics Division*., Eden Prairie, Minnesota, USA, 1979. 190 pp. $195, 3 (1981) .

[332] D. Li, Y. Gong, M. Wang, C. Pan, ‘Preparation of Sandwich-like NiCo2O4/rGO/NiO Heterostructure on Nickel Foam for High-Performance Supercapacitor Electrodes’, *Nano-Micro Letters*., vol. 9, 16, 2016, https://doi.org/10.1007/s40820-016-0117-1.

[333] I. Paulraj, T.-F. Liang, T.-S. Yang, C.-H. Wang, J.-L. Chen, Y.W. Wang, C.-J. Liu, High ‘Performance of Post-Treated PEDOT: PSS Thin Films for Thermoelectric Power Generation Applications’, *ACS Applied Materials & Interfaces*., vol. 13, pp. 42977-42990, 2021, https://doi.org/10.1021/acsami.1c13968.

[334] Q. Meng, Y. Qiu, K. Cai, Y. Ding, M. Wang, H. Pu, Q. Yao, L. Chen, J. He, ‘High Performance and Flexible Polyvinylpyrrolidone/Ag/Ag2Te Ternary Composite Film for Thermoelectric Power Generator’, *ACS Appl. Mater. Interfaces*, vol. 11, pp. 33254, 2019 https://doi.org/10.1021/acsami.9b11217.

[335] Liang, B., Song, Z., Wang, M., Wang, L., & Jiang, ‘Fabrication and thermoelectric properties of graphene/Bi2Te3 composite materials’, *Journal of Nanomaterials.*, vol. 1, pp. 210767, 2013, https://doi.org/10.1155/2013/210767.

[336] Liang, B., et al., Fabrication and Thermoelectric Properties of Graphene/Bi2Te3 Composite Materials. *Journal of Nanomaterials*, 2013, https://doi.org/10.1155/2013/210767.

LIST OF PUBLICATIONS

A. Published

1. **Vaishali Rathi**, Kamal Singh, K.P.S. Parmar, Ranjeet K. Brajpuriya and Ashish Kumar Graphene-derived composites: a new Frontier in thermoelectric energy conversion, Energy Advance, *(SCI IF 3.2)*; DOI: 10.1039/D3YA00526G
2. **Vaishali Rathi**, Kamal Singh, K.P.S. Parmar, Ranjeet K. Brajpuriya and Ashish Kumar, Boosting thermoelectric performance of PEDOT: PSS/Bi2Te3 hybrid films, Organic Electronics *(SCI IF 2.9)* https://doi.org/10.1016/j.orgel.2024.107103
3. **Vaishali Rathi**, Kamal Singh, K.P.S. Parmar, Ranjeet K. Brajpuriya and Ashish Kumar, improved thermoelectric performance of PEDOT: PSS/Bi2Te3/reduced graphene oxide ternary composite films for energy harvesting applications *RSC (SCI IF 3.9)*; DOI: 10.1039/d4ra06184e
4. **Vaishali Rathi**, Manoj Sathwane, Kamal Singh, K.P.S. Parmar, Pradip K. Maji, Ranjeet K. Brajpuriya and Ashish Kumar, Ferric Chloride Doped P3HT Flexible films: A promising Materials for Thermoelectric Devices,), Scientific Reports, Under Review.
5. **Vaishali Rathi**, Kamal Singh, K.P.S. Parmar, Ranjeet K. Brajpuriya and Ashish Kumar, High efficiency and flexibility in n-type PVDF Thermoelectric film with incorporation of Nickel nanowire. Polymer Composites, Under Review.
6. **Vaishali Rathi**, Kamal Singh, K.P.S. Parmar, Ranjeet K. Brajpuriya and Ashish Kumar, Doping Strategies in Organic Thermoelectric Materials: Advances, Mechanisms, and Challenges for Enhanced Performance, RSC Advances, Under Review.

B. Collaboration Work

1. Kamal Singh, **Vaishali Rathi,** et.al., Ion-induced transformation of shallow defects into deep-level defects in GaN epilayers, NIMB, 522,165362(2024).
2. Kamal Singh, **Vaishali Rathi**, et.al., Disorder induced in GaN thin films by 200 MeV silver ions, NIMB, 551,165346(2024).
3. Kamal Singh, **Vaishali Rathi**, et.al., Impact of swift heavy oxygen ion irradiation on the performance of Pt/GaN Schottky diodes and epitaxial layers: A comparative study, J. Appl. Phys. 134, 165704 (2023).
4. Priyanka Bishnoi, **Vaishali Rathi** et.al., Investigating NIR radiated Luminescence Temperature sensing and Laser induced thermal effect of Ho, Yb doped MgOY2O3 nanocomposites for security ink applications, ACS, Applied Nanomaterials, (manuscript communicated and under review).

NATIONAL AND INTERNATIONAL CONFERENCE

1. **Vaishali Rathi**, Kamal Singh, K.P.S. Parmar, Ranjeet K. Brajpuriya and Ashish Kumar "Optimising Thermoelectric Efficiency in N-type PVDF Films Through Nickel Nanowire Incorporation" **IUMRS-ICA**, 35th AGM of MRSI & 6th Indian Materials Conclave, Dec 03-06, 2024, Indore, India.
2. **Vaishali Rathi**, Kamal Singh, K.P.S. Parmar, Ranjeet K. Brajpuriya and Ashish Kumar International Conference on Physics for Sustainable Development (ICPSD-2024)" held at Central University of Jammu, J&K, (April 04-05, 2024).
3. **Vaishali Rathi**, Kamal Singh, K.P.S. Parmar, Ranjeet K. Brajpuriya and Ashish Kumar organized by Applied science cluster, UPES, (May 29 – 31, 2024).
4. **Vaishali Rathi**, Kamal Singh, K.P.S. Parmar, Ranjeet K. Brajpuriya and Ashish Kumar, "High performance Thermoelectric Performance of PEDOT: PSS/ Bi2Te3 Binary composite film", **(IYRC-24)**, organized by Applied science cluster, UPES, Dehradun on (Feb 25 – 28, 2023).
5. **Vaishali Rathi**, Kamal Singh, K.P.S. Parmar, Ranjeet K. Brajpuriya and Ashish Kumar, "Enhanced thermoelectric Performance of PEDOT: PSS/ Bi2Te3 composite film **(ICEMRB-2023)"** held at Manav Rachna University (MRU), Faridabad, Haryana, (Dec, 18 – 22, 2023).
6. **Vaishali Rathi**, Kamal Singh, K.P.S. Parmar, Ranjeet K. Brajpuriya and Ashish Kumar, "Organic-Inorganic Composite Materials for Thermoelectric Applications", **Materials for Energy & Sustainable Development (MESD-2023)"** organized by JNU New Delhi, (Oct 28 – 30, 2023).
7. **Vaishali Rathi**, Kamal Singh, K.P.S. Parmar, Ranjeet K. Brajpuriya and Ashish Kumar International Conference "Recent Progress in Thermal Transport Theory & Experiments" held at Trieste, Italy on (May 30-03, 2022) (Hybrid mode).
8. **Vaishali Rathi**, Kamal Singh, K.P.S. Parmar, Ranjeet K. Brajpuriya and Ashish Kumar, "Organic Thermoelectric Generator for Scalable Technology" **International Young Researchers Conclave 2023'** Organized by UPES R&D, (Jan 19- 20, 2023).

9. **‘STUTI’** program on Scientific and Technological Infrastructure Program Organizing by CASE, held at IIT Jodhpur. (Aug 8–14, 2022).
10. National Workshop on “Utilization of nanomaterials & instrumentation techniques for energy applications” held at SVGU, Jaipur on (March 01-15, 2022).
11. Awareness Program on Advance Materials and their Applications Organized by Applied science cluster, (UPES) (Sep 7–10, 2022).
12. International Conference on ‘Interdisciplinary research in cancer Biology (IC- IRCB) Organized by SoHST, UPES (Hybrid mode). (Sep 22-23, 2022)
13. International Conference “Recent Progress in Thermal Transport Theory & Experiments” held at Trieste, Italy on (May 30-03, 2022) (Hybrid mode).

Vaishali Rathi

FABRICATION OF PRINTABLE FLEXIBLE THERMOELECTRIC MATERIAL AND DEVICES

Quick Submit

Quick Submit

University of Petroleum & Energy Studies

Document Details

Submission ID

trn:oid:::1:3260725829

Submission Date

May 26, 2025, 4:12 PM GMT+5:30

Download Date

May 28, 2025, 4:25 PM GMT+5:30

File Name

Vaishali-thesis_final_for_plag_run.pdf

File Size

5.8 MB

141 Pages

44,557 Words

243,494 Characters

8% Overall Similarity

The combined total of all matches, including overlapping sources, for each database.

Filtered from the Report

- Bibliography
- Quoted Text
- Small Matches (less than 14 words)

Exclusions

- 7 Excluded Sources

Match Groups

109 Not Cited or Quoted 8%
Matches with neither in-text citation nor quotation marks

1 Missing Quotations 0%
Matches that are still very similar to source material

0 Missing Citation 0%
Matches that have quotation marks, but no in-text citation

0 Cited and Quoted 0%
Matches with in-text citation present, but no quotation marks

Top Sources

6% Internet sources
3% Publications
0% Submitted works (Student Papers)

Integrity Flags

1 Integrity Flag for Review

Replaced Characters
75 suspect characters on 56 pages
Letters are swapped with similar characters from another alphabet.

Our system's algorithms look deeply at a document for any inconsistencies that would set it apart from a normal submission. If we notice something strange, we flag it for you to review.

A Flag is not necessarily an indicator of a problem. However, we'd recommend you focus your attention there for further review.